The cell biology of the FcRn-albumin recycling system

Andreas-Joachim Pannek

ORCID ID:

0000-0001-9430-2840

From Bad Hersfeld, Germany

Submitted in total fulfilment of the requirements of the joint degree of Doctor of Philosophy (PhD)

of

The Department of Biochemistry and Pharmacology

The University of Melbourne

and

The Medical Faculty

The Rheinische Friedrich-Wilhelms-Universität Bonn

Bonn/Melbourne, 2022

Performed and approved by The Medical Faculty of The Rheinische Friedrich-Wilhelms-Universität Bonn and The University of Melbourne

1. Supervisor: Prof. Dr. Christian Kurts

2. Supervisor: Prof. Dr. Paul Gleeson

Month and year of the original thesis submission: October 2021

Month and year of the oral examination: May 2022

Institute in Bonn: Institute of Experimental Immunology

Director: Prof. Dr. med. Christian Kurts

Table of contents

Abbreviations

Abbreviation	Full name
AAV	Adeno associated virus
AB	Antibody
ABD	Albumin binding domain
ACK	Ammonium-chloride-potassium
ADP	Adenosine diphosphate
AF-488	Alexa Fluor® 488
AF-568	Alexa Fluor® 567
AF-647	Alexa Fluor® 647
AP-2	Adaptor protein 2
APC	Antigen presenting cell
Arf6	ADP ribosylation factor
AS	AS2863619
ATP	Adenosine triphosphate
B2M/β_2m	β2-microglobulin
BCR	B cell receptor
BM	Bone marrow
BMDM	Bone marrow-derived macrophage
BOEC	Blood outgrowth endothelial cell
BSA	Bovine serum albumin
BU	Bethesda unit
C (e.g., C-DMEM)	Complete (DMEM)
CAR	Chimeric antigen receptor
CCR4	C-C motif chemokine receptor 4
CD	Cluster of differentiation
Cdc42	Cell division cycle 42
CDK8/19	Cyclin-dependent kinase 8 and 19
CEC	Circulating endothelial cell
CFSE	Carboxyfluorescein succinimidyl ester
CLIC	Clathrin-independent carrier
CSF-1/M-CSF	Colony stimulating factor 1/macrophage stimulating factor
DAPI	4',6-diamidino-2-phenylindole
DC	Dendritic cell
DMEM	Dulbecco's modified eagle medium
DMSO	Dimethyl sulfoxide
DNA	Deoxyribonucleic acid
EBM	Endothelial basal medium
ECFC	Endothelial colony forming cell
EDTA	Ethylenediaminetetraacetic acid
EEA1	Early endosome antigen 1
EGF	Epidermal growth factor
EGFR	Epidermal growth factor receptor

Abbreviation	Full name
EGM	Endothelial growth medium
EIPA	5-(N-ethyl-N-isopropyl) amiloride
ELISA	Enzyme-linked immunosorbent assay
EPC	Endothelial progenitor cell
ER	Endoplasmic reticulum
ESCRT	Endosomal sorting complexes required for transport
FACS	Fluorescence-activated cell scanning
FC	Flow cytometry
FcRn	Neonatal Fc receptor
FCS	Foetal calf serum
FFS	Fluorescence fluctuation spectroscopy
FGFR3	Fibroblast growth factor receptor 3
FGF-β	Basic fibroblast growth factor
FIX	Coagulation factor IX
FIXa	Activated coagulation factor IX
FLIM	Fluorescence lifetime imaging microscopy
FMO	Fluorescence minus one
Foxp3	Forkhead box P3
FRET	Förster resonance energy transfer
FVIII	Coagulation factor VIII
FVIIIa	Activated coagulation factor VIII
FVIII-Alb	FVIII-Albumin fusion protein
FX	Coagulation factor X
GaAsP	Gallium arsenide phosphide
GAPDH	Glyceraldehyde 3-phosphate dehydrogenase
GEEC	Glycosylphosphotidylinositol-anchored protein enriched compartment
GFP	Green fluorescent protein
gp60	Glycoprotein 60/albondin
GTP	Green fluorescent protein
Gy	Gray
HBS	HEPES-buffered saline
HCV	Hepatitis C virus
HEK293	Human embryonic kidney 293 cells
HeLa	Immortalised cervical cancer cell line isolated from Henrietta Lacks
HemA	Hemophilia A
HEPES	4-(2-hydroxyethyl)-1-piperaziineethanesulfonic acid
HER2	Human epidermal growth factor receptor 2
hFcRn	Human neonatal Fc receptor
hFVIII	Human coagulation factor VIII
HIV	Human immunodeficient virus
HMEC-1	Human microvascular endothelial cell line 1
HSA	Human serum albumin
Hsc70	Heat shock protein 70

Abbreviation	Full name
hTRAIL	Human tumor necrosis factor superfamily member 10
i.v.	Intravenous
IF	Immunofluorescence
IFNγ	Interferon gamma
Ig	Immunoglobulin
IL (e.g., IL-2)	Interleukin (e.g., interleukin-2)
ILV	Intralumenal vesicles
IRES	Internal ribosomal entry site
ITI	Immune tolerance induction
IU	Injection unit
kDa	Kilodalton
KDEL-R	KDEL receptor
KIF13A	Kinesin family member 13A
KO	Knock-out
LAMP	Lysosomal associated membrane (glyco-)protein
LB	Lysogeny broth
LDS	Lithium dodecyl sulfate
lgp-A	Lysosomal glycoprotein A
LSEC	Liver sinusoidal endothelial cell
LV	Lentivirus/lentiviral
M6PR	Mannose 6-phosphate receptor
MACS	Magnetic-activated cell sorting
MEM	Minimum essential media
MeOH	Methanol
MFI	Mean fluorescent intensity
MHC	Major histocompatibility complex
MOPS	3-(N-morpholino)-propanesulfonic acid
MSA	Murine serum albumin
MSA	Murine serum albumin
MTOC	Microtubule-organising centre
MVB	Multivesicular body
NA	Numerical aperture
OEC	Outgrowth endothelial cell
ORF	Open reading frame
OVA	Ovalbumin
PAGE	Polyacrylamide gel electrophoresis
PBMC	Peripheral blood mononuclear cell
PBS	Phosphate-buffered saline
PD-1	Programmed cell death protein 1
PD-L1	Programmed death-ligand 1
PECAM	Platelet endothelial cell adhesion molecule
PEG	Polyethylene glycol
PFA	Paraformaldehyde
PI	Protease inhibitor
PI3K	Phosphoinositide 3-kinase

Abbreviation	Full name
PMA	Phorbol-12-myristae-13-acetate
PtdIns(3)P	Phosphatidylinositol 3-phosphate
PVDF	Polyvinylidene fluoride
R3-IGF-1	Recombinant (R3G) Insulin-like growth factor 1
Rab	Ras associated binding protein
Rac1	Rac family small GTPase 1
RBC	Red blood cell
rFVIII	Recombinant FVIII
rHSA	Recombinant human serum albumin
RICS	Raster image correlation spectroscopy
RIPA	Radioimmunoprecipitation assay buffer
RNA	Ribonucleic acid
ROI	Region of interest
rpm	Revolutions per minute
RPMI	Roswell Park Memorial Institute
RT	Room temperature
SATA	S-acetylthioacetate
SDS	Sodium dodecyl sulfate
SEM	Standard error of the mean
SFM	Serum free
SMCC	Succinimidyl 4-(N-maleimidomethyl)-cyclohexane-1-carboxylate
SNARE	Soluble N-ethylmaleimide-sensitive-factor attachment receptor
SNX	Sorting nexin
SP	Signal peptide
SV40	Simian (vacuolating) virus 40
TCA	Trichloroacetic acid
TCR	T cell receptor
Tg	Transgenic
TGF-β	Transforming growth factor beta
TGN	*Trans*-Golgi network
TLR	Toll like receptor
Treg	Regulatory T cell
TxRed	Texas Red
U	Unit
VAMP	Vesicle associated membrane protein
VE	Vascular endothelial
VEGF	Vascular endothelial growth factor
VPS35	Vacuolar protein sorting 35 ortholog/retromer complex component
vWF	Van Willebrand factor
WB	Western Blot
WPB	Weibel Palade body
WT	Wildtype

List of tables

List of figures

Abstract

Human serum albumin (HSA) is the most abundant protein in plasma and has an exceptionally long circulatory half-life of around three weeks in humans. The enhanced half-life properties of HSA result from the selective interaction with the neonatal Fc receptor (FcRn) in acidic endosomes, which protects endocytosed albumin from lysosomal degradation and mediates recycling back to the plasma membrane. Endothelial and innate immune cells are considered the most relevant cells for FcRn-mediated albumin homeostasis *in vivo.* However, little is known about FcRn-albumin cell biology in physiologically relevant primary cells and the spatiotemporal aspects of the FcRn-albumin interaction within intracellular endosomes. My studies have used cell biological and biophysical approaches to examine FcRn-albumin interactions and trafficking in primary macrophages and endothelial cells.

Here, I used two independent biophysical approaches to visualise the intracellular receptor-ligand interactions within globular endosomes and tubular transport carriers of primary macrophages. Firstly, fluorescence lifetime imaging microscopy (FLIM) of Förster resonance energy transfer (FRET) and secondly, raster image correlation spectroscopy (RICS) to monitor the diffusion kinetics of single fluorescent-labelled HSA molecules. Based on these analyses, I identified an interaction between FcRn and albumin within intracellular endosomes, and emerging tubules, in human FcRn-expressing macrophages. Furthermore, I detected a higher population of immobile, FcRn-bound wildtype HSA molecules within the lumen of endosomal structures compared to the non-FcRn binding rHSA^{H464Q} mutant. My findings revealed the kinetics of FcRn-albumin binding within endosomal structures for recruitment into transport carriers for recycling.

To investigate FcRn-albumin cell biology in physiologically relevant primary endothelial cells, I established cell lines of primary human vascular endothelial cells from the outgrowth in culture of blood endothelial precursors known as blood outgrowth endothelial cells (BOECs). My observations show that these endothelial cell lines internalised fluorescent-labelled HSA efficiently via fluid

phase macropinocytosis. Intracellular HSA molecules co-localised with FcRn in endosomal structures potentially allowing the interaction of the receptor with its ligand. Wildtype HSA, but not the non-FcRn binding rHSA^{H464Q} mutant, was sorted into FcRn-positive tubular transport carriers, that are likely to mediate recycling of endocytosed HSA back to the plasma membrane. These findings support the proposed contribution of vascular endothelial cells to albumin homeostasis *in vivo*.

Understanding the underlying mechanisms of FcRn-albumin cell biology and the contribution of different cell types to albumin homeostasis is important for the design and generation of half-life extended albumin fusion proteins for the treatment of serum protein-related diseases such as hemophilia A (HemA). Despite exhibiting enhanced pharmacological properties, to date, very few albumin fusion protein therapeutics have been approved for the treatment of human patients. In particular for HemA, the treatment using recombinant coagulation factor VIII (FVIII) products is aggravated by the frequent development of inhibitory antibodies against FVIII in HemA patients which subsequently have to undergo highly expensive and burdensome immune tolerance induction protocols.

In this study, I have established an imaging flow cytometry-based antigen uptake assay to investigate the internalisation of FVIII-Albumin fusion proteins by FVIII-specific B cells expanding the knowledge about how albumin fusion proteins might contribute to immune tolerance induction towards FVIII *in vivo*. Additionally, I established two *in vitro* protocols which, in combination, allow the generation of high numbers of FVIII-specific regulatory T cells. These antigen-specific Tregs have the potential to suppress immune responses against recombinant FVIII *in vivo* and represent an alternative approach to facilitate immune tolerance towards FVIII in HemA patients.

In summary, this thesis has revealed the fundamental aspects of FcRn-albumin cell biology and trafficking in primary macrophages and endothelial cells, and potential strategies for immune tolerance induction using FVIII-Albumin fusion proteins in the context of HemA.

Declaration

The work presented in this thesis was carried out at the Department of Biochemistry and Pharmacology, Bio21 Molecular Science and Biotechnology Institute, The University of Melbourne and the Medical Faculty, Institute for Experimental Immunology, The Rheinische Friedrich-Wilhelms Universität Bonn from December 2017 to October 2021. This is to certify that:

I. This thesis comprises only my original work towards my joint PhD award except where indicated in the preface;
II. Due acknowledgement has been made in the text to all other material used; and
III. This thesis is fewer than 100,000 words in length, exclusive of tables, bibliographies and appendices.

Andreas-Joachim Pannek, October 2021

Preface

The experiments outlined in Chapter 3 were carried out in collaboration with Dr. Elizabeth Hinde (School of Physics, Bio21 Molecular Science and Biotechnology Institute, The University of Melbourne) and were submitted in form of a manuscript with the title “Dynamics of intracellular neonatal Fc receptor-ligand interactions in primary macrophages using biophysical fluorescence techniques” for publication on 04.08.2021.

Fluorescence lifetime imaging microscopy in combination with Förster resonance energy transfer and raster image correlation spectroscopy data was acquired under the supervision of Dr. Elizabeth Hinde (School of Physics, Bio21 Molecular Science and Biotechnology Institute, The University of Melbourne).

Data analysis of fluorescence lifetime imaging microscopy in combination with Förster resonance energy transfer and raster image correlation spectroscopy was carried out by Dr. Elizabeth Hinde (School of Physics, Bio21 Molecular Science and Biotechnology Institute, The University of Melbourne).

Experiments shown in Figure 3.4 and Figure 3.8A were carried out by Fiona Houghton (Bio21 Molecular Science and Biotechnology Institute, The University of Melbourne).

This work was supported by funding from the Australian Research council (LP160101373) and the Melbourne Research Scholarship by the University of Melbourne.

Acknowledgements

First and foremost, I want to thank my primary supervisors, Prof. Paul A. Gleeson and Dr. Janine Becker-Gotot, who gave me the opportunity to work on this amazing project; I could not have wished for better supervisors during this hard and long, but also exciting journey. Your support and advice, inside and outside of the lab, is very much appreciated and I cannot thank you enough for being so understanding and enthusiastic about science in general and this project in particular. Thank you for all the effort you put into meeting regularly and all the lively discussions we had over the past years, which not only let this project grow and prosper, but also me as a person.

I want to thank my co-supervisor A/Prof. Justine Mintern and the remaining members of my PhD committee, Dr. Diana Stojanovski, Prof. Malcolm McConville and Dr. Anne Verhagen, for providing valuable input and great suggestions for improving my PhD project during my committee meetings. Also I want to thank Dr. Elizabeth Hinde for all her help in bringing cell biology and biophysics together and her incredible expertise in biophysical analyses. I really enjoyed learning so much about biophysics from you during our countless microscopy sessions.

A special thanks to all the amazing people from the Bio21 Molecular Science and Biotechnology Institute in Melbourne and the Institute of Experimental Immunology in Bonn I go to know during my time as a PhD student. In particular, I want to thank past and present members of the Gleeson lab, Dr. Lou Fourriere-Chea, Dr. Wei Hong Toh, Fiona Houghton, Christian Makhoul, Xiao Peng Lin and Melinda Wang, and the Becker-Gotot lab, Dr. Mirjam Meiβner, Vadim Kotov, Andrea Maione and Blanca Jurado Mestre. Both labs made me feel welcome from the very first day and you cannot imagine how much you made life easier over the last 4 years. Special thanks to Fiona Houghton, the mother of the Gleeson lab, who works so much behind the scenes and keeps the lab running at any time. Furthermore, a huge thank you to Andrea Maione and Blanca Jurado Mestre, for all the good times in- and outside of the lab during the last 1.5 years. I am so grateful for meeting you and all the support, discussions, and nights out

you two amazing and strong persons provided during the tough times in the midst of a pandemic.

I want to thank all the BAMBII members and fellow PhD students of the Bio21 Molecular Science and Biotechnology Institute I met during my two years in Melbourne; In particular, Erin McGowan, Kayla Wilson, Jasmina Markulic, Beth Anderson, Emily Crisafulli, Emily Zelik, Alexander Anderson, Thomas Jackson and Markus Fleischmann. I enjoyed every second of your company and you made my stay in Melbourne unforgettable.

I want to acknowledge our collaborators from CSL Limited, namely Prof. Steven Dower and Dr. Anne Verhagen as well as all the other people involved for all the helpful discussions and suggestions during our monthly FcRn meetings, and the financial support for funding this project.

A huge thank you to all the people within the IRTG2168 program, in particular Prof. Sammy Bedoui and Prof. Dr. Christian Kurts as well as the program coordinators Dr. Marie Greyer, Lucie Hrvat-Delforge and Sandra Rathmann. Coordinating such an international graduate school involving two universities at the opposite sides of the world is a challenging task and without your effort it would have not been possible to stay on track with all the things to organise and manage all the bureaucratic hurdles.

Furthermore, I want to thank all the people in the background, in particular the animal caretakers, research assistants and cleaning staff, who keep both institutes running and provide all the infrastructure needed for conducting our research. I want to acknowledge the financial support I obtained during my candidature by The University of Melbourne, The Melbourne Research Scholarship, and the Biochemistry Graduate Researcher Travel Award. Many thanks to the Biological Optical Microscopy Platform (BOMP) at the University of Melbourne and the Flow Cytometry Core Facility (FCCF) at the Medical Faculty of The University of Bonn for providing and maintaining all the instruments for confocal microscopy and flow cytometry, and helping so much by giving valuable advice and super interesting seminars.

Last but not least, I want to thank my family and friends, no matter where located in the world, who have always been so supportive and encouraged me to stay on track over the last four years. I cannot thank you enough for all the video calls, pictures, or messages I received to remind me of your love and your friendship despite the enormous physical distance between us. I hope I can make up for all the missed celebrations, nights out and moments somehow and provide the same good times to you as you did for me. A huge thanks to all of you and lots of hugs and kisses, this would not have been possible without all of you.

List of publication

Sydow A, **Pannek A**, Krieg T, Huth I, Guilluoet SE and Holtmann D. Expanding the genetic tool box for Cupriavidus necator by a stabilized L-rhamnose inducible plasmid system. J. Biotechnol. 2017; 263: 1-10
DOI: 10.1016/j.jbiotec.2017.10.002

Chapter 1: Literature review

1.1: Endocytic pathways

Endocytosis is a process by which cells internalise various molecules like proteins, membrane lipids and nutrients from the extracellular space. Due to the versatility and the distinct properties of these molecules, cells have developed several endocytic pathways to allow efficient endocytosis of different molecule classes (Doherty and McMahon, 2009). Broadly, endocytosis can be classified into clathrin-dependent and clathrin-independent endocytosis. Clathrin-dependent endocytosis relies on the recognition of extracellular cargo by membrane-bound adaptor proteins and results in the formation of clathrin-coated vesicles, whereas clathrin-independent endocytosis exploits other mechanisms to transport cargo into the cell (Sandvig *et al.*, 2008). Endocytic pathways are not only differentiated by the involvement of clathrin but also by their cargo recognition and specificity, their mechanism of endosome formation and the morphology of resulting endosomal structures. The most common endocytic pathways in cells include classic clathrin-dependent endocytosis, caveolin-dependent endocytosis, phagocytosis and macropinocytosis (Figure 1.1).

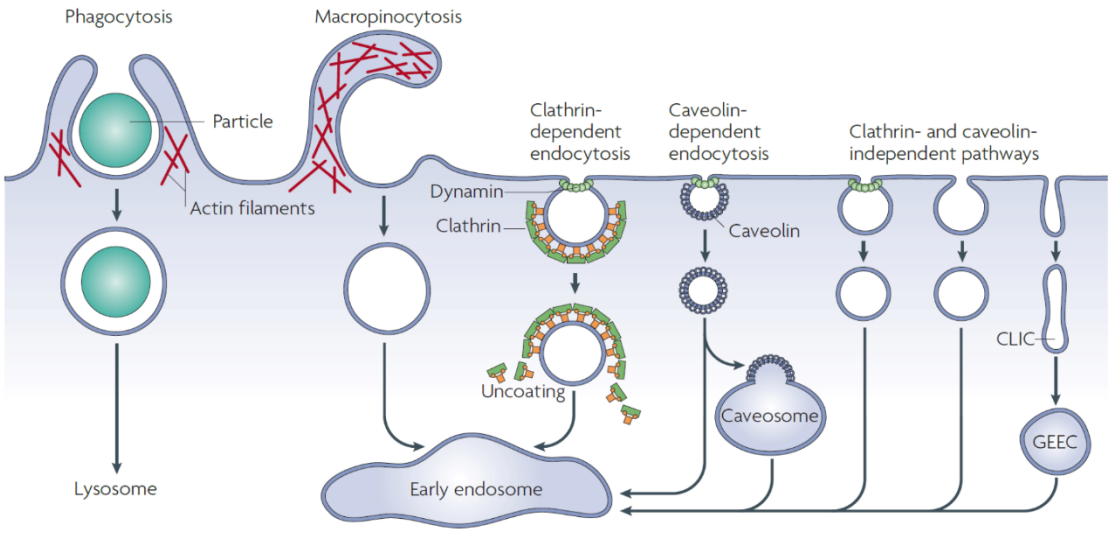

Figure 1.1: Overview of clathrin-dependent and independent endocytic pathways in eukaryotic cells
Schematic overview of different endocytic mechanisms for the internalisation of molecules in eukaryotic cells. Depicted are the principles of endosome biogenesis at the plasma membrane and endosomal target destinations for phagocytosis, macropinocytosis, clathrin- and caveolae(caveolin)-dependent endocytosis as well as other clathrin- and caveolae(caveolin)-independent endocytic pathways. Figure taken from (Mayor and Pagano, 2007).

1.1.1: Clathrin-dependent endocytosis

Clathrin-dependent, also referred to as clathrin-mediated, endocytosis is the most studied endocytic pathway; partially because of its importance in the recycling of synaptic-vesicle components upon neurotransmitter release in synapses of nerve cells and the involvement of the pathway in the internalisation of key molecules and nutrients, such as cholesterol and iron (Jung and Haucke, 2007; Antonescu *et al.*, 2014). In addition, clathrin-dependent endocytosis is responsible for the internalisation of (activated) receptor molecules embedded in the plasma membrane (Traub and Bonifacino, 2013). Clathrin is a triskelion-shaped protein consisting of three heavy chains, which each are non-covalently associated with a light chain, respectively (Kirchhausen and Harrison, 1981; Ungewickell, 1999). Clathrin, in combination with the adaptor protein 2 (AP-2) and other auxiliary proteins, can form coated pits at the cytoplasmic side of the plasma membrane

initiating the endocytosis of specific cargo (Mousavi *et al.*, 2004). Coated pit formation is triggered by the recognition of short endocytosis motifs in the cytoplasmic tail of surface receptors by AP-2 (Bonifacino and Traub, 2003). Polymerising clathrin scaffolds the pit with a penta- and hexagonal lattice and stabilises membrane curvature (McMahon and Boucrot, 2011). The clathrin-coated vesicle remains connected to the membrane via a bottleneck architecture and is subsequently completely separated from the plasma membrane by dynamin in a GTP hydrolysis-dependent process (Ferguson and Camilli, 2012). Fully detached clathrin-coated vesicles display diameters in the range of 35 – 200 nm depending on the cell type, coat assembly mechanism and type of cargo (Cheng *et al.*, 2007; McMahon and Boucrot, 2011; Paraan *et al.*, 2020). After pinching off the plasma membrane, the clathrin coat is removed by heat shock protein-70 (Hsc70), identified as an uncoating ATPase, in combination with the co-chaperone auxilin, and the uncoated vesicles containing endocytosed cargo are transported to the early endosomes (Popova *et al.*, 2013).

1.1.2: Macropinocytosis

Macropinocytosis describes a clathrin-independent endocytic pathway facilitating the non-selective fluid-phase uptake of soluble proteins, nutrients, and antigens (Lim and Gleeson, 2011). The process of macropinocytosis was first defined in 1931 by Warren Lewis and is characterised by actin-dependent membrane ruffling, which leads to the formation of large uncoated endosomal vesicles called macropinosomes with a size of at least 0.2 µm in diameter (Lewis, 1931; Swanson and Watts, 1995). Normally, macropinocytosis is a signal-dependent process, with cells becoming active in macropinocytosis upon stimulation by growth factors such as colony-stimulating factor-1 (CSF-1), epidermal growth factor (EGF), platelet-derived growth factor or tumour-promoting factors (Haigler *et al.*, 1979; Swanson, 1989; Racoosin and Swanson, 1989). However, some specialised cells such as dendritic cells (DCs), macrophages and endothelial cells are capable of performing macropinocytosis constitutively (Sallusto *et al.*, 1995; Raheel *et al.*, 2019; Doodnauth *et al.*, 2019). Besides providing the cell with

large quantities of soluble molecules and membrane components, the macropinocytotic pathway contributes to chemotactic cell motility and can be exploited as cellular entry point by various bacteria and viruses including *Salmonella spp.*, *Legionella spp.*, HIV-1, adenovirus and ebolavirus (Lim and Gleeson, 2011). Furthermore, high macropinocytic activity is common among various cancer cells and has been proposed to play an important role in the nutrient uptake and survival of tumours (Palm, 2019).

1.1.3: Biogenesis of macropinosomes and regulation of macropinocytosis

Macropinocytosis requires actin rearrangements to induce the formation of membrane ruffles at the cell surface (Lim and Gleeson, 2011) (Figure 1.2). These actin-rich extensions of the cell membrane fold back and fuse with the plasma membrane encapsulating large volumes of the extracellular fluid phase. This gives rise to a heterogenous population of large endosomal structures, called macropinosomes, with a typical size of 0.2 – 5 µm in diameter (Kerr and Teasdale, 2009) (Figure 1.2). Membrane ruffling can occur at the peripheral edges or the dorsal surface of the cell. Peripheral ruffles have been linked to be important for initiating macropinocytosis whereas dorsal ruffling was primarily described to mediate receptor signalling and occur upon growth factor stimulation of cells (Suetsugu *et al.*, 2003; Buccione *et al.*, 2004; Hoon *et al.*, 2012). However, the contributions of the two distinct pathways to macropinocytosis and their regulation in different cell types remain unclear.

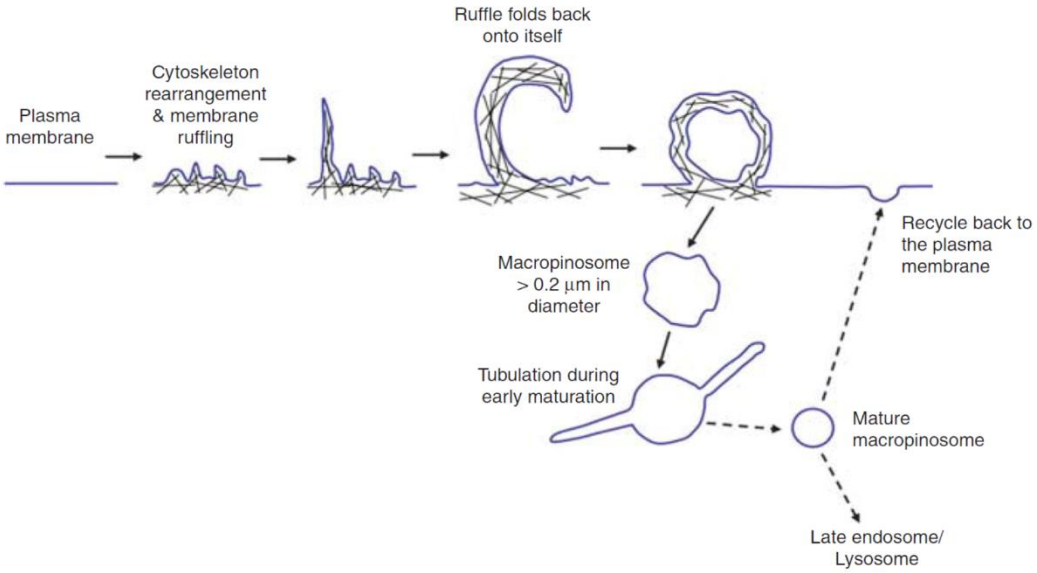

Figure 1.2: The pathway of macropinocytosis
Membrane ruffling is mediated by actin cytoskeleton (black lines) re-arrangements. Ruffles folding back onto themselves and fusing with the plasma membrane trap extracellular fluid phase and give rise to a heterogeneous population of macropinosomes with sizes of >0.2 µm in diameter. During early maturation, macropinosomes shrink due to extensive tubulation emerging from the macropinosomal body. Spherical mature macropinosomes are either recycled back to the plasma membrane or degraded in late endosomes and lysosomes. Figure taken from (Lim and Gleeson, 2011).

Actin remodelling for the formation of membrane ruffles is mediated by members of the Rho small G protein (Rho-GTPase) family including Rho, Cdc42 and Rac1 (Swanson, 2008). The recruitment of Cdc42 and Rac1 to the plasma membrane is dependent on sub-membranous acidification and impaired by the Na^+/H^+-exchanger inhibitor amiloride and its derivates (Koivusalo *et al.*, 2010). Several other proteins like phosphoinositide 3-kinase (PI3K), Rab5, Rab34 and members of the sorting nexin (SNX) family are also believed to contribute to the membrane ruffle and macropinosome formation (Lim and Gleeson, 2011). Indeed, sorting nexin 5 (SNX5) was shown to be an important regulator of macropinocytosis in CSF-1-stimulated bone marrow-derived macrophages (BMDMs), especially in the formation of dorsal membrane ruffles, whereas the

deletion of SNX5 did not affect macropinocytosis in splenic dendritic cells (Lim *et al.*, 2008; Lim *et al.*, 2012; Lim *et al.*, 2015).

Although it is widely accepted that many cell types are capable of macropinocytosis, it becomes increasingly apparent that macropinocytosis is regulated by various stimuli and protein machineries in a cell type-dependent manner (Lin *et al.*, 2020).

1.1.4: Macropinosome maturation

After budding off the cell membrane, macropinosomes undergo a maturation process, which is believed to vary between different cell types. In the human squamous carcinoma cell line A431, macropinosomes, formed upon EGF-stimulation, were reported to be positive for transferrin receptor and faintly positive for the early endosome antigen 1 (EEA1) (Hamasaki *et al.*, 2004). EEA1 persists on the limiting membrane of macropinosomes in EGF-treated A431 cells and is thought to mediate homotypic fusion between macropinosomes (Araki *et al.*, 2006). Macropinosomes eventually fuse with the plasma membrane, recycle their content to the extracellular space and do not mature into late endosomes or lysosomes (Buckley and King, 2017). In addition, there are some reports suggesting that recycling of macropinosomal content can also be mediated by EEA1-negative tubular extensions emerging from macropinosome bodies (Hamasaki *et al.*, 2004).

In contrast to A431 cells discussed above, freshly formed, transferrin receptor-positive macropinosomes in EGF-treated HEK293 cells and CSF-I-treated bone marrow-derived macrophages (BMDMs) mature as they migrate to the centre of the cell (Lim and Gleeson, 2011). In both cell types, highly dynamic tubular extensions positive for SNX5 have been described emerging from macropinosomal bodies during the maturation process (Kerr *et al.*, 2006; Lim *et al.*, 2008). The tubulation process is linked to recycling of macropinocytosed cargo back to the plasma membrane and occurs within the first 5 to 10 minutes after macropinosome formation (Kerr *et al.*, 2006; Van Weering *et al.*, 2012; Toh

et al., 2020). The generation of tubular extensions followed by their scission into tubular carriers from the macropinosomes leads to the shrinkage of the macropinosomal surface area (Lim *et al.*, 2008). Maturing macropinosomes lose transferrin receptor but acquire the late endosomal marker Rab7 and lysosomal glycoprotein A (lgp-A). Eventually, macropinosomes are depleted of Rab7-staining while sustaining high levels of lgp-A-staining before fusing with existing lysosomal compartments (Racoosin and Swanson, 1993).

The maturation of macropinosomes, and the mechanisms involved, in different cell types remain poorly understood and need further investigation.

1.1.5: Caveolae-dependent endocytosis

Caveolae are flasks-shaped invaginations of the plasma membrane with a size of 60 – 80 nm (Parton and Simons, 2007). They are present in all cell types of the cardiovascular system but especially enriched in vascular endothelial cells (Sowa, 2012). Caveolae are characterised as cholesterol-and sphingolipid-rich lipid rafts and enable the local concentration of certain membrane proteins to effectively regulate various cellular processes such as signal transduction and endocytosis (Allen *et al.*, 2006; Patel *et al.*, 2008; Rahman and Swärd, 2009; Chaudhary *et al.*, 2014). A major component of caveolae is the coat protein caveolin-1, which stabilises the invaginated lipid rafts at the cell surface and prevents the internalisation of most caveolae (Nabi and Le, 2003). The internalisation of caveolae is sensitive to cholesterol depletion and initiated by surface receptor activation leading to the disruption of the actin cytoskeleton (Rodal *et al.*, 1999; Pelkmans and Helenius, 2002). Although caveolae-dependent endocytosis is clathrin-independent, the budding of caveolar vesicles from the plasma membrane is mediated by dynamin similar to the process described for clathrin-dependent endocytosis (Henley *et al.*, 1998). The majority of internalised caveolar vesicles fuse with early endosomes or are directly recycled back to the plasma membrane (Pelkmans *et al.*, 2004; Pelkmans and Zerial, 2005). Some caveolar structures have been shown to be trafficked to

specialised endosomal compartments, called caveosomes, however other studies suggest that caveosomes represent late endosomal structures modified by the enrichment of caveolin-1 (Parton and Howes, 2010). Caveolae-mediated endocytosis mediates the internalisation of various molecules and pathogens like sphingolipids, cholera toxin, interleukin-2 (IL-2), and simian virus 40 (SV40) (Pelkmans and Helenius, 2002). Furthermore, albumin was shown to be endocytosed via caveolae in a glycoprotein 60 (gp60)-dependent process using cultured endothelial cells (Tiruppathi *et al.*, 1997; Vogel *et al.*, 2001). However, the function and nature of the albumin-gp60 interaction has never been fully elucidated.

1.2: Endosomal compartments

Upon internalisation, endocytosed cargo enters a highly regulated network of endosomal compartments and trafficking pathways in eukaryotic cells. Specific subsets of endosomes are characterised by a unique set of membrane receptors and are responsible for the recycling or degradation of endocytosed material and membrane components (Gruenberg, 2001; Elkin *et al.*, 2016) (Figure 1.3). The highly regulated and interconnected endosomal network enables the transport of specific cargo to their target membranes and regulates various cellular processes such as signal transduction, antigen presentation and cell survival (Wilson and Villadangos, 2005; Pálfy *et al.*, 2012; Villaseñor *et al.*, 2016). The most prominent endosomal subsets, namely early, recycling, and late endosomes as well as lysosomes, will be discussed in the following sections.

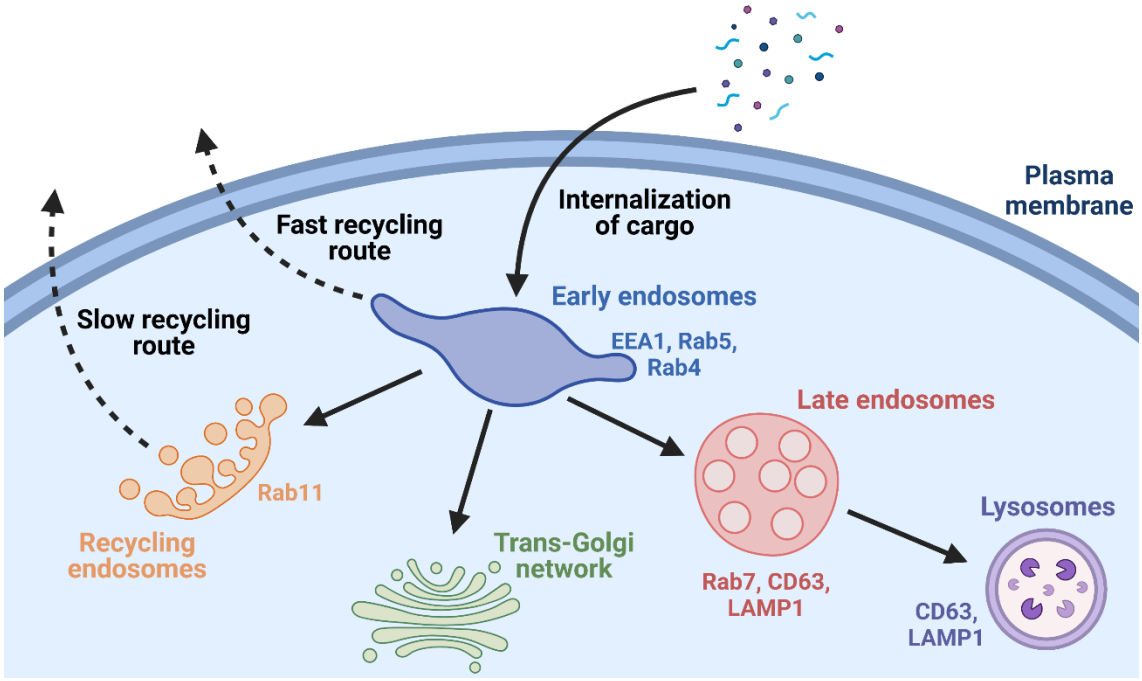

Figure 1.3: Overview of endocytic pathways and compartments
Internalised cargo is recycled from EEA1-, Rab5- and Rab4-positive early endosomes (blue) either directly (fast recycling route) or via Rab11-positive recycling endosomes (orange) back to the plasma membrane (slow recycling route). Alternatively, cargo can be sorted from early endosomes to the *trans*-Golgi network (green). The early endosomal body matures into late endosomes (red) by losing early endosomal markers and acquiring Rab7, CD63 and LAMP1. Late endosomes fuse with CD63- and LAMP1-positive lysosomes, where protein cargo gets degraded by proteases. Figure created with BioRender.com.

1.2.1: Early endosomes

Early or sorting endosomes are usually the first organelles internalised cargo reaches within the endosomal network, indicated by the presence of endocytic tracers 1 – 5 minutes after endocytosis depending on the cell type (Schmid *et al.*, 1988; Tooze and Hollinshead, 1991; Kleijmeer *et al.*, 1997; Pavelka *et al.*, 1998; De Wit *et al.*, 1999). It is believed that cargo internalised via different endocytic pathways converges within the early endosomal compartment, which then defines the fate of internalised material by regulating intracellular sorting into degradation or recycling pathways (Jovic *et al.*, 2010). Early endosomes are

highly dynamic and pleomorphic structures undergoing various homotypic fusion events and are characterised by the association with the early endosomal markers EEA1, Rab5 and Rab4 (Gruenberg *et al.*, 1989; Sachse *et al.*, 2002; Huotari and Helenius, 2011). These endosomal markers fulfill distinct roles in early endosomal biology. Rab5 mediates the entry of cargo into early endosomes, the generation of phoshpotidylinositol-3-phosphate (PtdIns(3)P), important for selective recruitment of proteins to microdomains at the early endosomal membrane, and, together with EEA1, the homotypic fusion of early endosomes (Nielsen *et al.*, 1999; Lawe *et al.*, 2001; Gillooly *et al.*, 2003). Rab4 plays an important role in the recycling of cargo by sorting internalised material directly back to the plasma membrane or to Rab11-positive recycling endosomes (van der Sluijs *et al.*, 1992; Mohrmann *et al.*, 2002). Typically, early endosomes are composed of large vesicular bodies with diameters up to 400 nm and thin tubular extensions with a diameter of ~ 60 nm (Gruenberg, 2001). The morphologically distinct regions of early endosomes form several microdomains within these organelles and enable the local concentration of internalised cargo and the selective sorting of endocytosed material to their respective target membrane (Raiborg *et al.*, 2002; Jovic *et al.*, 2010; Norris and Grant, 2020).

Most soluble ligands within early endosomes are sorted to the late endosomal and lysosomal degradation pathway, whereas endocytosed receptors are often recycled back to the plasma membrane and can undergo various rounds of internalisation and ligand binding (Maxfield and McGraw, 2004). The separation of ligand and receptor into distinct endocytic pathways is facilitated by the slightly acidic luminal pH (~ 6.3 – 6.8) of early endosomes allowing the dissociation of most receptor-ligand complexes (Mellman, 1996). Membrane-bound receptors designated for recycling are concentrated in the tubular microdomains of early endosomes, which mediate the sorting of cargo to Rab11-positive recycling endosomes (slow recycling route) or directly back to the plasma membrane (fast recycling route) (Maxfield and McGraw, 2004; Jovic *et al.*, 2010). The identification of the two distinct recycling routes was observed studying the intracellular fate of transferrin. It was shown that internalised transferrin located to early endosomes can undergo both, direct and rapid as well as slow recycling

via Rab11-positive recycling endosomes (Hopkins and Trowbridge, 1983; Ullrich *et al.*, 1996). In CHO cells, receptors recycled via the fast pathway return to the plasma membrane after 10 minutes, whereas internalised receptors recycled slowly via Rab11-positive compartments reach the plasma membrane after 30 minutes (Johnson *et al.*, 1998; Mayor *et al.*, 1998).

In contrast, unbound soluble ligands remain in the globular early endosome body. After accepting cargo and mediating recycling for 8 – 15 minutes, early endosomes mature into late endosomes by losing association with early endosomal markers and acquire the late endosomal marker Rab7 initiating the sorting of lysosome-targeted cargo into the degradation pathway (Dunn and Maxfield, 1992; Huotari and Helenius, 2011). Alternatively, some internalised cargo such as the *trans*-Golgi network integral network protein TGN-38 or Shiga toxin can be sorted from early endosomes directly to the *trans*-Golgi network (TGN) without entering the recycling or degradation pathway (Bujny *et al.*, 2007; Lieu and Gleeson, 2010).

While the transport of soluble ligands to the degradation pathway is a consequence of remaining in the lumen of early endosomes throughout endosomal maturation, the sorting of receptors to the plasma membrane, the *trans*-Golgi network and to late or recycling endosomes is facilitated by the recognition of sorting motifs in the cytosolic tail of membrane-bound receptor molecules or local concentration of receptors in early endosomal microdomains (Jovic *et al.*, 2010; Huotari and Helenius, 2011; Elkin *et al.*, 2016). It was long believed that receptors lacking any specific sorting motifs undergo canonical recycling by default association with tubular early endosomal microdomains mediating trafficking back to the plasma membrane. However, other studies using hybrid receptors revealed the existence of specific cytosolic sorting motifs facilitating the active sorting of membrane-bound receptors into the slow or fast recycling pathway (Dai *et al.*, 2004; Mahmoud *et al.*, 2017; Cullen and Steinberg, 2018).

Over the last decades, more and more proteins involved in mediating the recycling of internalised receptors have been identified (Cullen and Steinberg,

2018). Rab4-positive microdomains of early endosomes play a crucial role in the sorting of transferrin receptor into the fast and slow recycling pathway by regulating the formation and budding of tubular extension from the early endosomes (Daro *et al.*, 1996; Mohrmann *et al.*, 2002). Other proteins like Rabenosyn-5 and members of the sorting nexin (SNX) family have also been linked to mediate selective trafficking of internalised cargo (Cullen, 2008; Navaroli *et al.*, 2012). SNX proteins, as integral parts of the retromer complex, are essential for the formation of tubular carriers emerging from early endosomes. Specific members of the SNX family are either linked to mediate recycling of cargo to the plasma membrane (SNX5, SNX27) or retrograde transport to the TGN (SNX1, SNX3) (Merino-Trigo *et al.*, 2004; Van Weering *et al.*, 2012; Gallon and Cullen, 2015).

Similar to recycling, retromer-mediated transport of cargo from early endosomes to the TGN is mediated via tubular extensions and involves the recognition of specific sorting motifs by VPS35 or other members of the retromer complex (Seaman, 2007; McGough and Cullen, 2011). Sorting of membrane-bound receptors to late endosomes is regulated in a similar fashion. The sorting of receptor tyrosine kinases like epidermal growth factor receptor (EGFR) into the degradation pathway relies on the recognition of mono-ubiquitinated lysine residues within sorting motifs by hepatocyte growth factor-regulated tyrosine kinase substrate (Hrs) (Shih *et al.*, 2002). This eventually leads to the recruitment of endosomal sorting complexes required for transport (ESCRTs) resulting in the formation of multivesicular bodies (MVBs), an essential step in the maturation of early into late endosomes (Babst *et al.*, 2002; Bache *et al.*, 2003). Lysosomal sorting motifs and mechanisms have been identified for several other receptors including activated fibroblast growth factor receptor 3 (FGFR3) and major histocompatibility complex (MHC) class II peptide complexes (Bonifacino and Traub, 2003; Cho *et al.*, 2004; Furuta *et al.*, 2013).

Although the main function of early endosomes as intracellular sorting hubs and main principles of selective sorting of cargo into distinct endocytic pathways are established, the knowledge about the details of the highly regulated and

coordinated processes and protein machineries involved in early endosomal sorting is still evolving.

1.2.2: Recycling endosomes

Recycling endosomes are composed of a heterogeneous, tubulovesicular subpopulation of endosomes mediating the recycling of internalised cargo back to the plasma membrane. These endosomal structures vary in size (40 – 60 nm diameter) and possess long, multi-branching tubular extensions (2 µm or longer) emerging from the endosomal body (Tooze and Hollinshead, 1991; Sachse *et al.*, 2002). The intraluminal pH of the recycling endosome compartment is between 6.4 and 6.5 (Mayor *et al.*, 1993). Recycling endosomes are characteristically located to the perinuclear region of the cell in close proximity to the microtubule-organising centre (MTOC) and often closely associated with the TGN (Urbé *et al.*, 1993; Ullrich *et al.*, 1996; Welz *et al.*, 2014). After receiving cargo from early endosomes, recycling endosomes mediate the trafficking of membrane-bound receptors back to the plasma membrane within 10 – 12 minutes (Maxfield and McGraw, 2004). Although the primary function of recycling endosomes is to facilitate the recycling of internalised cargo received from early endosomes back to the plasma membrane, some proteins like Shiga toxin and the v-SNARE protein VAMP4 are transported from recycling endosomes to the TGN (Tran *et al.*, 2007; Lieu and Gleeson, 2010).

Recycling endosomes were first characterised by investigating the slow recycling route of transferrin involving tubulovesicular compartments distinct from early endosomes (Marsh *et al.*, 1995). Thus, recycling endosomes can be identified by the localisation of internalised transferrin and transferrin receptor or the association with the small GTPase Rab11 (Maxfield and McGraw, 2004). The Rab11 family is comprised of three members, the ubiquitously expressed Rab11a and Rab11b and the epithelial-specific Rab25 (Prekeris, 2003). Rab11a, the best characterised member of the Rab11 family, is co-localised with transferrin in pericentriolar recycling endosomes and is linked to various functions including

the promotion and formation of tubular extensions in the recycling endosomal compartment and the recycling of cargo like transferrin back to the cell surface (Ullrich *et al.*, 1996; Ren *et al.*, 1998; Delevoye *et al.*, 2014).

Some studies suggest the existence of several distinct recycling mechanisms for specific cargo mediated by recycling endosomes (Goldenring, 2015). On the one hand, Rab11a-dependent tubulation of recycling endosomes is regulated by multiple mechanisms mediated by the interaction of the small GTPase with various proteins like kinesin family member 13A (KIF13A), spastin and ESCRTs (Allison *et al.*, 2013; Delevoye *et al.*, 2014; Le and Chung, 2021). On the other hand, recycling endosomes were shown to be sub-compartmentalised in Rab11a- and Rab8- as well as transferrin receptor- and Arf6-positive membranes facilitating distinct mechanisms for the recycling of internalised cargo varying in the pathway for entering and leaving the recycling compartment (Kobayashi and Fukuda, 2013; Baetz and Goldenring, 2013; Baetz and Goldenring, 2014). However, it remains yet to be understood how these multiple recycling mechanisms are regulated, to which extent they are interconnected and how the distribution of Rab11a and Rab8 for the formation of microdomains within recycling endosomes is orchestrated.

1.2.3: Late endosomes

Late endosomes derive from globular early endosomal bodies, which acquired the late endosomal marker Rab7 during their maturation in a Rab5-dependent process. This leads to the development of Rab5- and Rab7-double-positive hybrid endosomes, which lose their association with Rab5 within a few minutes completing the Rab switch from Rab5 to Rab7 to form late endosomes (Rink *et al.*, 2005). Endocytic tracers are located to mature late endosomes after 10 – 15 minutes. However, solute molecules and bulk fluids reach late endosomes up to 30 minutes after internalisation (Griffiths *et al.*, 1989; Van Deurs *et al.*, 1993; Kleijmeer *et al.*, 1997; De Wit *et al.*, 1999).

Typically, late endosomes are globular- or oval-shaped structures with sizes ranging from 250 to 1000 nm in diameter and an acidic luminal pH between 4.9 and 6.0 (Huotari and Helenius, 2011). Late endosomes undergo various homotypic fusion events and accumulate in the perinuclear region close to the MTOC (Luzio *et al.*, 2007). They are characterised by the presence of numerous spherical-shaped intralumenal vesicles (ILVs) with a typical diameter of 50 nm in eukaryotic cells, and hence are often referred to as multivesicular bodies (Piper and Luzio, 2001; Bissig and Gruenberg, 2013). The formation of ILVs starts during early endosome maturation with some ILVs already present during the early endosomal stage (Piper and Katzmann, 2007). In a highly regulated process mediated by microdomains in the limiting membrane of late endosomes and components of ESCRT, ILVs are generated by the inward-budding of vesicles from the limiting membrane of early endosomes (Gireud-Goss *et al.*, 2018). ILVs are important for the lysosomal delivery of cargo allowing efficient degradation by proteases and for the inactivation of membrane-bound receptor-mediated signalling processes by depriving them of contact with the cytosol (Huotari and Helenius, 2011). Especially, mono-ubiquitinated signalling receptors were shown to be sorted into ILVs in an ESCRT-regulated process to target them for lysosomal degradation (Hurley and Emr, 2006).

The limiting membrane of ILVs contains members of the tetraspanin family such as CD63 (LAMP3), important for ILV formation, and being negatively charged in an acidic milieu, promotes the recruitment of positively charged hydrolases (Kolter and Sandhoff, 2005; Pols and Klumperman, 2009). In contrast, the limiting membrane of late endosomes is enriched in hydrolase-resistant lysosomal glycoproteins including lysosomal-associated membrane protein 1 (LAMP1), whereas the lumen contains several acid hydrolases (Fukuda, 1991).

Usually, late endosomes fuse with lysosomes 10 – 40 minutes after their generation to initiate proteolytic degradation of internalised cargo (Huotari and Helenius, 2011). To allow maintenance and continuous generation of late endosomes, some components essential for late endosome biogenesis, such as mannose-6-phosphate receptor (M6PR), are retrieved instead of being sorted to

lysosomes for degradation (Lu and Hong, 2014). M6PR molecules, which introduce acid hydrolases into the lumen of late endosomes, shuttle between the limiting membrane of late endosomes and the TGN in a retromer-mediated mechanism, and thus can undergo several rounds of facilitating late endosome biogenesis and maturation (Braulke and Bonifacino, 2009). Furthermore, a variety of immune cells, including B cells, T cells and DCs, as well as epithelial cells can secrete late endosomal proteins and cargo located in ILVs to the extracellular environment. In this process, late endosomes fuse with the plasma membrane and release ILV-derived exosomes in a size of 30 – 100 nm in diameter into the extracellular space (Lotvall and Valadi, 2007). However, many regulatory mechanisms of late endosomal motility and membrane fusion events remain poorly understood.

1.2.4: Lysosomes

Lysosomes are pre-existing organelles and function as the main degradative compartment in eukaryotic cells. The lysosomal compartment is composed of electron dense, spherical and tubular organelles with heterogenous morphology, location, and composition to allow efficient degradation of cargo received from the canonical endocytic or other cellular pathways (Appelqvist *et al.*, 2013). They possess an acidic luminal pH (4.5 – 5.0) enriched in acid hydrolases, including proteases, lipases and glucosidases, and are positive for endocytic tracers 30 minutes after their internalisation (Sachse *et al.*, 2002; Schröder *et al.*, 2010). For most proteins, the entry to lysosomes marks a point-of-no-return, and thus is highly regulated by preceding segregation of proteins or molecules not intended for degradation into other endosomal pathways (Huotari and Helenius, 2011).

In the endocytic pathway, cargo within ILVs of late endosomes is delivered to lysosomes via fusion of both endosomal structures resulting in the formation hybrid organelles exhibiting a multivesicular phenotype. These structures sometimes are referred to as endolysosomes, to distinguish them from classic pre-existing lysosomes and lysosomes which are originated from the fusion with

other endosomal structures such as phagosomes, macropinosomes or autophagosomes (Huotari and Helenius, 2011). Interestingly, endolysosomes are the main intracellular site of hydrolase activity, whereas terminal lysosomes rather function as storage organelles for degraded cargo (Bright *et al.*, 2016). The degradation of internalised cargo by endolysosomes and lysosomes fulfills several important cellular functions including cell survival, pathogen removal, nutrient homeostasis, regeneration of basic building blocks and antigen processing (Hsing and Rudensky, 2005; Luzio *et al.*, 2007; Turk and Turk, 2009; Mony *et al.*, 2016).

Similar to late endosomes, lysosomes are characterised by the presence of the lysosomal-associated membrane proteins LAMP1 and LAMP2, as well as CD63 (LAMP3) (Fukuda, 1991). Although morphologically and functionally related to late endosomes and endolysosomes, lysosomes are negative for M6PR and often contain intraluminal membrane sheets formed during fusion events (Griffiths *et al.*, 1988; Mattie *et al.*, 2017). Lysosomes are highly dynamic and undergo constant homotypic or heterotypic fusion with late endosomes. Therefore, late endosomes, endolysosomes and lysosomes are often considered as a fluid continuum exchanging endosomal content and transitioning from one phenotype to another constantly, rather than representing explicitly distinct organelles (Luzio *et al.*, 2007; Huotari and Helenius, 2011).

1.3: Human Serum Albumin

Human serum albumin (HSA) is the most abundant protein in human blood with concentrations between 35 – 50 g/l and represents more than 50 % of the total protein fraction in blood plasma (Quinlan *et al.*, 2005; Arques and Ambrosi, 2011). In human blood, HSA displays various physiological functions including the binding and transport of various endogenous and exogenous molecules and plays a vital role in the maintenance of the colloid osmotic pressure (Sudlow *et al.*, 1975; Quinlan *et al.*, 2005; Sitar and Cakatay, 2013). HSA is predominantly synthesised by hepatocytes in the liver and 10 to 15 g albumin are released into

the vascular system each day in healthy individuals (Arques and Ambrosi, 2011). However, 60 – 70 % of the albumin pool *in vivo* is located to the intravascular and interstitial space (Arques, 2018). Albumin molecules have been described to be exchanged steadily between the intra- and extravascular pool via transcytosis mediated by endothelial cells or drainage through the lymphatic system (Bodega *et al.*, 2002). The small globular protein has a size of 66.5 kDa (585 amino acids) and is composed of three homologous domains DI, DII and DIII (Carter *et al.*, 1989). Each of the three albumin domains contains two sub-domains (A and B) which are connected by flexible loops and allow for movement of the sub-domains relative to each other (Quinlan *et al.*, 2005). The heart-shaped tertiary structure of albumin is predominantly comprised of α-helices (67%) and stabilised by 17 disulfide bridges between cysteine residues. The majority of the cysteine residues, 34 of 35, of albumin participate in the formation of intramolecular disulfide bridges, whereas Cys34 retains a redox-active thiol group (-SH) (Quinlan *et al.*, 2005) (Figure 1.4).

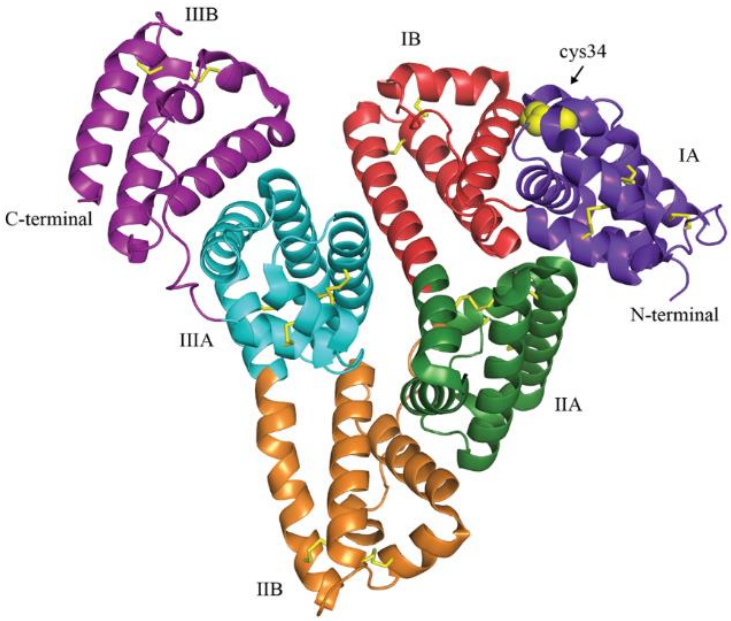

Figure 1.4: Crystal structure of human serum albumin (HSA)
The ribbon diagram shows the six subdomains of HSA, namely IA (purple), IB (red), IIA (green), IIB (orange), IIIA (cyan) and IIIB (purple). Intramolecular disulfide bridges and Cys34 containing a redox-reactive thiol-group are highlighted in yellow. Figure taken from (Larsen *et al.*, 2016)**.**

The free thiol group acts as an important scavenger for reactive oxygen species in blood and can furthermore interact with drugs like captopril or D-penicillamine to facilitate their transport or conduct antitoxic properties (Sitar and Cakatay, 2013; Yamasaki *et al.*, 2013). In addition to Cys34, albumin possesses various other ligand binding sites for interactions with several compounds including fatty acids, metal ions, pharmaceuticals and metabolites such as flavonoids (Ashbrook *et al.*, 1975; Bolli *et al.*, 2010; Yamasaki *et al.*, 2013; Bal *et al.*, 2013). This versatility underlines the complex functions of human serum albumin including the binding and targeted delivery of compounds and the role in detoxification and antioxidant protection.

In contrast to most other serum proteins, albumin displays not only higher concentration but also enhanced half-life properties. The half-life of HSA, alongside Immunoglobulin G (IgG) molecules, is around three weeks in humans, whereas other serum proteins are cleared from circulation within hours or days (Waldmann *et al.*, 1971; Quinlan *et al.*, 2005; Takata *et al.*, 2011). This half-life extension is linked to the ability of albumin and IgG to interact with the neonatal Fc receptor (FcRn) in endosomal structures upon internalisation by a variety of cells, which leads to the salvation of the two FcRn ligands from lysosomal degradation and recycling back into the blood stream (Chaudhury *et al.*, 2003; Roopenian *et al.*, 2003). In addition to FcRn, other receptors have been found to potentially interact with HSA. One of these receptors, glycoprotein 60 (gp60 or albondin) predominantly expressed on vascular endothelial cells, is believed to mediate caveolae-dependent endocytosis of albumin (Minshall *et al.*, 2000; Vogel *et al.*, 2001). However, the studies which have linked gp60 to albumin endocytosis have been mostly conducted in non-human cell models and the sequence and function of gp60 has not been fully elucidated (Tiruppathi *et al.*, 1996; Minshall *et al.*, 2000; Vogel *et al.*, 2001; Pyzik *et al.*, 2019). Recent studies using primary murine bone marrow-derived macrophages (BMDMs) indicate that albumin is predominantly endocytosed by macropinocytosis by this cell type (Toh *et al.*, 2020). This finding is in line with other studies also suggesting an important role of macropinocytosis in the uptake of albumin by endothelial and epithelial cell lines (Yumoto *et al.*, 2012; Li *et al.*, 2013).

Although it is widely appreciated that the half-life of albumin is dependent on the presence of FcRn and relies on the intracellular interactions of both molecules, the details of albumin uptake and trafficking by different cell types remain unclear and need to be further defined using suitable *in vivo* models, or alternatively *in vitro* models of primary cells to reflect the physiological pathways of albumin homeostasis.

1.4: The neonatal Fc receptor

1.4.1: Structure and function of FcRn

In humans, the heterodimeric neonatal Fc receptor (FcRn) consists of a α-chain with a molecular mass of 40 kDa and a β2-microglobulin (B2M) chain with a mass of 12 kDa (Simister and Mostov, 1989; Simister and Ahouse, 1996). The heavy α-chain of FcRn is composed of three extracellular domains (α1, α2 and α3), a transmembrane domain and a short C-terminal cytosolic tail of 44 amino acids (Burmeister *et al.*, 1994). The heavy chain is non-covalently associated with the light chain β2-microglobulin (Figure 1.5).

Thus, FcRn shares structural similarities with MHC-I receptors but unlike other MHC-I class molecules, FcRn is not able to present antigens to $CD8^+$ T cells (Burmeister *et al.*, 1994). The peptide groove of human FcRn (hFcRn) is occluded by the side chain of Arg162 and a kink in the α2-domain helix near Pro160, which prohibits the binding and subsequent presentation of antigen-derived peptides (West and Bjorkman, 2000). FcRn is widely expressed among several organs, tissues and cell types including the vascular endothelium, kidney, adult gut, lung, blood-brain barrier, and myeloid-derived antigen presenting cells (APCs) such as macrophages and dendritic cells (Israel *et al.*, 1997; Borvak *et al.*, 1998; Akilesh *et al.*, 2007; Latvala *et al.*, 2017; Li *et al.*, 2018). Evolutionary studies suggest that FcRn diverged from classic MHC-I class receptors to specifically regulate IgG and albumin homeostasis in mammals (West *et al.*, 2004).

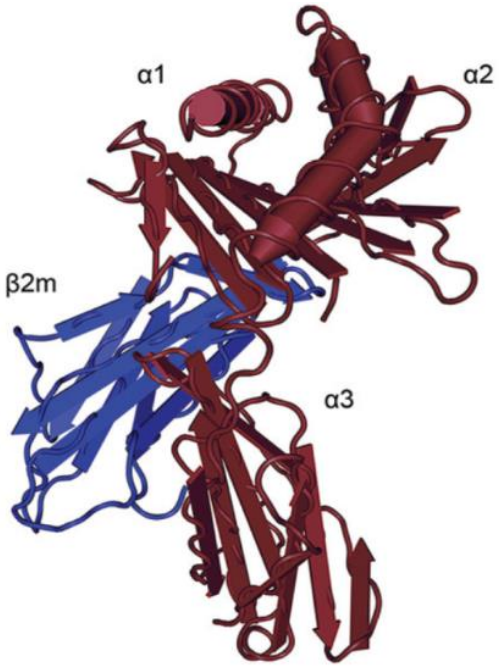

Figure 1.5: Crystal structure of the human neonatal Fc receptor (FcRn)
The ribbon diagram shows the FcRn heavy α-chain (brown) consisting of three extracellular domains, α1, α2 and α3. Then non-covalently associated light chain of FcRn, beta-2-microglobulin (β2m) is illustrated in blue. Figure taken from (Rath *et al.*, 2013)**.**

FcRn was initially believed to mainly facilitate the transfer of maternal IgG molecules to the foetus or neonates providing for humoral immunity in newboms. The transcytosis of IgG molecules from the mother to the newborn across the placenta in humans or intestinal epithelium in rodents relies on the pH-dependent interaction of FcRn with IgG molecules (Story *et al.*, 1994). However, the evidence of FcRn expression in adult cells led to the hypothesis that FcRn exhibits an additional function throughout life. Indeed, FcRn was shown to be an important regulator of not only IgG but also albumin homeostasis using FcRn-deficient mouse models (Chaudhury *et al.*, 2003). The lack of functional FcRn expression in B2M- or FcRn heavy chain-knock-out mice leads to a decrease of the serum concentration and the reduction serum half-life of both proteins (Chaudhury *et al.*, 2003; Roopenian *et al.*, 2003). Later studies using cellular models confirmed the role of FcRn in the rescue of albumin and IgG from

lysosomal degradation and the resulting extension of their half-life by the verification of FcRn-mediated recycling pathways *in vitro* and *in vivo* (Kim *et al.*, 2006; Montoyo *et al.*, 2009; Schmidt *et al.*, 2017; Toh *et al.*, 2020). Similar to the transfer of maternal IgG molecules to the foetus, the protection of FcRn ligands from lysosomal degradation relies on the pH-dependent interaction with FcRn. Albumin and IgG were shown to bind FcRn under acidic, but not neutral pH, indicating a possible interaction of the receptor with its ligands within acidified endosomes and subsequent release at the cell surface (Chaudhury *et al.*, 2003). Due to the lack of an interaction between the receptor and its ligands at neutral pH, FcRn is not believed to play a role in the cellular uptake of either albumin or IgG *in vivo*. However, for cells in an acidic extracellular environment like gastric cells or cell lines cultured in acidic medium FcRn might contribute to receptor-mediated endocytosis of IgG and albumin (Cooper *et al.*, 2014; Chia *et al.*, 2018; Zhang *et al.*, 2020; Lawrence *et al.*, 2021). In addition to the transfer of adaptive immunity to the foetus and the rescue of IgG and albumin from lysosomal degradation, FcRn was shown to play an important role in anti-tumour activities by facilitating nutrient depletion via albumin recycling in tumour cells and furthermore, FcRn can be exploited as entry or uncoating receptor by several viruses such as echoviruses and enterovirus B (Roopenian and Akilesh, 2007; Zhao *et al.*, 2019; Morosky *et al.*, 2019).

1.4.2: Interaction of FcRn with albumin

Albumin and FcRn are able to bind in an acidic environment with a high affinity in a low µM range (1.1 µM at pH 6), whereas no binding of the two molecules is observed at neutral pH (Sand *et al.*, 2014). The interaction of albumin and hFcRn is mediated by the protonation of His166 in FcRn and three additional conserved histidine residues (His464, His510 and His535) in the DIII domain of HSA under acidic conditions (Andersen *et al.*, 2012). Protonated His166 in FcRn forms charge-stabilised intramolecular hydrogen bonds with Glu54 and Tyr60 and leads to the stabilisation of a surface-exposed loop (residues 51 – 60) in the α1-domain of FcRn. The surface-exposed loop is characterised by the presence of four

conserved tryptophane residues (Trp51, Trp53, Trp59 and Trp61) within the loop structure (Andersen *et al.*, 2012) (Figure 1.6A).

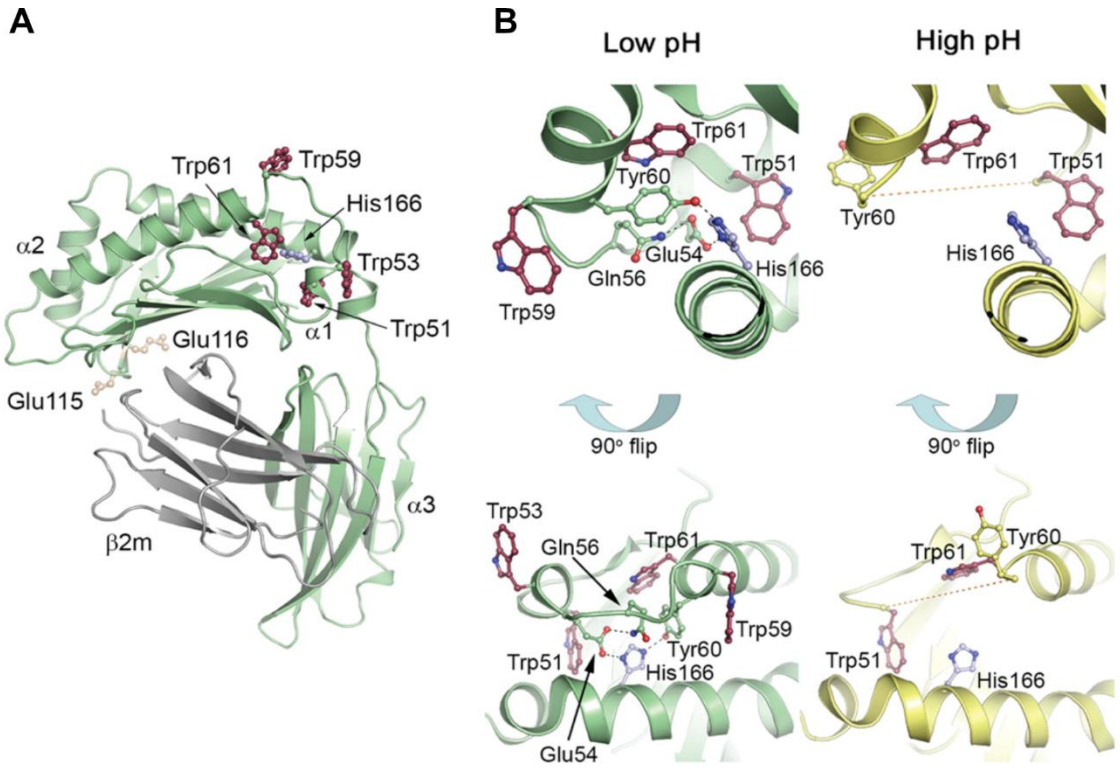

Figure 1.6: The structure of the pH-dependent flexible loop at the surface of human FcRn
(A) Ribbon diagram of the extracellular domains of human FcRn. The heavy α-chain is shown in green, the light chain (β_2m) is shown in grey. The residues Glu115, Glu116 and His166 within the α2 domain as well as the four conserved tryptophane residues, Trp51, Trp53, Trp59 and Trp61, within the pH-dependent flexible loop structure in the α1 domain of FcRn are highlighted as ball-and-stick models. **(B)** Close up view of the pH-dependent flexible loop structure in the α1 domain of FcRn at low pH (4.2, green) and high pH (8.2, yellow). In addition to highlighted amino acid residues before, Glu54, Gln56 and Tyr60 are shown as ball-and-stick models. Charge-stabilised hydrogen bond interactions of His166 at low pH are indicated by blue dashed lines. At high pH, uncharged His166 loses the ability to undergo stabilising interactions with Glu54 and Tyr60 and the tryptophane-rich loop structure becomes structurally disordered (yellow dashed line). Figure taken from (Sand *et al.*, 2014)**.**

These conserved tryptophane residues were shown to be essential for the interaction of FcRn with albumin since mutation of any one of the four residues to alanine abolished the ligand-receptor binding (Schmidt *et al.*, 2013; Sand *et al.*, 2014). Trp53 and Trp59 are exposed on the surface of FcRn and can interact with hydrophobic pockets formed in the DIIIa and DIIIb domain of albumin (Schmidt *et al.*, 2013). This interaction is highly dependent on the four conserved amino acids on albumin, Phe502, Phe507, Phe551 and Thr527, forming a hydrophobic cleft for binding to Trp53 of FcRn. Trp59 of FcRn is inserted into a proximal hydrophobic cleft formed by two α-helices of the DIII and DI domain of albumin (Sand *et al.*, 2014) (Figure 1.7).

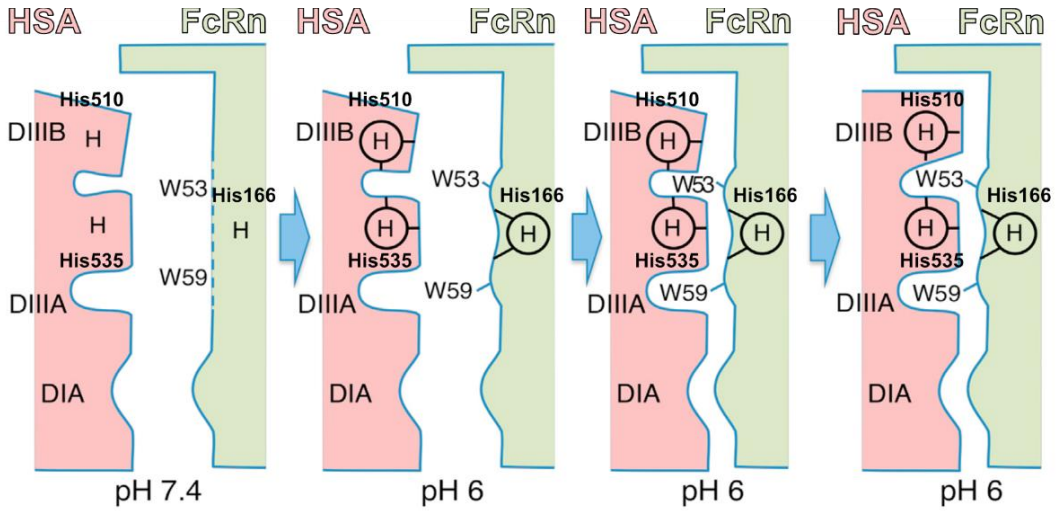

Figure 1.7: The pH-dependent binding of FcRn and HSA
Schematic model of the pH-dependent interactions between HSA (red) and FcRn (green). At pH 7.4, the surface-exposed looped of FcRn containing the two tryptophane residues, W53 and W59, is disordered (blue dashed line) and histidine residues of HSA and FcRn are deprotonated (H). At pH6, histidine residues in both molecules become protonated (circled H) and can form hydrogen bonds (black lines). Protonated His166 of FcRn stabilises the W53- and W59-containing loop and both tryptophane residues are exposed on the protein surface. Hydrogen bond networks mediated by His510 and His535 anchor hydrophobic binding pockets in the DIIIA and DIIIB domain of HSA in an open position. The albumin-FcRn interaction is stabilised by the insertion of W53 and W59 of FcRn into the hydrophobic binding pockets of HSA. Figure adapted from (Schmidt *et al.*, 2013)**.**

The Trp53 binding pocket is hereby held in an open position by two histidine residues on albumin (His510 and His535), which are fully protonated at acidic pH. His464 on albumin is proposed to directly interact with Trp59 in the respective binding pocket. (Schmidt *et al.*, 2013). The albumin-FcRn interaction is further stabilised by the formation of salt bridges between Lys500 of albumin and Gln46 on FcRn (Sand *et al.*, 2015). Interestingly, His166 does not interact directly with albumin but the substitution of His166 in hFcRn (His168 in murine FcRn) to alanine or phenylalanine leads to abolishment of the FcRn-albumin interaction highlighting the importance of the His166-mediated stabilisation of the loop structure in the α1-domain of FcRn (Schmidt *et al.*, 2013). Mutation of the albumin residues His464, His510 or His535 was also shown to significantly reduce the affinity of albumin to FcRn (Andersen *et al.*, 2012). In humans, the DI domain of albumin stabilises the binding to FcRn via the contact of two exposed loops with the α1 and α2 helices of FcRn. Interestingly, the participation of albumin DI in binding FcRn has not been observed in rodents indicating major species-dependent differences in the albumin-FcRn biology (Andersen *et al.*, 2010; Nilsen *et al.*, 2018). At neutral pH, the essential histidine residues on albumin and FcRn are deprotonated and no interaction of both molecules is observed (Sand *et al.*, 2014) (Figure 1.6B). In contrast to DI and DIII, DII of albumin does not participate in the interaction with FcRn (Andersen *et al.*, 2012).

Similar to the albumin-FcRn interaction, the binding of IgG molecules to FcRn relies on a pH-dependent interaction network of essential histidine residues and salt bridges (Vaughn *et al.*, 1997). The contact area of FcRn and IgG is much smaller than for the albumin interaction and the IgG binding site is located at the other site of the FcRn molecule (Chaudhury *et al.*, 2006). This allows FcRn to independently interact with albumin and IgG simultaneously (Oganesyan *et al.*, 2014). However, the simultaneous binding of both ligands to FcRn was investigated using soluble forms of FcRn. It remains unclear, if and how membrane-bound FcRn circumvents sterical hindrances and facilitates the simultaneous interaction with IgG and albumin molecules (Pyzik *et al.*, 2019). Furthermore, FcRn binds IgG molecules in a 2:1 molar ratio, whereas binding to

the other FcRn ligand, albumin, occurs with a stoichiometry of 1:1 (Sánchez *et al.*, 1999; Chaudhury *et al.*, 2006).

1.4.3: Intracellular localisation of FcRn

In contrast to other MHC-I class receptors, FcRn is predominantly localised to intracellular structures and only low levels are found at the cell surface (Blander, 2016; D'hooghe *et al.*, 2017). In steady state, FcRn was shown to be mainly associated with EEA1-positive early endosomes and Rab11- and transferrin-positive recycling endosomal structures in immortalised HeLa or HMEC-1 (human dermal microvascular endothelial cells) cell lines overexpressing hFcRn. Only small proportions of FcRn have been found to be presented on the cell surface or associated with CD63- and LAMP1-positive late endosomal and lysosomal structures (Ward *et al.*, 2005; Mahmoud *et al.*, 2017). Over the past two decades, sorting motifs within the cytoplasmic tail of FcRn were identified, which regulate FcRn trafficking and steady state localisation of FcRn in transfected cell lines via two main mechanisms (Newton *et al.*, 2005; Tesar and Björkman, 2010). On the one hand, the unique WXXφ (WISL) and acidic di-leucine (DXXXLL) motifs were shown to mediate clathrin-mediated endocytosis of surface FcRn into EEA1-positive early endosomes and lead to the rapid internalisation of surface-bound FcRn via adaptor protein 2 (AP-2) (Wu and Simister, 2001; Wernick *et al.*, 2005; D'hooghe *et al.*, 2017). On the other hand, the extended GLPAPWISL sorting motif was identified to be essential for the targeted trafficking of FcRn from EEA1-positive early endosomes into Rab11-positive recycling endosomes. The replacement of the cytoplasmic FcRn tail with the cytoplasmic tail of CD8 led to the exclusion of the hybrid receptor from Rab11-positive structures and the sorting of FcRn-CD8 into the late endosomal and lysosomal pathway (Mahmoud *et al.*, 2017). Hence, the active sorting of FcRn in transfected immortalised cell lines is mediated by sorting motifs in the cytoplasmic tail. However, the mechanisms or protein machinery responsible for the targeted FcRn trafficking have yet to be identified.

Although it is widely accepted that FcRn is not localised to CD63- or LAMP1-positive late endosomes and lysosomes, Gan *et al.* have shown that fluorescent-labelled FcRn can be trafficked into lysosomes using transfected HMEC-1 cells (Gan *et al.*, 2009). In contrast to most other receptor molecules destined for intracellular degradation, FcRn is not present in the intraluminal vesicles (ILVs) of $Rab5^{+}Rab7^{+}$ late endosomes but rather is associated with the limiting membrane of these organelles, a topology which allows FcRn to be potentially recycled back to the plasma membrane. In addition, some of the FcRn located to the limiting membrane of late endosomes can be delivered into lysosomal structures by tubular extensions or “kiss and run”-like interactions between late endosomes and lysosomes suggesting constitutive intracellular degradation of FcRn in immortalised cell lines (Gan *et al.*, 2009).

Most studies investigating the intracellular localisation of FcRn at steady state have used immortalised cell lines overexpressing FcRn. Studies in bone marrow-derived macrophages (BMDMs) isolated from humanised transgenic mice have revealed that FcRn is associated with enlarged EEA1-positive early endosomes and macropinosomes but is not localised to Rab11-positive recycling endosomes (Mahmoud, 2015). Furthermore, FcRn showed more than 50 % overlap with SNX5, which is heavily expressed in cells active in macropinocytosis and linked to newly formed macropinosomes (Lim *et al.*, 2012; Toh *et al.*, 2020). SNX5 was also detected on tubular extensions emerging from macropinosome bodies and, given the importance of SNX5 in driving membrane curvature, possibly facilitates a rapid recycling mechanism of endocytosed cargo back to the plasma membrane (Kerr *et al.*, 2006; Cullen and Korswagen, 2012).

In summary, differences in the intracellular distribution of FcRn under steady state conditions have been observed between distinct cell types underlining the complexity and gaps in understanding of the intracellular trafficking and recycling pathways of FcRn. It remains unclear whether the localisation of FcRn to specific endosomal structures is dependent on the particular cell type or differences in expression levels of the receptor can influence the intracellular distribution of the receptor.

1.5: The FcRn-dependent recycling system

The role of systemic FcRn expression in the homeostasis of IgG molecules was first suggested by Roger Brambell and colleagues in 1964 (Brambell *et al.*, 1964). The mechanisms of FcRn-dependent IgG homeostasis have been slowly deciphered over 30 years. A key study was the investigation of the IgG serum levels of mice bearing a knock-out of either the light (B2M) or heavy chain of FcRn (Ghetie *et al.*, 1996; Israel *et al.*, 1996; Christianson *et al.*, 1997; Roopenian *et al.*, 2003). These knock-out mice showed lower serum concentrations and enhanced IgG catabolism compared to WT mice. It was also discovered that FcRn is able to bind albumin and prolong its lifetime by rescuing endocytosed albumin from lysosomal degradation (Chaudhury *et al.*, 2003). The deletion of the FcRn heavy chain in mice led to a decrease of circulating levels of IgG and albumin of around 20 – 30 or 40 %, respectively. Additionally, the serum half-life of both, IgG and albumin, dropped from 95 and 39 hours to around 20 – 25 hours in the absence of functional FcRn (Ghetie *et al.*, 1996; Chaudhury *et al.*, 2003; Roopenian *et al.*, 2003).

1.5.1: The FcRn-IgG cell biology

Since the FcRn-dependent recycling pathway was first proposed in 1964, the cell biology underlying the FcRn cell biology has been studied extensively by Ward and colleagues, mostly in immortalised endothelial cell lines transfected with fluorescent-labelled FcRn (Ober *et al.*, 2004; Ward *et al.*, 2005; Gan *et al.*, 2013; Ober *et al.*, 2014). These studies have shown that endocytosed IgG molecules bind to FcRn in EEA1-, Rab4-, Rab5- and Rab11-positive endosomal structures, which are characterised by a luminal pH of around 6 (Ober *et al.*, 2004; Ward *et al.*, 2005; Zhou *et al.*, 2011). The FcRn-IgG complex is sorted into Rab4- and Rab11-positive recycling endosomes and subsequently trafficked to the plasma membrane via exocytic processes. Finally, the ligand dissociates from the receptor at neutral pH of the cell surface and IgG is then released into the extracellular environment (Ober *et al.*, 2014). IgG molecules, which do not bind

intracellular FcRn, or IgG variants not capable of binding FcRn, are sorted from endosomes into the lysosomal pathway (Ward *et al.*, 2003; Ober *et al.*, 2004). Similar results have been described for large FcRn-bound IgG immune complexes in human monocyte-derived dendritic cells, which upon endocytosis are sorted into degradative LAMP1$^+$ compartments and are processed for antigen-derived peptide presentation (Qiao *et al.*, 2008; Weflen *et al.*, 2013).

1.5.2: Mechanism of FcRn-dependent albumin recycling

Compared to the intracellular itinerary and the FcRn interaction of IgG molecules, much less is known about pathways and mechanisms of albumin-FcRn cell biology. There are contradictory findings about the primary endocytic pathways of albumin in different cell types. On the one hand, albumin is believed to bind to surface-exposed receptors like gp60 on endothelial cells or megalin, which then triggers receptor-mediated and caveolae-dependent endocytosis of albumin (Tiruppathi *et al.*, 1997; Vogel *et al.*, 2001; Bryniarski *et al.*, 2020). This selective albumin uptake was predominantly observed using immortalised endothelial cell lines. On the other hand, some studies using immortalised cell lines or primary bone marrow-derived macrophages showed that albumin uptake is facilitated non-selectively via macropinocytosis (Yumoto *et al.*, 2012; Liu *et al.*, 2019; Toh *et al.*, 2020).

Most studies agree that upon endocytosis albumin is associated with EEA1- and Rab5-positive early endosomal or macropinosomal structures (Schmidt *et al.*, 2017; Larsen *et al.*, 2018; Toh *et al.*, 2020). Studies in immortalised cell lines have shown that instead of being sorted to late endosomes and lysosomes, internalised albumin is recycled back to the plasma membrane in a FcRn-dependent manner (Schmidt *et al.*, 2017). To this end, the amount of recycled albumin following cell uptake was quantified using ELISA-based assays. Albumin variants with high affinity FcRn binding were recycled more efficiently than low affinity FcRn binding variants by FcRn-expressing endothelial cell lines, indicating that the sorting of albumin into the recycling pathway is FcRn-dependent

(Schmidt *et al.*, 2017; Larsen *et al.*, 2018; Grevys *et al.*, 2018). Additionally, albumin was found to be trafficked via Rab11-positive recycling endosomes before reaching the plasma membrane, suggesting FcRn-mediated recycling follows the slow endocytic recycling route in immortalised cell lines (Chia *et al.*, 2018). Due to the inability of most immortalised cell lines to implement fluid-phase uptake efficiently, albumin uptake was either realised with extended incubation times or under acidic conditions (Schmidt *et al.*, 2017; Larsen *et al.*, 2018; Chia *et al.*, 2018). The latter allows binding of albumin and FcRn at the cell surface and triggers receptor-mediated endocytosis of the ligand into the cell (Chia *et al.*, 2018). However, albumin is endocytosed independently of FcRn *in vivo*, predominantly by rapid fluid phase endocytosis (Lim and Gleeson, 2011; Lim *et al.*, 2015). Due to the major differences in the pathways of albumin uptake exploited *in vivo* and *in vitro*, there is concern in studying the FcRn-albumin cell biology using immortalised cell lines by forcing receptor-mediated endocytosis of albumin under acidic conditions (Anderson, 2014). This concern highlights the importance of primary cell models to be capable of efficient albumin internalisation by fluid phase endocytosis, or macropinocytosis, to gain more knowledge about FcRn-mediated albumin cell biology under physiologically relevant conditions.

One such approach was the investigation of FcRn-dependent HSA recycling in CSF-1-activated bone marrow-derived macrophages (BMDMs) isolated from human FcRn-transgenic mice (Toh *et al.*, 2020). In BMDMs, albumin, as well as IgG, is endocytosed via macropinocytosis and rapidly recycled back to the plasma membrane via tubular transport carriers in a FcRn-dependent manner (Toh *et al.*, 2020) (Figure 1.8).

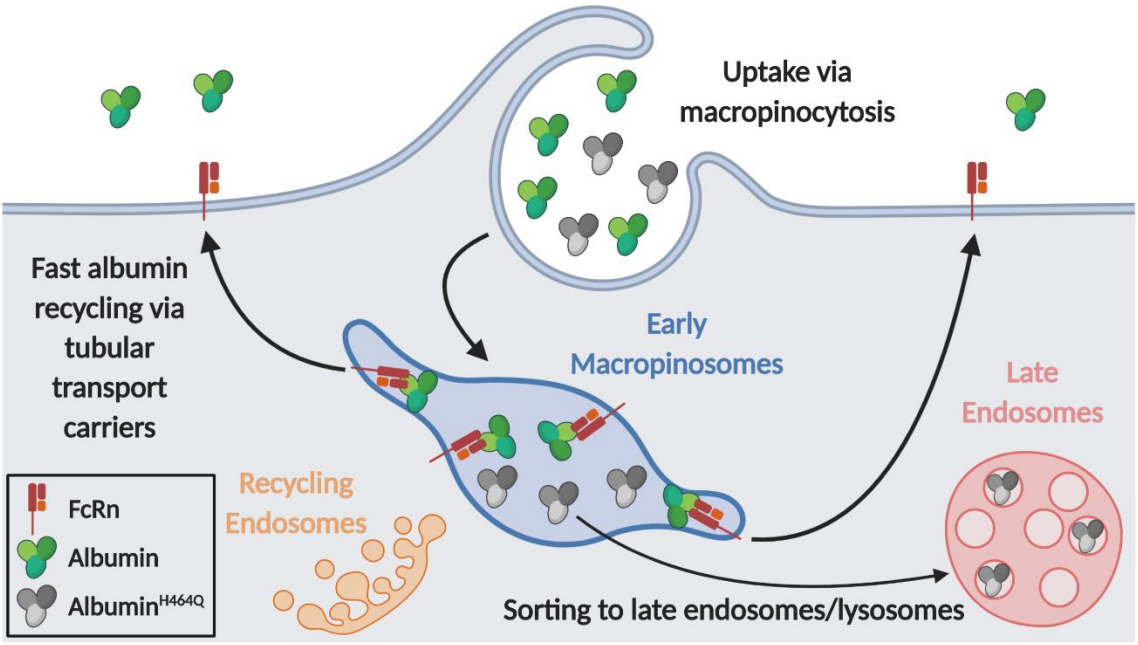

Figure 1.8: The FcRn-mediated albumin recycling in bone marrow-derived macrophages (BMDMs)
Human serum albumin (HSA, green) is endocytosed into CSF-1-activated bone marrow-derived macrophages (BMDMs) via macropinocytosis. HSA interacts with FcRn (red and orange) located at the limiting membrane of acidified early macropinosomes (blue). The receptor-ligand complex is sorted into tubular transport carriers mediating rapid FcRn-dependent HSA recycling. The non FcRn-binding albumin variant HSA^{H464Q} is sorted to late endosomes/lysosomes (red) and is eventually degraded. Recycling endosomes (orange) are not involved in FcRn-dependent HSA recycling on BMDMs. The figure was created with BioRender.com.

The tubular transport carriers mediating the recycling of albumin are positive for SNX5 and emerge from macropinosome bodies 15 – 20 minutes upon their internalisation (Toh *et al.*, 2020). Sorting of albumin into tubular carriers is thought to be mediated by the interaction of FcRn with its ligand in acidified maturing macropinosomes or early endosomes (Toh *et al.*, 2020). However, the details of the intracellular FcRn-albumin interaction within endosomes are yet to be defined. Once the transport carriers reach the plasma membrane, albumin is released from the receptor at neutral pH (Roopenian and Akilesh, 2007). The albumin variant HSA^{H464Q}, which is not able to interact with FcRn, is absent from SNX5-positive transport carriers and is rapidly degraded in lysosomes (Toh *et al.*,

2020). In contrast to studies using immortalised cell lines, Rab11-positive recycling endosomes are not involved in the FcRn-albumin recycling pathway in primary macrophages (Toh *et al.*, 2020).

In summary, the FcRn-mediated albumin cell biology is not fully understood. On the one hand, studies using immortalised cell lines suggest HSA recycling is facilitated via the slow recycling route (Chia *et al.*, 2018; Grevys *et al.*, 2018), whereas on the other hand primary BMDMs recycle HSA directly back to the plasma membrane in a rapid and FcRn-dependent manner (Toh *et al.*, 2020). For future studies, the establishment of primary cell models capable of effective fluid phase uptake is essential to investigate FcRn-albumin cell biology under physiologically relevant conditions.

1.5.3: Physiologically relevant sites for albumin homeostasis

The distribution and expression of FcRn across several tissues aggravates the identification of the most important sites of albumin homeostasis *in vivo* based solely on the location of FcRn (Latvala *et al.*, 2017). However, from a variety of approaches, including conditional FcRn knock-out in vascular and hematopoietic cells or macrophages, there is evidence on specific cell types playing a dominant role in regulating albumin homeostasis *in vivo* in a FcRn-dependent manner (Montoyo *et al.*, 2009; Challa *et al.*, 2019). Among these cells are hepatocytes in the liver, proximal tubule epithelial cells in the kidney, myeloid-derived antigen presenting cells (APCs) such as macrophages and dendritic cells (DCs), as well as vascular endothelial cells (Pyzik *et al.*, 2019).

Hepatocytes are responsible for albumin biosynthesis *in vivo* (Peters, 1997; Bern *et al.*, 2015). In hypoalbuminemic *Fcrgt*$^{-/-}$ mice, albumin production rates in the liver are increased by approximately 20 %, presumably to compensate for the loss of FcRn-mediated albumin recycling in these knock-out mice (Kim *et al.*, 2006). Interestingly, the conditional knock-out of FcRn expression in hepatocytes of Alb^{cre} FcRn$^{fl/fl}$ mice results in a less efficient transport of intracellular albumin from hepatocytes into the blood circulation compared to wildtype mice (Pyzik *et*

al., 2017). Instead, albumin is accumulated within hepatocytes or excreted into the bile suggesting an important role of FcRn in the selective sorting of intracellular albumin to the basolateral membrane of hepatocytes and subsequent release of the ligand into the circulation (Pyzik *et al.*, 2017).

The kidney controls the properties of various body fluids and removes waste products or toxins by filtration of the blood in the glomeruli (Finco, 1997). To avoid the accumulation of blood proteins in the urine, the presence of a charge- and size-dependent filtration barrier prevents the passage of high molecular weight proteins larger than ~ 40 kDa into the glomerular filtrate (D'Amico and Bazzi, 2003). Human serum albumin (HSA) with a size of ~ 66.5 kDa is close to the filtration cut-off size and is partially capable of entering the filtrate (Russo *et al.*, 2007). However, FcRn-expressing proximal tubule epithelial cells mediate the reabsorption of HSA from the glomerular filtrate into the blood circulation via a transcytosis pathway involving the cubilin-megalin receptor complex, which regulates the specific internalisation of HSA from the renal filtrate (Sarav *et al.*, 2009; Amsellem *et al.*, 2010). The importance of FcRn expression in proximal tubule epithelial cells and the involvement in the reabsorption of albumin into the circulation is supported by studies using FcRn knock-out models or inducible expression of tagged albumin in podocytes. In FcRn knock-out mice, hypoalbuminemia is reversed by the transplantation of WT kidneys indicating an important role of renal FcRn expression in albumin homeostasis (Sarav *et al.*, 2009). V5- and HA-tagged albumin expressed in podocytes upon doxycycline induction is transcytosed by proximal tubular epithelial cells in a FcRn-dependent manner and accumulates in the circulation (Tenten *et al.*, 2013).

FcRn is highly expressed in cells of hematopoietic origin, especially in monocytes, dendritic cells (DCs) and macrophages, which are therefore proposed to play a crucial role in maintaining high serum concentrations of albumin (Zhu *et al.*, 2001). Indeed, the deletion of the heavy or light chain of FcRn in cells of bone marrow (BM) origin significantly reduces the albumin half-life and concentration in the circulation of mice (Montoyo *et al.*, 2009). Similar effects are described for BM chimeras using human FcRn-transgenic recipient mice and

Fcrgt$^{-/-}$ BM donors (Richter *et al.*, 2018). The BM chimeras display lower albumin serum concentration than WT mice but significantly higher albumin levels than complete FcRn knock-out mice. The reconstitution of the BM compartment with human FcRn-expressing cells in *Fcrgt*$^{-/-}$ mice partially restores the normal levels of circulating albumin observed in wildtype mice (Roopenian *et al.*, 2015; Richter *et al.*, 2018). In mice harbouring a conditional knock-out for FcRn in the vascular and hematopoietic (*Tie2*^{cre}) or the macrophage compartment (*LysM*^{cre}) albumin levels are reduced 2-fold in comparison to WT mice highlighting the important role of these cells in the albumin homeostasis *in vivo* (Montoyo *et al.*, 2009; Challa *et al.*, 2019). Studies using primary bone marrow-derived macrophages isolated from mice transgenic for human FcRn also support the conclusion that these cells play an important role in albumin homeostasis, by mediating FcRn-dependent recycling of endocytosed albumin *in vitro* (Toh *et al.*, 2020). However, in contrast to previous findings, the deletion of FcRn in the CD11c compartment (*Itgax*^{cre}) has no effect on albumin serum concentrations in mice (Pyzik *et al.*, 2017). Collectively, these studies suggest that cells of hematopoietic origin, predominantly macrophages, are important in maintaining high circulating levels and long serum half-life of albumin, although their precise contribution *in vivo* is unclear since the reconstitution of BM in *Fcrgt*$^{-/-}$ mice with FcRn-expressing cells only leads to a partial recovery of the serum half-life and concentration of albumin (Richter *et al.*, 2018).

Endothelial cells line the blood vessels of the entire vascular system and hence are proposed to be key players in regulating albumin homeostasis *in vivo* due to their large contact area with blood (Pyzik *et al.*, 2019). The conditional knock-out of FcRn in endothelial (and hematopoietic) cells in Tie2^{cre} mice leads to reduced albumin serum levels and half-life suggesting endothelial cells may have a role in maintaining high concentrations of circulating albumin (Montoyo *et al.*, 2009). This conclusion is further supported by the bone marrow chimeras using human FcRn-expressing recipient mice and *Fcrgt*$^{-/-}$ BM donors discussed above, where albumin half-life is higher compared with complete FcRn knock-out mice suggesting that other cell types in addition to hematopoietic cells contribute to albumin homeostasis *in vivo* (Richter *et al.*, 2018). Studies using endothelial cell

lines *in vitro* have also demonstrated that intracellular FcRn rescues internalised albumin from lysosomal degradation by sorting albumin located to early endosomes into recycling pathways and avoiding the transport of the ligand to late endosomes and lysosomes. Rather, albumin was shown to be recycled back to the plasma membrane and released into the medium using non-polarised immortalised endothelial cell lines cultured in monolayers (Schmidt *et al.*, 2017; Grevys *et al.*, 2018). However, endothelial cells *in vivo* are polarised and regulate the passage of molecules from the circulation to the extravascular space beneath the endothelium or vice versa (Potente and Mäkinen, 2017). Additionally, albumin is not only present in high levels within the circulation but also in the extravascular space, where two-thirds of the total albumin molecules are proposed to reside (Arques, 2018). To which extent FcRn in endothelial cells regulate the biodistribution of circulating and extravascular albumin, and their contribution to FcRn-dependent albumin recycling or transcytosis *in vivo* remain poorly understood. A further complication is the heterogeneity of endothelial cells *in vivo*, as endothelial cells differ between arteries and veins as well as small and large vessels (Aird, 2007). Therefore, the establishment of primary endothelial cell models is essential to assess the role of vascular endothelial cells in FcRn-mediated albumin cell biology under physiologically relevant conditions *in vitro*.

Prominent FcRn expression in the adult is also reported for several other tissues and organs including intestinal mucosal surfaces, the blood-brain barrier and the lung epithelium (Sakagami *et al.*, 2006; Latvala *et al.*, 2017). Although FcRn-mediated regulation in the homeostasis of monomeric IgG and IgG immune complexes is well documented for these sites, they are not considered to fulfill important functions in albumin homeostasis (Roopenian and Akilesh, 2007; Pyzik *et al.*, 2019).

1.5.4: Exploiting FcRn-mediated albumin cell biology by the design of albumin fusion proteins

The downfall of many therapeutic proteins is their short half-life in *vivo* due to high renal clearance rates or their rapid degradation upon endocytosis. One strategy to overcome this issue is the design of half-life extended therapeutic fusion proteins with the Fc region of IgG molecules or albumin (Kontermann, 2016). On the one hand, the fusion to the Fc domain or albumin increases the size of the product decreasing the renal clearance rates of the particular fusion protein. On the other hand, fusion to one of the FcRn ligands allows FcRn-dependent recycling of the therapeutic fusion protein rescuing it from lysosomal degradation and thereby extending its circulatory half-life (Zaman *et al.*, 2019).

Albumin fusion proteins, in particular, are a promising approach for designing half-life extended therapeutics since recombinant HSA is stable, inert, non-immunogenic and with many surface-exposed binding sites for various compounds present on the albumin domain, the albumin fusion proteins can be used as vehicle molecules for co-administration of additional therapeutical compounds (Sleep *et al.*, 2013; Larsen *et al.*, 2016; Pilati and Howard, 2020; Chia *et al.*, 2021). Furthermore, therapeutic albumin fusion proteins can potentially be engineered to bind FcRn more efficiently or to target specific cell types and tissues including cancer cells or tumours, which dysregulate their expression of albumin-binding receptors such as FcRn to effectively endocytose and catabolise albumin as a nutrient source for allowing their rapid growth and propagation (Andersen *et al.*, 2014; Bern *et al.*, 2015; Cadena Castaneda *et al.*, 2020; Ribeiro *et al.*, 2021).

During the 21st century, several genetically engineered albumin fusion proteins with extended half-life properties have been designed for the potential treatment of various diseases and disorders including diabetes, hepatitis C and hemophilia B (Subramanian *et al.*, 2007; Gao *et al.*, 2009; Lyseng-Williamson, 2017). The first and only commercially available genetic albumin fusion protein Idelvion®, a fusion of recombinant FIX to albumin, was FDA-approved in March 2016 for the treatment of children and adults suffering from hemophilia B

(Choy, 2016). In contrast to recombinant FIX, Idelvion® exhibits improved pharmacological properties including extended serum half-life and reduces the frequency of prophylactic hemophilia B treatment with recombinant FIX products from injections every 3 – 4 days to 1 – 2 injections per fortnight (Lyseng-Williamson, 2017). One reason for the prolonged half-life of Idelvion® *in vivo* might be the exploitation of FcRn-dependent recycling upon endocytosis. Studies using FcRn-expressing HEK293 cells have indicated that FIX-albumin fusion proteins are able to engage with FcRn via their albumin moiety and FcRn-dependent fusion protein recycling is mediated via Rab11-positive recycling endosomes (Chia *et al.*, 2018). However, the cell biological details in primary cells and the contribution of FcRn-dependent recycling mechanisms in the half-life extension of albumin fusion proteins *in vivo* are not yet defined.

Instead of designing genetic albumin fusion proteins, albumin-based therapeutics can also be linked covalently to lysine residues or the free thiol group of Cys34 in human serum albumin via maleimide chemistry (Sleep *et al.*, 2013; Kuhlmann *et al.*, 2017). Alternatively, therapeutic proteins can be engineered to bind endogenous albumin by the introduction of bacterial albumin-binding domains (ABDs) or albumin binding lipids. Both strategies improve pharmacological parameters and increase circulatory half-life of engineered albumin-based therapeutics including the attachment of albumin-binding C14-myrisitic acid to insulin detemir or the conjugation of ABDs to IgA molecules, human epidermal growth factor 2 (HER2)-directed antibody mimetics (affibodies) and human TNF-related apoptosis-inducing ligand (hTRAIL) (Soran and Younis, 2006; Andersen *et al.*, 2011; Li *et al.*, 2016; Mester *et al.*, 2021). Other approaches focus on the use of albumin-binding nanobodies to extend the half-life of potential therapeutics for the treatment of various diseases like rheumatoid arthritis (Van Roy *et al.*, 2015; Jovčevska and Muyldermans, 2019).

Although albumin-based approaches to design half-life extended therapeutic proteins show promising results during clinical trials, particularly genetically engineered albumin fusion proteins are yet to increase their share on the open market (Pilati and Howard, 2020). The cell biological background of how half-life

extension of albumin-based fusion proteins is facilitated by different cell types *in vivo* and to which extent the exploitation of FcRn-dependent albumin recycling contributes to the improvement of pharmacological parameters remains unknown. Further investigations on FcRn-albumin cell biology in primary cells are required to identify possible limitations and to further improve the design and therapeutic outcome of albumin fusion proteins.

1.6: Hemophilia A and coagulation factor VIII

Hemophilia A (HemA) is an inherited, X-chromosome linked bleeding disorder affecting approximately 1 in 5000 males worldwide resulting in life-long bleeding tendencies in patients (Soucie *et al.*, 1998; Mannucci and Tuddenham, 2001). Also known as the “royal disease”, congenital HemA in females is very rare due to the recessive mode of the disease (Byams *et al.*, 2011). However, recent studies raise more awareness about female carriers exhibiting clinical symptoms of HemA, albeit mostly mild, and recommend prophylactic treatment analogous to male HemA patients (Bryant *et al.*, 2020).

HemA is caused by the total absence or impaired function of coagulation factor VIII (FVIII), an essential glycoprotein cofactor in the blood coagulation cascade (Bhopale and Nanda, 2003). FVIII is produced by liver sinusoidal endothelial cells (LSECs) and, upon activation by thrombin, activated FVIII (FVIIIa), together with activated coagulation factor IX (FIXa) forms the intrinsic tenase complex (Autin *et al.*, 2005). The tenase complex activates coagulation factor X, which by forming the prothrombinase complex with activated factor V stimulates the generation of high amounts of thrombin completing a thrombin-dependent positive feedback loop. Eventually, the blood coagulation process is finalised by the generation of stable clots formed by thrombin-mediated conversion of fibrinogen into insoluble fibrin polymers (Schenone *et al.*, 2004).

The severity of HemA correlates with plasma concentrations of FVIII and thus, patients are categorised according to their residual FVIII activity levels. Patients with mild (5 – 40 IU/dl FVIII) or moderate (1 – 5 IU/dl FVIII) HemA suffer from

prolonged bleeding periods throughout life and are susceptive to trauma-induced bleedings without a significant decrease in quality of life (White *et al.*, 2001; Blanchette *et al.*, 2014). In contrast, patients suffering from severe HemA (< 1 IU/dl FVIII) may experience spontaneous bleeding events within joints and muscles resulting in irreversible cartilage and bone damage, which both drastically reduce the quality of life (Knobe and Berntorp, 2011). In addition, severe HemA patients bear an increased risk of experiencing brain haemorrhages and their life expectancy, even upon FVIII replacement therapy, is reduced up to 37 % in high-income countries compared to healthy individuals (Hu *et al.*, 2018; Iorio *et al.*, 2019).

1.6.1: Treatment of hemophilia A and inhibitor formation

Beginning in the 1950's, HemA patients originally were treated with infusions of whole blood or plasma to recover FVIII activity and prevent bleeding events (Franchini and Mannucci, 2012). Due to the inefficiency of the treatment with whole blood, it was quickly discovered that lyophilised plasma concentrates rich in FVIII were far more effective in preventing bleeding events improving symptomatic outcomes of HemA patients (Pool *et al.*, 1964). However, the use of plasma-derived plasma products led to a massive transmission of human immunodeficiency virus (HIV) and hepatitis C virus (HCV) to HemA patients caused by product contamination (Mannucci, 2003). Despite the emerge of new technologies significantly increasing the safety of plasma-derived FVIII products, the gold standard for treating patients suffering from HemA today is protein replacement therapy using recombinant FVIII (rFVIII) products (Franchini, 2013).

Recombinant FVIII products are applied via intravenous injections either on demand upon suffering from severe bleeding events or in a prophylactic manner. Particularly in patients with severe HemA protein replacement therapy is conducted prophylactically to prevent spontaneous bleeding events within joints and muscles (Brackmann *et al.*, 1992; Berntorp *et al.*, 2021). Prophylactic FVIII treatment requires frequent intravenous injections due to the relative short

half-life of recombinant FVIII (~ 12 hours) in the circulation, and is very burdensome and expensive for HemA patients (Lillicrap, 2008). Therefore, current research is focussed on the development of half-life extended FVIII products, such as FVIII fusion and PEGylated proteins, or non-factor therapies including bispecific antibodies mimicking the *in vivo* function of FVIII (Coyle *et al.*, 2014; Nolan *et al.*, 2016; Oldenburg *et al.*, 2017). However, these new generation products are often less effective and more expensive and thus, the standard treatment of HemA patients today remains the intravenous application of recombinant FVIII products (Aledort *et al.*, 2019; Berntorp *et al.*, 2021).

One major complication resulting from rFVIII-dependent protein replacement therapy is the development of neutralising antibodies against FVIII in HemA patients, usually observed within the first 15 days of exposure (Gouw *et al.*, 2013). These neutralising antibodies, also referred to as inhibitors, are formed in up to 30 % of patients suffering from severe HemA and approximately 5 % of patients with mild or moderate forms of HemA (Meeks and Batsuli, 2016). Inhibitors are polyclonal high-affinity antibodies, which most commonly bind to functional epitopes of FVIII and inhibit FVIII function by sterically blocking enzymatic functions (Ananyeva *et al.*, 2004; Saint-Remy *et al.*, 2004). Additionally, inhibitors can bind to non-functional FVIII epitopes and increase the clearance rate of rFVIII *in vivo* via the formation of immune complexes (Lacroix-Desmazes *et al.*, 1999). Taken together, the formation of inhibitors directed against FVIII drastically decreases the efficiency of protein replacement therapy using rFVIII and leads to increased morbidity and reduced quality of life in HemA patients (Walsh *et al.*, 2016).

The formation of inhibitors, in addition to the influence of several environmental and genetic risk factors, is caused by a lack of central and peripheral tolerance to FVIII in HemA patients, which triggers a pathophysiological immune response mediated by FVIII-specific B and T cells (Figure 1.9) (Saint-Remy *et al.*, 2004; Garagiola *et al.*, 2018; Cormier *et al.*, 2020; Hart, 2020).

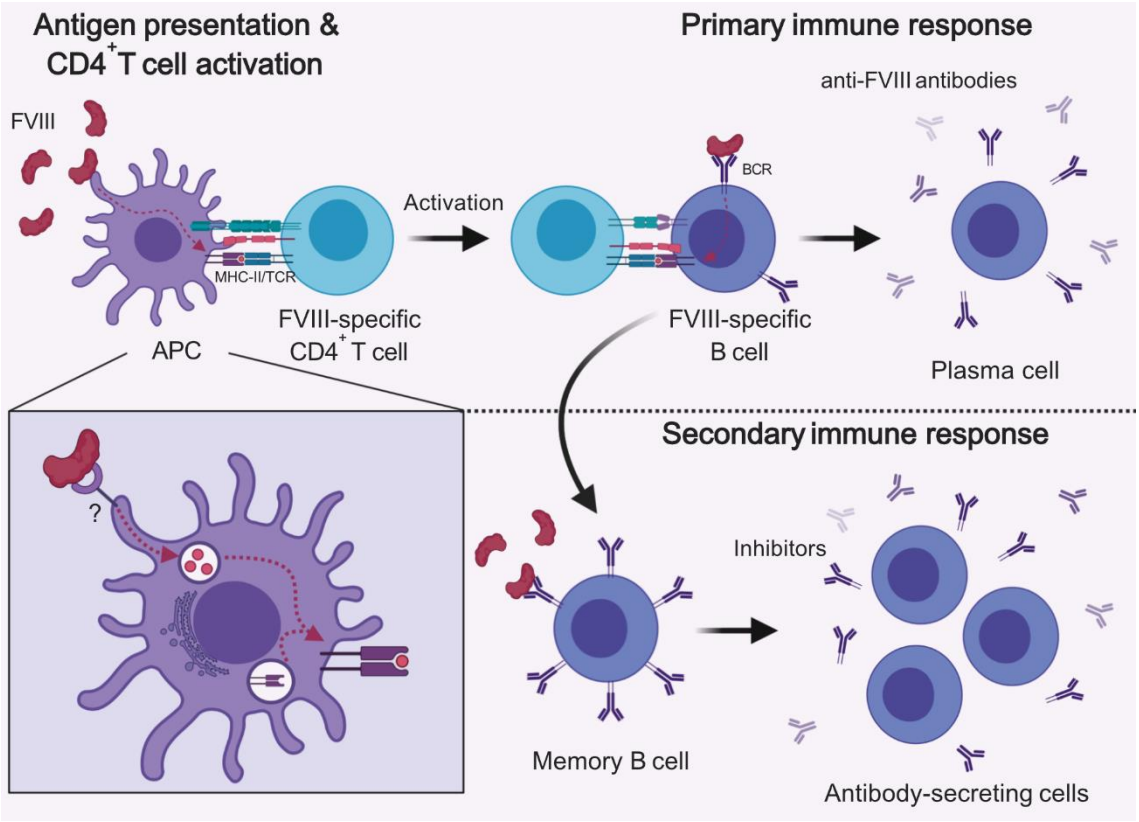

Figure 1.9: Cellular mechanisms of inhibitor development in hemophilia A (HemA) patients
Extracellular FVIII is endocytosed by antigen-presenting cells (APCs) via receptor-mediated endocytosis by binding to surface receptors expressed on APCs. Endocytosed FVIII is trafficked along the endocytic pathway and processed to peptides, which subsequently are loaded onto MHC-II molecules within the MHC-compartment. MHC-II-loaded peptides are presented to FVIII-specific $CD4^+$ and together with co-stimulatory signals induce the activation of these $CD4^+$ T helper cells. Activated $CD4^+$ T cells stimulate FVIII-specific B cells, which upon recognition of FVIII via their B cell receptor (BCR) present FVIII epitopes on their cell surface. Activated B cells differentiate into anti-FVIII antibody-secreting plasma cells triggering primary immune response against FVIII. Some activated B cells differentiate into memory B cells, which secrete inhibitory anti-FVIII antibodies upon re-exposure to FVIII in a secondary immune response. Figure taken from (Meißner, 2020). The figure was originally created with BioRender.com.

FVIII injected into hemophilic mice was shown to accumulate in the marginal zone of the spleen, where it is endocytosed by antigen-presenting cells (APCs), presumably dendritic cells (DCs) (Navarrete *et al.*, 2009). The endocytosis of

FVIII by DCs is believed to be mediated by binding to surface receptors but remains yet to be fully understood (Dasgupta *et al.*, 2007; Repessé *et al.*, 2012). Upon endocytosis, FVIII is trafficked along the endocytic pathway and eventually reaches degradative lysosomes. FVIII-derived peptides, usually with lengths of 9 – 20 amino acids, are loaded onto MHC class II molecules, which are then sorted to the plasma membrane. Loaded MHC class II molecules present processed FVIII peptides to $CD4^+$ T cells, which potentially are activated by binding to the MHC-presented FVIII peptide via their T cell receptor (TCR) (van Haren *et al.*, 2011; Wroblewska *et al.*, 2013). To activate naïve $CD4^+$ T cells, DCs additionally have to undergo a maturation process, which is induced by the presence of danger signals in the microenvironment. The presence of rFVIII alone is not sufficient to initiate the danger signal-dependent DC maturation *in vitro* (Pfistershammer *et al.*, 2006).

FVIII-specific naïve $CD4^+$ T cells located to secondary lymphoid organs are activated upon encountering mature DCs presenting FVIII-derived peptides on their cell surface. The activation of T cells is amplified by the engagement of co-stimulatory surface receptors (e.g. CD80/86 and CD28) and the presence of cytokines secreted by DCs and T cells (Lacroix-Desmazes *et al.*, 2008). Activated $CD4^+$ T helper cells migrate to the splenic B cell follicles, where they activate FVIII-specific B cells. These B cells derive from the bone marrow and upon recognition of extracellular FVIII via their epitope-specific B cell receptor (BCR) require co-stimulatory signals from FVIII-specific activated $CD4^+$ T helper cells to become fully activated. Activated FVIII-specific B cells undergo rapid proliferation and differentiate into anti-FVIII antibody-secreting plasma cells, responsible for initiating primary immune responses against exogeneous FVIII, or memory B cells (André *et al.*, 2009). Some of the antibody-secreting plasma cells migrate to the bone marrow and become long-lived plasma cells, where they continue secreting FVIII-neutralising antibodies over a long period of time. In contrast, memory B cells do not secrete any anti-FVIII antibodies. Upon encountering re-exposure of FVIII, however, they can rapidly differentiate into antibody-secreting cell initiating the secondary immune response against FVIII (Van Helden *et al.*, 2010). This leads to the constant secretion of FVIII-neutralising antibodies in

HemA patients receiving repetitious injections of rFVIII diminishing its therapeutic function (Saint-Remy *et al.*, 2004; Van Helden *et al.*, 2010).

1.6.2: Immune tolerance induction and the role of regulatory T cells in hemophilia A

To eradicate FVIII-neutralising antibodies, HemA patients who developed inhibitors undergo complex, empirically designed treatment regimens, referred to as immune tolerance induction (ITI) protocols (Schep *et al.*, 2018). The first ITI protocol, known as Bonn protocol, was developed in 1974 and relies on the repetitive administration of high doses of FVIII (100 – 150 IU/kg, twice daily) into inhibitor developing patients (Brackmann and Gormsen, 1977; Brackmann *et al.*, 1996). Several other ITI protocols have been established over the last decades using different treatment regimens including repetitive high- or low-dose injections of rFVIII (Wight *et al.*, 2003; Brackmann *et al.*, 2018). The success of ITI protocols in HemA patients is measured by diminished inhibitor titers (< 0.6 BU/ml), increased FVIII half-life (≥ 6 hours) and the recovery of FVIII activity levels to at least 66 % (Oldenburg *et al.*, 2014). Although successful ITI leads to long-lasting induction of tolerance to FVIII, the treatment regimens are very burdensome to the patient and highly expensive. In addition, the success rate of ITI is estimated to vary only between 59 – 87 % depending on the applied protocol (Schep *et al.*, 2018).

Therefore, recent research has focussed on identifying endo- and exogeneous factors to predict the outcome of ITI in HemA patients. Risk factors, which can lead to the failure of inducing immune tolerance, include the genetic FVIII background of the patient as well as experiencing viral infections and major bleeding events while undergoing the ITI treatment regimen (Valentino *et al.*, 2015; Schep *et al.*, 2018). The exact cellular and molecular mechanisms contributing to immune tolerance induction are unknown, but high doses of FVIII were shown to interfere with the differentiation of FVIII-specific B memory cells into inhibitor-secreting plasma cells *in vitro* and *in vivo* (Hausl *et al.*, 2005; Reipert

et al., 2007). In addition, regulatory T cells (Tregs) can be induced by the long-time exposure to antigens in a non-inflammatory microenvironment and studies using hemophilic mice have shown that the humoral response against FVIII is supressed after the induction of FVIII-specific Tregs *in vivo* (Chen *et al.*, 2004; Liu *et al.*, 2011). More recently, PD-L1-expression on Tregs has been discovered to be important for the suppression alloimmune responses against FVIII in hemophilia A mice (Figure 1.10) (Meißner, 2020).

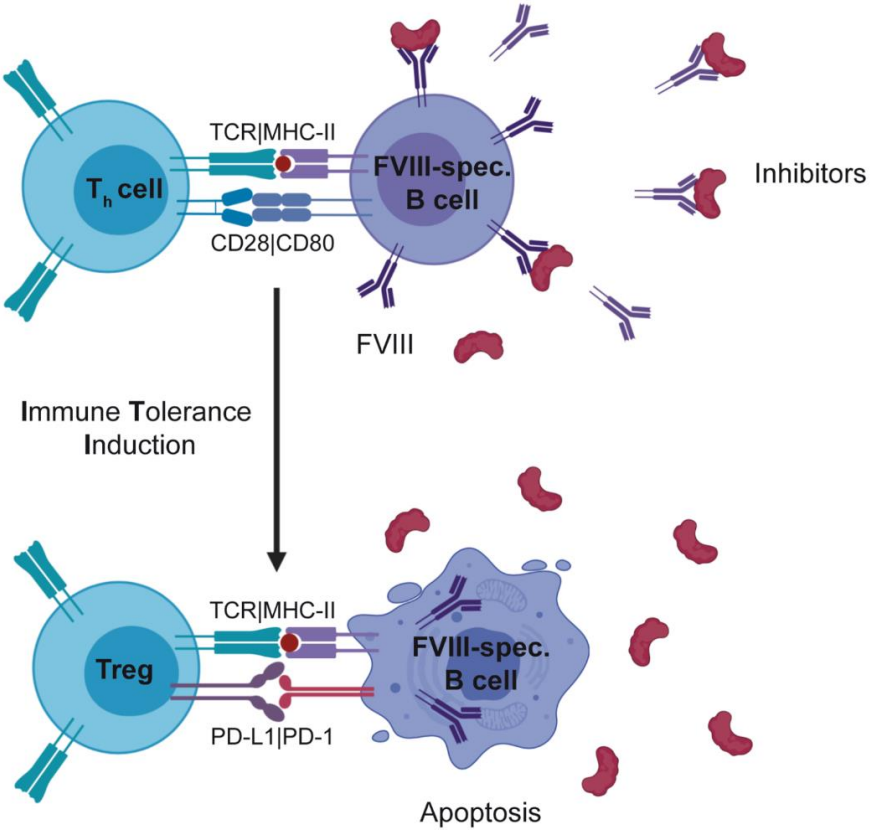

Figure 1.10: Treg-mediated immune tolerance induction via PD-1/PD-L1 signalling in hemophilia A (HemA) patients
Activated $CD4^+$ T helper cells recognise MHC-II-loaded FVIII peptides presented on the cell surface of FVIII-specific B cells and in combination with co-stimulatory signals (CD28/CD80 signalling) trigger B cell activation. Eventually, this leads to the production of neutralising anti-FVIII antibodies (inhibitors), which diminish the functionality of FVIII proteins injected during protein replacement therapy. Immune tolerance induction stimulates the generation of FVIII-specific regulatory T cells (Tregs), which induce apoptosis in FVIII-specific B cells via PD-1/PD-L1 signalling and prevent the formation of FVIII inhibitors. Figure taken from (Meißner, 2020). The figure was originally created with BioRender.com.

The ability of Tregs to directly supress autoreactive B cells *in vivo* mediated by PD-L1 has already been established earlier (Gotot *et al.*, 2012). Antigen-specific peripheral Tregs induce apoptosis in B cells in a contact-dependent and antigen-specific manner preventing the formation of autoreactive antibodies (Gotot *et al.*, 2018). Similar mechanisms have been suggested to play an essential role in mediating immune tolerance towards FVIII. FVIII-specific B cells in wildtype or human FVIII-expressing mice showing immune tolerant phenotypes towards FVIII display increased surface expression of PD-1 and undergo apoptosis. The induction of apoptosis in FVIII-specific B cells is mediated via contact-dependent PD-1/PD-L1 signalling initiated by the interaction of PD-1 on B cells with PD-L1 expressed on the surface of Tregs (Meißner, 2020). FVIII-specific Tregs, in particular, have been shown to effectively supress humoral and cellular responses against FVIII. However, cytokine-dependent suppression mechanisms mediated by FVIII-unspecific Tregs also might contribute to the induction of tolerance towards FVIII (Smith *et al.*, 2020; Fu *et al.*, 2020). During ITI, PD-L1 expression on Tregs is assumed to be elevated, leading to the induction of apoptosis in FVIII-specific B cells and preventing the formation of inhibitory FVIII antibodies (Meißner, 2020). Therefore, the repetitive exposure to FVIII during ITI leading to the Treg- and PD1-/PD-L1-dependent apoptosis of FVIII-specific B cells is described by the induction of high zone tolerance and possibly establishes long-lasting alloimmune effects in the context of hemophilia A (Diener and Feldmann, 1972; Steinman *et al.*, 2019).

1.6.3: Alternative strategies for the treatment of hemophilia A

There are two major downfalls of treating HemA patients prophylactically with standard protein replacement using rFVIII; Firstly, the therapy regimen requires repetitious intravenous injections of the recombinant protein due to its short half-life *in vivo* of approximately 12 hours. Usually, HemA patients need 2 – 3 injections weekly to maintain functional FVIII activities and to prevent spontaneous bleeding events effectively correcting for the hemophilic phenotype (Nilsson *et al.*, 1992; Sankar *et al.*, 2019). This procedure is very burdensome for

patients, reduces their quality of life and is quite challenging especially in young HemA patients due to limited vein access (Saxena, 2013). Secondly, the repetitive injection of rFVIII may trigger the development of anti-FVIII inhibitory antibodies, which neutralise the function of administered recombinant protein in HemA patients and lead to rapid clearance from the circulation further decreasing circulatory half-life of rFVIII (Lacroix-Desmazes *et al.*, 1999).

Over the past decades, several approaches have been assessed to overcome these two main challenges resulting from protein replacement therapy using standard recombinant FVIII proteins (Mannucci, 2003; Meeks and Batsuli, 2016; Mannucci, 2020). Since the secretion of neutralising FVIII antibodies relies on the stimulation of FVIII-specific B cells within a pro-inflammatory environment, some investigations on the prevention of inhibitor formation are focused on suppression of FVIII-specific B cell differentiation into antibody-secreting plasma cells. These approaches include the induction or transfer of FVIII-specific regulatory T cells (Tregs) or engineered CAR Tregs to prevent FVIII-specific B cell activation in hemophilic mice (Smith *et al.*, 2020; Scott, 2020; Chen *et al.*, 2020; Fu *et al.*, 2020). However, high numbers of regulatory T cells are required to fully prevent inhibitor formation in HemA patients and large-scale induction of antigen-specific Tregs *in vitro* and *in vivo* remains a major technical and cost-intensive challenge (Safinia *et al.*, 2010; Sicard *et al.*, 2018). Other alternative therapies include the use of non-factor products such as Emicizumab, a monoclonal, bi-specific antibody mimicking FVIII function *in vivo* by supporting the interaction of activated FIX and FX (Kitazawa *et al.*, 2012). Although Emicizumab exhibits long serum half-life of up to 5 weeks and was shown to significantly improve the clinical phenotype even in HemA patients with pre-existing inhibitors, it is still unknown if the bi-specific antibody promotes the same physiological long-term benefits as the presence of FVIII protein including the prevention of irreversible joint and bone damage as well as providing optimal support for wound healing (Shima *et al.*, 2016; Lenting *et al.*, 2017; Mannucci, 2020).

To reduce the number of injections of recombinant protein and providing cost-effective and less burdensome treatments for HemA patients, several half-life

extended FVIII products and strategies for FVIII half-life extension have been developed (Zaman *et al.*, 2019). In some studies, recombinant FVIII was modified by PEGylation to increase the protein size or was engineered to bind von Willebrand factor, which protects FVIII from degradation *in vivo*, with increased affinity. Both strategies increase the serum half-life of these products *in vivo* by protecting them from renal clearance or degradation upon endocytosis (Ivens *et al.*, 2013; Lenting *et al.*, 2016). Another approach to prolong the half-life of FVIII products *in vivo* includes the design of FVIII fusion proteins with the Fc-region of IgG molecules or albumin. These fusion proteins can potentially undergo FcRn-dependent recycling resulting in the extension of their half-lives (Figure 1.11) (Dumont *et al.*, 2012; Schulte, 2013). The pH-dependent interaction of albumin and IgG with FcRn allows sorting of the ligand-receptor complex into transport carriers mediating the recycling of endocytosed FcRn ligands back to the circulation (Pyzik *et al.*, 2019). Particularly, the design of therapeutic albumin fusion proteins is a promising approach to establish half-life extended FVIII products for the treatment of HemA, since they are simple to produce, inert, stable, non-immunogenic and the surface-exposed binding sites of albumin for various compounds potentially allows the co-administration of other synergistic drugs in combination with rFVIII (Rogers *et al.*, 2015; Sleep, 2015; Pilati and Howard, 2020).

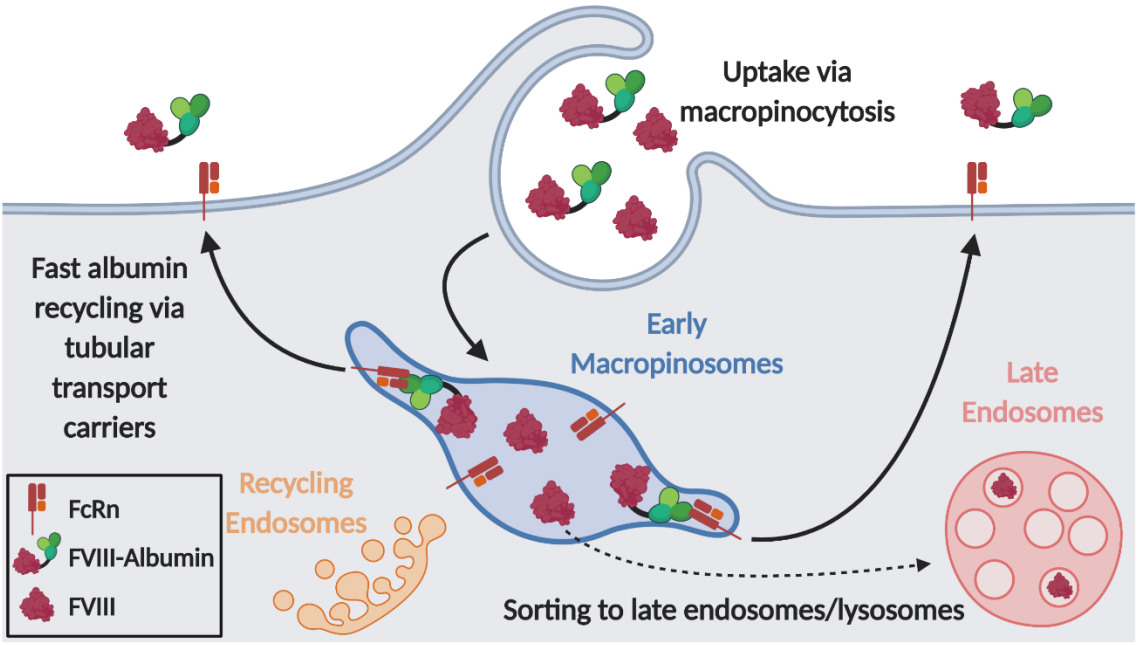

Figure 1.11: Principle of exploiting FcRn-mediated albumin recycling by the design of FVIII-Albumin fusion proteins
FVIII and FVIII-Albumin fusion protein are endocytosed via macropinocytosis and subsequently locate to early macropinosomes. FVIII is sorted to the late endosomal and lysosomal pathway resulting in its rapid proteolytic degradation. The albumin domain of FVIII-Albumin fusion proteins is able to interact with FcRn within acidified early macropinosomes. The ligand-receptor complex is sorted into tubular transport carriers mediating fast recycling back to the plasma membrane, where, at neutral pH, FVIII-Albumin dissociates from FcRn and is released into the circulation, therby extending the half-life of the fusion protein. The Figure was created with BioRender.com.

FVIII-Albumin fusion proteins are proposed to undergo FcRn-dependent recycling upon endocytosis resulting in their half-life extension by avoiding proteolytic degradation in lysosomes. Endocytosed FVIII proteins not able to interact with FcRn, however, are sorted into degradative lysosomal compartments leading to their rapid degradation upon endocytosis (Lillicrap, 2008). This hypothesis of exploiting FcRn-dependent recycling mechanisms is supported by studies using FIX-albumin fusion proteins and the approval of Idelvion®, a half-life extended FIX-albumin fusion product, for the treatment of hemophilia B patients (Lyseng-Williamson, 2017; Chia *et al.*, 2018). FIX-albumin fusion proteins endocytosed by HEK293 cells are recycled via Rab11-positive

recycling endosomes in a FcRn-dependent manner, possibly contributing to their half-life extension observed *in vivo* (Chia *et al.*, 2018). The longer half-life, elevated serum concentration and perhaps alternative processing mechanisms of such albumin fusion proteins might also contribute to the suppression of anti-FVIII inhibitor formation and the induction of high zone tolerance towards FVIII in HemA patients similar to what is observed for FVIII-Fc fusion proteins (Steinman *et al.*, 2019; Meeks and Lacroix-Desmazes, 2020).

With the breakthrough of gene therapeutic and technologic methods over the past decade, hemophilia research, especially in high-income countries, also focuses on establishing these techniques in the treatment of hemophilic patients (Park *et al.*, 2016; Reiss *et al.*, 2021; Mancuso *et al.*, 2021). The introduction of functional FVIII genes by using AAV-based vectors into hemophilic mice and dogs suffering from HemA showed promising clinical results by maintaining therapeutic FVIII serum levels over a long-period of time and the induction of immune tolerance (Samelson-Jones and Arruda, 2020). Similar results have been observed in adult human HemA patients receiving gene therapy with the vector AAV5-hFVIII-SQ (Rangarajan *et al.*, 2017). However, gene therapeutic treatment regimens for HemA patients are still evaluated in clinical trials and progress has been slow due to the large size of the FVIII gene and uncertainty about negative long-term effects of gene therapy (Franchini, 2013; Samelson-Jones and Arruda, 2020). Some studies suggest the integration of transgenes introduced by AAV-derived vectors into the host genome linking this gene therapeutic approach to potentially increased risks of genotoxicity and cancer development (Donsante *et al.*, 2007; Nowrouzi *et al.*, 2012; Nault *et al.*, 2015). In addition, patients might have pre-existing antibodies directed against AAV-derived transfer vectors diminishing their therapeutic function (Stanford *et al.*, 2019; Rajavel *et al.*, 2019). The use of gene therapy nowadays is still highly expensive and it might take a long time until affordable gene therapy-based HemA treatments become commercially available (Mancuso *et al.*, 2021). Furthermore, in most human trials using gene therapeutic approaches patients with pre-existing FVIII inhibitors have been excluded, and thus, the potential of gene therapeutic approaches to replace ITI protocols cannot be assessed (Miesbach *et al.*, 2019).

1.7: Aim of the study

The principle of FcRn-dependent recycling of albumin resulting in the extraordinary half-life of the most abundant serum protein is widely accepted and *in vitro* studies have deciphered various cell biological aspects underlying this recycling system (Schmidt *et al.*, 2017; Chia *et al.*, 2018; Grevys *et al.*, 2018). However, most studies have been conducted using immortalised cell lines, which, in contrast to primary cells, are not capable of performing rapid fluid-phase endocytosis effectively and thus, are not suitable for the investigation FcRn-albumin cell biology under physiologically relevant conditions (Anderson, 2014). The recent discovery of a fast FcRn-dependent albumin recycling pathway in primary macrophages, mediated by tubular-carriers emerging from early macropinosomes, highlights the cell biological differences in primary cells and immortalised cell lines (Toh *et al.*, 2020).

In this study, I have established a multiplexed approach using two independent biophysical methods, namely fluorescence lifetime imaging combined with Förster resonance energy transfer (FLIM-FRET) and raster image correlation spectroscopy (RICS), to map the intracellular interaction of fluorescent-labelled albumin and FcRn in a spatiotemporal manner and to quantify the mobility of single albumin molecules within endosomal structures in primary macrophages.

To investigate FcRn-dependent albumin trafficking in vascular endothelial cells, which are proposed to play an important role in regulating albumin homeostasis *in vivo*, I established a primary cell model using blood outgrowth cells isolated from human peripheral blood (Martin-Ramirez *et al.*, 2012). These cells were characterised for FcRn expression and intracellular localisation as well as for albumin uptake and FcRn-dependent trafficking within the endosomal network.

Lastly, I characterised the uptake of FVIII-Albumin by FVIII-specific B cells *ex vivo* using imaging flow cytometry, and established an *in vitro* platform for the expansion of FVIII-specific $CD4^+$ T cells and evaluated the potential of converting these antigen-specific cells into Foxp3-expressing Tregs using a CDK8/19

inhibitor (Akamatsu *et al.*, 2019). Both strategies are promising approaches to induce immune tolerance towards recombinant FVIII products in HemA patients.

Together, the overall goal of this study was to expand the knowledge about FcRn-albumin cell biology in physiologically relevant primary cell models to allow the effective design of half-life extended albumin proteins exploiting FcRn-dependent albumin recycling for the treatment of serum protein-related diseases. Within this study, FVIII-Albumin, a potential candidate for a half-life extended therapeutic protein undergoing FcRn-dependent recycling, was used to transfer cell biological insights into the immunological relevant aspects of high zone immune tolerance induction in a hemophilia A mouse model.

Chapter 2: Material and Methods

2.1: General materials, cell lines and mouse strains

2.1.1: Chemicals and reagents

Standard chemicals and solvents were in analytical grade and purchased from chemical suppliers, unless stated otherwise.

Table 2.1: Chemicals and reagents

Name	Supplier
(Animal-free) recombinant murine interleukin-2 (IL-2)	Peprotech (USA) Product-#: AF-212-12
2-(4-amidinophenyl)-6-indolecarbamidine dihydrochloride (DAPI)	Sigma Aldrich (USA) Product-#: D9542
5-(N-ethyl-N-isopropyl) amiloride (EIPA)	Sigma Aldrich (USA) Product-#: A3085
5-(and-6)-carboxyfluorescein diacetate, succinimidyl ester (CFSE)	Thermo Fisher Scientific (Germany) Product-#: C1157
Amersham ECL Western Blotting detection reagent	GE Healthcare/Cytiva (USA) Product-#: RPN2106
AS2863619 (AS)	MedChemExpress (USA) Product-#: HY-126675A
Collagen type I from rat tail	Corning (USA) Product-#: 354236
Collagenase from *Clostridium histolyticum*	Sigma Aldrich (USA) Product-#: C2674
cOmplete™ Mini protease inhibitor cocktail	Merck (Germany) Product-#: 11836170001
Deoxyribonuclease (DNAse) I from bovine pancreas	Sigma Aldrich (USA) Product-#: D5025
DQ™ Ovalbumin (DQ-OVA)	Thermo Fisher Scientific (Australia) Product-#: D12053
Dynabeads™ mouse T-Activator CD3/CD28 for T-Cell expansion and activation (Dynabeads)	Thermo Fisher Scientific (Germany) Product-#: 11452D
eBioscience™ fixable viability dye eFluor™ 506	Thermo Fisher Scientific (Germany) Product-#: 65-0866-14
eBioscience™ Foxp3/transcription factor staining buffer set	Thermo Fisher Scientific (Germany) Product-#: 00-5523-00

Name	Supplier
Ficoll-Paque™ PLUS	VWR International (USA) Product-#: 95021-205
FuGENE6® transfection reagent	Promega (Australia) Product-#: E2691
GlutaMax™ supplement (100x)	Thermo Fisher Scientific (Australia) Product-#: 35050061
Hoechst 33342 (Hoechst)	Thermo Fisher Scientific (Germany) Product-#: H3570
Invitrogen™ LysoTracker™ Red DND-99 (LysoTracker Red)	Thermo Fisher Scientific (Australia) Product-#: L7528
Lipofectamine™ 3000 transfection reagent	Thermo Fisher Scientific (Australia) Product-#: L3000008
LIVE/DEAD™ fixable dead cell stain sampler kit	Thermo Fisher Scientific (Germany) Product-#: L34960
NUPAGE™ Antioxidant	Thermo Fisher Scientific (Australia) Product-#: NP0005
PEG-it Virus precipitation solution	Integrated Sciences (Australia) Product-#: LV810A-1
Penicillin-Streptomycin (10,000 U/ml)	Sigma Aldrich (USA) Product-#: P4333
Phorbol-12-myristae-13-acetate (PMA)	Sigma-Aldrich (USA) Product-#: P1585
Recombinant human transforming growth factor β-1 (TGF-β)	Peprotech (USA) Product-#: 100-21
Recombinant macrophage colony-stimulating factor (CSF-1, M-CSF)	Sigma Aldrich (USA) Product-#: 234376
SIINFEKL peptide (OVA 257 – 264) peptide fragment)	AnaSpec (USA) Product-#: AS-60193
TrypLE™ express enzyme (1x) for trypsinisation	Thermo Fisher Scientific (Australia) Product-#: 12605010
UltraPure™ DNase/RNase-free distilled water	Thermo Fisher Scientific, Australia, Product-#: 10-977-015
Zombie UV™ fixable viability kit	BioLegend (USA) Product-#: 423107

2.1.2: Buffers and cell culture media

Table 2.2: Buffers

Name	Supplier/Composition
Blocking buffer (for IF)	1x PBS + 5 % v/v FCS + 0.02 % w/v sodium azide

Name	Supplier/Composition
Blocking buffer (for WB)	10 % w/v skim milk powder in PBS + 0.01 % w/v sodium azide
Collagen type I coating buffer	50 µg/ml collagen type I in 0.02 M acetic acid
CutSmart® buffer	New England Biolabs (USA) Product-#: B7204S
DAPI staining buffer	1 µg/ml DAPI in 1x PBS
Deacetylation solution	For 50 ml deacetylation solution: 38 ml PBS + 1.74 g Hydroxylamine x HCl + 2 ml 0.5 M EDTA solution Adjust pH to 7.2 – 8.5 using NaOH and fill up solution to 50 ml with H_2O
Digestion buffer	C-RPMI medium + 1 mg/ml Collagenase + 0.1 mg/ml DNAse
DNA transfection mix (for $CaPO_4$ transfection)	0.25 M $CaCl_2$ in UltraPure™ H_2O
FACS buffer (for adherent cells)	1x PBS + 2 % v/v FCS + 1 mM EDTA
FACS buffer (for suspension cells)	1x PBS + 0.1 % w/v BSA + 0.1 % w/v sodium azide
Fixation-permeabilisation (fix/perm) buffer (for intracellular flow cytometry staining)	Dilute 1 part fixation/permeabilisation concentrate in 3 parts diluent (both from Foxp3/transcription factor staining buffer set (Thermo Fischer Scientific, Germany))
HEPES-buffered saline, pH 7.0 (HBS, 2x for transfection)	Thermo Fisher Scientific (Australia) Product-#: J62623
Hoechst staining buffer	1 µg/ml Hoechst in 1x PBS
Invitrogen™ NUPAGE™ LDS sample buffer (4x)	Thermo Fisher Scientific (Australia) Product-#: NP0007
Invitrogen™ NUPAGE™ MOPS SDS running buffer (20x)	Thermo Fisher Scientific (Australia) Product-#: NP0001 Diluted in milliQ-H_2O to prepare 1x SDS running buffer, according to manufacturer's protocol

Name	Supplier/Composition
Invitrogen™ NUPAGE™ transfer buffer (20x)	Thermo Fisher Scientific (Australia) Product-#: NP00061 1x transfer buffer (100 ml): 5 ml 20x transfer buffer + 10 ml MeOH + 100 µl NUPAGE™ Antioxidant Fill up to 100 ml with milli-Q H_2O
MACS buffer	1x PBS + 0.5 % w/v BSA + 2 mM EDTA adjusted to pH 7.2
Neutralisation solution	0.1 % w/v BSA in 1x PBS
PBS-Tween20	0.1 % v/v Tween20 in 1x PBS
Permeabilisation (perm) buffer (for intracellular flow cytometry staining) (1 x)	Dilute 10 x permeabilisation buffer from Foxp3/transcription factor staining buffer set (Thermo Fischer Scientific, Germany) in milli-Q H_2O, according to manufacturer's protocol
Phosphate-buffered saline (PBS, 1x)	For 1 l 1x PBS (pH 7.4): 8 g NaCl (137 mM) + 0.2 g KCl (2.7 mM) + 1.44 g Na_2HPO_4 (10 mM) + 0.24 g KH_2PO_4 (1.8 mM) + 1 l milli-Q H_2O or: dissolve PBS tablets (Thermo Fisher Scientific, Germany) in milli-Q H_2O, according to the manufacturer's protocol Product-#: 18912014
Quenching buffer (for PFA fixation)	50 mM NH_4Cl in 1x PBS
Quenching buffer (for TCA fixation)	30 mM glycine in 1x PBS
Radioimmunoprecipitation assay buffer (RIPA)	50 mM Tris-HCl, pH 7.3 + 150 mM NaCl + 0.1 mM EDTA + 100 µM NA_3VO_4 + 1 % w/v sodium deoxycholate + 1 % v/v Triton-X-100 + 0.2 % w/v NaF
RBC lysis buffer	0.09 % w/v NH_4Cl in milli-Q H_2O
Saponin permeabilisation buffer	0.05 % w/v saponin in 1x PBS
TheraPEAK™ ACK lysis buffer (1x)	Lonza (Switzerland) Product-#: BP10-548E
Triton-X-100 permeabilisation buffer	0.1 % v/v Triton-X-100 in 1x PBS

Table 2.3: Cell culture media

Name	Supplier/Composition
BMDM freezing medium	80 % v/v FCS + 10 % v/v BMDM medium + 10 % v/v DMSO
BMDM medium	RPMI + 15 % v/v FCS + 20 % v/v L-conditioned medium + 1x GlutaMax™ Supplement + 100 U/ml penicillin + 100 U/ml streptomycin
BOEC freezing medium	95 % v/v FCS + 5 % v/v DMSO
BOEC medium	EGM2 + 18 % v/v FCS + 1x GlutaMax™ Supplement + 100 U/ml penicillin + 100 U/ml streptomycin
C-DMEM	DMEM + 10 % v/v FCS + 1x GlutaMax™ Supplement + 100 U/ml penicillin + 100 U/ml streptomycin
C-EGM2	EGM2 + 2 % v/v FCS (from BulletKit™) + 1x GlutaMax™ Supplement
C-RPMI	RPMI + 10 % v/v FCS + 1x GlutaMax™ Supplement + 100 U/ml penicillin + 100 U/ml streptomycin
C-X-Vivo medium	X-Vivo medium + 10 % v/v FCS + 1 % v/v β-mercaptoethanol (5 mM) + 100 U/ml penicillin + 100 U/ml streptomycin
Dulbecco's Modified Eagle Medium (DMEM, Gibco™ DMEM, high glucose)	Thermo Fisher Scientific (Australia) Product-#: 11-965-118
Endothelial growth medium-2 (EGM2) BulletKit™	Lonza (Switzerland) Product-#: CC-3162 Contains endothelial basal medium-2 (EBM2, CC-3156) and SingleQuots™ supplements (CC-4176) to prepare endothelial growth medium-2 (EGM2)

Name	Supplier/Composition
Gibco™ RPMI 1640 Medium (RPMI)	Thermo Fisher Scientific (Australia) Product-#: 11-875-119
GlutaMax-DMEM	DMEM + 10 % v/v FCS + 1x GlutaMax™ Supplement
High FCS-RPMI	RPMI + 20 % v/v FCS + 1x GlutaMax™ Supplement + 100 U/ml penicillin + 100 U/ml streptomycin
LB medium	For 1 l LB medium: 10 g tryptone 10 g NaCl 5 g yeast extract 2 l milli-Q H_2O For selection plates: Add 15 g/l Agar
MSA blocking medium	X-Vivo medium + 10 % v/v FCS + 1 % v/v β-mercaptoethanol (5 mM) + 0.2 % w/v MSA + 100 U/ml penicillin + 100 U/ml streptomycin
Opti-MEM™ reduced serum medium, no phenol red	Thermo Fisher Scientific (Australia) Product-#: 11058021
SFM-DMEM	DMEM + 1x GlutaMax™ Supplement + 100 U/ml penicillin + 100 U/ml streptomycin
SFM-EGM2	EGM2 w/o FCS from BulletKit™ + 1x GlutaMax™ Supplement
SFM-RPMI	RPMI + 1x GlutaMax™ Supplement + 100 U/ml penicillin + 100 U/ml streptomycin
SOC medium	New England Biolabs (USA) Product-#: B9020S
T cell medium	RPMI + 10 % v/v FCS + 1 % v/v β-mercaptoethanol (5 mM) + 100 U/ml penicillin + 100 U/ml streptomycin
X-Vivo™ 15 Serum-free Hematopoietic Cell medium (X-Vivo medium)	Lonza (Switzerland) Product-#: BE02-060F

2.1.3: PCR and sequencing primers

All primers were purchased from Sigma Aldrich (USA). Primer sequences (5' to 3') are listed in Table 2.4. Complementary overhangs for HiFi assembly introduced by primer design are highlighted in bold.

Table 2.4: PCR and sequencing primers

Name	5' to 3' sequence
B2M-FcRn-mCherry(FUGW)-fw	**GCTGCAGGTCGACTCTAGAGGCTAGC**ATGTCTCGCTCC
B2M-FcRn-mCherry(FUGW)-rev	**TATCGATAAGCTTGATATCGGCTAGC**CTACTTGTACAGCTCGTCC
backbone-pIRES-fw	**GGTGGCGACCGGTGGATCCCGGGC**GCCGAGAGCCATCTGAGC
backbone-pIRES-rev	GCCCAGAGATCCAGGCAG
FcRn-mCherry(pIRES)-fw	**TTGCCACAACCCGGGATCCTCTAGA**ATGGGAGTGCCTAGACCTC
FcRn-mCherry(pIRES)-rev	**AACCCTCACTAAAGGGAAGCGGCCG**CTACTTGTACAGCTCGTCC
mCherry-FcRn(IRES)-fw	**TTCTGCTGCCTGGATCTCTGGGC**ATGGTGAGCAAGGGCGAG
mCherry-FcRn(IRES)-rev	**AGGCTCAGATGGCTCTCGGCGCCCGGGATCCACCGGTCGCCACC**CTTGTACAGCTCGTCCATGC
Seq-End-IRES	TTGAAAAACACGATGATAAGC
Seq-End-mCherry	AACGTCAACATCAAGTTGG

2.1.4: Plasmids

The plasmid pEF1α-mCherry-N1 (Clontech Laboratories, USA, 631969) and the pEF1α-FcRn_mCherry plasmid were kindly provided by CSL Limited, Australia. pEF1α-FcRn_mCherry was generated by inserting the sequence of human FcRn heavy α-chain into pEF1α-mCherry-N1 upstream of mCherry. Both domains of the fusion protein were separated by polypeptide linker with the sequence Ala-Arg-Asp-Pro-Pro-Val-Ala-Thr.

The bicistronic plasmid pIRES-β_2-microglobulin/mycFcRn encoding for both, human B2M and FcRn using an internal ribosomal entry site (IRES), was generated by Ismail Mahmoud and obtained from laboratory stocks.

The plasmids pCMV-VSV-G (#8454) (Stewart *et al.*, 2003), psPAX2 (#12260) provided by Didier Trono (unpublished), and FUGW (#14883) (Lois *et al.*, 2002) for the production of lentiviral particles were purchased from Addgene (USA).

2.1.5: Antibodies and fluorescently labelled tetramers

Table 2.5: List of unconjugated primary antibodies used

Antigen	Clone/Product-#	Supplier	Used for	Dilution
CD144	16B1	Thermo Fisher Scientific (Australia)	FC/IF	1:400 (FC) 1:500 (IF)
CD31	390 (14-0311-82)	Thermo Fisher Scientific (Australia)	IF	1:500
CD63	MX-49.129.5	Santa Cruz (USA)	IF	1:400
EEA1	14/EEA1	BD Biosciences (Germany)	IF	1:400
GAPDH	6C5 (AM4300)	Thermo Fisher Scientific (Australia)	WB	1:1000
GM130	35/GM130	BD Biosciences (Germany)	IF	1:800
golgin97	CDF4	Thermo Fisher Scientific (Australia)	IF	1:300
hFcRn	HPA015130	Atlas Antibodies (Sweden)	IF/WB	1:500 (IF) 1:500 (WB)
KDEL	KR-10	Enzo Life Sciences (USA)	IF	1:100
KDEL-R	10C3	Enzo Life Sciences (USA)	IF	1:200
LAMP1	ab24170	Abcam (United Kingdom)	IF	1:500
mCherry	ab183628	Abcam (United Kingdom)	IF/WB	1:500 (IF) 1:500 (WB)
Rab11	47/Rab11	BD Biosciences (Germany)	IF	1:200
Rab11a	20229-1-AP	Proteintech (USA)	IF	1:1000
SNX5	(Lim *et al.*, 2012)	Lab-made antibody	IF	1:2000
vWF	ab6994	Abcam (United Kingdom	FC/IF	1:400 (FC) 1:400 (IF)

Secondary antibodies were used in a dilution of 1:500 for flow cytometry (FC) and immunofluorescence (IF), and in a 1:1000 dilution for Western Blot (WB).

Table 2.6: List of conjugated secondary antibodies

Specificity	Conjugate	Product-#	Supplier	Used for
Mouse IgG	AF488	A11001	Thermo Fisher Scientific (Australia)	IF
Mouse IgG	AF568	A11004	Thermo Fisher Scientific (Australia)	IF
Mouse IgG	AF647	A21236	Thermo Fisher Scientific (Australia)	IF
Mouse IgG	HRP	62-652-0	Thermo Fisher Scientific (Australia)	WB
Rabbit IgG	AF488	A11008	Thermo Fisher Scientific (Australia)	IF
Rabbit IgG	AF568	A11011	Thermo Fisher Scientific (Australia)	FC/IF
Rabbit IgG	AF647	A21245	Thermo Fisher Scientific (Australia	FC/IF
Rabbit IgG	HRP	65-612-0	Thermo Fisher Scientific (Australia)	WB
Rat IgG	AF568	A11077	Thermo Fisher Scientific (Australia)	IF

Table 2.7: List of fluorescence-conjugated antibodies used for flow cytometry and imaging flow cytometry

Antigen	Clone	Conjugate	Supplier	Dilution
B220	RA3-6B2	BV510	BioLegend (USA)	1:400
B220	RA3-6B2	FITC	BioLegend (USA)	1:400
CD11c	HL3	BV510	BD Biosciences (Germany)	1:400
CD25	PC61	PE	BioLegend (USA)	1:400
CD25	PC61	PE-Cy7	BioLegend (USA)	1:400
CD4	GK1.5	APC-Cy7	BioLegend (USA)	1:400
CD4	GK1.5	PerCP-Cy5.5	BioLegend (USA)	1:400
CD44	IM7	PE-Cy7	BioLegend (USA)	1:400
CD44	IM7	PerCP-Cy5.5	BD Biosciences (Germany)	1:400
CD8a	53-6.7	BV510	BioLegend (USA)	1:400
CD8a	53-6.7	APC	BioLegend (USA)	1:400
Foxp3	150D	FITC	BioLegend (USA)	1:200

To stain for FVIII-specific $CD4^+$ T cells a PE-labelled ProT2® MHC class II tetramer (ProImmune, United Kingdom) with the peptide sequence TASSYFTNMFATWSPSKARL was used.

2.1.6: Fluorescently labelled proteins

Plasma-derived human serum albumin (HSA) was labelled with Alexa Fluor® 488 (AF488) NHS ester (succinimidyl ester) (Thermo Fisher Scientific, Australia, A-20000) or Alexa Fluor® 568 (AF568) NHS ester (succinimidyl ester) (Thermo Fisher Scientific, Australia, A-37572), respectively, according to the manufacturer's protocol. Recombinant FcRn non-binding albumin variant HSA^{H464Q} ($rHSA^{H464Q}$) was generated and labelled with Alexa Fluor® 488 (AF488) NHS ester (succinimidyl ester) (Thermo Fisher Scientific, Australia, A-20000) (Toh *et al.*, 2020). Fluorescent-labelled HSA and $rHSA^{H464Q}$ conjugates were provided by CSL Limited, Australia.

Serum-derived human transferrin labelled with Alexa Fluor® 488 (AF488, T13342) or Alexa Fluor® 568 (AF568, T23365) and TexasRed (TxRed)-conjugated 70 kDa dextran (D1830) were purchased from Thermo Fisher Scientific, Australia.

FVIII protein (Kogenate® FS, Bayer, Germany) and murine serum albumin (MSA, Abcam, USA, ab183228) were coupled via succinimidyl esters to obtain FVIII-Albumin fusion protein. To this end, 1 mg N-succinimidyl S-acetylthioacetate (SATA, Thermo Fisher Scientific, Germany, 26102) was dissolved in 30 µl DMSO and 10 µl of the freshly prepared SATA solution added to 1 mg FVIII protein suspended in 1 ml PBS. The mixture was incubated for 30 minutes at room temperature and subsequently the FVIII protein solution desalted using ZEBA spin columns (1,000x g, 2 minutes) (Thermo Fisher Scientific, Germany, 89891). 100 µl freshly prepared deacetylation solution was added to 1 ml desalted FVIII suspension and incubated for 2 hours at room temperature before desalting the FVIII solution again using ZEBA spin columns (1,000x g, 2 minutes). Meanwhile, 1.5 mg succinimidyl 4-(N-maleimidomethyl)-cyclohexane-1-carboxylate) (SMCC,

Thermo Fisher Scientific, Germany, 22360) were resuspended in 100 µl DMSO and 15 µl freshly prepared SMCC solution added to 1 mg MSA resuspended in 1 ml PBS. The mixture was incubated for 30 minutes at room temperature and subsequently the MSA solution desalted using ZEBA spin columns (1,000x g, 2 minutes). The desalted FVIII and MSA solutions were transferred to a 15 ml tube in a 1:1 ratio (v/v) and incubated over night at 4 °C under constant rotation. Successful coupling of FVIII-Albumin fusion protein was examined by SDS-PAGE.

FVIII protein (Kogenate® FS, Bayer, Germany) and coupled FVIII-Albumin fusion protein were fluorescently labelled with CF® 647 (similar to APC and Alexa Fluor® 647) using CF® 647 succinimidyl ester protein labelling kit (Biotium, USA, 92218), according to the manufacturer's protocol.

2.1.7: Bacterial cells

Chemically competent α-Select Silver or NEB® 5-alpha (High Efficiency) *E. coli* bacterial cells were purchased from BIOLINE (United Kingdom) or New England Biolabs (USA) respectively.

2.1.8: Mammalian cell lines

HeLa, HEK293T (HEK293) and L-929 cells, verified by genome sequencing, were obtained from laboratory stocks and routinely tested for mycoplasma contamination using MycoAlert™ Mycoplasma Detection Kit (Lonza, Switzerland).

HeLa cells were originally derived from a tissue sample taken from African American woman Henrietta Lacks (Nature Publishing Group, 2020). In 1951, HeLa cells were established as the first continuous cancer cell line and are since widely used to study various cellular processes in human cells (Masters, 2002).

Human embryonic kidney 293 (HEK293) cell lines were first established in 1973 and since then several HEK293 variants have been derived from the parental cell line to address distinct purposes (Pulix *et al.*, 2021). The HEK293T daughter cell line harbors the sequence for the expression of a temperature-sensitive variant of the simian virus-40 (SV40) large T antigen, essential to produce large amounts of recombinant proteins encoded by plasmid vectors carrying the viral SV40 origin of replication, which is commonly used in lentiviral plasmids (Vargas *et al.*, 2004; Mitta *et al.*, 2004; Hartenbach and Fussenegger, 2005; Yuan *et al.*, 2018).

The parental L cell strain was derived from subcutaneous and adipose tissue of a 100-day-old male C3H/An mouse (American Type Culture Collection, 2022). Clone 929 (L-929) was one of the first L strains to be established in continuous culture and shown to express and secrete colony stimulating factor 1 (CSF-1), which drives the differentiation of haematopoietic stem cell into bone marrow-derived macrophages (BMDMs) (Price *et al.*, 1992; Englen *et al.*, 1995). Thus, the supernatant of L-929 cells (L-conditioned medium) is widely used as cheap and reliable source of CSF-1 for BMDM differentiation *in vitro* (Heap *et al.*, 2021).

2.1.9: Mouse strains

FcRn$^{-/-}$ mice (FcRn KO), which harbour a knockout allele of the mouse FcRn α-chain (*Fcgrt*^{tm1Dcr}), and FcRn$^{-/-}$hFcRn (line 276 and line 32) Tg mice (hFcRn$^{Tg/Tg}$), which have the null mutation for the mouse FcRn gene and a transgene expressing the human FcRn α-chain under the control of the β-actin promoter (line 276) or the native FcRn promoter (line 32), respectively (Chaudhury *et al.*, 2003; Roopenian *et al.*, 2003), were purchased from Jackson laboratory (USA) and mouse colonies established and maintained under specific pathogen-free conditions in the animal facility of Bio21 Institute, University of Melbourne. All experiments carried out on animals were approved by the institutional Animal Care and Use Committee and approved by the Animal Ethics Committee, Biochemistry & Molecular Biology, Dental Science, Medicine, Microbiology &

Immunology, and Surgery, The University of Melbourne (Ethics-ID: 1714375). Unless stated otherwise, hFcRn$^{Tg/Tg}$ line 276 mice were used for experiments.

C57BL/6J (WT B6) mice (Black *et al.*, 1998) and B6;1295-F8t^{m1Kaz}/J (HemA) mice, which harbour a homozygous mutation in the FVIII gene and are characterised by low FVIII activity levels (< 1 %) resulting in prolonged blood clotting times and a hemophilia A phenotype (Bi *et al.*, 1995), were purchased from Jackson Laboratory (USA). For *in vitro* suppression assays, C57BL/6-Tg(TcraTcrb)1100Mjb/J (OT-1) (Hogquist *et al.*, 1994), originally purchased from Jackson Laboratory (Bar Harbour, ME), crossed with B6;129P-Ccr4^{tm1Pwr}/J (CCR4 KO) mice (Chvatchko *et al.*, 2000) were used (OT-I x CCR4 KO). CD8^{+} T cells of these mice primarily recognise the ovalbumin peptide residues 257 – 264 (OVA$_{257-264}$, SINFEKL) presented on MHC class I molecules due to transgenic inserts for mouse Tcra-V2 and Tcrb-V5 (Hogquist *et al.*, 1994). The CCR4 KO background of these mice was not considered relevant for the conducted studies.

Mouse colonies were established under specific pathogen-free conditions at the central facility of the University Hospital Bonn, Germany (House of Experimental Therapy). Mouse studies and maintenance were performed in accordance with the recommendations of the Federation of European Animal Science Association (FELASA) and approved by the Landesamt für Natur, Umwelt und Verbraucherschutz Nordrhein-Westfalen (LANUV, Aktenzeichen: 81-02.04.2019.A.464).

2.2: Molecular biological methods

2.2.1: Polymerase chain reaction (PCR)

Plasmid DNA was used as a template for PCRs, and PCR reactions were prepared using the Phusion® High-Fidelity PCR Kit (New England Biolabs, USA) in a final volume of 25 or 50 µl, according to the manufacturer's protocol, and the addition of suitable forward and reverse oligonucleotide primers at a

concentration of 0.5 µM each. PCR reactions were performed in a thermocycler using the following standard protocol:

Table 2.8: Standard protocol for PCR reactions using the Phusion® High-Fidelity PCR Kit

Step	Temperature	Time	Cycles
Initial denaturation	98 °C	30 seconds	1x
Denaturation	98 °C	10 seconds	**30x**
Annealing	T_M	20 seconds	**30x**
Extension	72 °C	20 seconds/kb	**30x**
Final extension	72 °C	10 minutes	1x
Hold	4 °C	∞	1x

The annealing temperature T_M was calculated with the NEB Tm Calculator tool (New England Biolabs, USA). If the estimated annealing temperature exceeded 72 °C, a 2-step PCR was performed by skipping the annealing step. The duration for the extension step was estimated according to the respective size of the expected PCR product.

2.2.2: HiFi DNA assembly

Seamless HiFi assembly of DNA fragments was performed using NEBuilder® HiFi DNA Assembly Master Mix (New England Biolabs, USA), according to the manufacturer's protocol. Fragments with overlapping DNA overhangs were used in a molar ratio of 1:2 or 1:3 (vector to insert). The concentration, and the according mass, of DNA fragments was measured using a NanoDrop™ 2000/2000c microvolume spectrophotometer (Thermo Fisher Scientific, Australia) and the number of pmol for each fragment was determined using the following equation:

$$pmol = (weight\ in\ ng)\ x\ 1{,}000 \div (base\ pairs\ x\ 650\ daltons)$$

The HiFi assembly reaction was performed at 50 °C for 60 minutes. For the subsequent transformation of assembled DNA products into competent *E. coli.* cells, 2 µl of the assembly reaction was used and transformation was performed, as described below (Section 2.4.1).

2.2.3: Restriction enzyme digestion

Restriction enzyme digestions were performed in 25 µl or 50 µl reaction using the CutSmart® buffer system (New England Biolabs, USA). Briefly, 1 µg plasmid DNA was added to CutSmart® buffer diluted in nuclease-free H_2O at a final concentration of 1x. 1 µl of each respective restriction enzyme purchased from New England Biolabs (USA) was added and the restriction reactions were incubated for at least 1 hour at 37 °C.

Table 2.9: Overview of restriction enzymes

Name	Product-#
*Xba*I	R0145
*Eco*RI-HF®	R3101
*Bam*HI-HF®	R3136
*Not*I-HF®	R3189

2.2.4: Isolation of plasmid DNA

Small- and medium-scale plasmid DNA isolations from bacterial *E. coli* cultures were performed using the Wizard Plus SV Minipreps DNA Purification System (Promega, Australia) or NucleoBond Xtra Midi Plus EF kit (Macherey-Nagel, Germany), respectively, according to the manufacturer's protocol.

2.2.5: DNA sequencing

Sanger sequencing was performed by the Australian Genome Research Facility (AGRF, Department of Pathology, The University of Melbourne) and DNA samples prepared, according to the AGRF sample preparation guide.

2.2.6: Cell lysis and Western Blot

Cellular lysates were extracted using radioimmunoprecipitation assay buffer (RIPA) supplemented with 1x cOmplete™ Mini Protease Inhibitor Cocktail (Merck, Germany) for 5 – 15 minutes on ice. Cell debris was removed from cellular lysates by centrifugation and protein concentration of cellular lysates determined by Bradford assay. NuPAGE™ LDS Sample buffer (4x) (Thermo Fisher Scientific, Australia) at a final concentration of 1x was added to cell lysates and samples boiled at 100 °C for 10 minutes. Subsequently, 10 – 15 µg of protein were loaded into the pockets of NUPAGE™ 4 – 12 %, Bis-Tris mini gels (Thermo Fisher Scientific, Australia). Proteins were separated by SDS-PAGE at 200 V for 60 – 90 minutes in 1x SDS running buffer supplemented with NUPAGE™ Antioxidant (Thermo Fisher Scientific, Australia).

Transfer of separated proteins to polyvinylidene fluoride (PVDF) membranes was performed by a tank transfer system (wet transfer). To this end the PVDF membrane was activated for 15 seconds in methanol and the transfer cassette was assembled, according to the manufacturer's protocol (Thermo Fisher Scientific, Australia). Wet transfer was performed in 1x NUPAGE™ transfer buffer (Thermo Fisher Scientific, Australia) containing NUPAGE™ Antioxidant (Thermo Fisher Scientific, Australia) at 30 V for either 1 – 2 hours at room temperature or overnight at 4 °C.

After transfer, the PVDF membrane was dried at 37 °C for at least 30 minutes to avoid non-specific antibody binding and rehydrated in PBS-Tween20 (0.1 % v/v Tween20 in 1x PBS) for ~ 30 minutes. The rehydrated membrane was incubated with primary antibodies diluted in blocking buffer (10% skim milk in PBS +

0.01 % sodium azide) for 1 hour at room temperature or overnight at 4 °C, depending on the primary antibody used. The membrane was washed three times with PBS-Tween20 for 10 minutes and subsequently incubated with HRP-conjugated secondary antibodies diluted in blocking buffer for 1 hour at room temperature. Membranes were washed three times with PBS-Tween20 for 5 minutes and incubated with Amersham ECL Western Blotting Detection Reagent (GE Healthcare/Cytiva, USA) for 1 minute, according to the manufacturer's protocol. Chemiluminescent bands were detected using a Chemidoc imaging system (Bio-Rad Laboratories, USA). Densitometric analyses were performed using the Image Lab software (Bio-Rad Laboratories, USA). If necessary, bound antibodies were removed by incubating the membrane with Restore™ PLUS Western Blot stripping buffer (Thermo Fisher Scientific, Australia) for 5 – 15 minutes at room temperature. The membrane was washed extensively with PBS-Tween20 and subsequently a second round of membrane blocking, and antibody staining was performed, as described above.

2.3: Cell culture and maintenance

2.3.1: Maintenance of immortalised cell lines

HeLa and HEK293 cells were maintained as semi-confluent monolayers in C-DMEM medium, unless stated otherwise. L-929 cells were cultured in C-RPMI medium. All cells were grown in a H_2O-saturated atmosphere at 37 °C and 5 or 10 % CO_2.

2.3.2: Production of L-conditioned medium

L-929 cells were grown to confluency in high FCS-RPMI medium (20 % FBS) in T-175 flasks. Upon reaching confluency, cells were trypsinised using TrypLE™ express enzyme (Thermo Fisher Scientific, Australia) and resuspended in 400 ml C-RPMI medium without penicillin and streptomycin supplement. Resuspended cells were then transferred into 2 l roller bottles and the lid sealed with Parafilm.

After incubation at 37 °C and 5 % CO_2 for 1 – 2 weeks, medium was collected and centrifuged for 5 minutes at 300 x g to remove cells and debris. The supernatant was sterile filtered through 0.22 µm filters and 40 ml of L-conditioned medium aliquoted in 50 ml tubes. L-conditioned medium was stored at -20 °C until used for differentiation of bone marrow progenitor cells into bone marrow-derived macrophages.

2.3.3: Isolation of bone marrow progenitor cells

8 to 10-week-old FcRn KO and hFcRn$^{Tg/Tg}$ mice were killed by CO_2 asphyxiation and femur and tibia collected. Both ends of the bones were clipped and bone marrow extracted by flushing the bone with a 26-gauge (26g) needle and a syringe containing 10 ml C-RPMI medium. Extracted bone marrow cells were centrifuged for 5 minutes at 1400 rpm and 4 °C and the supernatant aspirated. Cells were resuspended in 5 ml RBC lysis buffer (0.09 % w/v NH_4Cl in milli-Q H_2O) and incubated for 5 minutes in a 37 °C water bath. 5 ml of cold neutralisation solution (0.1 % w/v BSA in PBS) was added, and the cell suspension centrifuged for 5 minutes at 1400 rpm and 4 °C. After aspirating the supernatant, the cell pellet was resuspended in 10 ml of CO_2-equilibrated C-RPMI medium and the cell suspension transferred into a 10 cm cell culture dish. Cells were incubated for 24 hours at 37 °C and 5 % CO_2. Non-adherent stem cells were transferred into a 50 ml tube by gently rocking the cell culture dish and collecting the supernatant. Progenitor cell concentration was adjusted to 5 x 10^6/ml in BMDM freezing medium (80 % FCS + 10 % BMDM medium + 10 % DMSO) and cells stored in vapor-phase liquid nitrogen.

2.3.4: Differentiation of bone marrow progenitor cells into bone marrow-derived macrophages

Frozen bone marrow progenitor cells were thawed, resuspended in CO_2-equilibrated BMDM medium containing L-conditioned medium, a source of colony

stimulating factor 1 (CSF-1 or M-CSF) promoting BMDM differentiation, and seeded into culture vessels with a density of 1 – 2 x 10^4 cells/cm^2. If not otherwise stated, cells were incubated for 72 hours at 37 °C and 5 %, then topped-up with CO_2-equilibrated BMDM medium and cultured for additional 24 - 48 hours. In the afternoon before conducting internalisation experiments, BMDMs were starved for CSF-1 in C-RPMI medium and incubated overnight at 37 °C and 5 % CO_2.

2.3.5: Production of FcRn-mCherry-containing lentiviral particles in HEK293T cells

2 x 10^6 HEK293T packaging cells were seeded into 10 cm culture dishes in GlutaMax-DMEM (DMEM medium + 10 % FCS + 1x GlutaMax™ (Thermo Fisher Scientific, Australia) and cultured at 37 °C and 5 % CO_2. After 24 hours, medium was replaced with fresh GlutaMax-DMEM, and cells incubated for additional 6 – 8 hours at 37 °C and 5 % CO_2 prior to transient $CaPO_4$ transfection. For this, freshly prepared DNA transfection mix (0.25 M $CaCl_2$), containing the envelope vector pCMV-VSV-G, the packaging vector psPAX2 and the transfer vector FUGW-B2M-IRES-FcRn_mCherry in a ratio of 1:2:2, was mixed with 2 x HEPES-buffered saline (HBS, pH 7.0, Sigma Aldrich, USA) and immediately vortexed for 30 seconds. After incubating the solution for 10 minutes at room temperature, 1 ml transfection mix per culture dish was added dropwise to the cells and mixed by gently swirling the culture dish. Cells were incubated overnight at 37 °C and 10 % CO_2. The next morning, medium was replaced with fresh GlutaMax-DMEM, and cells further incubated for 48 hours at 37 °C and 10 % CO_2 to allow production of lentiviral particles. Virus-containing medium was collected, and cell debris removed by centrifugation (3000x g, 10 minutes). The supernatant was filtered using the Steriflip® filter unit with a pore size of 0.45 µm (Merck, Germany). Lentiviral particles were concentrated overnight at 4 °C by adding PEG-it virus precipitation solution (Integrated Sciences, Australia) at a final concentration of 1x to the filtered medium. Viral particles were pelleted twice (1500x g, 30 minutes, 4 °C) and the supernatant aspirated carefully. To remove any remaining supernatant, cells we re-centrifuged for 5 minutes at 1500x g and 4 °C. Lentiviral

particles were resuspended in SFM-RPMI medium supplemented with 10 mM HEPES (Gibco®, Thermo Fisher Scientific, Australia) at 1:100 of its original harvested volume. Concentrated viral particles were transferred into cryovials and stored at -80 °C.

2.3.6: Collagen type I-coating of culture vessels

An appropriate volume of collagen type I coating buffer, containing 50 µg/ml collagen type I (Sigma Aldrich, USA) dissolved in 0.02 M acetic acid, was added to cover the growth area of culture vessels, and then incubated for at least 1 hour at 37 °C and 5 % CO_2. Collagen type I coating buffer was aspirated, and the culture vessels rinsed 3 three times with PBS prior to their use for BOEC generation and maintenance described as below (Sections 2.3.7 – 2.3.9).

2.3.7: Generation of blood outgrowth endothelial cells

30 ml peripheral human blood from healthy donors were collected in heparin tubes and provided by the Volunteer Blood Donor Registry service located at the Walter and Elizabeth Hall Institute (The University of Melbourne). Within 2 hours after collection, drawn blood was transferred to 50 ml tubes and topped-up with 20 ml PBS at room temperature (RT). Peripheral blood mononuclear cells (PBMCs) were isolated from human blood by discontinuous density gradient centrifugation using Ficoll-Paque™ Plus (VWR International, USA). For this, the blood-PBS solution was layered on top of 12.5 ml Ficoll-Paque™ Plus gradient and centrifuged for 20 minutes at 1000x g and RT with minimal acceleration and brake. The cloudy PBMC layer was carefully transferred into a 50 ml tube using a Pasteur pipette. The tube was filled up with PBS and the suspension was centrifuged for 7 minutes at 540x g and RT. Supernatant was removed and cells washed twice with 5 and 10 ml of BOEC medium, respectively (7 minutes, 540x g, RT). The cell pellet was resuspended in 20 ml BOEC medium, and cells counted using a hematocytometer. The cell suspension was adjusted to a

concentration of 2 – 2.5 x 10^6 cells/ml and 1 x 10^7 cells were seeded into collagen type I-coated T-25 flasks and cultured at 37 °C and 5 % CO_2. Medium was initially replaced after 48 hours with fresh CO_2-equilibrated BOEC medium and subsequently medium was changed after 2 – 3 days depending on the growth of cells.

The outgrowth of endothelial colonies was checked daily upon day 7 of culture using an inverted phase contrast microscope. Outgrowth of endothelial colonies was usually observed between day 14 and 28 of culture. Once radially-spreading colonies reached a diameter of ~ 1.5 – 2 cm, cells were trypsinised using TrypLE™ express enzyme (Thermo Fisher Scientific, Australia) and passaged into fresh collagen type I-coated T25-flask representing passage 1 of blood outgrowth endothelial cells (BOECs). BOECs were supplied with fresh CO_2-equilibrated BOEC medium every 2 – 3 days depending on their growth until BOEC monolayers were confluent and ready for further passaging.

The data shown in this work was generated from BOEC cell lines obtained from two different blood donors. Depending on the cell number and isolation efficiency several distinct BOEC lines (one per T-25 flask) were derived from one donor sample.

Experiments carried out using human peripheral blood samples from healthy donors were approved by the Human Research Ethics Committee, The University of Melbourne (Ethics-ID: 1749491).

2.3.8: Freezing and thawing of blood outgrowth endothelial cells

Confluent monolayers of blood outgrowth endothelial cells (BOECs) were trypsinised using TrypLE™ express enzyme (Thermo Fisher Scientific, Australia), washed with CO_2-equilibrated BOEC medium and centrifuged for 5 minutes at 300x g and 4 °C. The cell pellet was resuspended in BOEC freezing medium (95 % FCS + 5 % DMSO) and cell concentration adjusted to 3 – 7 x 10^5 cells/ml. 1 ml of BOEC suspension was transferred to cryovials and stored in vapor-phase liquid nitrogen.

Frozen cells were thawed in a 37 °C water bath, washed with CO_2-equilibrated BOEC medium and centrifuged for 5 minutes at 300x g and 4 °C. Supernatant was removed and the cell pellet resuspended in fresh CO_2-equilibrated BOEC medium. BOECs were seeded into collagen type I-coated culture vessels with a density of at least 1 x 10^4 cells/cm^2 and incubated at 37 °C and 5 % CO_2. After 48 hours, medium was replaced with fresh CO_2-equilibrated BOEC medium. Subsequently, medium changes were performed every 2 – 3 days depending on the cell growth until BOEC monolayers reached 70 – 80 % confluency. Afterwards, BOEC monolayers were maintained, as described below (Section 2.3.9).

2.3.9: Maintenance of blood outgrowth endothelial cells

Early passage (passage 2 or below) or freshly thawed BOECs were maintained in CO_2-equilibrated BOEC medium and collagen type I-coated culture vessels at 37 °C and 5 % CO_2. Established BOEC lines (passage 3 or higher) were maintained in C-EGM2 medium and uncoated culture vessels at 37 °C and 5 % CO_2. Medium was replaced with fresh BOEC or C-EGM2 medium every 2 – 3 days depending on the cell growth until BOECs reached 70 – 80 % confluency. Semi-confluent BOEC monolayers were trypsinised using TrypLE™ express enzyme (Thermo Fisher Scientific, Australia) and cells passaged into fresh culture vessels sustaining a density of at least 1 x 10^4 cells/cm^2. Subsequently, BOECs were maintained, as described above.

2.3.10: Isolation of primary murine splenocytes

Whole murine spleen samples were collected in cold PBS. Single cell suspensions were obtained by meshing the spleen through a 100 µm nylon cell strainer. For the isolation of $CD8^+$ T cells used for *in vitro* suppression assays inguinal and brachial lymph nodes were additionally collected and single cell suspensions prepared, as described for spleen samples. Cell suspensions were

washed with PBS and centrifuged for 5 – 10 minutes at 300x g and 4 °C. The supernatant was removed, and erythrocyte lysis was performed for 5 minutes at room temperature (RT) using RBC or ACK lysis solution (Lonza, Switzerland). The reaction was stopped by adding RPMI medium supplemented with 2 % FCS and cell suspensions were centrifuged for 5 minutes at 300x g and 4 °C. Splenocyte pellets were either resuspended in MACS buffer (0.5 % w/v BSA and 2 mM EDTA in PBS, pH 7.2) or FACS buffer (0.1 % w/v BSA and 0.1 % w/v sodium azide in PBS) depending on their further use.

2.3.11: Magnetic activated cell sorting (MACS) of single cell suspensions containing primary murine splenocytes

Single cell suspensions of primary murine splenocytes were prepared, as described above (Section 2.3.10), and resuspended in MACS buffer (0.5 % w/v BSA + 2 mM EDTA in PBS, pH 7.2). Immune cell subpopulations were isolated using suitable MACS® Isolation Kits purchased from Miltenyi Biotec (Germany), according to the manufacturer's protocol. The following kits were used:

Table 2.10: Overview of MACS Isolation Kits

MACS® Isolation Kit	Product-#
B Cell Isolation Kit, mouse	130-090-862
CD11c Microbeads Ultrapure, mouse	130-125-835
$CD4^+$ T Cell Isolation Kit, mouse	130-104-454
$CD4^+CD25^+$ Regulatory T cell Kit, mouse	130-091-041
$CD8a^+$ T Cell Isolation Kit, mouse	130-095-236

Regulatory T cells (Tregs) were isolated using the $CD4^+$ T Cell Isolation Kit to obtain single cell suspension of $CD4^+$ T cells, and subsequently, MACS separation of $CD4^+CD25^+$ Tregs was performed using the $CD4^+CD25^+$ Regulatory T cell Kit.

2.4: Gene transfer protocols

2.4.1: Transformation of competent *E. coli* bacteria

Heat shock transformation of plasmid DNA into chemically competent *E. coli* cells was performed, according to the manufacturer's protocol. Briefly, competent cells were thawed on ice for 10 minutes and 1 pg – 100 ng plasmid DNA were added to the cells. After 30 minutes incubation on ice, heat shock was performed for 30 seconds at 42 °C and cells directly placed on ice for 5 minutes. 950 µl SOC medium (room temperature) were added to the cells and cells allowed recovery for 60 minutes at 37 °C and 250 rpm. Subsequently, cells were plated on pre-warmed LB selection plates and incubated overnight at 37 °C to allow growth of successfully transformed colonies.

2.4.2: FuGENE® 6 transfection of immortalised cell lines

Semi-confluent cells were trypsinised using TrypLE™ express enzyme (Thermo Fisher Scientific, Australia) and 0.4 x 10^5 or 0.8 x 10^5 cells per well were seeded in 12-well or 6-well plates, respectively. Cells were incubated for 24 hours at 37 °C and 10 % CO_2. Subsequently, medium was changed to fresh C-DMEM, and transient transfection was performed using FuGENE® 6 transfection reagent (Promega, Australia). Briefly, FuGENE® 6 solution was warmed up to room temperature for 5 minutes and for every well of a 12-well plate 1.2 µl transfection reagent were diluted in 98.8 µl SFM-DMEM supplemented with 10 mM HEPES (double amounts for wells of 6-well plate). The mixture was incubated for 5 minutes at room temperature and added dropwise to 0.3 – 0.5 µg plasmid DNA per well placed in a fresh 1.5 ml tube. The FuGENE® 6/DNA mix was incubated for 15 minutes at room temperature and 100 µl of the transfection mix per well of a 12-well plate (200 µl for wells of 12-well plates) were added dropwise to the cells. Subsequently, transient transfected cells were incubated for 48 hours at 37 °C and 10 % CO_2 to allow expression of the respective transgene.

2.4.3: Lipofectamine™ transfection of blood outgrowth endothelial cells

Semi-confluent (60 – 80 %) BOEC monolayers growing in wells of a 12-well plate or µ-dishes (Ibidi, Germany) were transiently transfected using Lipofectamine™ 3000 transfection reagent (Thermo Fisher Scientific, Australia), according to the manufacturer's protocol, with slight adjustments. Briefly, 1.5 µl or 3 µl were diluted in 50 µl Opti-MEM per well/dish and mixed well. In a fresh 1.5 ml tube, the DNA master mix containing 1 – 2 µg plasmid DNA/well was prepared by diluting the respective amount of DNA in 50 µl Opti-MEM and adding 2 – 4 µl P3000 reagent. The DNA master mix was added to the diluted Lipofectamine™ 3000 and after extensively vortexing the tube, the transfection mix was incubated for 10 – 15 minutes at room temperature. 100 µl of the transfection mix per well/dish was added dropwise to the cells and plates incubated for 2 – 4 hours at 37 °C and 5 % CO_2. Subsequently, the Lipofectamine™ 3000-containing medium was removed and replaced with fresh C-EGM2 medium. Transient transfected BOECs were incubated for additional 48 hours at 37 °C and 5 % CO_2 to allow expression of the respective transgene.

2.4.4: Lentiviral transduction of primary macrophages

Bone marrow progenitor cells/BMDMs were transduced with FcRn-mCherry lentiviral particles (LV) on day 3 after seeding them into culture vessels. To this end, 10 – 15 µl concentrated lentivirus was diluted in 1.2 ml CO_2-equilibrated BMDM medium. Medium was replaced with freshly prepared LV-containing medium and BMDMs were incubated for 24 hours at 37 °C and 10 % CO_2. Subsequently, the LV-containing medium was removed, and cells washed extensively with 1x PBS three times. Fresh CO_2-equilibrated BMDM medium was added, and the transduced cells incubated for additional 24 hours at 37 °C and 5 % CO_2 to allow expression of the transgene. For uptake experiments, transduced BMDMS were starved for CSF-I overnight in C-RPMI medium the day before the experiment.

2.4.5: Lentiviral transduction of blood outgrowth endothelial cells

Semi-confluent (60 – 80 %) BOEC monolayers growing in wells of a 12-well plate or µ-dishes (Ibidi, Germany) were transduced with FcRn-mCherry lentiviral particles (LV). Briefly, 10 µl concentrated lentivirus was diluted in 1.2 ml C-EGM-2 medium. Medium was replaced with freshly prepared LV-containing medium and BOECs were incubated for 24 hours at 37 °C and 10 % CO_2. Subsequently, the LV-containing medium was removed, and cells washed extensively with 1x PBS three times. Fresh C-EGM-2 medium was added, and the transduced cells incubated for additional 24 hours at 37 °C and 5 % CO_2 to allow expression of the transgene.

2.5: Treatment of cells and cell culture assays

2.5.1: HSA uptake assay in HeLa cells

HeLa cells were transfected with FcRn-mCherry using FuGENE® 6 (Promega, Australia), as described above (Section 2.4.2). To check binding of HSA-AF488 to surface-exposed FcRn-mCherry, transfected HeLa cells were incubated for 60 minutes on ice in phosphate-buffered saline adjusted to the indicated pH (5.0 – 7.0) containing 100 µg/ml HSA-AF488. For FcRn-mCherry-mediated HSA internalisation by transfected HeLa cells, cells were incubated for 15 minutes at 37 °C in phosphate-buffered saline (PBS) adjusted to the indicated pH (5.0 – 7.0) and containing 100 µg/ml HSA-AF488 or $rHSA^{H464Q}$-AF488. HSA-AF488 uptake by fluid-phase endocytosis using confluent HeLa cells was performed for 4 hours at 37 °C in SFM-DMEM medium containing 100 µg/ml HSA-AF488. Cells were fixed with PFA, and confocal microscopy or FLIM-FRET experiments were performed, as described below (Section 2.6.1, Section 2.7.1, and Section 2.7.3).

2.5.2: HSA uptake assay in BMDMs

Differentiated BMDMs were starved for CSF-1 overnight in C-RPMI prior to the HSA uptake experiment and washed three times with PBS. Cells were pelleted (300x g, 5 minutes 4 °C) and resuspended in SFM-RPMI medium supplemented with 100 ng/ml recombinant CSF-1 in presence of fluorescently labelled HSA conjugates and incubated for 5 – 15 minutes at 37 °C and 5 % CO_2 to allow macropinocytosis.

For raster image correlation spectroscopy (RICS) experiments, BMDMs were pulsed in CSF-1 containing SFM-RPMI medium with 10 µg/ml each, rHSA^{H464Q}-AF488 and HSA-AF568, for 5 minutes at 37 °C and 5 % CO_2. Subsequently, extracellular fluorophores were washed away with SFM-RPMI three times and pre-warmed (37 °C) SFM-RPMI was added. RICS experiments were performed, as described below (Section 2.7.4).

For fluorescence lifetime imaging microscopy in combination with Förster resonance energy transfer (FLIM-FRET) experiments, FcRn-mCherry transduced or non-transduced BMDMs were pulsed in CSF-1 containing SFM-RPMI with 100 µg/ml HSA-AF488 for 5 minutes at 37 °C and 5 % CO_2. Subsequently, extracellular fluorophores were washed away with SFM-RPMI three times and pre-warmed (37 °C) SFM-RPMI was added. FLIM-FRET experiments were performed, as described below (Section 2.7.3).

2.5.3: Continuous uptake assays in BOECs

Confluent (80 – 100 %) BOEC monolayers were washed three times with PBS and pulsed for 30 or 60 minutes with 50 µg/ml fluorescently labelled transferrin (transferrin-AF488 or transferrin-AF568), 100 µg/ml fluorescently labelled HSA (HSA-AF488 or HSA-AF568) or 500 µg/ml 70 kDa Dextran-TxRed at 37 °C and 5 % CO_2. After the indicated pulse times, extracellular fluorophores were washed away, and cells were either fixed for confocal microscopy or prepared for flow cytometry, as described below (Sections 2.6.1 – 2.6.3 and Section 2.6.9).

For continuous DQ-OVA uptake experiments, BOEC monolayers were incubated for up to 120 minutes in SFM-EGM2 containing 50 µg/ml DQ-OVA at 37 °C and 5 % CO_2. At indicated uptake times, live cells were prepared for flow cytometry or imaged by confocal microscopy at 37 °C and 5 % CO_2, as described below (Section 2.6.9 and Section 2.7.2).

2.5.4: Pulse-chase assays in BOECs

Confluent (80 – 100 %) BOEC monolayers were washed three times with PBS and pulsed for 15 minutes (live cells) or 30 minutes (fixed cells) with 100 µg/ml of either HSA-AF488, HSA-AF568 or $rHSA^{H464Q}$-AF488 in SFM-EGM2 at 37 °C and 5 % CO_2. Extracellular fluorophores were washed away three times with SFM-EGM2, and fluorescent signals chased for 60 minutes in SFM-EGM2 at 37 °C and 5 % CO_2. At indicated times, cells were either fixed or live cells were imaged by confocal microscopy at 37 °C and 5 % CO_2, as described below (Sections 2.6.1 – 2.6.3 and Section 2.7.2).

For pulse chase assays using DQ-OVA, BOEC monolayers were washed three times with PBS and pulsed for 15 minutes with 50 µg/ml DQ-OVA in SFM-EGM2 at 37 °C and 5 % CO_2. Extracellular fluorophores were washed away three times with SFM-EGM2, and fluorescent signals chased for 120 minutes in SFM-EGM2 at 37 °C and 5 % CO_2. At indicated times, live cells were imaged by confocal microscopy at 37 °C and 5 % CO_2, as described below (Section 2.7.2).

If not stated otherwise, pulse-chase experiments were performed at least twice to confirm observed intracellular trafficking events.

2.5.5: PMA treatment of cultured BOECs

Confluent monolayers of BOECs were treated with C-EGM2 medium containing 80 nM phorbol-12-myristae-13-acetate (PMA, Sigma-Aldrich, USA) dissolved in DMSO for 20 minutes at 37 °C. For the carrier control, BOECs were incubated with C-EGM2 containing 0.5 % v/v DMSO to compensate for the addition of the

DMSO phase in PMA-treated cells. Monolayers were washed and cells fixed with MeOH, as described below (Section 2.6.3).

2.5.6: 5-(N-ethyl-N-isopropyl) amiloride treatment

A working solution of 10 mM 5(-(N-ethyl-N-isopropyl) amiloride (EIPA, Sigma Aldrich, USA) in MeOH was prepared. For adjusting EIPA concentrations the ratio of the MeOH phase in culture medium was kept to 2 %. Confluent BOEC monolayers were treated in SFM-EGM2 containing indicated concentrations of EIPA (0, 50, 100 or 200 µM) for 60 minutes at 37 °C and 5 % CO_2. The medium was removed, and subsequent internalisation assays were performed, as described above, in presence of the respective EIPA concentrations in SFM-EGM2 (Section 2.5.3). Cells were either prepared for flow cytometry or fixed to perform confocal microscopy, as described below (Sections 2.6.1 – 2.6.3 and Section 2.6.9).

2.5.7: Antigen uptake assay in primary B cells

B cells were isolated from single cell suspensions of primary murine splenocytes using the B Cell Isolation Kit (Miltenyi Biotec, Germany), according to the manufacturer's protocol. Isolated B cells were resuspended in X-Vivo medium (Lonza, Switzerland) supplemented with 2 mmol/l glutamine, 50 µmol/l 2-mercaptoethanol, 100 U/ml penicillin, 100 g/ml streptomycin and 10 % FCS (C-X-Vivo medium) and 4 – 5 x10^6 B cells were seeded into wells of a 48-well plate. Cells were pelleted for 5 minutes at 300x g and 4 °C, and, if not stated otherwise, resuspended in MSA blocking medium (0.2 % w/v MSA in C-X-Vivo medium). Blocking was performed on ice for 30 minutes and cells pelleted for 5 minutes at 300x g and 4 °C. Cells were resuspended in MSA blocking medium containing 2.5 µg/ml FVIII or FVIII-Albumin fusion protein (FVIII-Alb) coupled to APC. Cells were allowed binding the respective antigens for 30 minutes on ice, and then unbound antigen was washed off with X-Vivo medium. Cells were

resuspended in C-X-Vivo medium and incubated at 37 °C for the indicated times to allow uptake of the bound antigens. After uptake, cells were kept on ice to avoid further processing of bound or endocytosed antigens. Cells were washed with FACS buffer and prepared for imaging flow cytometry, as described below (Section 2.6.7). After staining of surface proteins for flow cytometry, B cells were fixed with 4 % PFA for 10 minutes on ice and resuspended in 50 – 100 µl FACS buffer. Imaging flow cytometry was performed, as described below (Section 2.7.6).

2.5.8: *In vitro* expansion of FVIII-specific $CD4^+$ T cells

The principle and cytokine composition for the *in vitro* expansion of FVIII-specific $CD4^+$ T cells was adapted from experiments performed by Smith and colleagues, who were able to expand pre-sorted $Foxp3^+$ Tregs in a FVIII-specific manner from FVIII-immunised HemA mice (Smith *et al.*, 2020). To this end, spleens from naïve or immunised (2 IU FVIII (Kogenate® FS, Bayer, Germany) i.v. at day -7 and day -14) HemA or B6 WT mice were collected in cold digestion buffer (C-RPMI medium + 1 mg/ml Collagenase + 0.1 mg/ml DNAse). Collected spleens were injected with 2 ml digestion buffer and incubated in wells of a 12-well plate for 15 – 20 minutes at 37 °C. Subsequently, the spleens were meshed using a syringe stamp and incubated for additional 15 – 20 minutes at 37 °C. After the digestion, single cell suspensions of primary murine splenocytes were prepared, as described above (Section 2.3.10). $CD4^+$ T cells were isolated from single cell suspensions of primary murine splenocytes using the $CD4^+$ T Cell Isolation Kit (Miltenyi Biotec, Germany), according to the manufacturer's protocol, and the cell concentration adjusted to 2 x 10^6 cells/ml in T cell medium containing 10 IU/ml human FVIII protein (Kogenate® FS, Bayer, Germany).

The $CD4^-$ negative population was collected and transferred to T-25 flasks. Cells were irradiated using the MultiRad 160 system (Faxitron Biooptics, USA) with the following settings: 0.5 mm aluminium filter, shelf position 6 (22 cm), field size Ø 15.2 cm, 160 kV, 25 mA and a target dosage of 20 Gy. Irradiated

$CD4^-$ cells were adjusted to a cell concentration of 2 x 10^6 cells/ml in T cell medium containing 10 IU/ml human FVIII protein (Kogenate® FS, Bayer, Germany) and used as antigen presenting cells (APCs) for the FVIII-specific expansion of antigen-specific $CD4^+$ T cells.

For the FVIII-specific expansion step, 5 x 10^5 $CD4^+$ T cells and 5 x 10^5 irradiated $CD4^-$ splenocytes were co-cultured in wells of a 48-well plate in a total volume of 500 µl T cell medium containing 50 U/ml mouse IL-2 (Peprotech, USA) and 10 IU/ml human FVIII protein (Kogenate® FS, Bayer, Germany) at 37 °C and 5 % CO_2. Culture medium was topped up after 48 hours with 500 µl of fresh T cell medium. For indicated samples 50 U/ml IL-2 (Peprotech, USA) were added to the T cell medium during the FVIII-specific expansion step. After 72 hours, cells were passaged, and 5 x 10^5 cells seeded into fresh wells of a 48-well plate 1 x 10^6 cells were stained for FVIII using a FVIII-specific tetramer and prepared for flow cytometry, as described below (Sections 2.6.6 – 2.6.7).

For the FVIII-unspecific expansion, Dynabeads™ Mouse T-Activator CD3/CD28 for T-Cell expansion and activation (T cell activator Dynabeads, Thermo Fisher Scientific, Germany) were added in a 1:1 ratio (12.5 µl) to $CD4^+$ T cells in wells of a 48-well plate. Cells were incubated in T cell medium containing T cell activator Dynabeads and 50 U/ml mouse IL-2 at 37 °C and 5 % CO_2. Medium was topped up every 2 days with fresh T cell medium containing 50 U/ml mouse IL-2 and cells were passaged every 3 days. During passaging, 1 x 10^6 cells were stained for FVIII using a FVIII-specific tetramer and prepared for flow cytometry, as described below (Sections 2.6.6 – 2.6.7). $CD4^+$ T cells were expanded up to day 12 of the experiment.

2.5.9: Chemical conversion of $CD4^+$ T helper cells to Foxp3-expressing regulatory T cells

The protocol for the chemical conversion of $CD4^+$ T cells into $CD25^+Foxp3^+$ Tregs was performed, as described by Akamatsu and colleagues, with slight adaptations (Akamatsu *et al.*, 2019). Briefly, $CD4^+$ T cells were isolated from

single cell suspensions of primary murine splenocytes using the $CD4^+$ T Cell Isolation Kit (Miltenyi Biotec, Germany), as described above (Section 2.3.11). To deplete $CD25^+$ Tregs in the $CD4^+$ T cell population, an additional MACS separation step was performed using the $CD4^+CD25^+$ Regulatory T cell Kit (Miltenyi Biotec, Germany), and the $CD4^+CD25^-$ population collected as Treg-depleted $CD4^+$ T cells. 5 x 10^5 Treg-depleted $CD4^+$ T cells in a volume of 500 µl were seeded per well of a 48-well plate. Chemical Treg conversion was performed for 72 hours at 37 °C and 5 % CO_2 in T cell medium containing 50 U/ml mouse IL-2 (Peprotech, United Kingdom), 2.5 µg/ml recombinant human TGF-β1 (TGF-β, HEK293-derived, Peprotech, United Kingdom) and 1 mM AS2863619 (AS, MedChemExpress, USA) and in the presence of Dynabeads™ Mouse T-Activator CD3/CD28 for T-Cell expansion and activation (T cell activator Dynabeads, Thermo Fisher Scientific, Germany) in a 1:1 beads-to-cell ratio. As controls, Treg-depleted $CD4^+$ T cells were either incubated in presence of T cell activator Dynabeads only or Tregs induced with TGF-β and in the absence of AS. After conversion, the phenotype of induced Tregs was assessed by flow cytometry and induced Tregs were used for *in vitro* suppression assays, as described below (Section 2.5.10). If necessary, converted Tregs were rested in the absence of T cell activator Dynabeads in T cell medium containing the respective conversion reagents and IL-2, as indicated.

2.5.10: *In vitro* suppression assay

For the isolation of $CD11c^+$ dendritic cells (DCs), spleens from B6 WT mice were collected in cold digestion buffer (C-RPMI medium + 1 mg/ml Collagenase + 0.1 mg/ml DNAse). Collected spleens were injected with 2 ml digestion buffer and incubated in wells of a 12-well plate for 15 – 20 minutes at 37 °C. Subsequently, the spleens were meshed using a syringe stamp and incubated for additional 15 – 20 minutes at 37 °C. After the digestion, single cell suspensions of primary murine splenocytes were prepared, as described above (Section 2.3.10). $CD11c^+$ dendritic cells were isolated from single cell suspensions of primary splenocytes obtained from B6 WT mice using CD11c Microbeads Ultrapure (Miltenyi Biotec,

Germany), according to the manufacturer's protocol. CD11c$^+$ DCs were washed twice with warm PBS and resuspended in 5 ml PBS containing 1 µg/ml SIINFEKL peptide (AnaSpec, USA). To load DCs with the SIINFEKL peptide, cells were incubated for 30 minutes at 37 °C in a water bath. SIINFEKL-loaded DCs were washed with C-RPMI, and the cell concentration adjusted to 1 x 10^6 cells/ml in T cell medium.

CD8$^+$ T cells were isolated from single cell suspensions of primary splenocytes and lymphocytes obtained from OT-1 x CCR4 KO mice using the CD8a$^+$ T cell Isolation Kit (Miltenyi Biotec, Germany), according to the manufacturer's protocol. Separated CD8$^+$ T cells were resuspended in 10 ml warm PBS in 50 ml tubes and 3 µl of 5 mM CFSE (Thermo Fisher Scientific, Germany) were added to the lid of the tube. The 50 ml tube was inverted 10 times and CFSE-labelling of CD8$^+$ T cells was performed for 10 minutes at 37 °C in a water bath. The reaction was stopped by adding 40 ml of PBS containing 10 % FCS. Cells were centrifuged at 300x g for 5 minutes and the cell concentration was adjusted to 1 x 10^6 cells/ml in T cell medium.

Naïve CD4$^+$ T cells were isolated from single cell suspensions of primary splenocytes from B6 WT mice using the CD4$^+$ T Cell Isolation Kit (Miltenyi Biotec, Germany), according to the manufacturer's protocol. Cell concentrations of freshly isolated CD4$^+$ T cells and freshly chemically converted or, after chemical conversion, rested regulatory T cells (Tregs) were adjusted to 1 x 10^6 cells/ml.

For *in vitro* suppression assays, 1 x 10^4 SIINFEKL-loaded DCs and 1 x 10^5 CFSE-labelled CD8$^+$ T cells were co-cultured in a final volume of 500 µl per well of a 48-well plate with either 1 x 10^5 freshly isolated CD4$^+$ T cells or chemically converted Tregs (fresh or rested for 24 hours) for 72 hours at 37 °C. Subsequently, cells were prepared for flow cytometry, as described below (Section 2.6.7) and the proliferation of CFSE-labelled CD8$^+$ T cells assessed using the FlowJo software (BD Biosciences, Germany).

2.6: Fixation and staining protocols

2.6.1: PFA cell fixation

Cell monolayers grown on coverslips were fixed in 4 % paraformaldehyde (PFA) for 10 – 15 minutes at room temperature (RT) and quenched in 50 mM NH_4Cl/PBS for 10 minutes at RT. For intracellular staining, fixed cells were also permeabilised with either 0.1 % v/v Triton-X-100/PBS for 4 minutes at RT or 0.05 % w/v Saponin/PBS for 15 minutes at RT and subsequently incubated in blocking solution (5 % v/v FCS and 0.02 % w/v sodium azide in PBS) for 30 minutes at RT to reduce non-specific binding before proceeding with immunofluorescence staining.

2.6.2: TCA cell fixation

Cell monolayers grown on coverslips were fixed in 10 % trichloroacetic acid (TCA) for 15 minutes on ice and quenched in cold 30 mM glycine/PBS for 10 minutes at RT. For intracellular staining, fixed cells were also permeabilised with either 0.1 % v/v Triton-X-100/PBS for 4 minutes at RT or 0.05 % w/v Saponin/PBS for 15 minutes at RT and subsequently incubated in blocking solution (5 % v/v FCS and 0.02 % w/v sodium azide in PBS) for 30 minutes at RT to reduce non-specific binding before proceeding with immunofluorescence staining.

2.6.3: MeOH cell fixation

Cell monolayers grown on coverslips were fixed in pre-cooled methanol (MeOH) for 5 – 10 minutes at -20 °C. Fixed cells were incubated in blocking solution (5 % v/v FCS and 0.02 % w/v sodium azide in PBS) for 30 minutes at RT to reduce non-specific binding before proceeding with immunofluorescence staining.

2.6.4: Indirect immunofluorescence staining for confocal microscopy

Fixed (and permeabilised) cells grown on coverslips were incubated with primary antibodies diluted in blocking solution (5 % v/v FCS and 0.02 % v/v sodium azide in PBS) for one hour at room temperature. Cells were washed three times with PBS and subsequently incubated with secondary antibodies diluted in blocking solution for 30 minutes at room temperature. Cells were washed three times with PBS and cell nuclei stained with DAPI (Sigma Aldrich, USA) for 5 minutes. Cells were washed three times with PBS, rinsed once with milli-Q H_2O and mounted in Mowiol (10 % w/w Hopval 5-88 (Hoechst, Australia), 25 % w/v glycerol, 0.1 M Tris). Mounted cells were imaged using a Leica SP8 confocal microscope, as described below (Section 2.7.1).

Indirect immunofluorescence staining of endosomal markers was performed at least three times to confirm the observed intracellular pattern of respective organelles and representative confocal images are shown.

2.6.5: LysoTracker™ Red staining

Confluent monolayers of live BOECs were incubated with 1 mM LysoTracker™ Red DND-99 (LysoTracker Red, Thermo Fisher Scientific, Australia) diluted 1:20,000 in C-EGM2 medium for 60 minutes at 37 °C and 5 % CO_2. Cells were washed and fresh C-EGM2 medium was added to directly proceed with live cell imaging or pulse-chase assays using HSA-AF488 were performed, as described above (Section 2.5.4).

2.6.6: Tetramer staining of FVIII-specific $CD4^+$ T cells for flow cytometry

The FVIII-specific MHC II tetramer (TASSYFTNMFATWSPSKARL) was prepared for staining by centrifugation at 14,000x g for 5 minutes and 4 °C. Freshly isolated splenocytes or *in vitro* expanded $CD4^+$ T cells were pelleted (300x g, 5 minutes, 4 °C), resuspended in 50 µl FACS buffer and stained with

2 µl FVIII tetramer per 1 x 10^6 cells. Cells were incubated for 2 hours at 37 °C and 5 % CO_2 in the dark. Cells were washed with FACS buffer and surface antigen staining was performed, as described below (Section 2.6.7).

2.6.7: Staining of surface antigens for flow cytometry

Cells were pelleted (300x g, 5 minutes, 4 °C) and resuspended in 100 or 200 µl FACS buffer containing the particular fluorescence-conjugated antibodies (Table 2.7) and LIVE/DEAD® fixable dead cell stains (Thermo Fisher Scientific, Germany). Surface marker staining was performed for 30 minutes at 4 °C in the dark. Cells were washed with FACS buffer and after pelleting (300x g, 5 minutes, 4 °C), cells were resuspended in appropriate volumes of FACS buffer or Hoechst staining buffer (0.1 µg/ml Hoechst in PBS) if no LIVE/DEAD® fixable dead cell stain was used to identify dead cells.

2.6.8: Staining of intracellular antigens (Foxp3) for flow cytometry

Intracellular antigens were stained using the eBioscience™ Foxp3/transcription factor staining buffer set (Thermo Fisher Scientific, Germany), according to the manufacturer's protocol. Briefly, cells following surface antigen staining were fixed and permeabilised in fix/perm buffer (Thermo Fisher Scientific, Germany) for 1 hour at 4 °C and washed with perm buffer (Thermo Fisher Scientific, Germany) subsequently. Pelleted cells were resuspended in perm buffer containing the particular fluorescent-labelled antibody directed against the intracellular antigen and stained for 30 minutes at 4 °C in the dark. Cells were washed with perm buffer, pelleted, and resuspended in appropriate volume of perm buffer.

2.6.9: Preparation of adherent cells (BOECs) for flow cytometry

BOEC monolayers were trypsinised using TrypLE™ express enzyme (Thermo Fisher Scientific, Australia) and transferred into FACS tubes. Cells were washed with FACS buffer for adherent cells (2 % v/v FCS + 1 mM EDTA in PBS) and pelleted at 300x g for 5 minutes and 4 °C. The cell pellet was resuspended in 100 µl FACS buffer containing the primary antibodies and cells were stained for 30 minutes at 4 °C in the dark. Cells were washed with FACS buffer, the cell pellet resuspended in FACS buffer containing the appropriate fluorescence-conjugated secondary antibodies, and staining was performed for 30 minutes at 4 °C in the dark. Cells were washed with FACS buffer, the cell pellet resuspended in DAPI staining buffer (1 µg/ml DAPI in PBS) and cells incubated for 5 minutes at 4 °C in the dark to stain dead cells. Cells were washed with FACS buffer and, after pelleting (300x g, 5 minutes, 4 °C), resuspended in an appropriate amount of FACS buffer.

2.7: Microscopy and flow cytometry methods

2.7.1: Confocal fluorescence microscopy of fixed cells

Images of fixed cell monolayers were acquired sequentially for multi-colour imaging on a laser confocal scanning microscope (Leica SP8 confocal imaging system, Leica Microsystems, Germany)) using a 63x (1.4 NA) HC PL APO CS2 oil immersion objective and Leica HyD photodetectors. Alexa Fluor® 488 (AF488) and GFP were excited using a 488 nm solid state laser. Alexa Fluor® 568 (AF568), Texas Red (TxRed) and mCherry were excited with a 543 nm solid state laser. Alexa Fluor® 647 (AF647) was excited using a 638 nm solid state laser. DAPI was excited with a 405 nm DMOD laser. Leica HyD photodetectors were set to the collecting bandwidths for collecting the respective fluorescent signals: 430 – 480 nm for DAPI, 500 – 500 nm for AF488 or GFP, 580 – 630 for AF568 or mCherry and 650 – 700 nm for AF647. z-stacks were acquired using a step size

of 0.3 µm per z slice. Single slices of confocal microscopy are shown, unless stated otherwise.

2.7.2: Live cell imaging

All live cell imaging experiments were performed on an Olympus FV3000 laser scanning microscope (Olympus, Australia) using a 60x (1.2 NA) U Plan S Apo water immersion objective and cells were imaged at 37 °C and 5 % CO_2. Alexa Fluor® (AF488), DQ-OVA and GFP were excited using a 488 nm solid-state laser diode. Alexa Fluor® 568 (AF568), LysoTracker Red and mCherry were excited using 561 nm solid-state laser diode. Fluorescent signals were collected with GaAsP detectors using the following bandwidths: 500 – 540 nm for AF488, DQ-OVA and GFP, 590 – 650 nm for AF568, LysoTracker Red and mCherry. Z-stacks were acquired using a step size of 0.5 µm per z slice. Single slices of live cell images are shown, unless stated otherwise.

2.7.3: FLIM-FRET

All fluorescence lifetime imaging microscopy (FLIM) measurements of Förster resonance energy transfer (FRET) were performed on an Olympus FV3000 laser scanning microscope coupled to a 488 nm pulsed laser operated at 80 MHz and an ISS A320 FastFLIM box for time resolved detection. A 60x (1.2 NA) U Plan S Apo water immersion objective was used for all experiments and live cells were imaged at 37 °C and 5 % CO_2. To first verify the presence of HSA-AF488 (donor) and FcRn-mCherry (acceptor) in selected BMDM or HeLa cells, sequential intensity images of this FRET pair were acquired via use of internal solid-state laser diodes operating at 488 nm and 561 nm, a 405/488/561 dichroic mirror and two internal GaAsP photomultiplier detectors set to collect the following bandwidths: 500 – 550 nm and 600 – 650 nm. Then a FLIM image (256 x 256 pixel frame size, 20 µs/pixel, 90 nm/pixel, 20 frame integration) was acquired of the donor only (HSA-AF488) via use of external 488 nm pulsed laser (80 MHz),

and the resulting fluorescence signal was directed through a 405/488/561 dichroic mirror as well as a 550 nm long pass filter, to an external photomultiplier detector (H7422P-40 of Hamamatsu) fitted with a 520/50 nm bandwidth filter. The FLIM image of HSA-AF488, the readout of FRET with FcRn-mCherry, was processed by the ISS Vista Vision software, which pre-calibrates the instrument and phasor space against a known reference lifetime (here fluorescein at pH 9 was used, which has a known single exponential lifetime of 4.04 ns (Hinde *et al.*, 2012).

RICS data was collected in collaboration with Dr. Elizabeth Hinde (School of Physics, Bio21 Institute, The University of Melbourne).

2.7.4: RICS

All raster image correlation spectroscopy (RICS) microscopy measurements were performed on an Olympus FV3000 laser scanning microscope coupled to an ISS A320 Fast FLIM box for fluorescence fluctuation data acquisition. A 60x (1.2 NA) U Plan S Apo water immersion objective was used for all experiments and live cells were imaged at 37 °C and 5 % CO_2. HSA-AF568 and $rHSA^{H464Q}$-AF488 were excited by solid-state laser diodes operating at 488 nm and 561 nm, respectively. The fluorescence signal was directed through a 405/488/561 dichroic mirror to remove laser light and the AF488 and AF568 emission was detected by two internal GaAsP photomultiplier detectors set to collect between the following bandwidths: 500 – 540 nm and 600 – 700 nm. A two-channel frame scan acquisition (100 frames) was then set-up to collect AF488 and AF568 signal at zoom 20 (10.76 μm^2 region of interest) within a selected bone marrow-derived macrophage that avoided free dye in the extracellular matrix. For a 256-pixel frame size this region of interest resulted in a pixel size of 41 nm and for a pixel dwell time set to 12.5 µs, this scan rate resulted in a line time of 4.313 ms and a frame time of 1.108 s.

RICS data was collected in collaboration with Dr. Elizabeth Hinde (School of Physics, Bio21 Institute, The University of Melbourne).

2.7.5: Flow cytometry

After staining, cells were measured in FACS buffer or Hoechst staining buffer by flow cytometry using a BD FACS Canto II (BD Biosciences, Germany) or BD LSR Fortessa (BD Biosciences, Germany) system. Freshly isolated cells or adherent cells were filtered through 100 µm nylon filter prior to flow cytometry measurements. For the calculation of absolute cell numbers, 10,000 CaliBRITE™ APC beads (BD Biosciences, Germany) were added per sample. Flow cytometry data was collected using the BD FACSDiva™ software (BD Biosciences, Germany). Data was analysed using the FlowJo software (BD Biosciences, Germany). Single, live cells were gated using forward (FSC) and sideward scatter (SSC), according to their typical morphology and the exclusion of the respective cell viability dye.

2.7.6: Imaging flow cytometry

After performing the antigen uptake assay in primary B cells, as described above (Section 2.5.7), PFA-fixed cells resuspended in 50 – 100 µl were transferred into 1.5 ml Eppendorf tubes and analysed by imaging flow cytometry using a Amnis® ImageStream® Mk II system (Luminex Corporation, USA).

2.8: Data analysis

2.8.1: The phasor approach to FLIM-FRET

All FLIM-FRET data was analysed in the SimFCS software developed at the Laboratory for Fluorescence Dynamics, as described in previously published papers (Digman *et al.*, 2008; Hinde *et al.*, 2012). In particular, the donor fluorescence lifetime recorded in each pixel of a FLIM image is described by a G and S coordinate (phasor) presented in the phasor plot. In pixels where a donor molecule undergoes FRET with an acceptor molecule, the phasor coordinate will be right shifted along a curved trajectory that is described by the classical

definition of FRET efficiency. To determine the efficiency of the FRET state, the phasor coordinates of HSA-AF488 in the absence of acceptor (unquenched donor) and background (cellular autofluorescence) were first determined independently and a FRET trajectory was extrapolated. Then from superimposition of the phasor plot distribution of HSA-AF488 in the presence of the C-terminal versus N-terminal FcRn fusion with mCherry (quenched donor) over the FRET trajectory, the efficiency of each ligand-receptor interaction was determined. This analysis then also enabled cursors to be placed at specific phasor coordinates along the FRET trajectory that quantifies the fraction of FRET within a FLIM image to highlight the spatial distribution of ligand-receptor interactions.

The analysis of FLIM-FRET data was conducted by Dr. Elizabeth Hinde (School of Physics, Bio21 Institute, The University of Melbourne).

2.8.2: RICS

Raster image correlation spectroscopy (RICS) data was processed and analysed in the SimFCS software developed at the Laboratory for Fluorescence Dynamics, as described in previously published papers (Digman *et al.*, 2005; Digman and Gratton, 2009; Rossow *et al.*, 2010). In particular, for each two-colour experiment, the RICS function was calculated in channel 1 (rHSA^{H464Q}-AF488) and channel 2 (HSA-AF568) for an entire image stack (n = 100 frames) with a moving average applied (n = 10 frames) to remove slow macromolecular movements. The resulting RICS profiles for channels 1 and 2 were then independently fit to a 2-component diffusion model, and the amplitudes (G_1 and G_2) versus diffusion coefficients (D_1 and D_2) of the fast versus slow components recorded. The fast component (described by G_1 and D_1) was interpreted to represent the fraction of HSA freely diffusing while the slow component (described by G_2 and D_2) was interpreted to represent the fraction of immobile HSA molecules bound to FcRn.

The analysis of RICS data was conducted by Dr. Elizabeth Hinde (School of Physics, Bio21 Institute, The University of Melbourne).

2.8.3: Macropinosome quantitation assay

BOECs were treated with EIPA and HSA-AF488 and transferrin-AF568 co-uptake was performed, as described above (Section 2.5.3 and Section 2.5.6). PFA-fixed BOECs were imaged by confocal microscopy and z-stacks of whole cells were acquired. The count of macropinosomal-like structures and fluorescent levels of endocytosed HSA-AF488 and transferrin-AF568 per cell were calculated using an adapted ImageJ-based macropinosome quantitation assay established by Wang *et al.* (Wang *et al.*, 2014). In particular, maximum projections of z-stacks were generated, and boundaries of single cells defined as regions of interests (ROIs) using the DAPI and the background signal of the transferrin-AF568 fluorescent channel. The Renyi Entropy threshold algorithm was used to identify HSA-positive endosomal structures and transferrin-positive endosomal structures were identified by the Iso Data threshold algorithm. To quantify the number of HSA-positive macropinosomes per cell, particles with an area of 0.2 – 20 μm^2, corresponding to globular structures with a diameter of ~ 0.5 – 5 µm, within single ROIs were counted. Fluorescence intensities of intracellular HSA-AF488 and transferrin-AF568 per cell were estimated by quantification of the integrated fluorescence intensities of the respective fluorescent channel limited to the thresholded structures within single ROIs. Macropinosome counts and fluorescent levels were quantified and compared within single datasets to minimize the influence of background fluorescence or fluorophore bleaching resulting from sample preparation and acquisition settings. Experiments were performed at least twice to confirm effects on HSA macropinocytosis in presence of EIPA.

2.8.4: Quantification of intracellular HSA fluorescence levels

Pulse-chase assays with BOEC monolayers using fluorescent-labelled HSA derivates were performed, as described above (Section 2.5.4), and PFA- or MeOH-fixed cells subsequently imaged by confocal microscopy. The maximum

projections of acquired z-stacks of fixed cells were generated and boundaries of single cells defined as regions of interest (ROI) using the DAPI and the background fluorescence of an antibody-specific channel. Intracellular HSA fluorescence levels were calculated using whole z-stacks by quantification of the HSA-specific integrated fluorescence densities within single ROIs. To this end, HSA-positive endosomal structures were identified by the Moments threshold algorithm and integrated densities calculated for single slices of the z-stack within single ROIs were summed up to obtain total intracellular HSA fluorescent levels per cell. The mean total intracellular HSA levels at 0 minutes chase within one experiment was set to 1 and data from 5 independent experiments (number of cells ≥ 19) was pooled. Intracellular fluorescence quantification was performed using the ImageJ software.

2.8.5: Quantification of co-localisation

Pulse-chase assays with BOEC monolayers using fluorescent-labelled HSA derivates were performed, as described above (Section 2.5.4), and PFA-fixed cells subsequently imaged by confocal microscopy. The maximum projections of acquired z-stacks of fixed cells were generated and boundaries of single cells defined as regions of interest (ROI) using the DAPI and the background fluorescence of an antibody-specific channel. Co-localisation was calculated within single ROIs throughout the single layers of whole z-stacks using the Coloc 2 plugin for Image J. Thresholds were calculated by Costes' auto-threshold regression and significance of obtained co-localisation parameters evaluated by Costes' randomisations (n=100) (Costes *et al.*, 2004). The Costes' p-value for all calculations was 1.00. Pearson's p value and Manders' correlation coefficients were calculated for two particular fluorescent channels to assess their co-localisation to endosomal structures (Manders *et al.*, 1992). Co-localisation was quantified and compared within single datasets to minimize the influence of background fluorescence or fluorophore bleaching resulting from sample preparation and acquisition settings. Experiments were performed at least twice to confirm effects on co-localisation observed during pulse-chase assays.

2.8.6: Quantification of internalisation coefficients using imaging flow cytometry

Antigen-uptake in primary B cells was performed, as described above (Section 2.5.7), and PFA-fixed cells analysed by imaging flow cytometry. Cells were gated on single, live cells and acquired bad-quality images were excluded by defining a contrast gate (Gradient RMS_M01_Ch01 ≥ 55). A mask corresponding to the complete cell area was defined using the B220-specific channel and the Morphology algorithm. This cell mask was further eroded (Adaptive Erode = 88) to define the cytosolic area of B cells (internalisation mask). The FVIII/FVIII-Alb internalisation parameter for single cells was defined using the antigen-specific fluorescent signal and the defined internalisation mask. The obtained internalisation coefficient estimates the ratio of antigen-specific fluorescence located within the mask versus antigen-specific fluorescence outside of the internalisation mask. The internalisation coefficient ranges from -3, corresponding to total exclusion, to 3, corresponding to complete internalisation, and a value of 0 represents no antigen internalisation. Imaging flow cytometry data analysis was performed using the IDEAS® software (Luminex Corporation, USA) and FlowJo software (BD Biosciences, Germany). To obtain reliable internalisation parameters, more than 1,000 $FVIII^+B220^+$ B cells were recorded per sample and analysed.

2.8.7: Calculation of division indices by flow cytometry

In vitro suppression assays and surface antigen staining were performed, as described above (Section 2.5.10 and Section 2.6.7). Stained cells wear analysed by flow cytometry and gated on single live $CD8^+$ T cells. A proliferation model was fit to the resulting CFSE histograms of $CD8^+$ T cells using the proliferation modelling tool of the FlowJo software (BD Biosciences, Germany). The division index, which estimates the average number of cell division the analysed cell population has undergone, was used as a read-out parameter for assessing the Treg-mediated suppression of $CD8^+$ T cell proliferation.

2.8.8: HSA uptake in FcRn-mCherry transduced HeLa cells

HSA uptake in FcRn-mCherry transduced HeLa cells was performed, as described above (Section 2.5.1), and cells fixed with PFA. Subsequently, fixed cells were imaged by confocal microscopy. Cell boundaries of single cells were defined as regions of interest (ROIs) using the background fluorescence of the HSA fluorescence channel. Mean fluorescence signals within single ROIs of single stacks were calculated for HSA-AF488, rHSA^{H464Q}-AF488, and FcRn-mCherry using the ImageJ software. HSA mean fluorescence was standardised to the FcRn-mCherry expression level of single cells by dividing the mean HSA fluorescence with FcRn-mCherry mean fluorescence. Standardised HSA-AF488 and rHSA^{H464Q}-AF488 fluorescent levels were analysed in relation to the respective pH during the ligand uptake.

2.8.9: Statistical analysis

Raw data was processed using Excel and statistically analysed using GraphPad Prism (GraphPad software, USA). Error bars of data are graphically represented as SEM. Statistical significance was determined using the indicated statistical tests with the GraphPad Prism software (GraphPad Software, USA). p values below 0.05 were considered statistically significant and indicated as follows: * $p \leq 0.05$, ** $p \leq 0.01$, *** $p \leq 0.001$, **** $p \leq 0.0001$, not significant (ns) $p > 0.05$

2.8.10: Graphical illustrations

Parts of the figures were created with BioRender.com, SnapGene software (GSL Biotech, USA) and Affinity Designer (Serif (Europe) Ltd., United Kingdom).

Chapter 3: Characterisation of the intracellular FcRn-albumin interaction in primary macrophages

3.1: Introduction

Many receptors recycle between the surface and intracellular compartments (Cullen and Steinberg, 2018). The site(s) of interactions between receptors and ligands vary depending on the particular receptor. For some receptors, such as toll-like receptor 4 (TLR4) and G protein coupled receptors, interactions with the ligand occurs not only at the cell surface but also within endosomal compartments and the receptor interaction within these endosomal structures play key roles in receptor functions (Gangloff, 2012; Hanyaloglu, 2018; Retamal *et al.*, 2019). In some instances, interactions between recycling receptors and ligands occur selectively within intracellular compartments following endocytic uptake of the ligand. One example of a recycling receptor interacting with its ligands exclusively within intracellular compartments is the MHC class I like neonatal Fc receptor (FcRn) (Tesar and Björkman, 2010). FcRn plays an important role in both, neonatal and adult life; in the neonate, FcRn facilitates the transfer of maternal IgG molecules to the embryo or newborn, while in the adult, FcRn rescues endocytosed IgG and albumin from lysosomal degradation by capturing these ligands in acidified endosomes, prior to their delivery to lysosomes. Instead, the receptor-ligand complex recycles back to the cell surface, where ligands dissociate from the receptor at neutral pH, and are released to the circulation extending their half-lives *in vivo* (Roopenian and Akilesh, 2007; Ward and Ober, 2009). Many studies have focussed on FcRn-IgG cell biology, however there is less knowledge about how FcRn mediates the rescue and recycling of endocytosed albumin, in particular within primary cells (Pyzik *et al.*, 2019). The investigation of FcRn-dependent albumin cell biology is of particular interest because both FcRn ligands, albumin and IgG, are potentially internalised by cells via distinct endocytic pathways and bind distinct sites of the receptor within intracellular compartments suggesting discrete FcRn-dependent, intracellular trafficking mechanisms (Chaudhury *et al.*, 2006; Pyzik *et al.*, 2019).

Recently, a FcRn-dependent recycling pathway for endocytosed albumin has been identified in primary macrophages (Toh *et al.*, 2020). Human serum albumin (HSA) is internalised by CSF-1 stimulated primary macrophages via macropinocytosis, a non-selective and efficient pathway for uptake of soluble molecules (Toh *et al.*, 2020). After endocytosis, HSA located to newly formed macropinosomes is recycled to the cell surface in a FcRn-dependent manner via a rapid and efficient recycling pathway mediated by tubular transport carriers emerging from early macropinosome bodies (Toh *et al.*, 2020). The non-FcRn binding HSA mutant, rHSA^{H464Q}, despite being internalised efficiently, is excluded from tubular transport carriers projecting to the cell surface and is transported to lysosomes for rapid degradation (Toh *et al.*, 2020).

Although FcRn-dependent recycling has been described in primary macrophages, a key unanswered question remains the relationship between the albumin recycling pathway and the temporal and spatial events with its intracellular interaction with FcRn. A major challenge in identifying interaction between ligands and membrane receptors within intracellular compartments, compared with the cell surface, is that such interactions need to be detected and quantified in the presence of a pool of unbound ligand. To this end, here two independent biophysical approaches were used to monitor the intracellular interaction of HSA with the membrane bound FcRn in primary macrophages following endocytosis of ligand. Namely, the phasor approach to fluorescence lifetime imaging microscopy (FLIM) of Förster resonance energy transfer (FRET) (Digman *et al.*, 2008; Hinde *et al.*, 2012) and a novel approach to single molecule fluorescence fluctuation spectroscopy (FFS) called raster image correlation spectroscopy (RICS) (Digman *et al.*, 2005; Digman and Gratton, 2009; Priest *et al.*, 2019), which together assess the direct interaction of albumin with FcRn, as well as the mobility of bound versus unbound ligand, have been established for the investigation of intracellular receptor-ligand interactions .

3.2: Results

3.2.1: Generation of bicistronic plasmids for the mammalian expression of β_2-microglobulin and mCherry-labelled FcRn fusion proteins

3.2.1.1: Generation of pIRES-derived plasmids expressing N-terminal or C-terminal labelled FcRn-mCherry fusion protein

To quantify the interaction of intracellular FcRn with the endocytosed ligand, albumin, and the impact endogenous FcRn binding has on albumin mobility, we have used FLIM-FRET and RICS, respectively. Both techniques rely on fluorescently tagged human serum albumin (either HSA-AF488 or HSA-AF568). FLIM-FRET also required a fluorescently tagged FcRn that, based on the spectrum, would undergo FRET with HSA, while RICS required a fluorescently tagged FcRn non-binding mutant of HSA ($rHSA^{H464Q}$) spectrally distinct from WT HSA. For the FLIM-FRET experiment HSA-AF488 (green) was employed and plasmids for the expression of mCherry (red) fused to either the N-terminus or C-terminal cytoplasmic tail of human FcRn were generated (Figure 3.1).The plasmids encoding human FcRn-mCherry constructs included the β_2-microglobulin (B2M) light chain in a polycistronic plasmid, with the FcRn heavy α-chain following B2M to optimise the assembly of transport competent FcRn-mCherry fusion proteins in the ER (Figure 3.1).

To generate the C-terminal labelled construct (pIRES-B2M-FcRn_mCherry), the FcRn-mCherry open reading frame (ORF) was amplified from pEF1α-FcRn_mCherry plasmid using the FcRn-mCherry(pIRES)-fw and FcRn-mCherry(pIRES)-rev primers. The amplified PCR product contained complementary overhangs which allowed the insertion of the PCR fragment into the pIRES plasmid backbone suitable for bicistronic expression of B2M and FcRn-mCherry. The plasmid pIRES-β_2-microglobulin/mycFcRn encoding B2M and myc-tagged FcRn was cut with *Xba*I and *Not*I-HF to remove the myc-FcRn ORF. Both fragments containing complementary overhangs were combined by HiFi assembly. This resulted in a bicistronic plasmid encoding B2M and FcRn-mCherry using an internal ribosomal entry site (IRES) under the control of the

CMV promoter (Figure 3.1A). The FcRn-mCherry ORF contained the native FcRn signal peptide (SP) to allow ER translocation of the receptor into the secretory pathway, and FcRn and mCherry were separated by a polypeptide linker with the sequence Ala-Arg-Asp-Pro-Pro-Val-Ala-Thr to allow independent folding of the two fusion protein domains (Figure 3.1B).

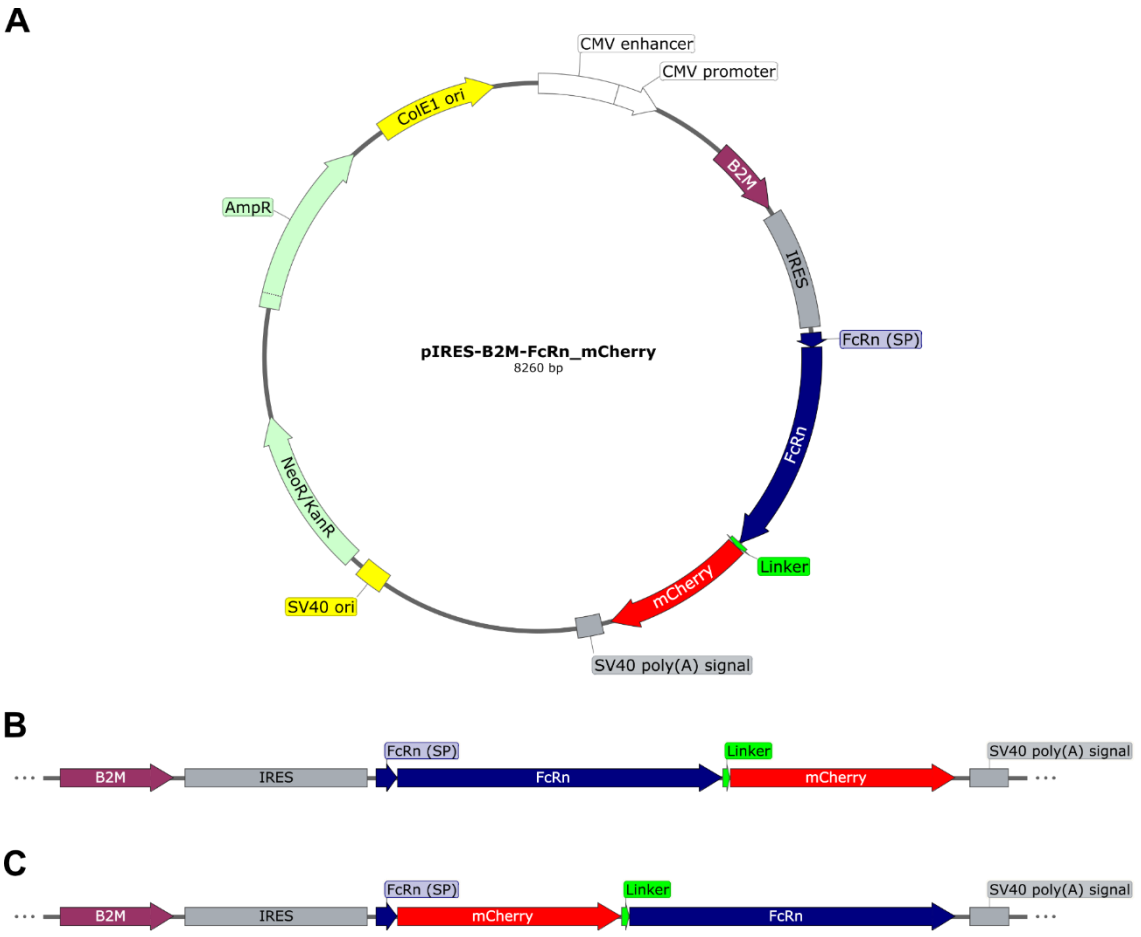

Figure 3.1: Bicistronic pIRES-derived plasmids for the expression of C- and N-terminal mCherry-labelled FcRn fusion proteins
(A) Plasmid map showing the most important features of the bicistronic plasmid pIRES-B2M-FcRn_mCherry allowing the co-expression of human FcRn light chain β2-microglobulin (B2M, purple) and human FcRn heavy α-chain (blue) labelled with mCherry (red) at the C-terminus under the control of the CMV promoter using an internal ribosomal entry site (IRES). The native signal peptide of human FcRn (SP) was included to allow efficient secretion of the fusion protein and the FcRn and mCherry domain were separated by a polypeptide linker with the sequence Ala-Arg-Asp-Pro-Pro-Val-Ala-Thr (green). Other important plasmid features such as SV40 poly(A) signal (grey), replication origins (yellow) and

antibiotic resistance cassettes (light green) are highlighted at their respective locations. **(B-C)** Detailed organisation of the open reading frames (ORFs) in bicistronic plasmids encoding for the co-expression of B2M and either C-terminal labelled FcRn-mCherry **(B)** or N-terminal mCherry-FcRn fusion proteins **(C).** The plasmid map and overview of ORFs were created with SnapGene.

To generate the N-terminal labelled construct (pIRES-B2M-IRES-mCherry_FcRn), the plasmid pIRES-β2-microglobulin/mycFcRn encoding for B2M and myc-tagged FcRn excluding the myc-tag was amplified using the primers backbone-pIRES-fw and backbone-pIRES-fw. The polypeptide linker sequence Ala-Arg-Asp-Pro-Pro-Val-Ala-Thr was added to the PCR product by primer design. The sequence of the mCherry insert was amplified from the pEF1α-mCherry plasmid using the primers mCherry-FcRn(IRES)-fw and mCherry-FcRn(IRES)-rev containing complementary overhangs to the amplified pIRES backbone construct. Both fragments were ligated by HiFi assembly and resulted in a bicistronic plasmid allowing the co-expression of B2M and C-terminal labelled mCherry-FcRn using an IRES under the control of the CMV promoter. The native FcRn signal peptide (SP) was included in the ORF upstream of the mCherry domain to allow efficient secretion of the fusion protein and both proteins were separated by a polypeptide linker with the sequence Ala-Arg-Asp-Pro-Pro-Val-Ala-Thr to allow independent folding of both fusion protein domains (Figure 3.1C).

The insertion of the two fusion protein domains and the correct assembly of both plasmid constructs was confirmed by sequencing using the primer Seq-End-IRES and Seq-End-mCherry.

3.2.1.2: Generation of a FUGW-derived bicistronic plasmid expressing β2-microglobulin and FcRn-mCherry for lentiviral transduction

To generate lentiviral particles containing a bicistronic plasmid encoding B2M and the C-terminal labelled FcRn-mCherry (FUGW-B2M-IRES-FcRn_mCherry), the

B2M-IRES-FcRn-mCherry sequence was subcloned into a FUGW backbone suitable for lentiviral packaging (Figure 3.2).

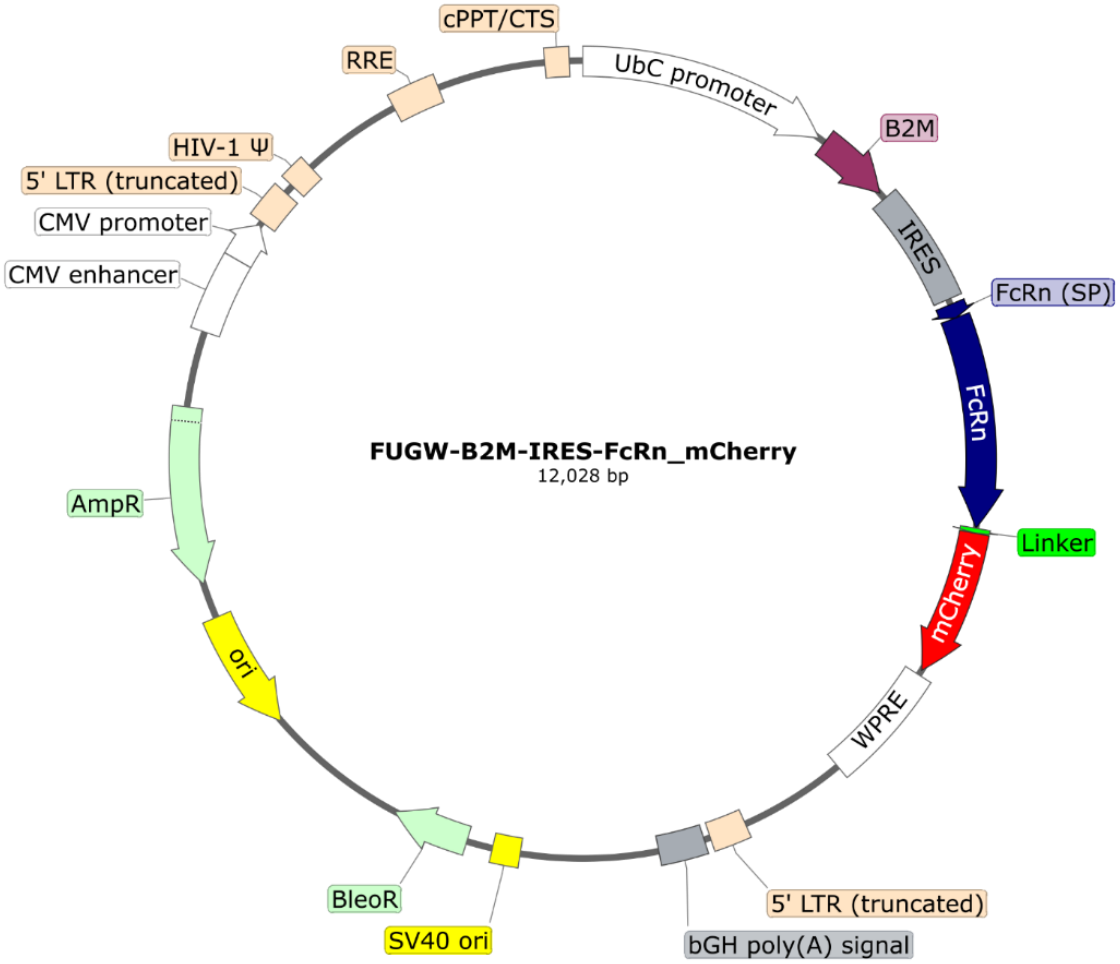

Figure 3.2: The bicistronic plasmid FUGW-B2M-IRES-FcRn_mCherry suitable for the generation of FcRn-mCherry containing lentiviral particles
Plasmid map showing the most important features of the bicistronic plasmid FUGW-B2M-FcRn_mCherry allowing the co-expression of human FcRn light chain β2-microglobulin (B2M, purple) and human FcRn heavy α-chain (blue) labelled with mCherry (red) at the C-terminus under the control of the UbC promoter using an internal ribosomal entry site (IRES). Additionally, elements important for the packaging into lentiviral particles (orange) are highlighted at their particular locations. Other important plasmid features such as bGH poly(A) signal (grey), replication origins (yellow), antibiotic resistance cassettes (light green) and promoters as well as other regulatory elements (white) are highlighted at their respective locations. The plasmid map was created with SnapGene.

To transfer the two ORFs, which are separated by an IRES, into the FUGW backbone, the B2M-IRES-FcRn-mCherry sequence was amplified from the pIRES-B2M-FcRn_mCherry plasmid using the B2M-FcRn-mCherry(FUGW)-fw and B2M-FcRn-mCherry(FUGW)-rev primers containing complementary overhangs to the FUGW backbone, and the FUGW plasmid was cut using *Eco*RI-HF and *Bam*HI-HF to remove the encoded enhanced green fluorescent protein (EGFP) sequence. The amplified B2M-IRES-FcRn-mCherry sequence and the linearised FUGW backbone were ligated by HiFi assembly, which resulted in a bicistronic plasmid allowing the co-expression of B2M and FcRn-mCherry fusion protein using an IRES, and furthermore contained lentiviral packaging elements allowing the generation of FcRn-mCherry encoding lentiviral particles to facilitate gene transfer into primary macrophages (Figure 3.2).

3.2.2: Assessment of FRET transfer between HSA-AF488 and FcRn-mCherry in HeLa cells

3.2.2.1: Expression and intracellular localisation of C-terminal labelled FcRn-mCherry in transfected HeLa cells

To assess the expression and correct assembly of FcRn-mCherry fusion proteins in cells, HeLa cells were transfected with C-terminal tagged FcRn-mCherry (Figure 3.3). The mCherry domain fused to the C-terminus of FcRn is orientated towards the cytosol; therefore to facilitate FRET transfer, the fluorescent energy of luminal HSA-AF488 interacting with FcRn has to be transferred to mCherry across the endosomal membrane corresponding to a distance (d) of at least 4 – 6 nm, the typical thickness of mammalian bilayer membranes (Shahane *et al.*, 2019) (Figure 3.3A).

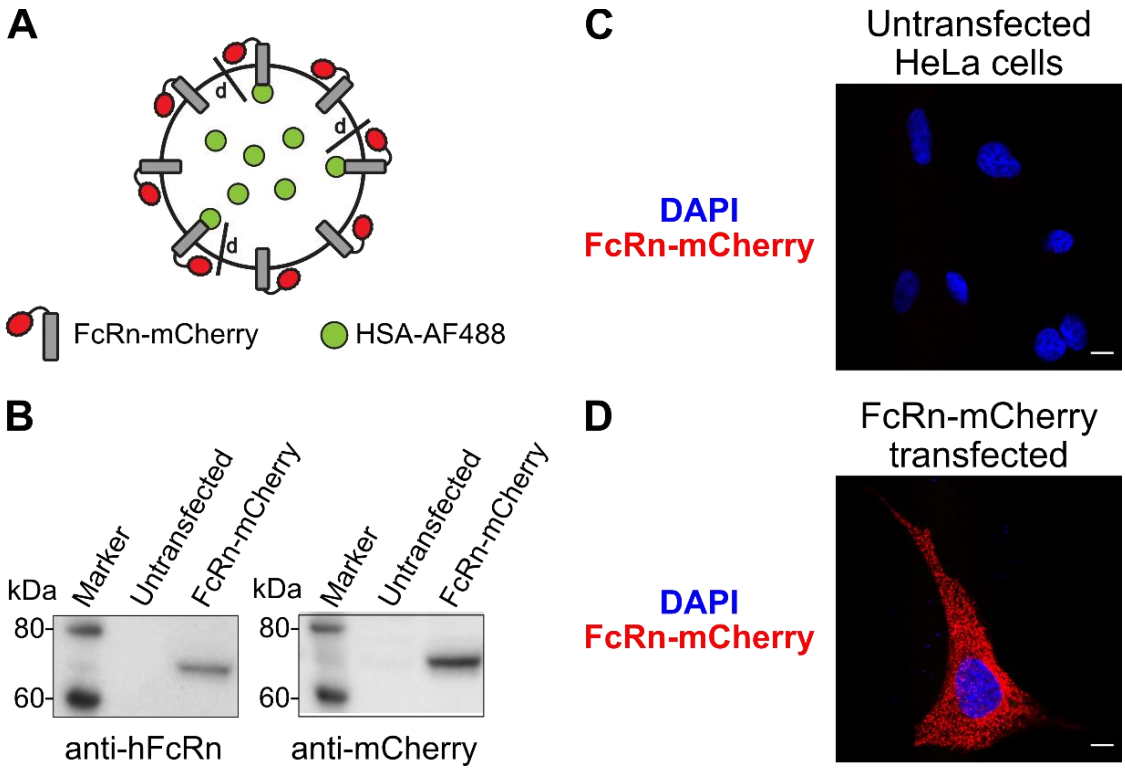

Figure 3.3: Transient transfection of C-terminal labelled FcRn-mCherry into HeLa cells
(A) Cartoon showing the membrane bound FcRn (grey) and mCherry (red) domain of the transgenic fusion protein, and endocytosed ligand, HSA-AF4488 (green), located to the endosomal lumen. FRET efficiency is dependent on the distance (d) in nm between the two fluorophores. **(B)** Total protein lysates of HeLa cells transfected with the bicistronic pIRES construct expressing B2M and FcRn-fusion protein were analysed by immunoblotting using anti-hFcRn and anti-mCherry antibodies. The detected bands in lysates of FcRn-mCherry transfected HeLa cells represented the expected size of the fusion protein (~ 72 kDa). **(C-D)** Untransfected **(C)** and FcRn-mCherry transfected **(D)** HeLa cells were analysed for mCherry fluorescence (red) by confocal microscopy. Cell nuclei were visualised using DAPI (blue). Scale bars represent 10 µm.

Cell lysates of FcRn-mCherry transfected cells were analysed by Western Blot using a hFcRn- and mCherry-specific antibody (Figure 3.3B). Both antibodies revealed a protein band in lysates of transfected cells corresponding to a size of ~ 72 kDa, the expected size of FcRn-mCherry fusion protein (Figure 3.3B). The respective bands were absent in lysates of untransfected cells. FcRn-mCherry was located to punctate endosomal structures throughout the cytosol in FcRn-

mCherry transfected cells (Figure 3.3D), whereas no fluorescence was detected in untransfected HeLa cells (Figure 3.3C), indicating efficient expression and localisation to endosomal structures of FcRn-mCherry in transiently transfected HeLa cells.

The localisation of C-terminal tagged FcRn-mCherry was further analysed by staining FcRn-mCherry transfected cells with markers of the early (EEA1) and recycling (Rab11) endosomes, ER/intermediate compartment (KDEL-receptor), late endosomes (CD63) and Golgi apparatus (GM130) (Figure 3.4).

C-terminal tagged FcRn-mCherry co-localised extensively with the early endosome marker EEA1 and recycling endosomes (Rab11), and showing little overlap with ER, Golgi, and late endosome markers (Figure 3.4). Hence, the distribution of the human FcRn tagged with mCherry in HeLa cells demonstrated efficient transport from the ER and Golgi apparatus and the intracellular distribution is consistent with the untagged human FcRn in immortalised cell lines (Ward *et al.*, 2005; Mahmoud *et al.*, 2017).

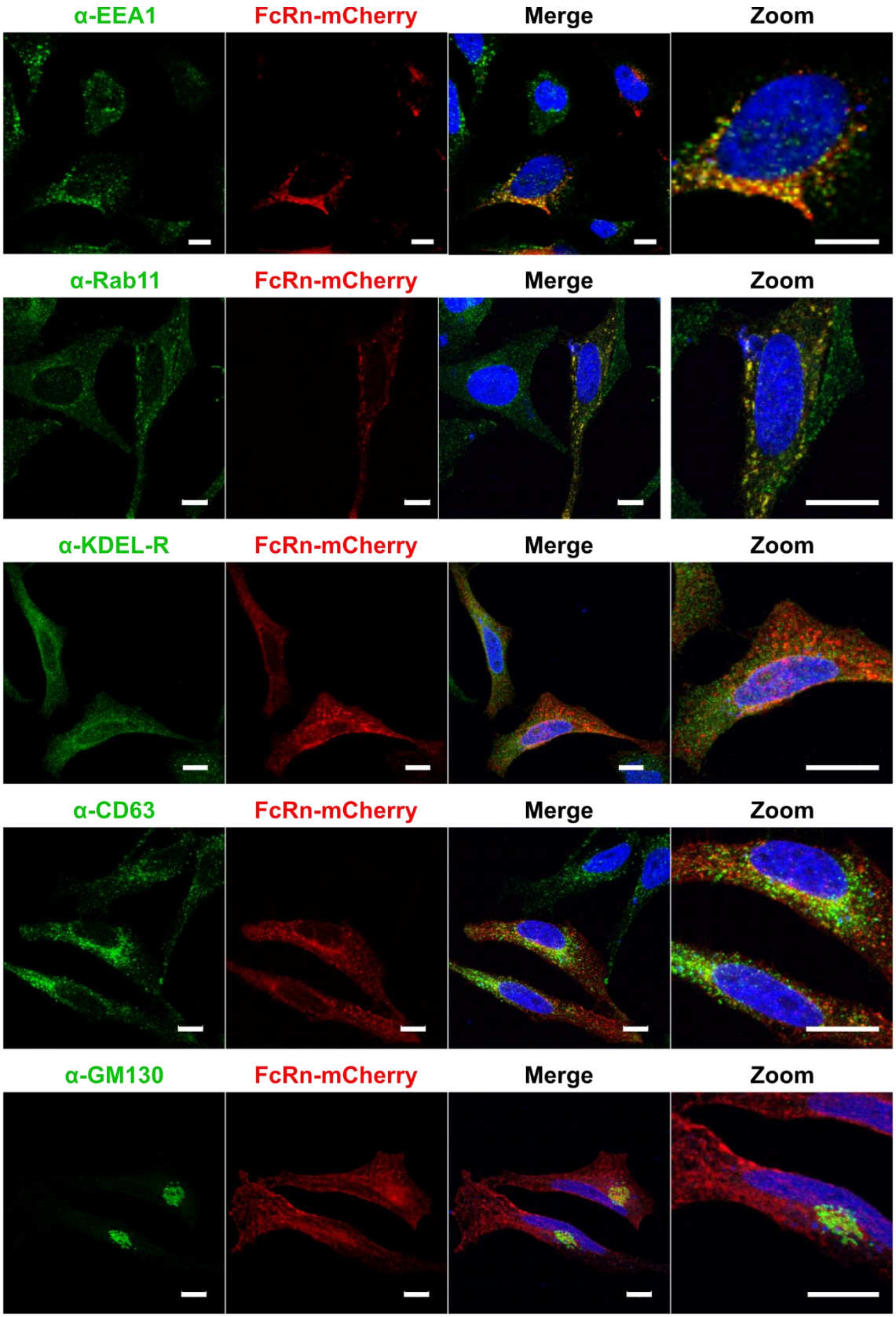
α-EEA1
FcRn-mCherry
Merge
Zoom
α-Rab11
FcRn-mCherry
Merge
Zoom
α-KDEL-R
FcRn-mCherry
Merge
Zoom
α-CD63
FcRn-mCherry
Merge
Zoom
α-GM130
FcRn-mCherry
Merge
Zoom

Figure 3.4: Intracellular distribution of FcRn-mCherry in transiently transfected HeLa cells
HeLa cells were transfected with the bicistronic pIRES construct expressing B2M and C-terminal labelled FcRn-mCherry fusion protein (red) for 48 hours. Cells were fixed and permeabilised and stained with the organelles markers (green) EEA1 (early endosomes), Rab11 (recycling endosomes), KDEL receptor (KDEL-R, ER/intermediate compartment), CD63 (late endosomes) and GM130 (Golgi), as indicated. Scale bars represent 10 µm.

3.2.2.2: Förster resonance energy transfer (FRET) between HSA-AF488 and mCherry-labelled FcRn fusion protein in transfected HeLa cells

To analyse whether the C-terminal tagged FcRn-mCherry fusion protein was functional and suitable for FLIM-FRET detection, FcRn-mCherry transduced HeLa cells were incubated with HSA-AF488. HSA endocytosis and FRET between HSA-AF488 and C-terminal labelled FcRn-mCherry was analysed by FLIM acquisition in fixed cells (Figure 3.5). As fluid phase endocytosis is inefficient in cultured HeLa cells, I used a strategy for HSA uptake by HeLa cells previously adopted by our laboratories for cultured HEK293 cells (Chia *et al.*, 2018). Namely, incubation of FcRn-mCherry transfected HeLa cells with HSA under acidic conditions to allow ligand binding to cell surface FcRn-mCherry receptor followed by receptor mediated endocytosis (Figure 3.5).

HSA-AF488 was efficiently bound at 4 °C under acidic conditions and endocytosed at 37 °C (Figure 3.5). In addition, surface bound HSA-AF488, and internalised HSA-AF488, showed a strong FLIM-FRET signal in FcRn-mCherry expressing cells, demonstrating that the receptor-ligand fluorescent probes mediated a FLIM-FRET signal following interaction (Figure 3.5). Although the majority of HSA-AF488 molecules were restricted to the boundaries of the cells after binding at 4 °C, some HSA-specific fluorescence was detected in the centre of the cell. This was probably due to a basal endocytic activity at 4 °C or HSA-AF488 molecules bound to the peripheral membrane of observed cells, since only single slices of cells were acquired by fluorescence microscopy.

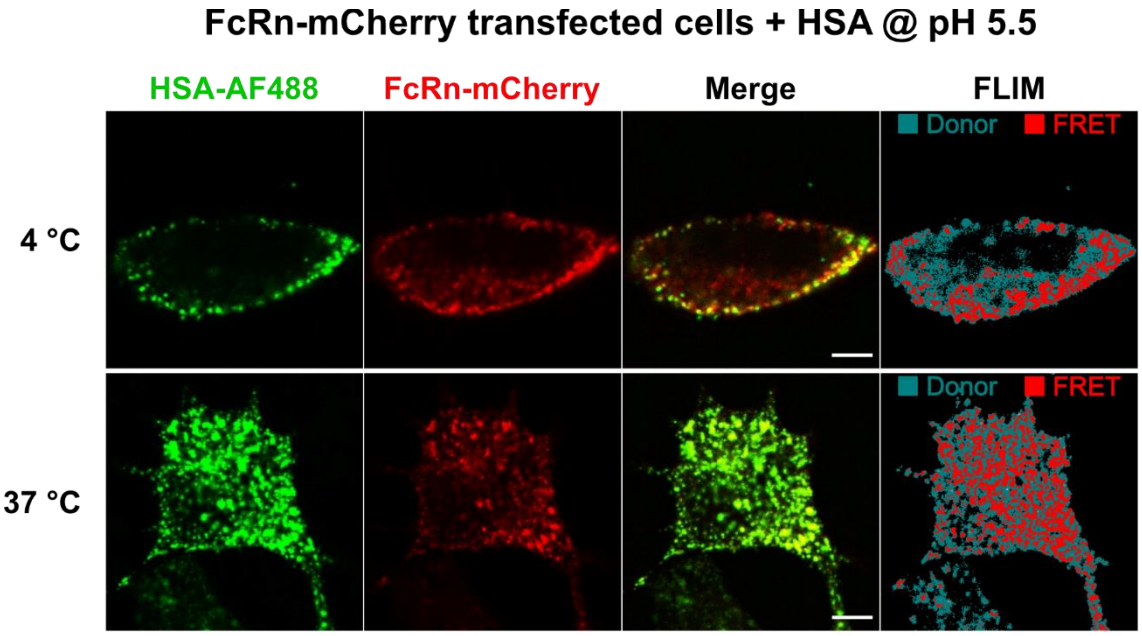

Figure 3.5: FLIM-FRET analysis of AF488-labelled HSA in FcRn-mCherry transfected HeLa cells
FcRn-mCherry (red) transfected HeLa cells were pulsed with HSA-AF488 (green) for 1 hour on ice or for 15 minutes at 37 °C in pH 5.5 buffer. Monolayers were washed and fixed in 4 % PFA. Representative confocal images (left 3 rows) were acquired with an Olympus FV3000 confocal microscope. FLIM-FRET (FLIM) acquisitions were performed with an Olympus FV3000 microscope using a FLIM detector, as described in the methods section. Pixels within obtained FLIM images were pseudo-coloured according to their FRET status, with FRET-negative pixels displayed in blue and FRET-positive pixels displayed in red. Scale bars represent 10 µm.

Using this assay, next I compared the binding and uptake of WT HSA-AF488 with a FcRn non-binding mutant of HSA, rHSA^{H464Q}-AF488, by HeLa cells transfected with C-terminal tagged FcRn-mCherry fusion protein over a pH range of pH 5.0 – 7.0 (Figure 3.6).

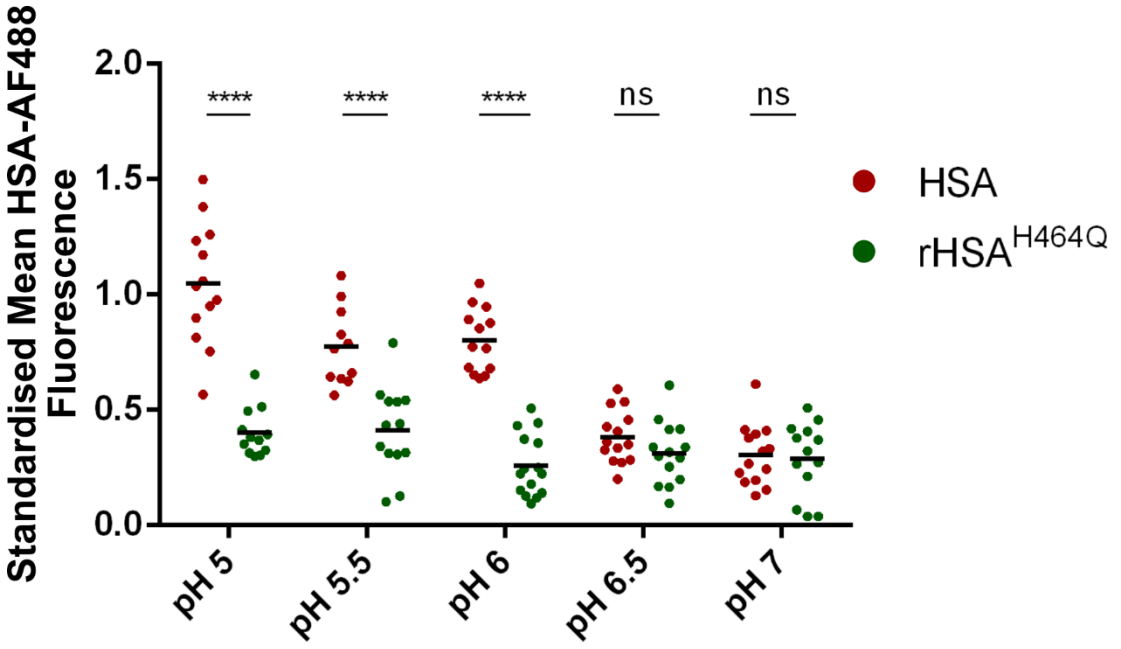

Figure 3.6: pH-dependent binding of HSA-AF488 and FcRn-mCherry in transfected HeLa cells
HeLa cells were transfected with the bicistronic pIRES construct expressing B2M and C-terminal labelled FcRn-mCherry fusion protein. FcRn-mCherry expressing HeLa cells were incubated with 100 µg/ml HSA-AF488 (red) or rHSA-^{H464Q}-AF488 (green) in buffer with a pH from 5.0 – 7.0, as indicated, for 15 minutes at 37 °C. Cells were then washed, fixed, and analysed by confocal microscopy. Fluorescence is expressed as a ratio of the mean fluorescence within cells in the green (HSA ligand) and red (FcRn-mCherry) channel. Each symbol represents an individual cell. The mean values are indicated as black bars. The quantification of HSA fluorescence is shown for a representative data set. n ≥ 11 (number of cells). p-values were calculated using an unpaired, two-tailed Student's t-test. **** $p \leq 0.0001$

HSA-AF488 was efficiently endocytosed under acidic conditions, that is pH 6.0 and lower, whereas the non-binding mutant, rHSA^{H464Q}-AF488, was very poorly taken up by FcRn-mCherry transfected cells over a pH range of 5.0 – 7.0, indicating pH-dependent binding of HSA-AF488 to FcRn-mCherry followed by receptor-mediated endocytosis (Figure 3.6). This was consistent with previous findings showing no binding of rHSA^{H464Q} to FcRn even under acidic conditions (Andersen *et al.*, 2012). The impaired endocytosis of rHSA^{H464Q}-AF488 compared

to HSA-AF488 at pH ≤ 6 was observed across several experiments using FcRn-mCherry transfected HeLa and HEK293 cells.

As the intracellular interaction of FcRn-mCherry and HSA-AF488 occurs in acidic compartments, the FRET probe, i.e., HSA-AF488, was analysed independently of FcRn-mCherry under acidic conditions in solution. No change in fluorescent lifetime of the donor probe was observed over the pH range 5.0 – 7.0, demonstrating that the system was viable for the conditions required for investigating intracellular receptor-ligand interactions (data not shown).

Next, the capacity of phasor FLIM analysis, which is based on the lifetime of the donor fluorophore, to detect FRET upon HSA-AF488 interaction with FcRn labelled with mCherry on either the N-terminus or the C-terminus was evaluated (Figure 3.7). To do so, HeLa cells transfected with one of the FcRn fusions with mCherry (acceptor molecules) were incubated with HSA-AF488 (donor molecule) for 15 minutes under acidic conditions to allow endocytosis by receptor-mediated endocytosis (Figure 3.7B-C).

This protocol led to high levels of HSA-AF488 being endocytosed, which showed a punctate endosomal staining similar to the expressed FcRn-mCherry constructs (Figure 3.7A-C). The unquenched fluorescence lifetime of the donor molecule was initially analysed in untransfected HeLa cells incubated with HSA-AF488 for 4 hours, where the ligand is slowly taken up by fluid phase endocytosis into large endocytic structures, to establish the baseline from which FRET interaction with FcRn-mCherry constructs could be detected in transfected HeLa cells (Figure 3.7A).

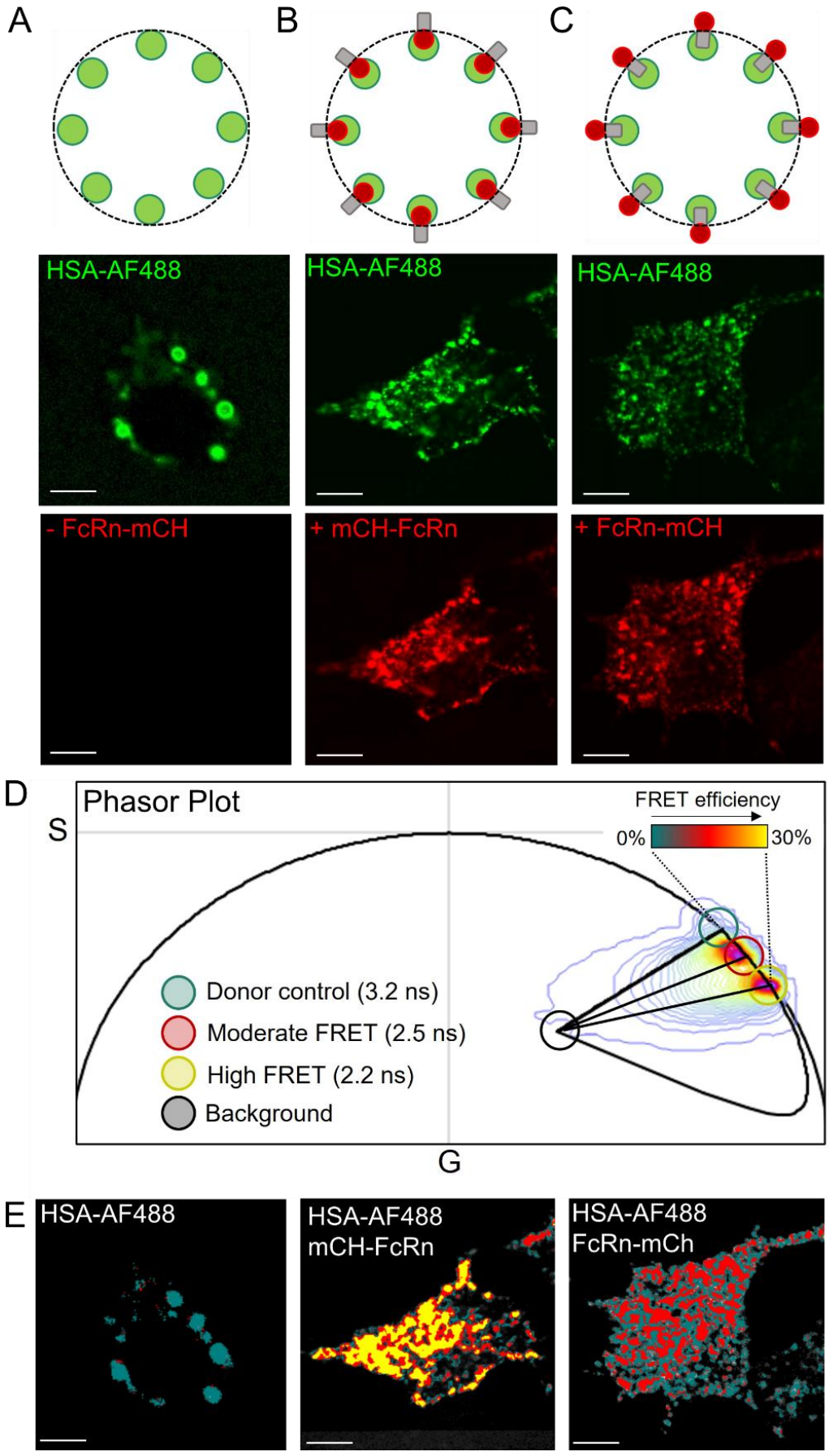
A
B
C
HSA-AF488
HSA-AF488
HSA-AF488
- FcRn-mCH
+ mCH-FcRn
+ FcRn-mCH
D
Phasor Plot
S
FRET efficiency
0%
30%
Donor control (3.2 ns)
Moderate FRET (2.5 ns)
High FRET (2.2 ns)
Background
G
E
HSA-AF488
HSA-AF488
mCH-FcRn
HSA-AF488
FcRn-mCh

Figure 3.7: Comparison of fluorescence lifetime imaging microscopy (FLIM) of HSA-AF488 interaction with N-terminal and C-terminal tagged FcRn fusion with mCherry by Förster resonance energy transfer (FRET) detection in HeLa cells
(A-C) Schematic of the donor control in the absence of FcRn **(A)** versus presence of either N-terminal labelled mCherry-FcRn (mCh-FcRn) **(B)** or C-terminal labelled FcRn-mCherry (FcRn-mCh) **(C)**. Untransfected HeLa cells were incubated with 100 µg/ml HSA-AF488 for 4 hours at 37 °C and HeLa cells transfected with mCherry-FcRn or FcRn-mCherry, as indicated, incubated with 100 µg/ml HSA-AF488 for 15 minutes at 37 °C in pH 5.5 buffer. Confocal microscopy images of fixed HeLa cells are shown in the donor (AF488, green) and acceptor (mCherry, red) channels. **(D)** Combined phasor distribution of HSA-AF 488 (donor) in the absence and presence of FcRn-mCherry fusions (acceptor) with a theoretical FRET trajectory for the donor control superimposed. The phasor blot localisations of pixels not undergoing FRET (blue), obtained from donor only controls, pixels undergoing moderate (red) and high (yellow) FRET, as well as background events (black) are indicated by circles. The respective fluorescent lifetimes of the donor molecules within the defined populations are displayed in the legend. **(E)** FLIM images matched to A-C and pseudo-colouring according to FRET (palette defined in D) reveal HSA-AF488 to undergo significant FRET interaction with both, N-terminal and C-terminal FcRn fusions to mCherry. Scale bars represent 5 µm.

The phasor distribution of the donor control (centred within teal cursor) revealed the unquenched fluorescence lifetime of HSA-AF488 to be ~ 3.2 ns and enabled extrapolation of a FRET trajectory (curved black line) to characterise the FRET efficiency of interaction with the FcRn-mCherry constructs in the presence of background signal (contained within black cursor) (Figure 3.7D). Specifically, from the superimposition of the phasor distribution of HSA-AF488 in the presence of N-terminal tagged FcRn (mCherry-FcRn, centred within yellow cursor) versus C-terminal tagged FcRn (FcRn-mCherry, centred within red cursor), over the donor control generated FRET trajectory, the HSA-AF488 interaction with mCherry-FcRn resulted in a high FRET efficiency (20 – 30 %) that significantly quenched the donor lifetime to ~ 2.2 ns and HSA-AF488 interaction with FcRn-mCherry resulted in a moderate FRET efficiency (10 – 20 %) that quenched the donor lifetime to ~ 2.5 ns (Figure 3.7D). This result, which was clearly observed upon pseudo-colouring the FLIM acquisitions of these different donor-acceptor experiments according to the FRET states identified along the FRET trajectory

(Figure 3.7E), was consistent with the difference in Förster distance between the different donor-acceptor locations with respect to the endosomal membrane (schematic shown in Figure 3.7A-C). Thus, both the N-terminal mCherry-FcRn construct and the C-terminal FcRn-mCherry construct have the potential to quantitatively assess intracellular FcRn-HSA interactions using the FLIM-FRET approach. For following experiments, the C-terminal FcRn-mCherry construct was used as higher expression levels of the fusion protein were more readily obtained in primary macrophages.

3.2.3: Intracellular localisation of exogeneous FcRn-mCherry in primary macrophages

Having established that the FLIM-FRET system was viable, mouse FcRn knock-out (FcRn KO) bone marrow-derived macrophages (BMDMs) were transduced with recombinant FcRn-mCherry lentivirus and then the intracellular localisation of the transgene in BMDMs was analysed by confocal microscopy (Figure 3.8). The distribution of human FcRn-mCherry in transduced BMDMs showed a punctate staining pattern and overlap with the early endosome marker, SNX5. There was very little mCherry fluorescence which overlapped with the ER marker, KDEL, indicating that the fluorescently tagged FcRn protein was transported efficiently from the ER after synthesis (Figure 3.8A).

To confirm that endocytosed HSA is delivered to an endosomal compartment positive for FcRn-mCherry, transduced BMDMs were pulsed with HSA-AF488 for 15 minutes and the cells fixed with PFA. Endocytosed HSA-AF488 showed substantial overlap with FcRn-mCherry, demonstrating that the FcRn fusion protein was located to the same compartments as the endocytosed HSA in BMDMs, and providing a system to examine the intracellular interactions of this ligand-receptor complex in primary cells (Figure 3.8B).

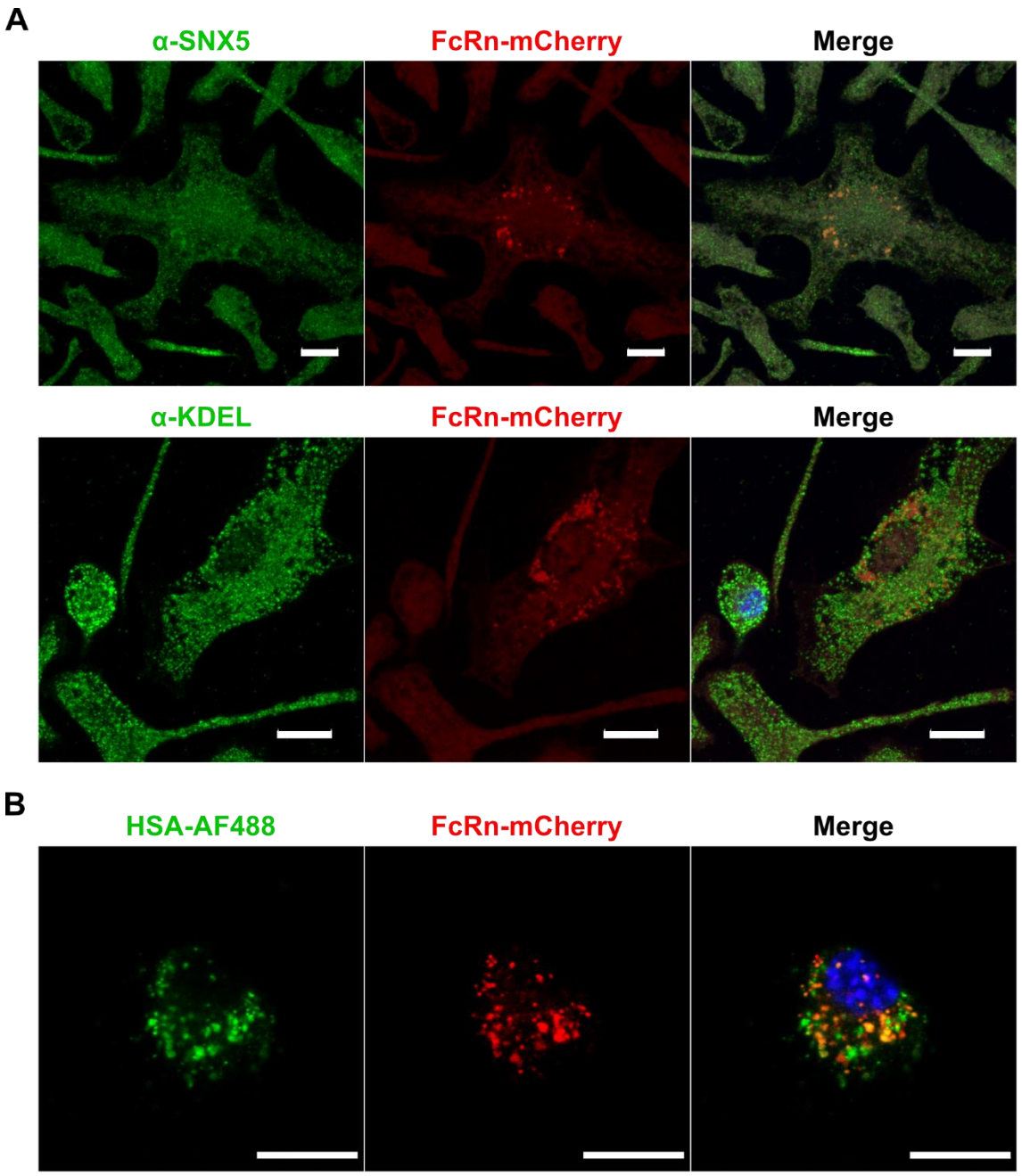

Figure 3.8: Intracellular distribution of FcRn-mCherry in transduced FcRn KO BMDMs

(A) FcRn KO BMDMs were transduced with recombinant FcRn-mCherry (red) lentivirus, as described in the methods section, fixed and permeabilised and stained with antibodies (green) to SNX5 (early endosomes) or KDEL (ER marker), as indicated. **(B)** FcRn-mCherry (red) transduced BMDMs were incubated with 100 µg/ml HSA-AF488 (green) for 15 minutes at 37 °C, to allow fluid phase endocytosis of HSA-AF488, and cells fixed, and nuclei visualised with DAPI (blue). Scale bars represent 10 µm.

3.2.4: FLIM-FRET analysis of FcRn-ligand interactions in endosomes of primary macrophages

To assess the intracellular FcRn-albumin interactions in primary cells, a series of FLIM-FRET experiments recording the receptor-ligand interaction in endosomes of BMDMs were performed (Figure 3.9). Transduced and non-transduced FcRn KO BMDMs were activated with CSF-1 to induce macropinocytosis (Lim *et al.*, 2015) and pulsed with either HSA-AF488 or FcRn non-binding HSA mutant, rHSA^{H464Q}-AF488 (donor molecules), in the absence versus presence of FcRn-mCherry for 5 minutes, and a time course of FLIM-FRET was performed (Figure 3.9A-C).

The time course for the phasor analysis of FLIM-FRET experiments was based on previous studies in the laboratory which tracked the location and recycling of endocytosed albumin in the presence and absence of FcRn (Toh *et al.*, 2020). FRET was firstly quantified by the phasor FLIM analysis of the donor molecule lifetime. HSA-AF488 alone (donor only) underwent an initial change in fluorescence lifetime to 3.2 ns (probably due to changes in the intracellular environment) which then stabilised (Figure 3.9D). The centre of the unquenched donor phasor distribution in the BMDMs was 3.2 ns (Figure 3.9D). HSA-AF488 in the presence of FcRn-mCherry (FRET experiment) maintained a quenched lifetime of ~ 2.5 ns beyond 20 minutes that was highly likely to be the result of a ligand-receptor interaction (i.e., FRET efficiency of 21 %) (Figure 3.9E). This conclusion was supported by the finding that the non-binding mutant, rHSA^{H464Q}-AF488, in the presence of FcRn-mCherry underwent the same initial change in fluorescence lifetime as the donor control which then stabilised after 20 minutes incubation with a negligible FRET interaction between rHSA^{H464Q}-AF488 and FcRn-mCherry (Figure 3.9F).

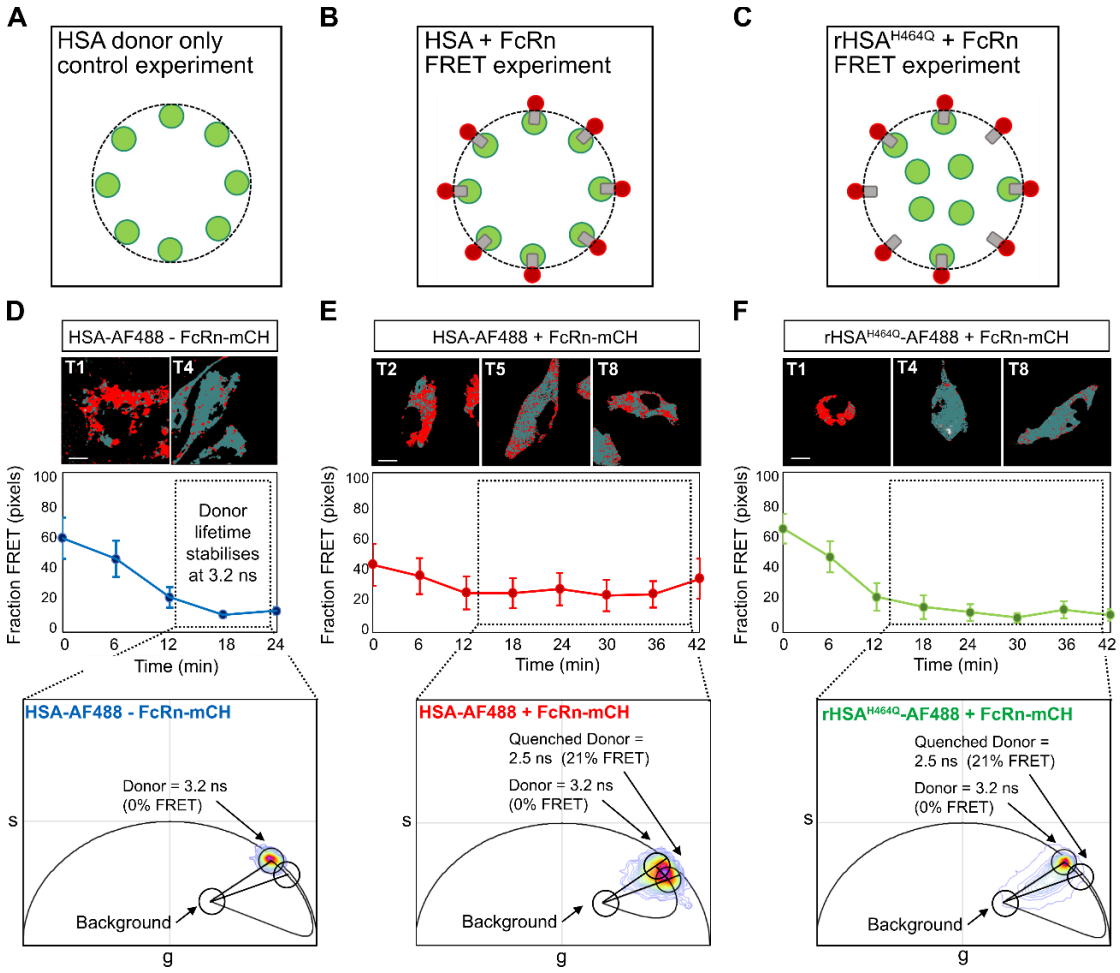

Figure 3.9: Time course of fluorescence lifetime imaging microscopy (FLIM) of HSA-AF488 in live BMDMs in presence and absence of FcRn-mCherry
(A-C) Schematic of the donor (HSA-AF488) control (HSA donor only, green) in absence of FcRn-mCherry **(A)** and the FRET experiments in presence of FcRn-mCherry (acceptor, grey and red) using either HSA-AF488 (green) **(B)** or rHSA^{H464Q}-AF488 (green) **(C)**. **(D-F)** FcRn KO BMDMs were either untransduced or transduced with recombinant FcRn-mCherry lentivirus, as described in the methods section, and incubated with 100 µg/ml HSA-AF488 or rHSA^{H464Q}-AF488 for 5 minutes at 37 °C. **(D)** FLIM images and phasor plots of HSA-AF488 in the absence of FcRn-mCherry as a function of time (N=4) reveal the fluorescence lifetime of AF488 to stabilise at 3.2 ns after 20 minutes incubation time. This is the fluorescence lifetime used to extrapolate the FRET trajectory along the universal circle. **(E)** FLIM images and phasor blots of HSA-AF488 in the presence of FcRn-mCherry as a function of time (N=6) reveal the efficiency of FRET interaction between HSA-AF488 and FcRn-mCherry to be 21 % (i.e., quenched lifetime of 2.5 ns) after 20 minutes incubation time. **(F)** FLIM images and phasor plots of rHSA^{H464Q}-AF488 in the presence of FcRn-mCherry as a function of time (N=5) demonstrate a similar initial change in fluorescence lifetime to the donor control that stabilises after 20 minutes incubation time. A negligible FRET interaction is detected between rHSA^{H464Q}-AF488 and FcRn-mCherry. Error bars indicate SEM.

Since the donor fluorescence lifetime was found to stabilise after 20 minutes (Figure 3.9D), FLIM-FRET acquisitions of a series of cells were performed at this particular timepoint (Figure 3.10).

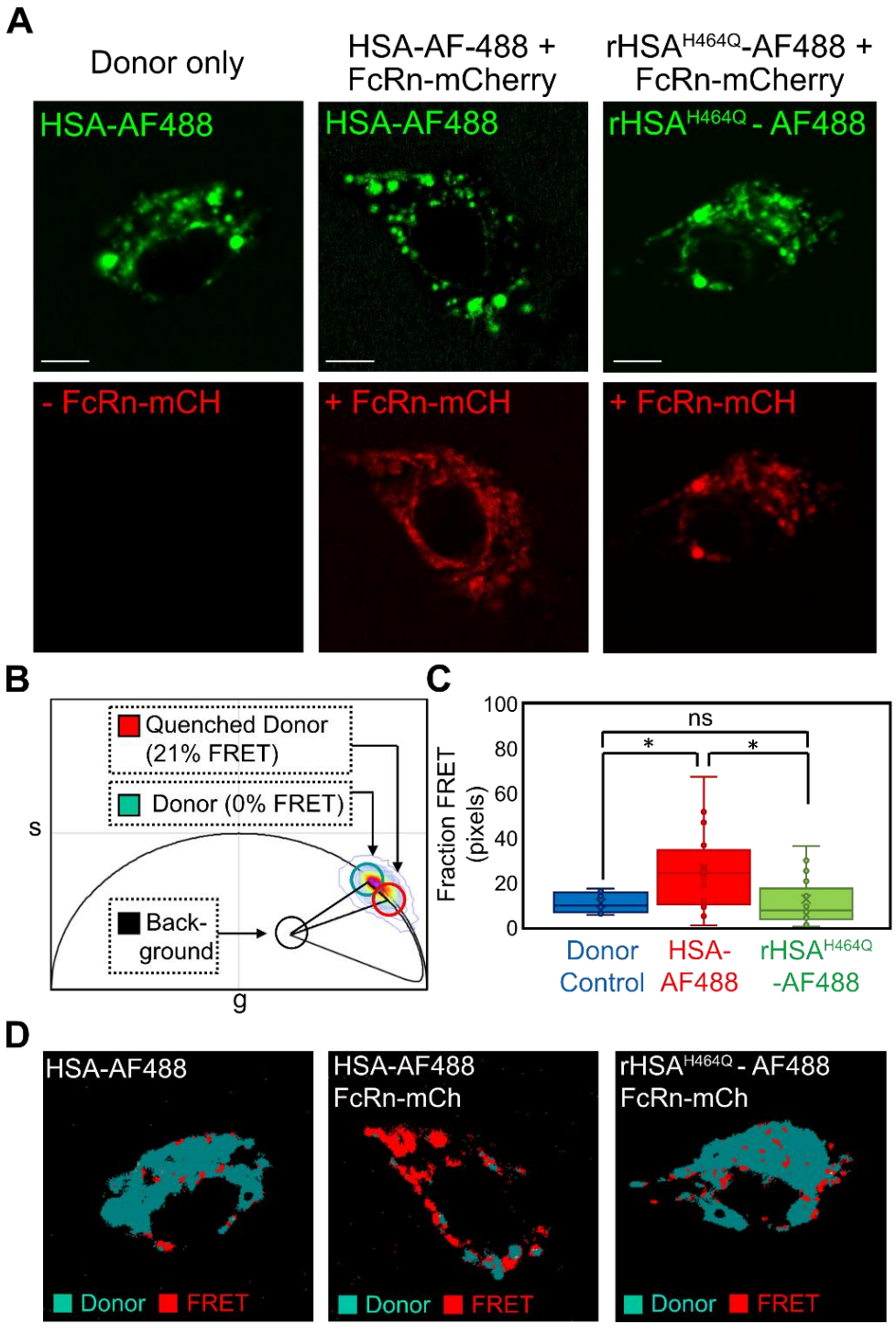

Figure 3.10: Fluorescence lifetime imaging microscopy (FLIM) of HSA-AF488 interaction with FcRn-mCherry by Förster resonance energy transfer (FRET) detection in BMDMs
FcRn KO BMDMs were either untransduced or transduced with recombinant FcRn-mCherry lentivirus, as described in the methods section, and incubated with 100 µg/ml HSA-AF488 or rHSA^{H464Q}-AF488 for 5 minutes at 37 °C. Cells were washed and incubated for 20 minutes at 37 °C before FLIM measurements were performed. **(A)** Intensity images of parental BMDMs incubated for 20 minutes after endocytosis of either HSA-AF488 or rHSA^{H464Q}-AF488 in the donor (AF488, green) and acceptor (mCherry, red) channel. **(B)** Combined phasor distribution of HSA-AF488 and rHSA^{H464Q}-AF488 (donor) in the absence or presence of FcRn-mCherry (acceptor) with a theoretical FRET trajectory for the donor control superimposed. Populations of acquired pixels not undergoing FRET (donor, blue) and pixels undergoing FRET (quenched donor, red) as well as background pixels (black) are indicated by circles at their respective location in the phasor plot. The FRET trajectory identifies the efficiency of interaction between HSA-AF488 and FcRn-mCherry after 20 minutes incubation to be 21 %. **(C)** Quantitation of the ratio of pixels undergoing FRET (defined in B) in FLIM acquisitions of the donor control (8 measurements across 4 cells) versus HSA-AF488 (20 measurements across 6 cells) and rHSA^{H464Q}-AF488 (21 measurements across 5 cells) in the presence of FcRn-mCherry. For each cell, an individual HSA uptake experiment was performed and 2 – 6 measurements were acquired per cell. **(D)** FLIM images matched to A and pseudo-colouring according to FRET (palette defined in D) reveal only wildtype HSA-AF488 to undergo significant FRET interaction with FcRn-mCherry. Scale bars represent 5 µm. The box and whisker plots **(C)** show minimum, maximum, sample median and first and third quartiles. Data was analysed by an unpaired, two-tailed Student's t-test. * $p \leq 0.05$

Quantitation of multiple FLIM-FRET experiments were performed after 20 minutes incubation with HSA-AF488 or rHSA^{H464Q}-AF488. Both ligands were efficiently internalised into large globular structures, typical of macropinosomes, in FcRn-mCherry-positive BMDMs, which showed considerable overlap with the FcRn-mCherry fusion protein (Figure 3.10A). The efficiency of FRET interaction between HSA and FcRn was calculated to be 21 % (i.e., percent of donor with a quenched lifetime of 2.5 ns) (Figure 3.10B). This was similar to the FRET level initially observed for this biosensor in HeLa cells (Figure 3.7D). Quantitative analysis of the fraction of pixels undergoing FRET revealed a significantly higher fraction for HSA-AF488 and FcRn-mCherry (~ 23 % FRET pixels) compared to the non-binding mutant rHSA^{H464Q}-AF488 and the donor only control (Figure

3.10C). Additionally, pseudo-colouring of FLIM images revealed the presence of FRET-positive pixels (red) in experiments with both HSA-AF488 and FcRn-mCherry, whereas in the donor only controls or in the rHSA^{H464Q}-AF488 and FcRn-mCherry experiments, the majority of acquired pixels were not undergoing FRET (blue) (Figure 3.10D).

Thus, these data demonstrated a specific receptor-ligand interaction between HSA and FcRn in primary macrophages after internalisation into large endosomal structures. It was previously shown that internalised HSA-AF488 was detected in tubules emerging from early macropinosomes and these ligand-loaded tubules then directed towards the plasma membrane, whereas in absence of FcRn, HSA was neither partitioned into tubules nor recycled but remained within the body of macropinosomes (Toh *et al.*, 2020). Notably, in FcRn-mCherry transduced BMDMs, HSA-AF488 was prominent not only in endosomal structures but also in thin tubular structures emanating from large endosomes, consistent with previous findings (Toh *et al.*, 2020) (Figure 3.11).

At the 20- and 25-minute timepoints after endocytosis with stable fluorescent lifetime, FRET was detected in HSA-AF488- and FcRn-mCherry-double-positive tubular-like structures (Figure 3.11). Based on the geometry and mobility, these tubular structures were reminiscent of emerging tubular carriers and the detected FRET signal indicated FcRn-albumin interaction within these tubules. In contrast, FcRn-mCherry-positive tubular carriers were devoid of the non-binding mutant, rHSA^{H464Q}-AF488 (data not shown), consistent with previous findings in BMDMs (Toh *et al.*, 2020).

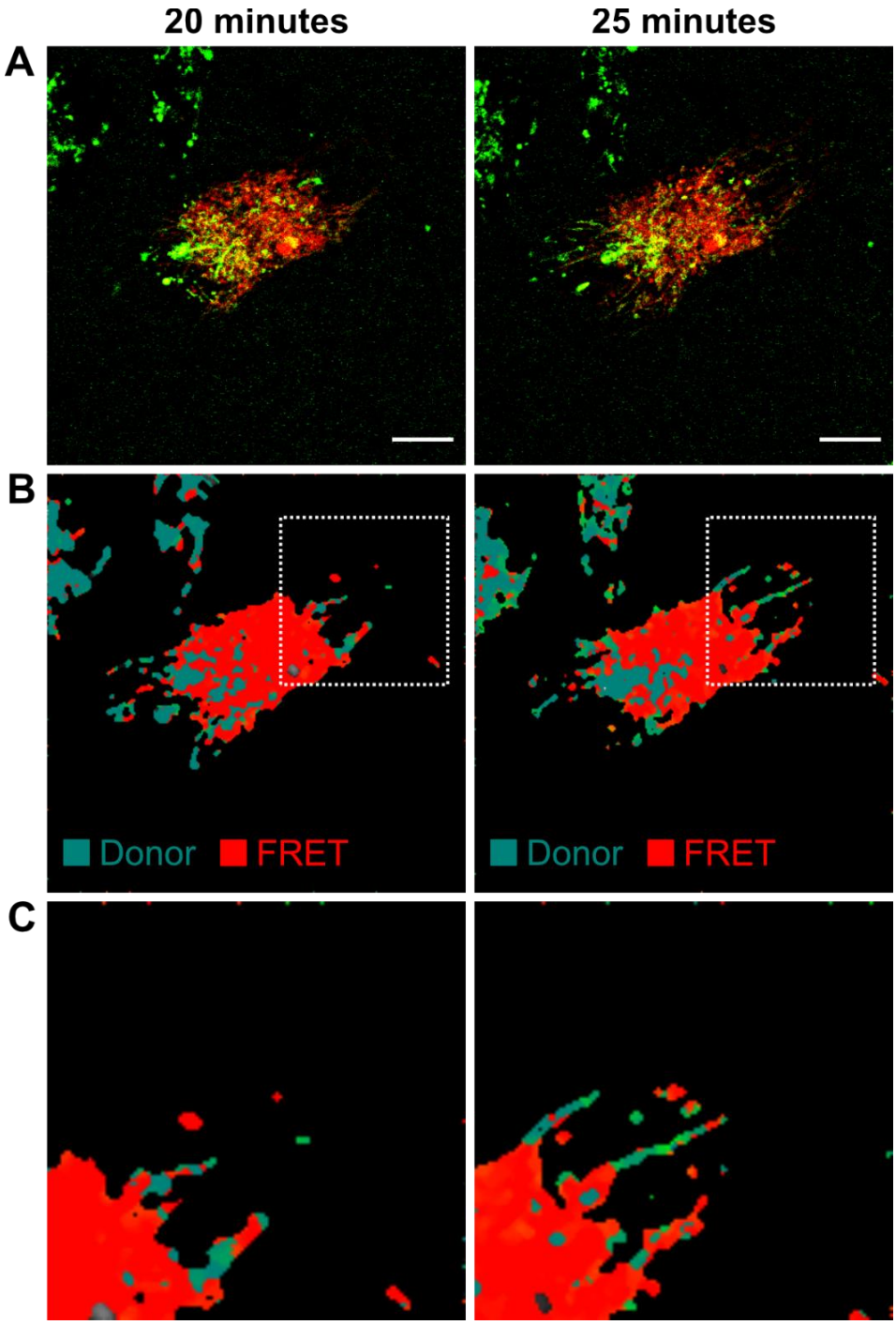

Figure 3.11: Fluorescence lifetime imaging microscopy (FLIM) of HSA-AF488 in FcRn-mCherry-positive tubules

FcRn-mCherry transduced FcRn KO BMDMs were activated with CSF-1 to induce macropinocytosis and pulsed with 100 µg/ml HSA-AF488 for 5 minutes and the fluorescent signal chased for up to 25 minutes. Images shown were taken at 20 minutes (left) and 25 minutes (right) **(A)** Fluorescence intensity images and FRET maps **(B-C)** with detection of FRET in FcRn-positive tubular structures. **(C)** Enlarged images (boxed area in B) of FRET-positive tubules. Scale bars represent 10 µm.

3.2.5: Raster image correlation spectroscopy (RICS) of single albumin molecules within endosomes of primary macrophages

To further investigate the dynamics of the HSA-FcRn interaction, an FFS based method of analysis called RICS that can extract single molecule information on HSA mobility and infer the fraction of HSA molecules bound to FcRn in a living cell was used. A major advantage of RICS is that it enables detection of the interaction of the HSA ligand with endogenous, untagged, FcRn. RICS extracts this information on HSA by spatially correlating the intensity signal that originates from a population of fluorescently labelled HSA molecules diffusing throughout a time series acquisition of intensity frames and fitting the resulting three-dimensional correlation profile to a diffusion model. It was reasoned that unbound fluorescent HSA-AF488 molecules would be highly mobile in the lumen of endosomes and essentially undergo free diffusion, while fluorescent HSA molecules engaged with FcRn, its membrane receptor, would be transiently immobilised and exhibit a significantly slower apparent diffusion coefficient. Thus, by monitoring the fraction of HSA molecules exhibiting a slow apparent diffusion coefficient, the fraction of endocytosed ligand engaged with FcRn could be quantified. To validate this assumption, I employed the FcRn non-binding mutant $rHSA^{H464Q}$ which shows minimum interaction with intracellular FcRn in BMDMs, as demonstrated by FLIM-FRET (Figure 3.10C-D) and a two-channel RICS analysis on BMDMs isolated from a FcRn KO mouse transgenically expressing untagged human FcRn ($hFcRn^{Tg/Tg}$) was performed (Chaudhury *et al.*, 2003); the BMDMs from $hFcRn^{Tg/Tg}$ mice were CSF-1 activated and incubated with 10 µg/ml of both, WT HSA-AF568 (red) and the FcRn non-binding mutant $rHSA^{H464Q}$-AF488 (green) (Figure 3.12A). Thus, binding of the ligand is monitored to an untagged receptor expressed endogenously rather than under transfection or transduction conditions.

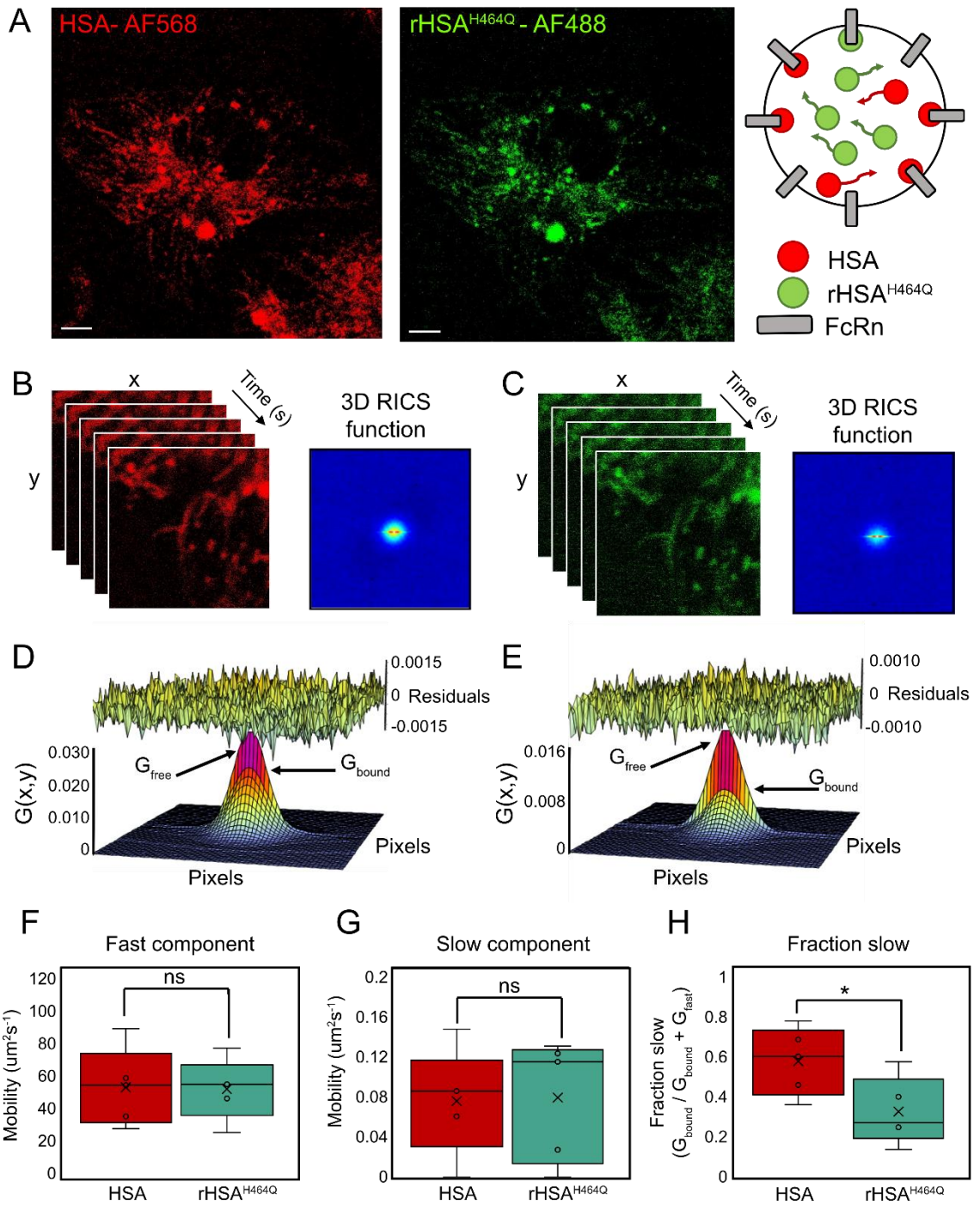

Figure 3.12: Raster image correlation spectroscopy (RICS) of HSA-AF568 versus rHSA^{H464Q}-AF488 diffusion dynamics in moving endocytic vesicles of BMDMs

(A) Confocal images of CSF-1-stimulated BMDMs incubated for 15 – 30 minutes with 10 µg/ml of both HSA-AF568 (red) and rHSA^{H464Q}-AF488 (green) alongside a schematic of HSA (red) versus rHSA^{H464Q} (green) molecules inside a moving endosomal vesicle engaging with the membrane bound FcRn receptor (grey rectangles). Scale bars represent 5 µm. **(B-C)** A two-channel RICS data acquisition involves recording a time series of frames in the HSA-AF568 channel

(red) **(B)** versus rHSA^{H464Q}-AF488 channel (green) **(C)** and spatiotemporal correlation of the pixels within each frame, which upon averaging gives rise to two three-dimensional (3D) RICS profiles. **(D-E)** The 3D RICS profiles derived from measurement of HSA-AF568 channel **(D)** versus rHSA^{H464Q}-AF488 channel **(E)** in each case fits a two-component diffusion model to assess the mobility of the respective molecules within endosomal vesicles. Residuals of the fits are shown above the profile. G_{free} is the amplitude of the component describing free diffusion and G_{bound} is the amplitude of the component describing the bound molecule population. **(F-G)** Apparent diffusion coefficients (D) of the fast (freely diffusing) **(F)** versus slow (FcRn bound) **(G)** component of HSA-AF568 (red) and rHSA^{H464Q}-AF488 (green) mobility. **(H)** Fraction of HSA-A568 (red) and rHSA^{H464Q}-AF488 (green) molecules exhibiting slow mobility (FcRn bound). **(F-H)** N=5 cells and the box and whisker plots show the minimum, maximum, sample median, and first and third quartiles. Means are indicated by a cross. The data was analysed by unpaired, two-tailed Student's t-test. * $p \leq 0.05$

Following uptake of the two fluorescent HSA conjugates, the RICS workflow involved scanning a small region of interest (ROI) within a selected cell, rapidly as a function of time, in both the HSA-AF568 (red) and rHSA^{H464Q}-AF488 (green) channels, then application of a moving average to the recorded fluctuations in fluorescence intensity to remove slow macromolecular movements of the endosomes internalising the HSA conjugates (Material and Methods) and calculation of the RICS spatiotemporal correlation function (Figure 3.12B-C). This resulted in two three-dimensional RICS profiles describing HSA-AF568 versus rHSA^{H464Q}-AF488 mobility that could each be fit to a 2-component diffusion model (Figure 3.12D-E). The fits in each channel returned an apparent diffusion coefficient (D) and amplitude (G) for a fast versus slow component that are interpreted to describe the mobility and fraction of the free (G_{FREE}) versus FcRn bound (G_{BOUND}) HSA molecules, respectively. From performing this two-channel RICS analysis on multiple BMDM cells (n = 5), it was found that while the mobility coefficients of the free (Figure 3.12F) and FcRn bound (Figure 3.12G) components of HSA-AF568 (red) versus rHSA^{H464Q} (green) molecules were not significantly different, the fraction of HSA-AF568 molecules bound to FcRn (slow component) was significantly higher than the fraction of FcRn bound rHSA^{H464Q}-AF488 molecules (Figure 3.12H). This result confirmed the interpretation of the

2-component fit and revealed that while 45 % of the HSA molecules were freely diffusing within the lumen of an endosome at a rate of 51 ± 7 $\mu m^2 s^{-1}$, the remaining 55 % of the HSA molecules were FcRn bound with an apparent mobility of 0.07 ± 0.02 $\mu m^2 s^{-1}$, a significant difference from the freely diffusing population (Figure 3.12F-H).

3.3: Discussion

The ability to identify interactions between membrane receptors and ligands in space and time within intracellular compartments is important in defining cell biological events associated with intracellular membrane receptor interactions. A major challenge in identifying ligand-membrane receptor interactions within intracellular compartments, as distinct from the cell surface, has been that these interactions need to be detected and quantified in the presence of an unbound pool of ligand. Here, two independent biophysical techniques were applied to detect the interaction of the soluble ligand albumin with its membrane receptor, FcRn, an interaction which requires an acidic endosomal environment, within primary macrophages. The use of biophysical techniques to probe interactions in primary cells has broad application for a variety of biophysical systems and is particularly relevant to our studies on albumin uptake and interaction with FcRn.

Macropinocytosis is the major pathway for endocytic uptake of soluble FcRn ligands, a pathway particularly active in primary cells, especially immune cells (Lim and Gleeson, 2011). Previously, it was demonstrated that albumin is rapidly internalised by fluid phase macropinocytosis in primary macrophages and recycled in an FcRn dependent manner (Toh *et al.*, 2020). By multiplexed biophysical fluorescent microscopy, here I have shown a direct interaction of albumin with FcRn following uptake of albumin within endosomal structures. A strength of the approach used in this study was the inclusion of primary macrophages deficient in FcRn and the use of a non-binding mutant of albumin (Andersen *et al.*, 2012) to demonstrate that the observed FRET and changes in ligand mobility were directly related to a ligand-receptor interaction.

The use of both FLIM-FRET and RICS provided complimentary approaches which not only confirmed the detection of an interaction between ligand and receptor within endosomes but also provided additional information on the spatial dynamics of the interaction. FLIM-FRET detected ~ 23 % of the HSA molecules bound to FcRn-mCherry ~ 20 minutes after uptake of HSA-AF488 (Figure 3.10). I was unable to quantify the ligand binding at earlier time points due to a transient non-specific change in fluorescent lifetime of the donor fluorophore following endocytosis (Figure 3.9). This was likely due to the transition of the fluorophore between two environments (i.e., extracellular versus acidic endosomal); a time course of the donor showed that the fluorescent lifetime stabilised after approximately 15 minutes. Therefore, the use of FLIM was particularly informative on the conditions within the endosomal system which were compatible with a specific FRET signal between HSA and FcRn. The detection of FRET within FcRn-positive tubular structures (Figure 3.11), albeit qualitative, is consistent with the recruitment of albumin in transport carriers for recycling to the cell surface and, together with the previous findings that HSA but not rHSA^{H464Q} was detected in tubules in live BMDMs, purports that an interaction with FcRn is required for entry into these putative transport carriers (Toh *et al.*, 2020). Confirmation of these findings with quantitative analysis on the FRET signals of HSA and FcRn within the tubular transport carriers would be instructive, although a technical challenge may be the gradual loss of acidity and the disruption of the ligand-receptor complex within the lumen of the tubules prior to arrival at the cell surface.

The application of RICS for detection of ligand-receptor engagement in endosomes is powerful, as the experiments avoid the need for a tagged FcRn construct and enable detection of FcRn-HSA engagement at an endogenous level, in contrast to FLIM-FRET which requires fluorescently tagged FcRn. FLIM-FRET and RICS are independent techniques which are complimentary as they analyse heterologous and endogenous FcRn interactions, respectively, with the fluorescently labelled HSA ligand. The findings from RICS analysis of fluorescence-labelled WT HSA versus an HSA non-binding mutant (rHSA^{H464Q}) showed that the mobility of single ligand molecules can be described by a two-component diffusion model where the fast component reports on the fraction of

ligand molecules freely diffusing within the lumen of the endosomes, and the slow component reports the fraction of ligand molecules bound to the receptor. The RICS data indicated that approximately 55 % of HSA-AF568 molecules were bound to endogenous FcRn, and in agreement with FLIM-FRET, the rHSA^{H464Q} mutation reduced this fraction 2-fold (Figure 3.12). The observation that ~ 55 % of HSA-AF568 molecules were bound to endogenous receptor by this biophysical technique is consistent with our previous finding that 50 % of the total internalised HSA fraction were recycled in a FcRn dependent manner by hFcRn $^{Tg/Tg}$ BMDMs (Toh *et al.*, 2020). A challenge in the application of RICS is the analysis of ligand-receptor interaction within endosomes as the mobility of the ligand needs to be determined within the context of the relatively slowly mobile endosomal structures. Future work to overcome this challenge would be to couple RICS analysis of ligand-receptor interaction with orbital tracking of endosomal movement.

In conclusion, the biophysical approaches used here provide a convenient *ex vivo* assay to quantify receptor-ligand interactions. Using FLIM-FRET and RICS allows quantification and comparison of receptor-ligand interaction within endosomal structures of live cells. Fluorescence fluctuation spectroscopy (FFS) has been increasingly utilised to study the dynamic behaviour of macromolecules in cells and this study expands the potential of this approach to determine the dynamics of ligand interactions within the lumen of the endosomal system (Kolin and Wiseman, 2007; Jameson *et al.*, 2009; Priest *et al.*, 2019). The use of these biophysical techniques to probe interactions within primary cells has broad applications in a variety of physiological systems, such as receptor signalling mediated by ligand interactions with intracellular toll like receptors in endosomes (Blasius and Beutler, 2010), ligand activation of G protein coupled receptors within the endosomal systems (Sposini and Hanyaloglu, 2017), intracellular interactions of cargo with cargo receptors (Van Vliet *et al.*, 2003; Nyfeler *et al.*, 2008), and loading of antigens onto MHC molecules within specialised endosomal loading compartments (Rocha and Neefjes, 2008; Donaldson and Williams, 2009).

Chapter 4: The albumin-FcRn recycling system in primary vascular endothelial cells

4.1: Introduction

The endothelium is a monolayer composed of specialised endothelial cells covering the entire vascular system. Endothelial cells are multifunctional, polarised cells and function as a selective permeability barrier and control the influx and efflux of nutrients, molecules and cells between the blood circulation and the underlying tissue. Consequently, they are crucial for regulating various physiological processes such as hemostasis, inflammation, and angiogenesis (Potente and Mäkinen, 2017; Khaddaj Mallat *et al.*, 2017). As endothelial cells express FcRn and have a large contact area with blood, the endothelium is considered to be one of the most important locations for FcRn-mediated IgG and albumin homeostasis (Borvak *et al.*, 1998; Ward *et al.*, 2003). Furthermore, endothelial cells are known to efficiently endocytose serum proteins in various *in vitro* and *in vivo* experiments (Smedsrød *et al.*, 1984; Pitas *et al.*, 1985; Vogel *et al.*, 2001; John *et al.*, 2003).

The uptake of IgG molecules in immortalised endothelial cells was shown to be predominantly facilitated by fluid-phase (macro)pinocytosis, whereas in some studies albumin uptake was found to be dependent on receptor-mediated endocytosis involving the albumin receptor albondin also known as gp60 (Tiruppathi *et al.*, 1997; Ward *et al.*, 2003). Several other studies using immortalised endothelial cell lines, however, suggest that albumin uptake in endothelial cells is also accomplished via macropinocytosis and partly via the caveolae-mediated endocytosis pathway (Li *et al.*, 2013). Once endocytosed, albumin was shown to localise in Rab4-associated early endosomes and the recycling of albumin variants with high affinity to FcRn could be observed using an immortalised cell line HMEC-1, which stably overexpressed human FcRn (Schmidt *et al.*, 2017). In contrast, albumin variants with low affinity to FcRn were trafficked into lysosomal compartments. Interestingly, FcRn distribution was also described to be predominantly linked to early endosomal compartments

suggesting potential interactions of FcRn and albumin within endosomal structures of endothelial cells (Antohe *et al.*, 2001; Ober *et al.*, 2004). Endocytosed IgG molecules were shown to bind FcRn in acidified EEA1-, Rab5-Rab4- and Rab11-positive endosomes and FcRn-dependent IgG recycling via Rab11-positive tubular and globular carriers was observed (Ward *et al.*, 2005). It is not known, if the trafficking of albumin follows a similar itinerary and, furthermore, there is still no direct evidence of albumin and FcRn co-localisation within endosomal structures of endothelial cells.

There is a substantial gap in knowledge of the FcRn-dependent albumin cell biology in endothelial cells. *In vivo* studies in mice using conditional FcRn-knockout in endothelial cells and bone marrow-derived cells ($Tie2^{cre}$) underline the importance of FcRn expression in the endothelium for maintaining high albumin serum concentrations, but the extent and the molecular mechanisms of FcRn-mediated albumin recycling in endothelial cells is not understood (Montoyo *et al.*, 2009). The two main reasons for lack of information on the cell biology of albumin uptake by endothelial cells are, first, the cell heterogeneity of the endothelium and, second, the absence of a reliable primary vascular endothelial cell model to decipher intracellular albumin trafficking (Potente and Mäkinen, 2017). Trafficking and recycling of albumin in endothelial cells has been predominantly investigated in immortalised cell lines or highly specialised endothelial cells originated from the placenta, umbilical vein or dermal microvasculature (Lambot *et al.*, 2006; Schmidt *et al.*, 2017; Larsen *et al.*, 2018; Azevedo *et al.*, 2020). These cellular model systems do not represent endothelial cells from the classic vasculature since immortalised endothelial cell lines are often derived from specialised vessels like the placenta or vessels from the blood-brain barrier and were shown to be phenotypically and functionally distinct to endothelial cells *in vivo* (Bouïs *et al.*, 2001).

A promising approach to circumvent this problem, is the generation of primary human vascular endothelial cell lines from circulating endothelial progenitor cells found in adult peripheral blood (Martin-Ramirez *et al.*, 2012). Although there have been early reports on endothelial cell outgrowth during culturing of peripheral

blood for periods of 2 – 4 weeks, it was long assumed that circulating endothelial cells (CECs) exhibit a senescent state with low proliferative capacity and were derived directly from the vessel walls and thus functioned as a biomarker for vascular injury (Asahara *et al.*, 1997; Lin *et al.*, 2000; Attia *et al.*, 2011). Indeed, it could be shown by investigating the origin of CECs in patients receiving bone marrow transplants that most of these endothelial cells (~ 95 %) were directly derived from the vessel walls of recipients. Nevertheless, about 5 % of the CECs were found to originate from bone marrow cells of the donor (Lin *et al.*, 2000). Surprisingly, these bone marrow-derived cells, in contrast to CECs from the blood vessels, showed high proliferative potential and gave rise to approximately 80 % of total blood outgrowth endothelial cells (BOECs) after four weeks of culture and, therefore, were considered endothelial progenitor cells (EPCs) (Lin *et al.*, 2000).

The origin of EPCs is not fully understood yet, but it is speculated that they are derived from circulating hemangioblasts as they exhibit a monocyte-like transcriptional and proteomic fingerprint (Choi *et al.*, 1998; Medina *et al.*, 2010). EPCs can further be divided into cellular subpopulations according to their proliferative capacity in culture and resemble the hierarchy of hematopoietic progenitor cells, which also have a hemangioblastic origin (Ingram *et al.*, 2004). This hierarchy could explain the differences in the lifetime, proliferative potential, and formation time of BOEC colonies amongst individual clones or donors. It is estimated that less than one cell per 1 x 10^6 nucleated peripheral blood cell represents EPCs possessing enough proliferative capacities to form stable endothelial outgrowth colonies (Reinisch *et al.*, 2009). In contrast to the “precursor” phenotype of EPCs, BOECs, also known as outgrowth endothelial cells (OECs), endothelial colony-forming cells (ECFCs) or late-outgrowth endothelial cells, obtained after culture display an endothelial-typical “cobblestone-like” morphology, express endothelial-specific proteins like VE-Cadherin (CD144), von Willebrand factor (vWF) as well as PECAM-1 (CD31) and are negative for the monocyte marker CD14 (Reinisch *et al.*, 2009; Martin-Ramirez *et al.*, 2012). Once established, BOEC cell lines have been reported to exhibit a stable endothelial-like phenotype across several passages and could be

expanded up to 10^{18}-fold (Martin-Ramirez *et al.*, 2012). Additionally, BOECs have been shown to promote *de novo* vessel generation *in vitro* and *in vivo* as well have been used in various gene transfer studies evaluating the therapeutic potential of BOECs in context of blood-related diseases or disorders like malaria and hemophilia A (Lin *et al.*, 2002; Hirschi *et al.*, 2008; Ecklu-Mensah *et al.*, 2018). Besides the therapeutic potential of BOECs *in vivo*, the generation and maintenance of a stable primary human vascular endothelial cell line isolated from adult peripheral blood could be valuable tool for investigating the FcRn-albumin cell biology in endothelial cells *in vitro* and decipher the role of the endothelium in albumin homeostasis.

In this chapter, I generated primary human vascular endothelial cell lines from peripheral blood, characterised the FcRn expression in endosomal compartments of these cells and tracked the intracellular fate of internalised albumin after uptake.

4.2: Results

4.2.1: Generation and characterisation of blood outgrowth endothelial cells (BOECs) isolated from human peripheral blood

For the generation of stable blood outgrowth endothelial cell (BOEC) lines, fresh peripheral blood from healthy donors was prepared, according to the protocol described in the methods section. Briefly, peripheral mononuclear cells (PBMCs) were isolated using Ficoll gradient centrifugation and seeded into collagen type I-coated T-75 flasks. PBMCs were cultured in endothelial growth factor-containing BOEC generation medium for up to four weeks and the appearance of endothelial-like cell colonies was monitored regularly.

In principle, the establishment of a BOEC line relies on the stimulation of circulating endothelial progenitor cells (EPCs) with high proliferative capacities by endothelial growth factors, including human epidermal growth factor (hEGF), vascular endothelial growth factor (VEGF), human fibroblast growth factor-beta

(hFGF-β) and R3-insulin-like growth factor-1 (R3-IGF-1), in the culture medium (Figure 4.1A). This rare cell population will eventually form endothelial cell colonies exhibiting cobblestone-like morphology after 14 – 28 days of culture. To date, only a few protocols for stable human BOEC generation have been described ranging from generation of single clones in 48-well plates to large-scale BOEC cultures in multi-layered cell factories (Reinisch *et al.*, 2009; Martin-Ramirez *et al.*, 2012; Ormiston *et al.*, 2015). Most of the established BOEC protocols have been designed for disease-associated studies and treatments, in which either single clone approaches are required for characterising endothelial cell-linked disorders or high BOEC numbers are essential to trigger *de novo* vessel formation *in vivo* after adoptive cell transfer. In this study I adapted the protocol for the generation of BOECs to meet the requirements for investigating FcRn-albumin cell biology in vascular endothelial cells (Figure 4.1B). The goal was to design a BOEC protocol which allowed a reliable and fast establishment of endothelial cell lines with high proliferative properties in T-75 flasks without the need of extensive passaging and expansion required in a single clone approach. Therefore, 10 x 10^6 isolated PBMCs were directly seeded into Collagen-I-coated T-75 flasks and cultured in FCS- and endothelial growth factor-rich BOEC generation medium to stimulate the propagation of EPCs. To maintain a sufficient supply of growth factors, the culture medium was replenished every 2 – 3 days.

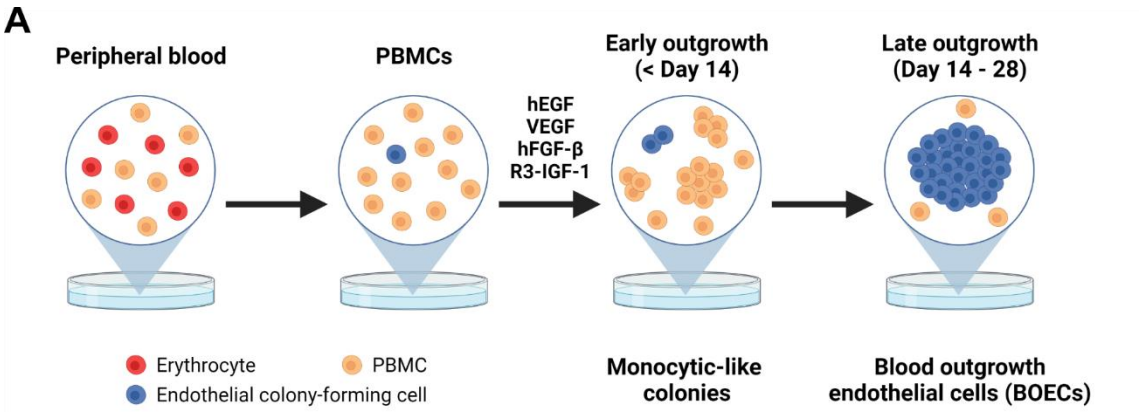
A
Peripheral blood
PBMCs
hEGF
VEGF
hFGF-β
R3-IGF-1
Early outgrowth
(< Day 14)
Late outgrowth
(Day 14 - 28)
Erythrocyte
PBMC
Endothelial colony-forming cell
Monocytic-like colonies
Blood outgrowth endothelial cells (BOECs)

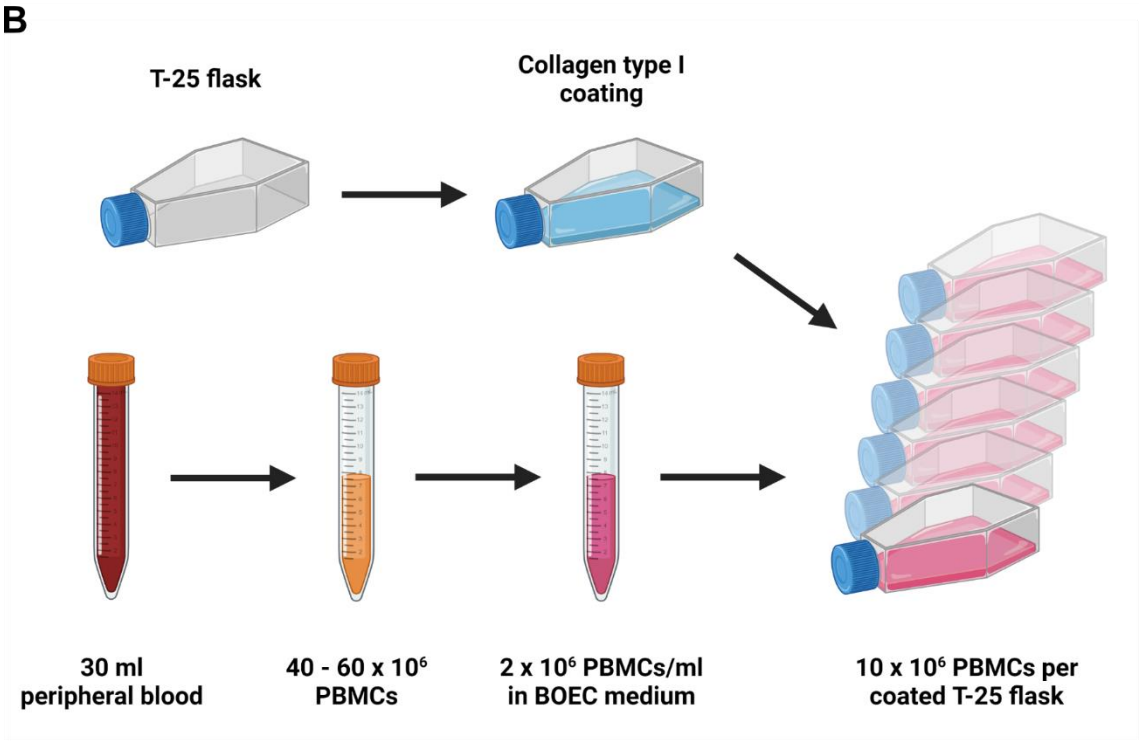
B
T-25 flask
Collagen type I coating
30 ml peripheral blood
40 - 60 x 10⁶ PBMCs
2 x 10⁶ PBMCs/ml in BOEC medium
10 x 10⁶ PBMCs per coated T-25 flask

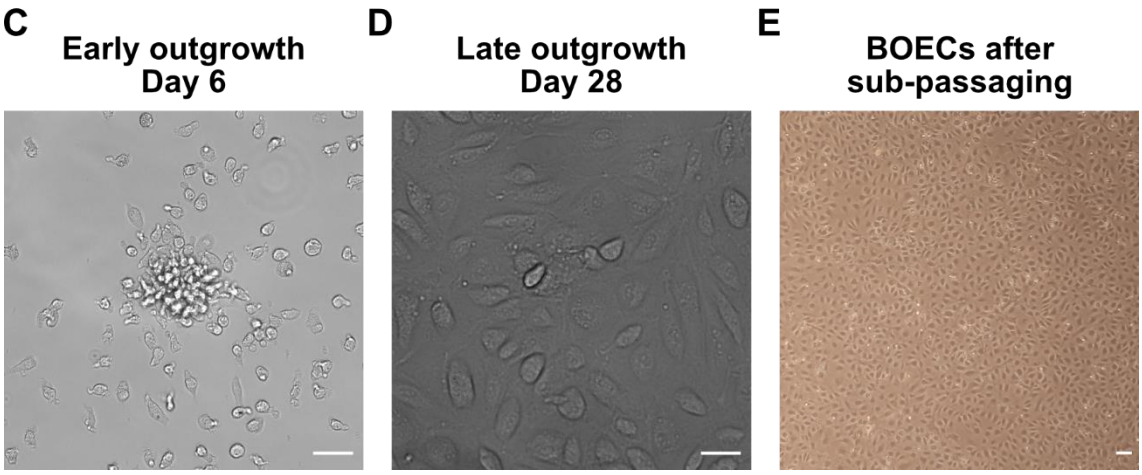
C
Early outgrowth Day 6
D
Late outgrowth Day 28
E
BOECs after sub-passaging

Figure 4.1: BOEC generation and morphology of blood outgrowth endothelial colonies
(A) Principle of the generation of BOEC lines from human peripheral blood. **(B)** Established protocol for the generation of stable BOEC lines from PBMCs using Collagen-coated T-25 flasks. The generation protocol was adapted from Martin-Ramirez *et al.* and Ormiston *et al.*(Martin-Ramirez *et al.*, 2012; Ormiston *et al.*, 2015). **(C-D)** Brightfield microscopy images of early **(C)** and late **(D)** outgrowth cell colonies obtained on day 6 or 28 of culture, respectively, using the established BOEC generation protocol. Scale bars represent 50 µm. **(E)** Brightfield microscopy image of a confluent established BOEC line exhibiting cobblestone-like morphology after sub-passaging. Scale bar represents 100 µm. Figures were created with BioRender.com.

The propagation of EPCs in the cultures led to visible endothelial outgrowth. Within the first two weeks of culture, early outgrowth colonies were observed compromised of a small number of cells (Figure 4.1C). However, these colonies tended to have a short half-life and failed to propagate into a stable cell line. Presumably, these early outgrowth cells arose from EPCs with low proliferative capacities and have been described to exhibit a monocytic phenotype rather than being “true” endothelial cells (Medina *et al.*, 2010). With extended culture periods of more than two weeks, dense and rapidly proliferating cell colonies with cobblestone-like morphology started to propagate in the culture flasks (Figure 4.1D). On Average, 2 – 3 of these colonies were observed per flask and emerged between days 14 and 28 of culture. A week after their initial occurrence, the radially spreading cell colonies reached a diameter of around 2 cm and were then passaged into Collagen-I-coated T-25 flasks. Two to three days after sub-passaging, the cells covered almost the whole area of the culture flask and exhibited endothelial-specific cobblestone-like morphology (Figure 4.1E). On reaching 70 – 80 % confluency, established BOEC lines were further passaged and cultured in Collagen-I-coated flasks or cryopreserved in liquid nitrogen.

To confirm the endothelial character of established BOEC lines, the expression of vascular endothelial markers was assessed using confocal fluorescence microscopy and flow cytometry (Figure 4.2). Vascular endothelial cadherin (VE-Cadherin or CD144) is a major regulator of endothelial integrity by regulating

homophilic adherens junctions between endothelial cells. In addition to maintaining and controlling endothelial cell contacts, CD144 plays a vital role in regulating other cellular processes in endothelial cells like cell proliferation, apoptosis and orchestrating growth factor responses; hence, it represents an essential marker for the endothelial phenotype (Harris and Nelson, 2010). The expression of CD144 was verified in the established BOEC lines by confocal fluorescence microscopy and flow cytometry using CD144-specific polyclonal antibodies (Figure 4.2A). Indeed, fluorescence microscopy confirmed the localisation of CD144 to the plasma membrane and tight junctions between individual BOECs. Furthermore, flow cytometric analyses of some of the BOEC lines revealed a single peak of CD144-positive cells, indicating a homologous population of BOECs exhibiting an endothelial phenotype. However, donor- and clone-dependent differences in CD144 expression of the established cell lines were observed ranging from 75 to 96 % of cells expressing CD144 (not shown). Established BOEC lines were analysed regularly for CD144 expression during sub-passaging and cell lines discarded once the percentage of CD144-positive cells dropped below 75 %.

To further analyse the presence of endothelial adherens junctions in BOEC lines, the expression of platelet endothelial cell adhesion molecule (PECAM-1 or CD31) was also assessed by confocal fluorescence microscopy (Figure 4.2B). CD31 is expressed at the cell surface of various immune cells, such as monocytes and B and T cells and is also found at intercellular junctions of endothelial cells, where it regulates the vascular permeability at endothelial cell borders and the attachment of leukocytes to the endothelium (Watt *et al.*, 1995). Co-staining of CD31 and CD144 revealed the co-localisation of both markers to the cell borders of BOECs (Figure 4.2B) and indicated an intimate contribution to adherens junctions.

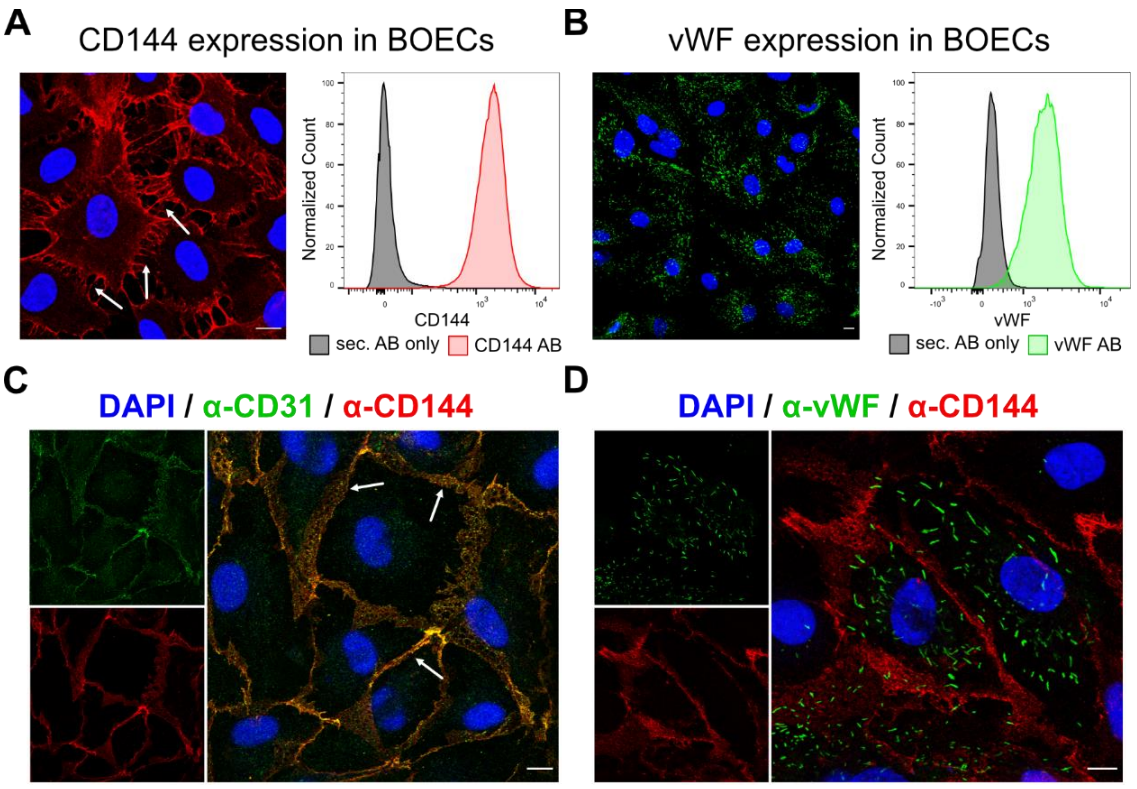

Figure 4.2: Expression of endothelial-specific markers in established BOEC lines

(A-D) Confluent monolayers of BOECs were prepared for immunofluorescence microscopy and flow cytometry, as described in the methods section, respectively. **(A-B)** BOECs were stained with either CD144 (red) **(A)** or intracellular vWF (green) **(B)** to assess the expression of endothelial-specific markers by flow cytometry. Cells were gated on single, live cells and the histograms are shown for CD144- (red) and vWF-specific (green) fluorescent signals. Control cells were stained using the respective secondary antibodies only (grey). **(C-D)** Confluent monolayers of BOECs were fixed with PFA or MeOH, as described in the methods section, and fixed cells were either stained for CD31 (green) and CD144 (red) **(C)** or vWF (green) and CD144 (red) **(D)**. Cell nuclei were visualised using DAPI (blue). White arrows indicate intracellular junctions between single BOECs. Scale bars represent 10 µm.

In addition to the staining for surface endothelial-specific cell markers of BOECs, intracellular von Willebrand factor (vWF) expression was evaluated in the BOEC lines by confocal fluorescence microscopy and flow cytometry (Figure 4.2C). The glycoprotein vWF is one of the main components of endothelial-specific storage organelles called Weibel-Palade bodies (WPBs), which exhibit a characteristic

rod-shaped morphology. Von Willebrand factor plays a crucial role in FVIII homeostasis and platelet adhesion upon vascular injury (Sadler, 1998). Von Willebrand factor was found to be expressed in over 95 % of BOECs as detected by vWF-specific signals by confocal microscopy and flow cytometry (Figure 4.2C). Confocal microscopy revealed the localisation of vWF to rod-shaped intracellular organelle structures suggesting the association of vWF with WPBs (Figure 4.2D). Co-staining with CD144, to define the cell boundary, verified the intracellular localisation of VWF in contrast to the membrane-bound surface molecule.

To assess whether intracellular vWF was associated with functional endothelial storage granules, BOECs were treated with phorbol-12-myristate-13-acetate (PMA), which is known to trigger release of WPBs in primary endothelial cells (Nightingale *et al.*, 2018). In BOECs treated with DMSO alone (carrier), vWF was localised to rod-shaped organelle structured like described above, which also stained with the tetraspanin CD63 (LAMP-3) (Figure 4.3). CD63 is used as an intracellular marker for late endosomes and lysosomes. However, in endothelial cells CD63 is also associated with WPBs (Vischer and Wagner, 1993). The co-localisation of vWF and CD63 indicates the presence of WPBs in BOECs.

The treatment of BOECs with 80 nM PMA led to the loss of intracellular vWF fluorescence and the disappearance of rod-shaped organelles (Figure 4.3). Furthermore, CD63 in PMA-treated cells appeared to be exclusively localised to globular endosomal structures in contrast to cigar-shaped organelles in the carrier control. PMA diminished intracellular vWF and WPB-associated CD63 fluorescence, however CD63 fluorescence was preserved and located to endosomal-like structures. These findings indicate the specific release of WPBs in PMA-treated BOECs. Collectively the observations confirm that BOEC lines I have established are able to form vWF- and CD63-positive WPB structures, which supports the endothelial character of these cell lines.

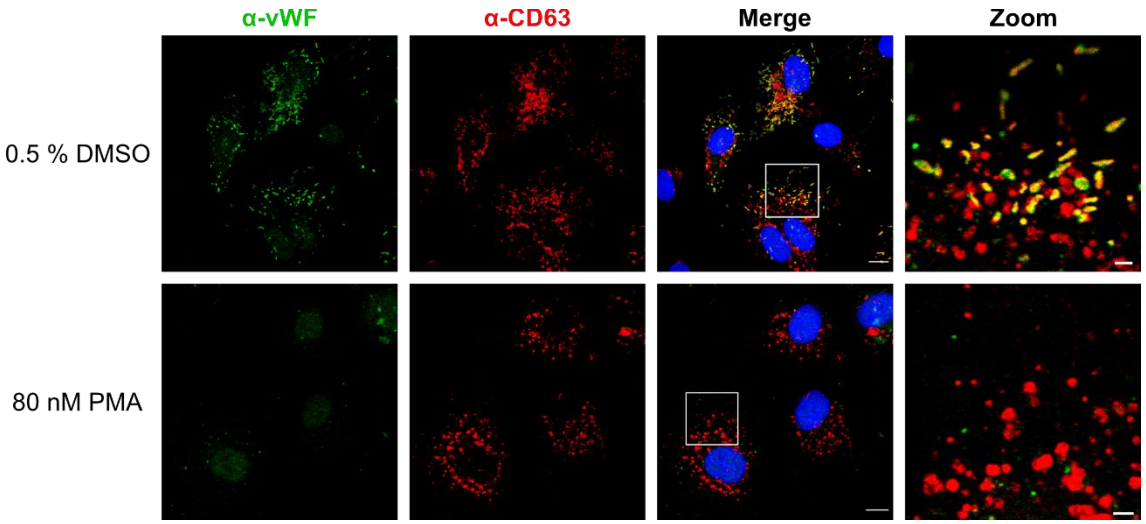

Figure 4.3: Release of vWF-positive Weibel-Palade bodies in BOECs upon PMA treatment
Cultured BOECs were treated with 0.5 % DMSO (carrier control) or 80 nM phorbol-12-myristate-13-acetate (PMA) for 20 minutes and subsequently fixed with MeOH. Cells were co-stained with anti-vWF (green) and CD63 (red) antibodies and nuclei were visualised using DAPI (blue). Scale bars represent 10 µm (Merge) or 2 µm (Zoom).

Taken together, a reliable protocol for the generation of stable BOEC lines suitable for several sub-passaging and cryopreservation was established. The BOEC lines generated were shown to homogeneously express the endothelial surface markers CD31 and CD144 and, moreover, the formation of vWF-positive WPBs bodies was observed. Therefore, these BOEC lines should represent a suitable cell model to study albumin-FcRn cell biology in primary human vascular endothelial cells.

4.2.2: Characterisation of endosomal compartments in BOECs

To study intracellular trafficking pathways in BOECs, firstly it was important to map the endosomal compartments and their morphology using endosomal markers. LAMP1 and CD63 are markers for late endosomes and lysosomes and show strong co-localisation of large punctate structures with the majority of

staining in close proximity to the cell nucleus in fixed BOECs (Figure 4.4A). Additionally, as discussed above, CD63 staining was detected in rod-shaped structures in the cell periphery (Figure 4.4A). To assess the relation of late endosomal structures with the Rab11a-positive recycling compartment, co-staining with site-specific antibodies, namely CD63 and Rab11a, was performed in fixed and permeabilised BOECs (Figure 4.4B). There was very little overlap between CD63 and Rab11a-positive compartments, which were both concentrated in the juxtanuclear position. In addition to the prominent occurrence in juxtanuclear position, tubulovesicular Rab11a-positive structures were present throughout the cytoplasm; however, they also did not co-localise with CD63-positive structures.

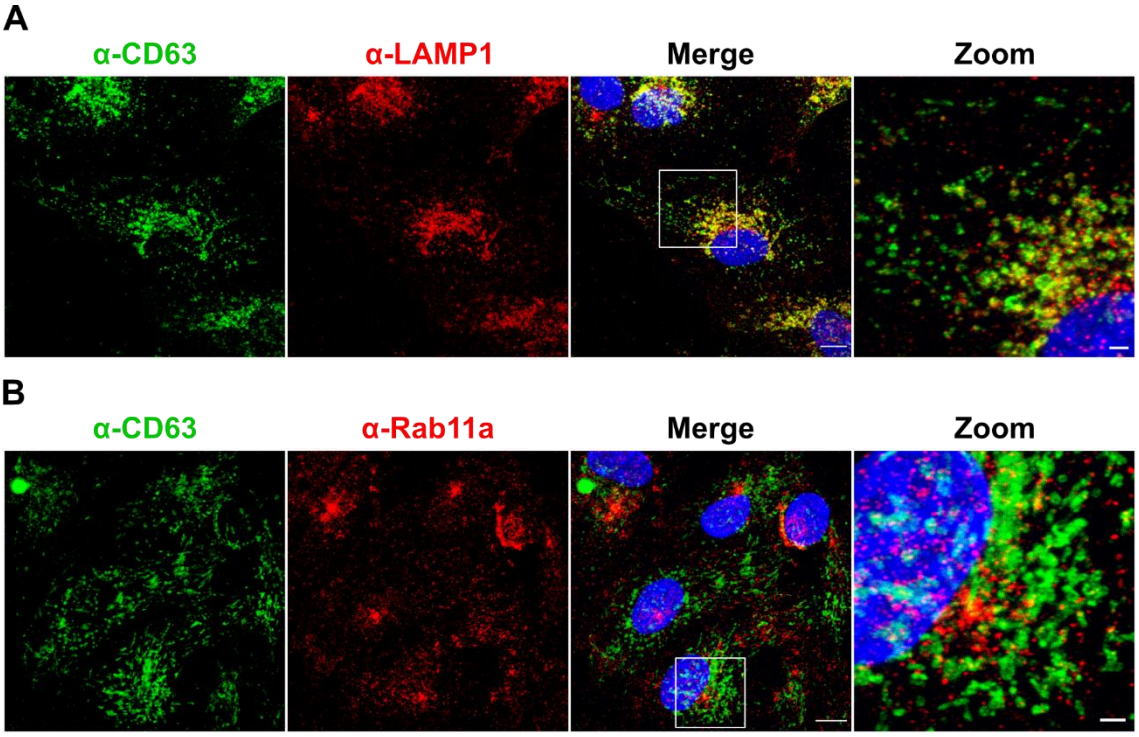

Figure 4.4: CD63-, LAMP1- and Rab11a-positive endosomal structures in fixed BOEC lines
Cultured BOECs were fixed with MeOH and co-stained for CD63 (green) and LAMP1 (red) **(A)** or CD63 (green) and Rab11a (red) **(B)** using site-specific antibodies. Nuclei were visualised using DAPI (blue). Scale bars represent 10 µm (Merge) or 2 µm (Zoom).

In addition to endosomal subpopulations, the Golgi apparatus plays an important role in the mediation and regulation of intracellular trafficking pathways (Ravichandran *et al.*, 2020). To evaluate the location of the Golgi apparatus to endosomal compartments, the *cis*-Golgi or *trans*-Golgi network (TGN) were stained with GM130- and golgin97-specific antibodies, respectively, and the spatial relationship with Rab11a-positive recycling endosomes assessed (Figure 4.5A-B). There was no overlap detected between the GM130 and Rab11a staining. However, Rab11a-positive recycling endosomes were localised in very close proximity to GM130-positive structures. Co-staining of Rab11a and the *trans*-Golgi marker, golgin97, showed distinct staining patterns with some overlap between both markers in the juxtanuclear position, indicating close association of recycling endosomes and the *trans*-Golgi network. Indeed, a close association between the *trans*-Golgi network and Rab11-positive endosomal structures has been described in various cell lines (Urbé *et al.*, 1993; Ullrich *et al.*, 1996; Welz *et al.*, 2014).

Lastly, the relationship of golgin97-positive structures and vWF-positive WPBs was assessed by confocal fluorescence microscopy (Figure 4.5C). The *trans*-Golgi network is an important site in the biogenesis of WPBs in endothelial cells. The *trans*-Golgi network is proposed to drive the sorting of vWF, the main component of WPBs, into the rod-shaped storage organelles of endothelial cells and thus facilitates the regulated secretion of completely assembled WPBs (van Mourik *et al.*, 2002). Indeed, some co-localisation between vWF- and golgin97-positive structures was observed at the edges of the *trans*-Golgi network (Figure 4.5C, zoom).

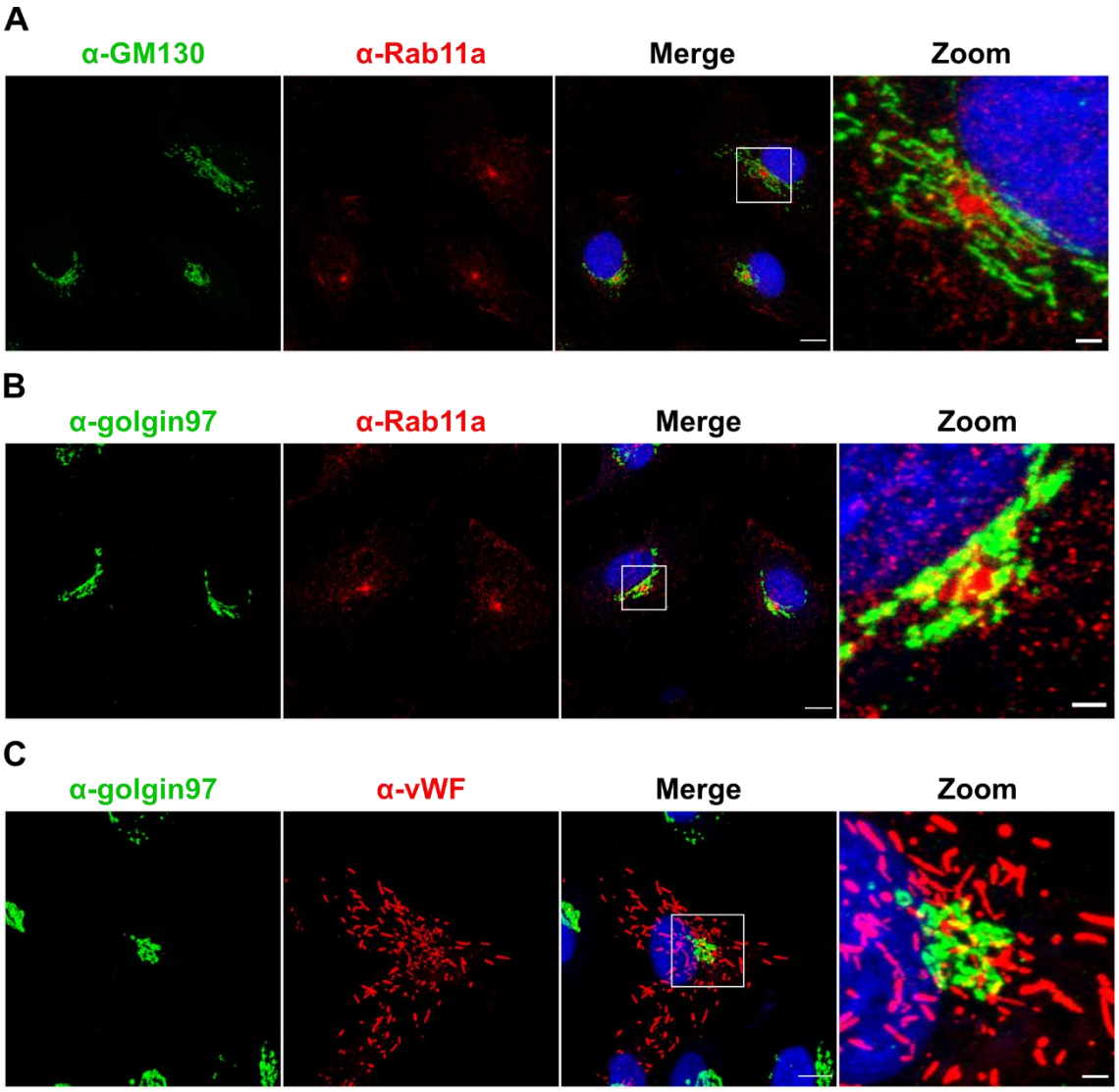

Figure 4.5: Association of Rab11a- and vWF-positive endosomal structures with the Golgi apparatus in fixed BOECs
Cultured BOECs were fixed with MeOH and co-stained for GM130 (green) and Rab11a (red) **(A)**, golgin97 (green) and Rab11a (red) **(B)** or golgin97 (green) and vWF (red) **(C)** using site-specific antibodies. Nuclei were visualised using DAPI (blue). Scale bars represent 10 µm (Merge) or 2 µm (Zoom).

Overall, the characterisation of intracellular compartments revealed some valuable spatial relationships between different endosomal compartments. LAMP1 and CD63 co-localised in globular structures around the nucleus but LAMP1 was excluded from rod-shaped CD63-positive structures in the cell periphery. CD63- and LAMP1-positive late endosomes and lysosomes were

clearly distinguishable from Rab11-positive recycling endosomes in the juxtanuclear positions. These Rab11-positive structures were closely associated with the Golgi-apparatus, especially the golgin-97-positive *trans*-Golgi network.

4.2.3: Expression and intracellular localisation of FcRn in BOECs

4.2.3.1: Endogenous FcRn expression and intracellular localisation in fixed BOECs

To investigate albumin-FcRn cell biology in primary vascular endothelial cells using BOECs, an essential prerequisite is to verify the expression of FcRn and determine its intracellular location in the established primary cell lines.

To detect FcRn in BOEC lines, cell lysates were prepared and FcRn analysed by Western Blot using a polyclonal antibody specific for human FcRn heavy chain (Figure 4.6A). Additionally, cell lysates of bone marrow-derived macrophages isolated from two different humanised mouse lines and a FcRn KO line were included for comparison. The humanised mouse models harbour a knock-out for murine FcRn and express the heavy chain of human FcRn transgenically under the control of the strong chicken β-actin promoter (hFcRn$^{Tg/Tg}$ line 276) or the native human FcRn promoter (hFcRn$^{Tg/Tg}$ line 32) (Chaudhury *et al.*, 2003; Roopenian *et al.*, 2003; Petkova *et al.*, 2006). Both mouse models have been established to decipher the FcRn-dependent cell biology *in vitro* and *in vivo*, especially in the context of half-life extension of IgG molecules or therapeutic antibodies (Roopenian *et al.*, 2003; Roopenian *et al.*, 2010; Avery *et al.*, 2016). Furthermore, it was shown that bone marrow-derived macrophages isolated from hFcRn$^{Tg/Tg}$ line 276 mice were able to facilitate FcRn-dependent recycling of human serum albumin *in vitro* (Chaudhury *et al.*, 2003; Toh *et al.*, 2020). Thus, these BMDM variants could be used as benchmarks to evaluate the FcRn expression level in BOECs. As expected, a band corresponding to the size of human FcRn α-chain of ~ 45 kDa was detected in extracts of BMDMs isolated from hFcRn$^{Tg/Tg}$ mice (line 276 and line 32), but not in FcRn KO BMDMs (Figure 4.6A). In addition, a FcRn-specific band of ~ 45 kDa was also observed

in cell lysates of BOECs confirming the endogenous expression of FcRn in these primary vascular endothelial cells. To compare the expression levels among the three FcRn-positive cell types, FcRn levels were quantified densitometrically and normalised using the respective GAPDH levels in the extracts (Figure 4.6B). Since the FcRn expression level in BMDMs from hFcRn$^{Tg/Tg}$ line 276 mice was found to be the highest, it was set to 100 % and compared with the expression level in the other lysates. Interestingly, FcRn expression in hFcRn$^{Tg/Tg}$ line 32 BMDMs was 39 % of the level in hFcRn$^{Tg/Tg}$ line 276 BMDMs, whereas FcRn expression in BOECs was approximately 15 % of the level in hFcRn$^{Tg/Tg}$ line 276 BMDMs. The difference in FcRn expression between hFcRn$^{Tg/Tg}$ line 32 BMDMs, expressing the transgene under the control of the endogenous FcRn promoter, and BOECs is consistent with human single cell RNA-seq data, where the expression of FcRn in macrophages has been reported to be more than twice that of endothelial cells (The Human Protein Atlas, 2021b). However, these findings reflected only rough estimates about the relative FcRn expression levels in BMDMs and BOECs and need to be confirmed by additional experimental repeats. Furthermore, it is advisory to quantify FcRn expression levels in hFcRn$^{Tg/Tg}$ BMDMs and cultured BOECs using more sensitive and robust methods such as RNAseq or mass spectroscopy.

To determine the intracellular localisation of FcRn in BOECs, endogenous FcRn was visualised using a polyclonal antibody against human FcRn. Fixed and permeabilised BOECs were stained and analysed by confocal fluorescence microscopy (Figure 4.6C). FcRn was associated with endosomal-like structures throughout the cytoplasm confirming the presence of endogenous FcRn in BOECs. Strikingly, FcRn was localised predominantly to enlarged endosomal structures with diameters up to 2 µm (white arrows). The association of FcRn with large endosomal structures was observed using either Triton-X-100- or saponin-based permeabilisation protocols (Figure 4.6C), which indicated that these large structures were not an artefact of the permeabilisation method.

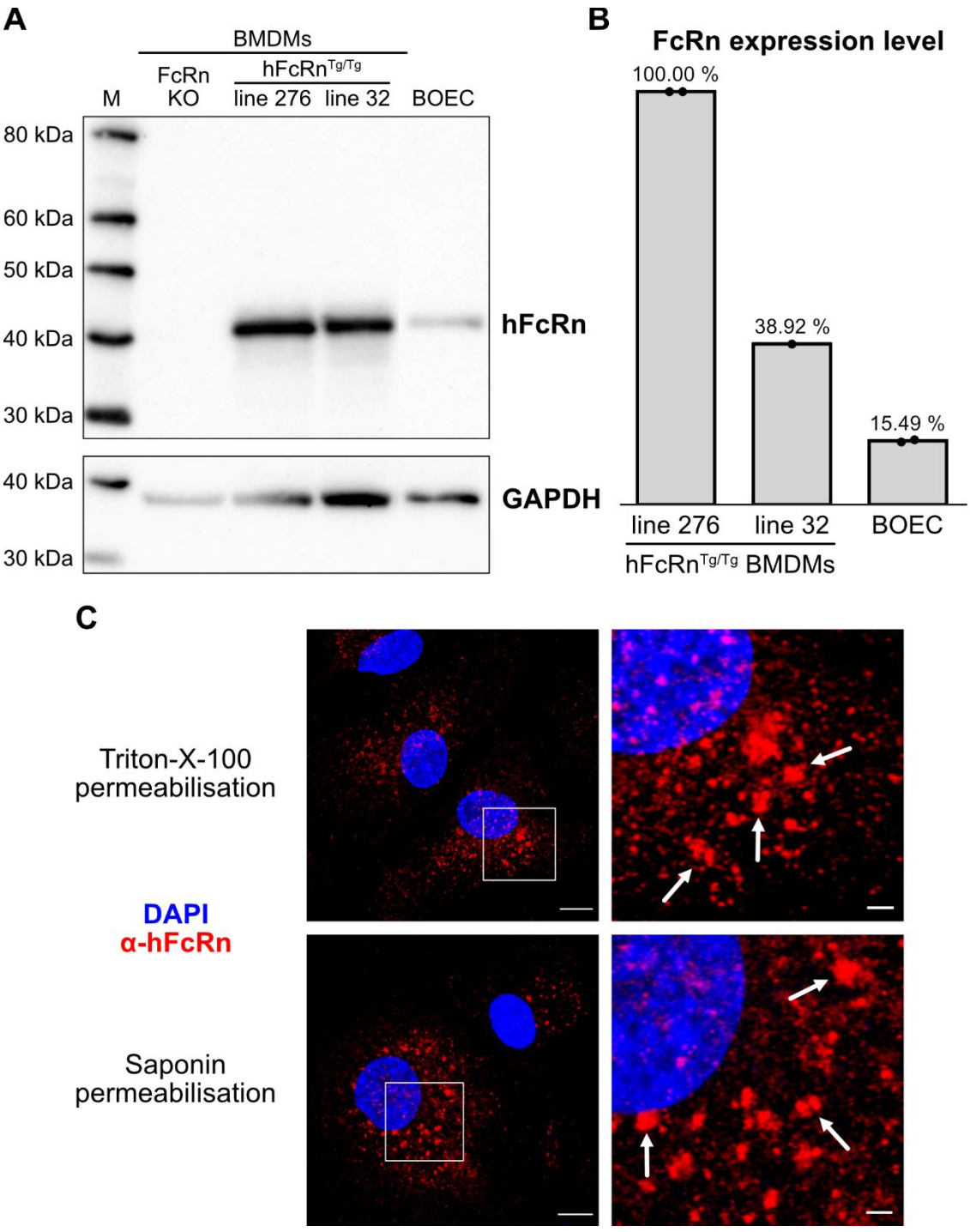

Figure 4.6: Endogenous FcRn expression in established BOEC lines
(A) BMDMs isolated from FcRn KO, hFcRn$^{Tg/Tg}$ line 276 or hFcRn$^{Tg/Tg}$ line 32 mice as well as cultured BOECs were lysed, and Western Blot analysis was performed, as described in the methods section. The membrane was probed with antibodies against human FcRn or GAPDH and HRP-conjugated secondary antibodies. Chemiluminescence was detected using a ChemiDoc™ system (BioRad). The marker line (M) was loaded with MagicMark™ Protein Standard (ThermoFisher Scientific). **(B)** Densitometric analysis of detected bands specific

for human FcRn. FcRn levels were normalised to detected GAPDH levels and the quantified FcRn level in lysates from hFcRn$^{Tg/Tg}$ line 276 BMDMs was set to 100 %. Percentages of FcRn levels are shown above the respective columns. FcRn levels for hFcRn$^{Tg/Tg}$ line 276 cells and BOECs were quantified in two independent experiments, the FcRn level in hFcRn$^{Tg/Tg}$ line 32 cells was quantified in a single experiment. **(C)** BOECs were fixed with TCA and permeabilised with 0.1 % Triton-X-100 or 0.05 % Saponin. Cells were stained for human FcRn (red) and cell nuclei visualised with DAPI (blue). Scale bars represent 10 µm (left images) or 2 µm (right images).

To identify the FcRn-positive endosomal structures in BOECs, co-staining for FcRn and the early or late endosomal markers EEA1 (Figure 4.7) and CD63 (Figure 4.8), respectively, was performed.

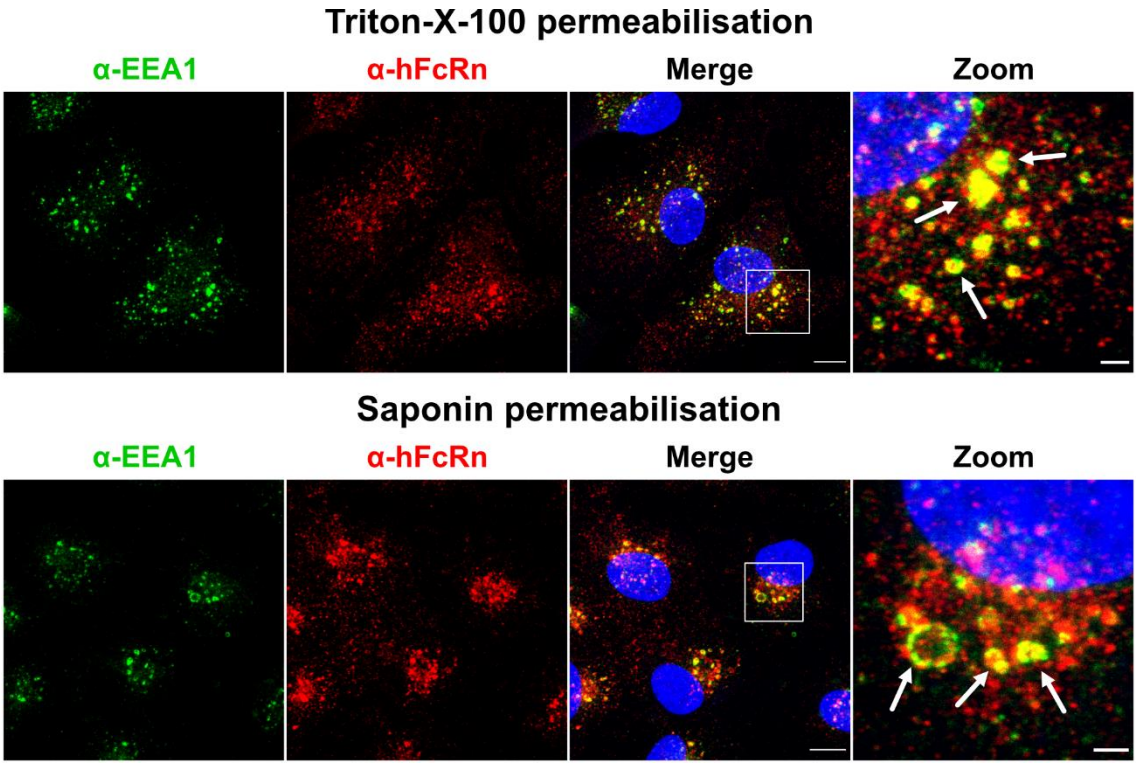

Figure 4.7: Localisation of endogenous FcRn to EEA1-positive endosomal structures in fixed BOECs
Cultured BOECs were fixed with TCA and permeabilised with 0.1 % Triton-X-100 or 0.05 % Saponin. Cells were co-stained for EEA1 (green) and human FcRn (red) and cell nuclei visualised with DAPI (blue). Scale bars represent 10 µm (Merge) or 2 µm (Zoom).

FcRn co-localised extensively with EEA1-positive early endosomal structures in BOECs. The co-localisation of both molecules was consistent using two different permeabilisation detergents, Triton-X-100 and Saponin, confirming the association of FcRn with early endosomes (Figure 4.7). There was heterogeneity of the size of FcRn- and EEA1-positive structures, with some structures having diameters up to 2 µm (white arrows), suggesting the presence of FcRn, not only in early endosomes but also early macropinosomes, which are positive for EEA1, in BOECs.

Co-staining with CD63 revealed no detectable overlap with FcRn indicating the absence of the receptor in late endosomal and lysosomal compartments (Figure 4.8).

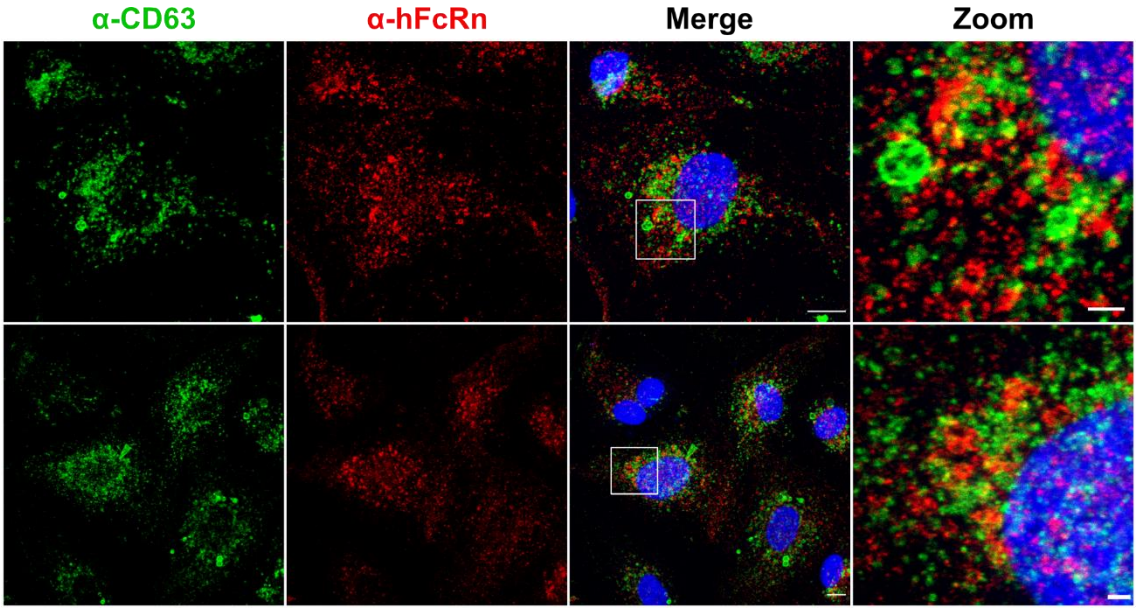

Figure 4.8: Localisation of endogenous FcRn to CD63-positive endosomal structures in fixed BOECs
Cultured BOECs were fixed with MeOH. Cells were co-stained for CD63 (green) and human FcRn (red) and cell nuclei visualised with DAPI (blue). Scale bars represent 10 µm (Merge) or 2 µm (Zoom).

Studies on the FcRn distribution in immortalised endothelial cell lines have reported FcRn to be associated with Rab11-positive recycling endosomes (Ward *et al.*, 2005). However, I was unable to determine the co-localisation of FcRn and Rab11-positive compartments using site-specific antibodies because the particular antibodies required different fixation protocols.

Collectively, these data confirmed the expression of endogenous FcRn in primary endothelial BOEC lines and revealed the localisation of FcRn to enlarged EEA1-positive endosomal structures with diameters up to approximately 2 µm. In contrast, FcRn showed no overlap with CD63-positive late endosomes suggesting the absence of FcRn in the late endosomal and lysosomal pathway.

4.2.3.2: Transient gene transfer protocols for inducing FcRn-mCherry expression in BOEC lines

The intracellular localisation of endogenous FcRn in BOECs can be identified in fixed cells with the use of FcRn-specific antibodies and endosomal markers. However, the expression of a fluorescently tagged FcRn would allow the direct observation of transgenic FcRn in live BOECs without fixation or permeabilisation procedures. Therefore, gene transfer protocols were investigated to induce the transient expression of mCherry-labelled FcRn in cultured BOECs.

Transient transfection using Lipofectamine™ 3000 was established to introduce the FcRn-mCherry plasmid, pIRES-B2M-FcRn_mCherry, into BOECs. This bicistronic plasmid allows the simultaneous expression of the human FcRn heavy chain labelled with mCherry at the C-terminus and the human FcRn light chain β-2-microglobulin (B2M) to guarantee proper association, and ER export, of the two FcRn subunits. For the verification of the successful transfection of FcRn-mCherry into BOECs, fixed cells were initially analysed by confocal fluorescence microscopy for FcRn-mCherry fluorescence (Figure 4.9).

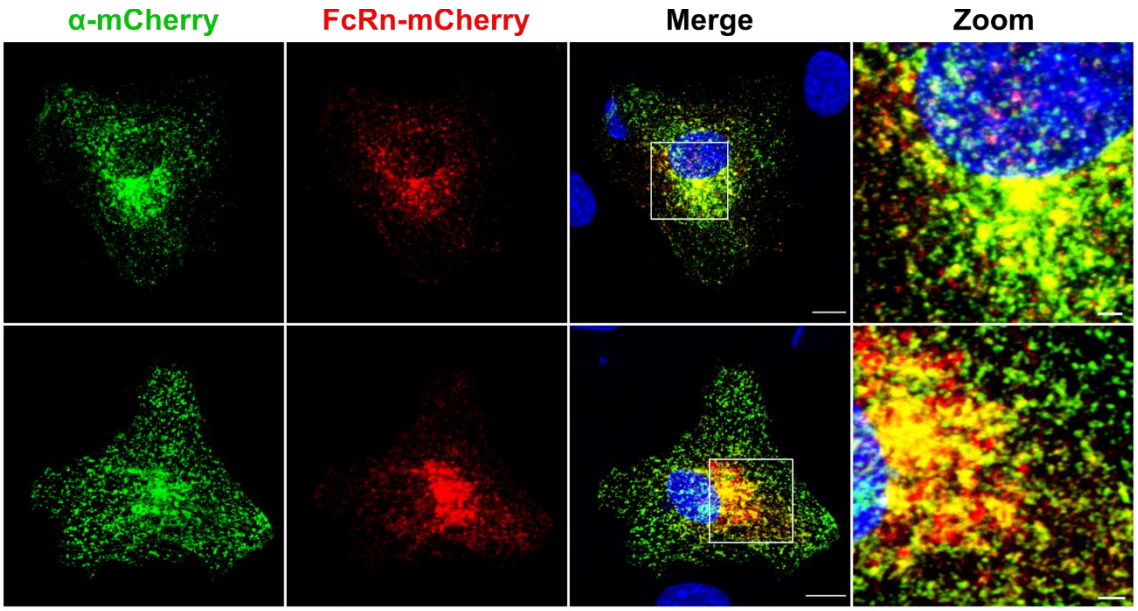

Figure 4.9: Transient transfection of FcRn-mCherry in cultured BOECs
BOECs were transfected with pIRES-B2M-FcRn_mCherry (red) and cultured for 48 hours to allow expression of the transgene. Cells were fixed with PFA and stained with a mCherry-specific antibody (green). Cell nuclei were visualised using DAPI (blue). Scale bars represent 10 µm (Merge) or 2 µm (Zoom).

BOECs exhibited mCherry fluorescence after transfection indicating the successful gene transfer of FcRn-mCherry into the primary cell line. The use of a polyclonal mCherry-specific antibody further confirmed the expression of the fluorescent-labelled FcRn construct (Figure 4.9). Both fluorescent signals showed a significant overlap. FcRn-mCherry was predominantly localised to juxtanuclear organelles resembling the typical morphology of Rab11-positive recycling endosomes or the Golgi apparatus. In addition to the prominent localisation to juxtanuclear organelles, FcRn-mCherry was also detected in endosomal structures throughout the cell periphery. This is supported by the fluorescence obtained with the use of anti-mCherry antibody, whereas the FcRn-mCherry fluorescence in the cell periphery was weak. The localisation of FcRn-mCherry to these peripheral and large endosomal structures was consistent with the intracellular distribution of endogenous FcRn in BOECs described above.

Nevertheless, two major technical issues were identified from the transient transfection of BOECs. Firstly, the transfection of BOECs was very inefficient with less than 1 % of cells transfected, highlighting a difficulty in transfecting BOEC lines. Secondly, the transgenic expression of FcRn-mCherry under the control of the relatively strong CMV promoter is a potential concern as it may lead to an altered intracellular distribution of the transgenic fusion protein.

To increase the percentage of cells expressing the heterogenous fusion protein and to moderate the level of expression of FcRn-mCherry in BOECs, the open reading frames encoding for β_2-microglobulin and FcRn-mCherry were introduced into the plasmid backbone FUGW, suitable for the production of lentiviral particles (Chapter 3). The expression of the transgenes in FUGW is under the control of the constitutive UbC promoter, which has been described to drive low ectopic gene expression compared to the CMV promoter in most mammalian cells (Qin *et al.*, 2010). Earlier studies on BOECs isolated from human peripheral blood have described the efficient transient gene transfer of plasmids using lentiviral transduction protocols (De Meyer *et al.*, 2006; Coppens *et al.*, 2013).

Lentiviral particles containing the FUGW-B2M-FcRn_mCherry plasmid were generated and cultured BOECs were transduced with different amounts of concentrated lentivirus over a 24-hour period. After additional 24 hours to allow sufficient expression of the transgene in transduced BOECs, cell lysates were analysed for the presence of FcRn-mCherry fusion protein by Western Blot (Figure 4.10A). Using a polyclonal antibody directed against the heavy chain of human FcRn, a band corresponding to the size of endogenous FcRn α-chain of approximately 45 kDa was detected in both non-transduced and transduced cells. In lysates of BOECs transduced with 10, 20 or 30 µl of concentrated virus, but not in untransduced cells, a band with the size of ~ 72 kDa was also detected, corresponding to the predicted size of the FcRn-mCherry fusion protein. To confirm the identity of 72 kDa bands, membranes were stripped and probed with an antibody directed against mCherry. The anti-mCherry antibody detected a band of 72 kDa in all transduced cells (Figure 4.10A); in addition, faint bands

corresponding to the size of mCherry (27 kDa) were also present in lysates of transduced BOECs indicating some cleavage of the FcRn-mCherry fusion protein either in the BOECs or in the process of sample preparation under denaturing conditions.

The blots were quantified by densitometric analysis to estimate the relative levels of FcRn-mCherry fusion protein to the total FcRn pool (Figure 4.10B). Transduction of BOECs with FcRn-mCherry expressing lentivirus led to a 1.5-fold increase of total FcRn levels compared to wildtype BOECs with no differences between BOECs transduced with 10, 20 or 30 µl concentrated lentivirus. In transduced cells, total FcRn levels increased to approximately 1.5-fold and ~ 38 % of the total FcRn pool consisted of transgenic FcRn-mCherry (Figure 4.10B).

Transduced live BOECs were analysed by confocal microscopy to estimate the transduction efficiency and evaluate intracellular distribution of FcRn-mCherry (Figure 4.10C). BOECs transduced with 10 µl lentivirus showed >90 % positive cells for FcRn-mCherry fluorescence, indicating a very high transduction efficiency. In untransduced BOECs only background fluorescence levels were detected. In line with the distribution of endogenous FcRn, FcRn-mCherry was localised to endosomal structures throughout the cell periphery reaching diameters up to 2 µm (Figure 4.10C, indicated by white arrows). FcRn-mCherry was also found to be associated with tubular transport carriers emerging from globular endosomal structures in transduced live cells (indicated by sky blue arrows) (see also Section 4.2.3.3).

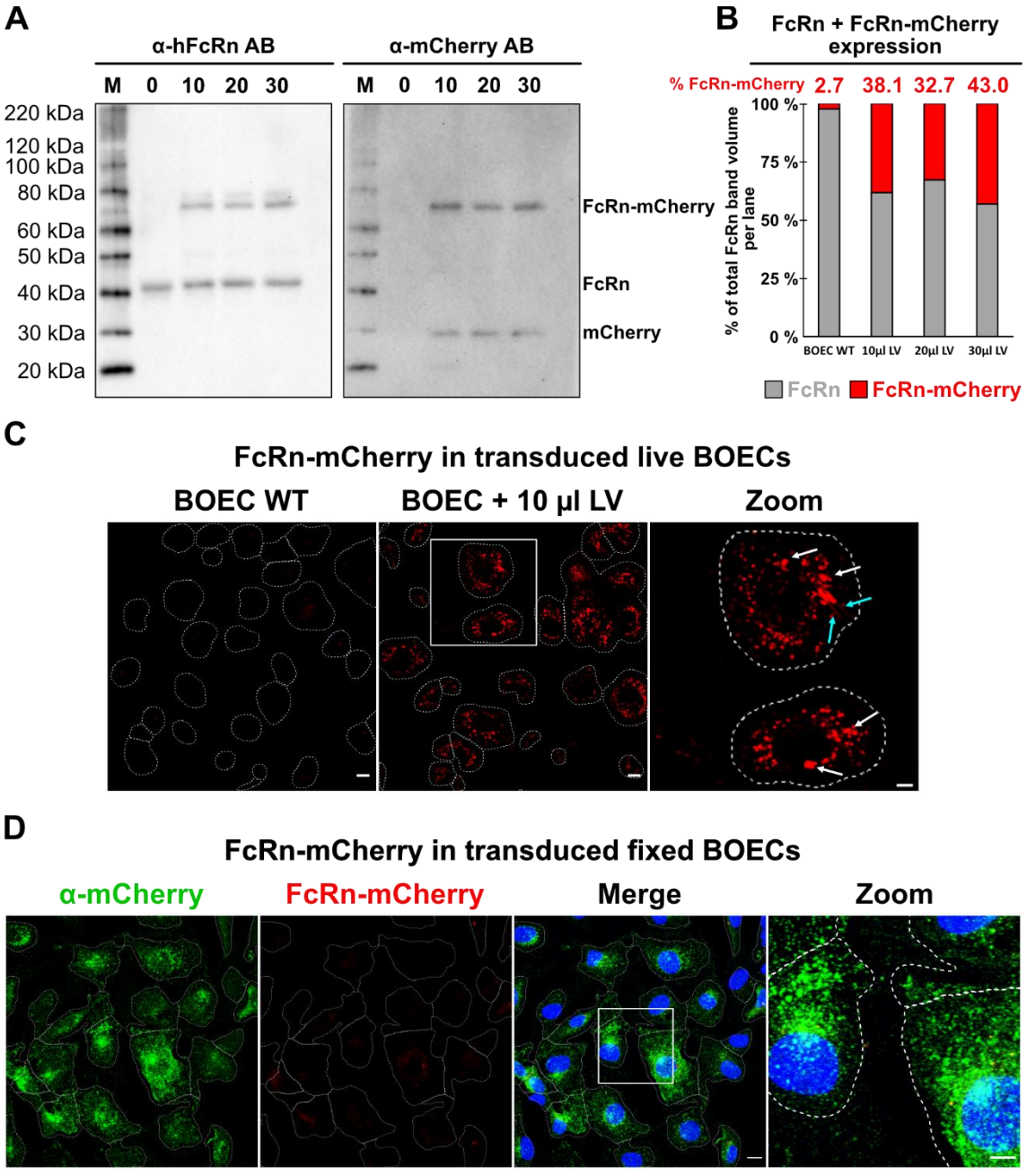

Figure 4.10: Lentiviral transduction of FcRn-mCherry in cultured BOECs
(A-D) BOECs were transduced with 0, 10, 20 or 30 µl of lentivirus containing pFUGW-B2M-FcRn_mCherry (red) for 24 hours. Remaining lentiviral particles were washed away and cells were allowed expressing the transgene for additional 24 hours. **(A)** Transduced BOECs were lysed and proteins resolved by SDS-PAGE using a 4 – 12 % gradient Bis-Tris gel. Separated proteins were transferred onto PVDF membranes and probed with an antibody against human FcRn and an HRP-conjugated secondary antibody. Chemiluminescence was detected using a ChemiDoc™ system. After detection, membranes were stripped and reprobed with an anti-mCherry and a suitable HRP-conjugated secondary antibody to detect mCherry-specific chemiluminescence. The marker line (M)

was loaded with MagicMark™ Protein Standard. **(B)** Densitometric analysis of detected bands specific for human FcRn and FcRn-mCherry in cell lysates of transduced BOECs. Total FcRn levels were quantified by adding up the densities of FcRn-specific bands detected by the anti-FcRn antibody. The total FcRn level of untransduced cells was set to 1. Additionally, the ratio of the FcRn- and FcRn-mCherry detected by the anti-FcRn antibody was calculated. **(C)** Transduced live BOECs were imaged at 37 °C and 5 % CO_2 with a FV3000 Olympus confocal microscope. Enlarged FcRn-positive endosomal structures are indicated by white, tubular extensions by sky blue arrows. **(D)** Transduced BOECs were fixed with PFA and stained with a mCherry-specific antibody (green). Cell nuclei were visualised using DAPI (blue). Images in **(D)** show maximum projections of whole cell z-stacks. Scale bars represent 10 µm or 5 µm (Zoom).

To confirm the observations of successful FcRn-mCherry transduction and localisation in BOECs, transduced cells were fixed and FcRn-mCherry fluorescence examined by confocal fluorescence microscopy (Figure 4.10D). Only a low fluorescent signal corresponding to FcRn-mCherry expression was detected in transduced and fixed BOECs (Figure 4.10), presumably due to the low expression levels of the transgene using lentiviral transduction in comparison to transient transfection of FcRn-mCherry (Figure 4.9). However, by using an antibody directed against mCherry, the FcRn-mCherry fusion protein was readily detected in fixed BOECs. The intracellular localisation of mCherry-positive structures in transduced BOECs resembled the distribution observed in transfected cells (Figure 4.9).

Taken together, these data demonstrate successful lentiviral-based expression of FcRn-mCherry fusion protein in primary BOEC lines. The FcRn pool in transduced BOECs consisted of approximately one third the transgenically introduced FcRn-mCherry and two thirds the endogenous FcRn. This system provides a strategy for direct observation of FcRn-mCherry localisation in live cells.

4.2.3.3: Dynamic FcRn trafficking in live BOECs

To visualise the dynamics of intracellular FcRn trafficking in BOECs, live fluorescence microscopy using FcRn-mCherry transduced cells was carried out and images of three different cells are shown in Figure 4.11.

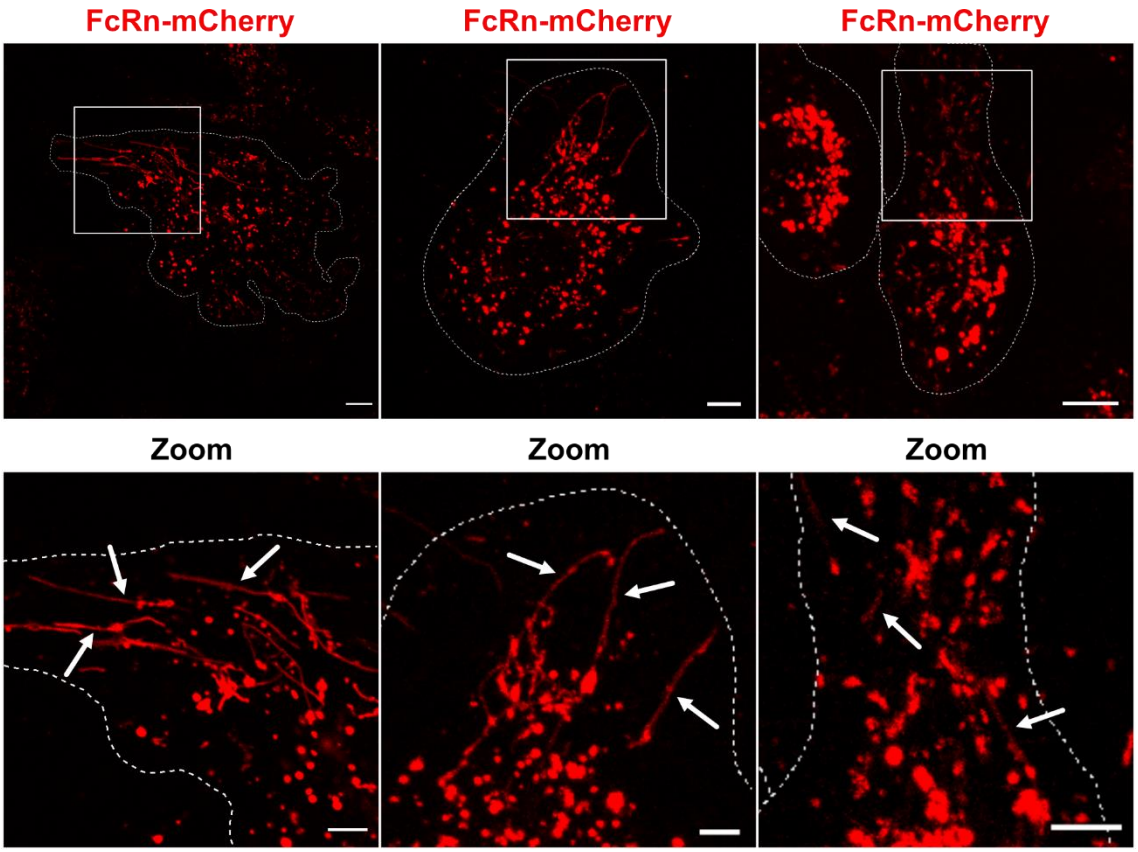

Figure 4.11: Live cell imaging of FcRn-mCherry transduced BOECs
BOECs were transduced with 10 µl lentivirus containing pFUGW-B2M-FcRn_mCherry (red) for 24 hours. Remaining lentiviral particles were washed away and cells were allowed expressing the transgene for additional 24 hours. Live BOECs were imaged at 37 °C and 5 % CO_2 with a FV3000 Olympus confocal microscope. White arrows are indicating FcRn-mCherry-positive tubules emerging from endosomal structures. Cell boundaries are indicated by dotted lines. The far right images represent the maximum projection of a whole cell z-stack. Scale bars represent 10 µm (FcRn-mCherry) or 5 µm (Zoom).

The FcRn-mCherry fusion protein was predominantly localised to enlarged, globular structures throughout the cytoplasm of transduced cells. Many of these structures reached up to a diameter of 2 µm and suggested the association of the FcRn-mCherry transgene with macropinosomes. Interestingly, FcRn-mCherry was not only localised to these endosomal compartments but also found in tubular transport carriers emerging from these large globular structures (indicated by white arrows). These tubular carriers were up to 20 µm long, 0.5 – 0.6 µm in diameter and appeared to be directed towards the edges of the cell. Many tubular carriers had a length of around 2 – 5 µm. To further assess the dynamics and direction of these FcRn-mCherry-positive tubular transport carriers, a time series of single transduced BOECs were recorded and single tubular events followed over time (Figure 4.12).

Following these FcRn-mCherry-positive structures in transduced BOECs over a time series revealed dynamic trafficking of FcRn-mCherry-positive tubular transport carriers towards the cell periphery (Figure 4.12A). Within a time span of 2 minutes, the FcRn-mCherry-positive tubular structures progressed up to 30 µm within the BOEC indicating highly dynamic transport carriers bearing FcRn-mCherry within the endosomal network.

To further confirm the dynamic trafficking of FcRn-mCherry-positive tubular transport carriers, the itinerary of these endosomal structures was analysed within shorter time intervals during a continuous acquisition timeframe (Figure 4.12B). Again, highly dynamic movement of these tubular transport carriers directed to the outer perimeter of the cell was observed. Within the 23 seconds observation frame, FcRn-mCherry-positive tubules moved about 10 µm within the cytoplasm of transduced BOECs corresponding to a velocity of approximately 0.43 µm/s.

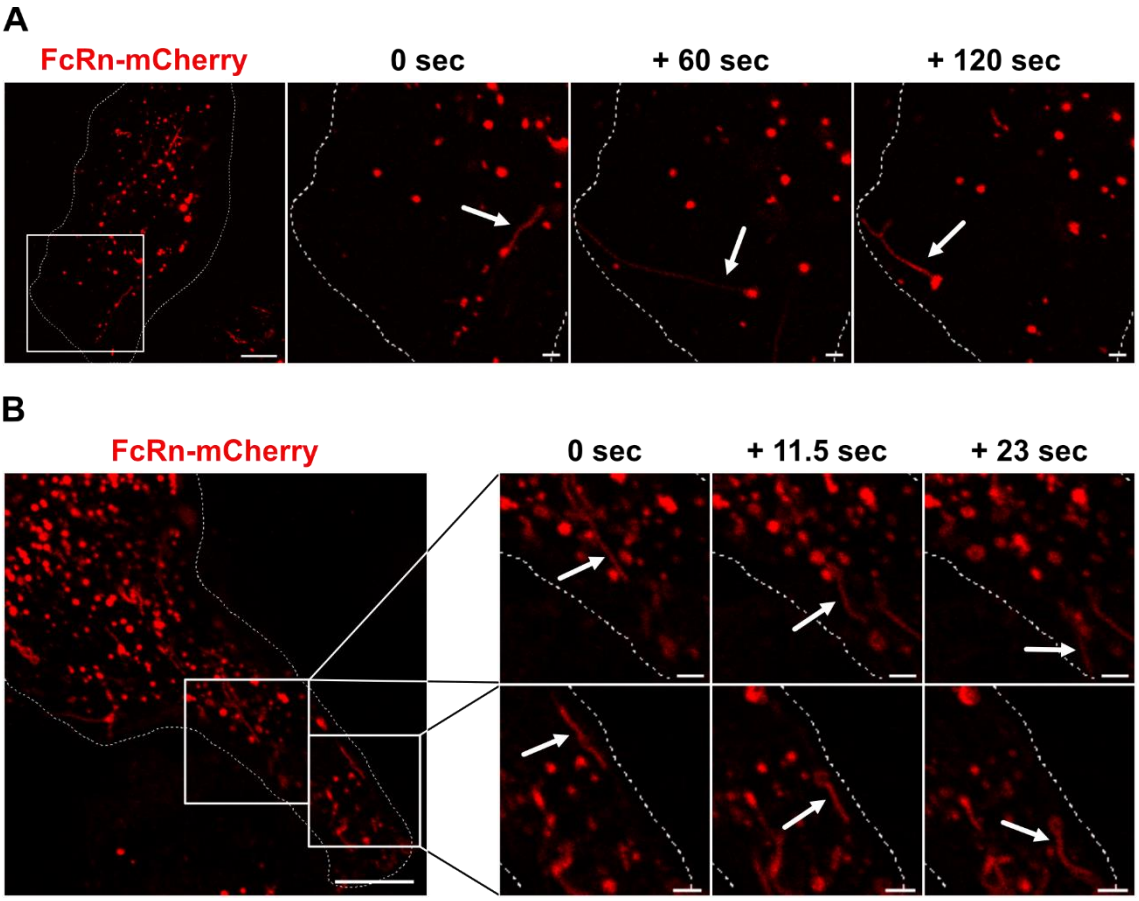

Figure 4.12: Dynamic tubular trafficking of FcRn-mCherry in transduced live BOECs
(A-B) BOECs were transduced with 10 µl lentivirus containing pFUGW-B2M-FcRn_mCherry (red) for 24 hours. Remaining lentiviral particles were washed away and cells were allowed expressing the transgene for additional 24 hours. Live BOECs were imaged at 37 °C and 5 % CO_2 with a FV3000 Olympus confocal microscope. Time lapses of live cells were recorded with a pause of 60 seconds **(A)** or continuously **(B)**. Three representative frames are shown for both time lapses. Cell boundaries are indicated by dotted lines. Scale bars represent 10 µm (original images) or 2 µm (zoomed frames).

Taken together, the transduction of FcRn-mCherry into BOEC lines and subsequent live imaging revealed a tubulovesicular endosomal network facilitating highly dynamic FcRn trafficking in primary vascular endothelial cells. FcRn-mCherry-positive tubular transport carriers emerging from enlarged globular endosomes were trafficked towards the edges of the cell.

4.2.3.4: Association of FcRn-mCherry with Rab11a-positive compartments in live BOECs

As described above, endogenous FcRn in BOECs was predominantly localised to EEA1-positive but not to CD63-positive endosomes. However, the association of FcRn with Rab11-positive recycling endosomes could not be evaluated in fixed cells due to the lack of reliable antibodies. Therefore, the established gene transfer protocols were used to introduce Rab11a-GFP in BOECs to allow direct observation of Rab11-positive recycling endosomes in transfected cells (Figure 4.13A). Fluorescent-labelled transferrin, which is known to localise to recycling endosomes, was used to confirm the morphology for recycling endosomal structures in transfected live BOECs. Indeed, Rab11a-GFP and transferrin-AF568 highly co-localised in transfected BOECs confirming that both molecules were present in recycling endosomes. Furthermore, transferrin and Rab11a were predominantly concentrated in a juxtanuclear position and associated with heterogeneous tubular and globular structures across the cell periphery. This phenotype is in line with the morphology of Rab11-positive structures in most cell types. More importantly, these results confirmed the localisation of transferrin to Rab11-positive structures and justified the use of fluorescent-labelled transferrin as a marker for recycling endosomes in BOECs; transferrin-AF568 will mark recycling endosomes in the entire cell population whereas Rab11a-GFP will only label a few cells given the poor transfection efficiency of BOECs. Since FcRn is labelled with mCherry, transferrin-AF488 was used for the efficient marking of recycling endosomes in transduced BOECs (Figure 4.13B).

To evaluate the association of FcRn with transferrin-labelled recycling endosomes in live BOECs, FcRn-mCherry-transduced BOECs were pulsed with transferrin-AF488 for 15 minutes and the co-localisation of both molecules assessed (Figure 4.13B). Throughout different timepoints after the transferrin-pulse, no co-localisation of both molecules was observed. Especially in the cell periphery, FcRn-mCherry and transferrin-AF488 were associated with distinct endosomal structures. However, there was some degree of overlap between

FcRn- and transferrin-positive structures in the juxtanuclear region. FcRn-positive tubules (indicated by white arrows) were observed to emerge from the perinuclear transferrin-positive structure, which presumably represented the main body of Rab11-positive recycling endosomes next to the microtubule organising centre (MTOC). Co-localisation of FcRn and transferrin was only observed in these tubular extensions but not in the centre of the transferrin-positive structure in juxtanuclear position. These data suggest that only low levels of FcRn are associated with recycling endosomes of BOECs.

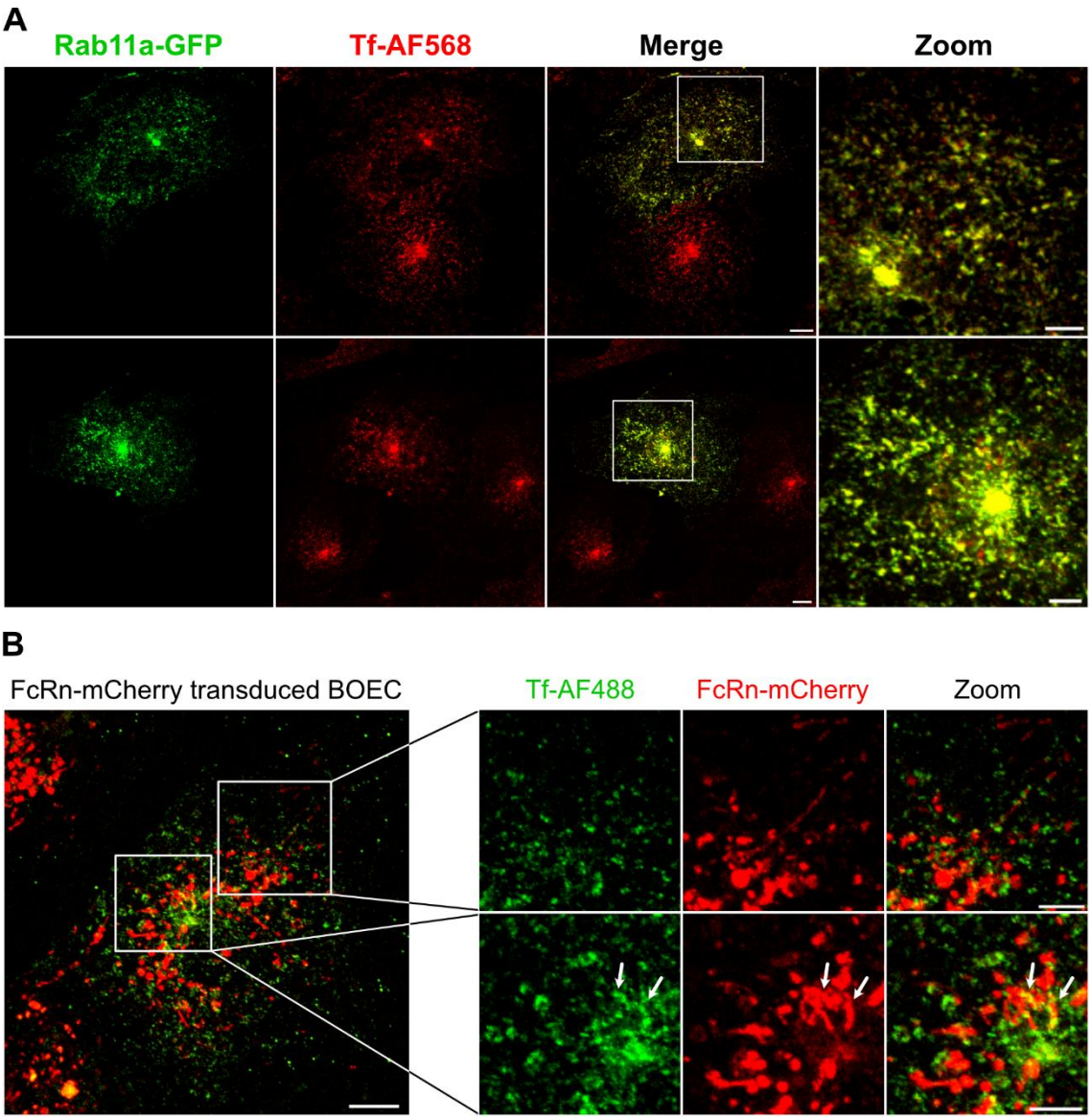

Figure 4.13: Association of transferrin-positive recycling endosomal compartments with FcRn-mCherry in transduced live BOECs
(A) BOECs were transfected with a Rab11a-GFP-expressing plasmid (green) using Lipofectamine3000™. After 48 hours, cells were pulsed for 15 minutes with Alexa Fluor®-568-labelled transferrin (Tf-AF568, red) at 37 °C. **(B)** BOECs were transduced with 10 µl lentivirus containing pFUGW-B2M-FcRn_mCherry (red) for 24 hours. Remaining lentiviral particles were washed away and cells were allowed expressing the transgene for additional 24 hours. Transduced cells were pulsed for 15 minutes with Alexa Fluor®-488-labelled transferrin (Tf-AF488, green) at 37 °C. **(A-B)** Excess fluorophores were washed away and transfected or transduced BOECs were imaged at 37 °C and 5 % CO_2 with a FV3000 Olympus confocal microscope. Images represent maximum projections of whole cell z-stacks. Scale bars represent 10 µm (original images) and 5 µm (zoomed images).

4.2.4: Uptake of human serum albumin in BOECs

Macropinocytosis was shown to be the main mechanism for the uptake of human serum albumin (HSA) in a number of cell types (Yumoto *et al.*, 2012; Palm, 2019; Toh *et al.*, 2020). However, studies using bovine and rat microvascular lung endothelial cells suggested that HSA is endocytosed via caveolae-mediated endocytosis initiated by the binding of HSA to the surface receptor gp60 (Minshall *et al.*, 2000; Vogel *et al.*, 2001). To evaluate how the HSA uptake is facilitated in cultured primary BOEC lines, BOECs were incubated with fluorescent-labelled HSA (HSA-AF488) and HSA endocytosis analysed by flow cytometry and confocal fluorescence microscopy (Figure 4.14). Flow cytometric analysis of BOECs pulsed with fluorescence-labelled albumin for 30 or 60 minutes at 37 °C revealed a considerable right-shift of the histograms compared to cells incubated on ice. The mean fluorescence intensity for the albumin signal increased 30-fold (MFI: 1.9×10^3) after 30 minutes and 110-fold (MFI: 7.3×10^3) after 60 minutes uptake. These results were consistent across several experiments (n=4) (Figure 4.14A). BOECs incubated on ice for 60 minutes did not exhibit a higher fluorescent signal than unstained cells, indicating no binding of fluorescence-labelled HSA to the surface of BOECs and moreover, suggesting that the uptake of HSA by primary endothelial cells was by fluid phase uptake (Figure 4.14A).

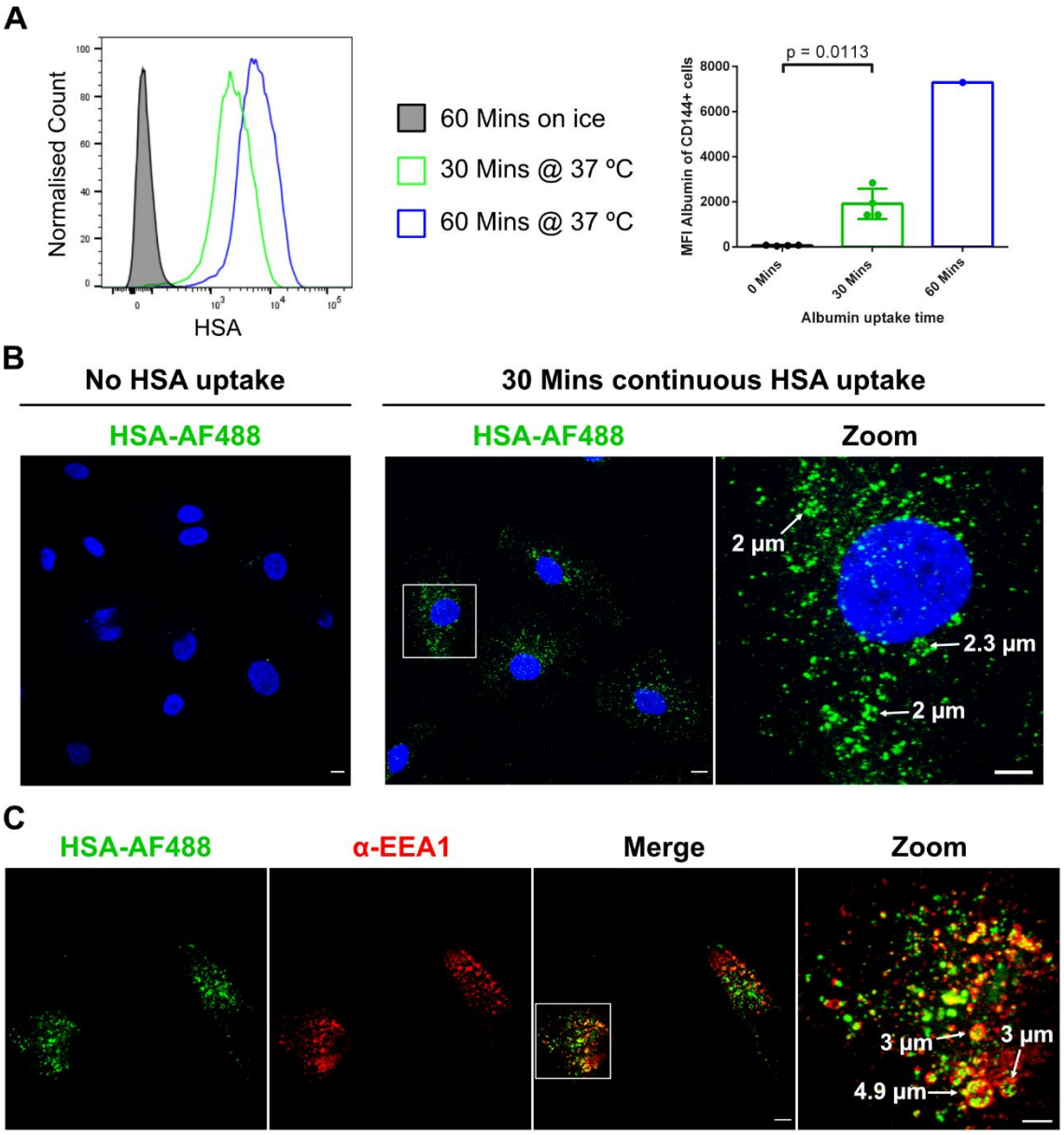

Figure 4.14: HSA uptake in cultured BOECs
(A) Cultured BOECs were pulsed for 30 (green, n = 4) or 60 (blue, n = 1) minutes with Alexa Fluor®-568-labelled HSA at 37 °C or on ice (grey, n = 4). Monolayers were washed to remove excess fluorophore and BOECs detached from the culture vessels. Cells were stained for CD144 and dead cells were identified by DAPI staining. HSA uptake was analysed by flow cytometry. Histograms are shown for single, live CD144$^+$ cells. The mean fluorescence intensity was calculated to quantify HSA uptake. Data for 0 minutes (60 Mins on ice) and 30 minutes (37 °C) of HSA uptake was pooled from four individual experiments. Errors are shown as SEM. p-values were calculated using the paired Student's t-test. **(B-C)** Cultured BOECs were pulsed for 30 minutes with Alexa Fluor®-488-labelled HSA (HSA-AF488, green) at 37 °C. Excess fluorophore was washed away and cells fixed with PFA or MeOH. HSA-AF488 uptake in fixed BOECs was either assessed directly **(B)** or after staining for EEA1-positive endosomal

compartments (red) using a site-specific antibody **(C)**. Nuclei were visualised using DAPI (blue). Selected enlarged HSA-positive structures are highlighted by white arrows and their estimated diameter is shown. Images represent maximum projections of whole cell z-stacks. Scale bars represent 10 µm (original images) and 5 µm (Zoom).

To evaluate the presence of endocytosed HSA in intracellular structures of BOECs, cells were pulsed with fluorescent-labelled albumin for 30 minutes, fixed with PFA and HSA-specific fluorescence assessed by confocal fluorescence microscopy (Figure 4.14B). Similar to flow cytometry, a significant increase of HSA fluorescence was observed in BOECs after 30 minutes of uptake at 37 °C. HSA fluorescence was associated with enlarged donut-shaped endosomal structures. In most cells, these structures reached sizes up to 2 – 2.5 µm in diameter. To further characterise these large HSA-positive structures, a co-staining with the early endosomal marker EEA1 in HSA-pulsed BOECs was performed (Figure 4.14C). The co-staining confirmed the presence of large HSA- and EEA1-double-positive endosomal structures in BOECs. In some cells these enlarged donut-shaped structures were observed to have a size of up to 4.9 µm in diameter (Figure 4.14C).

The localisation of endocytosed HSA within large EEA1-positive structures indicated that HSA may be predominantly endocytosed by BOECs via macropinocytosis and associated with EEA1-positive early macropinosomes. To confirm the macropinocytic activity of BOECs, a co-uptake of fluorescent-labelled HSA and 70 kDa dextran was performed (Figure 4.15A). 70 kDa dextran is known to be exclusively endocytosed via macropinocytosis because of its size and is widely used as a marker for fluid-phase uptake and macropinosomal structures (Li *et al.*, 2015). Endocytosed HSA and 70 kDa dextran co-localised in large endosomal structures with diameters up to 2 µm. A Pearson's correlation coefficient of 0.83 (no threshold) was calculated for the overlap of the fluorescent signal corresponding to HSA and 70 kDa dextran.

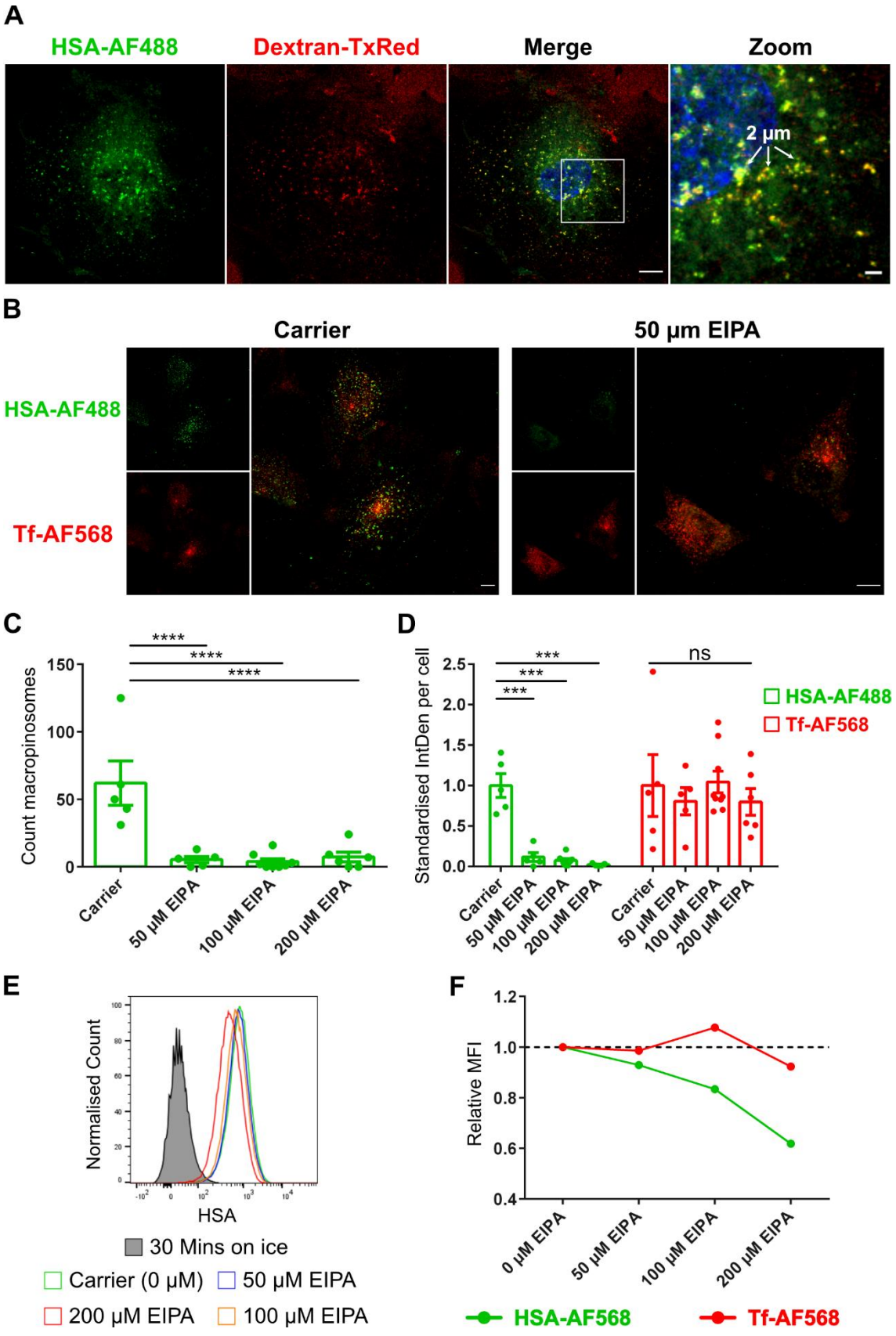
A
HSA-AF488
Dextran-TxRed
Merge
Zoom
2 µm
B
Carrier
50 µm EIPA
HSA-AF488
Tf-AF568
C
Count macropinosomes
****
****
****
Carrier
50 µM EIPA
100 µM EIPA
200 µM EIPA
D
Standardised IntDen per cell
***
***
***
ns
HSA-AF488
Tf-AF568
Carrier
50 µM EIPA
100 µM EIPA
200 µM EIPA
E
Normalised Count
HSA
30 Mins on ice
Carrier (0 µM)
50 µM EIPA
200 µM EIPA
100 µM EIPA
F
Relative MFI
0 µM EIPA
50 µM EIPA
100 µM EIPA
200 µM EIPA
HSA-AF568
Tf-AF568

Figure 4.15: HSA uptake by macropinocytosis in cultured BOECs
(A) BOECs were allowed co-uptake of Alexa Fluor®-488-labelled HSA (HSA-AF488, green) and 70 kDa dextran labelled with TexasRed (Dextran-TxRed, red) for 30 minutes at 37 °C. After internalisation, excess fluorophores were washed away, cells were fixed with PFA and imaged by confocal fluorescence microscopy. Nuclei were visualised using DAPI (blue). Enlarged HSA- and dextran-positive endosomal structures are indicated by white arrows and their estimated diameter is shown. **(B)** BOECs were pre-treated with 50, 100 or 200 µM EIPA or with MeOH alone (carrier) for 60 minutes at 37 °C before performing uptake experiments in presence of the respective amiloride concentration. EIPA-treated BOECs were pulsed with Alexa Fluor®-488-labelled HSA (HSA-AF488, green) and Alexa Fluor®-568-labelled transferrin (Tf-AF568, red) at 37 °C for 30 minutes. Cells were fixed with PFA and imaged by confocal fluorescence microscopy. **(C-D)** Representative quantification of macro-pinosomes and intracellular fluorescence levels in cultured BOECs in absence and presence of EIPA. **(C)** HSA-AF488-positive macropinosomes from maximum projections of acquired z-stacks of fixed cells were quantified, according to an adapted protocol from Wang *et al.* (Wang *et al.*, 2014). Macropinosomal-like structures were defined as endosomes with a size of 0.2 – 20 µm^2 (~ 0.5 – 5 µm in diameter). **(D)** Intracellular fluorescence levels (integrated density = IntDen) per cell for HSA-AF488 (green) and Tf-AF568 (red) were quantified using maximum projections of acquired z-stacks. Integrated densities were normalised to the mean values of the carrier control for both internalised molecules, respectively. n ≥ 5 (number of cells). **(E-F)** EIPA pre-treated BOECs were allowed uptake of Alexa Fluor®-568-labelled HSA or transferrin at 37 °C for 30 minutes in presence of 0 (green), 50 (blue), 100 (orange) or 200 (red) µM EIPA. Excess fluorophores were washed away and cells detached from the culture vessel. **(E)** HSA uptake was analysed by flow cytometry. After a 30-minute pulse with HSA-AF568, confluent BOEC monolayers were prepared, as described in the methods section, and stained for CD144. Histograms are shown for single, live CD144$^+$ cells. To evaluate background levels, BOECs were incubated with Alexa Fluor®-568-labelled HSA for 30 minutes on ice (grey). **(F)** The mean fluorescence intensity (MFI) was calculated to quantify Alexa Fluor® 568-labelled HSA (green) or transferrin (red) uptake in dependence of the EIPA concentration. The MFI values for the control group (0 µM EIPA) were set to 1, and the MFI values for EIPA-treated cells expressed as relative MFIs. Confocal images represent maximum projections of whole cell z-stacks. Scale bars represent 10 µm (original images) and 2 µm (Zoom). Errors are shown as SEM. p-values were calculated using Fisher's LSD test. *** $p < 0.001$, **** $p < 0.0001$

Amiloride and its derivates selectively inhibit macropinocytosis by lowering the sub-membranous pH and preventing the formation of macropinosomes (Koivusalo *et al.*, 2010). Although other endocytic pathways are known to be

affected by sub-membranous acidification, treatment with low concentrations of amiloride have been proposed to specifically impair macropinocytosis without considerable off-target effects (Koivusalo *et al.*, 2010). To inhibit macropinocytosis in cultured BOECs, cells were treated with the amiloride derivative 5-(N-ethyl-N-isopropyl)amiloride (EIPA), as described in methods section, and HSA and transferrin uptake was assessed by confocal fluorescence microscopy (Figure 4.15B). After allowing for 30 minutes of uptake, HSA was found to be localised to punctuate endosomal structures throughout the cell in BOECs treated with the carrier (MeOH) alone. Treatment with 50 µM EIPA led to a significant reduction of the HSA uptake in BOECs in comparison to the carrier control. Furthermore, macropinosomal-like structures with a diameter of 0.5 – 5 µm were quantified using an ImageJ-based macropinosome quantitation assay adapted from Wang and colleagues (Wang *et al.*, 2014) (Figure 4.15C). In the carrier control on average 62 HSA-positive macropinosome-like structures were detected per cell, whereas the treatment with 50 µM EIPA dramatically reduced presence of HSA-positive macropinosomal-like structures to 5.5 per cell. The treatment of BOECs with higher concentrations of EIPA (100 and 200 µM) showed a similar reduction in macropinosomes as 50 µM EIPA.

In contrast to HSA, the uptake of transferrin in BOECs was not impaired by the presence of EIPA (Figure 4.15B). In cells treated with 50 µM EIPA similar levels of transferrin fluorescence were detected within analysed cells. To verify the effects described for HSA and transferrin uptake upon EIPA treatment, the total fluorescence levels per cell for both cargoes was calculated using z-projections and appropriate thresholding algorithms (Figure 4.15D). Again, the uptake of HSA was strongly inhibited in the presence of EIPA with very low fluorescent levels detected in BOECs treated with 50, 100 or 200 µM of the inhibitor. Transferrin fluorescent levels were not affected by the presence of EIPA. The profound impairment, albeit to different extent, of HSA internalisation in presence of the macropinocytosis inhibitor EIPA was observed across several experiments. The differences in inhibition were probably due to the poor solubility of EIPA, however, in all experiments the presence of 50 µM or higher concentrations of EIPA significantly reduced the uptake of HSA by cultured BOECs.

Flow cytometry also detected some reduction in the uptake of fluorescent-labelled HSA following EIPA (Figure 4.15E-F). For flow cytometric uptake assays, HSA-AF568 was used due to high autofluorescence levels in the green channel resulting in poor resolution when uptake of AF488-labelled HSA was assessed. HSA-AF568 uptake was reduced by 40 % in presence of 200 µM EIPA in comparison to the carrier control (Figure 4.15E). In contrast to microscopic analysis, concentrations less than 200 µM had only slight effects on the detected fluorescent levels in BOECs (Figure 4.15E). The difference in findings between microscopic and flow cytometric analyses may reflect the fact that cells were fixed for the former whereas flow cytometry was performed on live cells. Nonetheless, the mean fluorescence intensity (MFI) revealed that HSA-AF568 uptake in BOECs was steadily reduced in an EIPA-dependent manner (Figure 4.15F). The MFI of endocytosed transferrin seemed not to be influenced considerably by the presence of EIPA.

Together, these data showed that BOECs were able to endocytose significant amounts of fluorescence-labelled HSA within 30 minutes of continuous uptake and intracellular albumin was detected within large endosomal structures with diameters up to 5 µM which co-localised with the early endosome marker EEA1 and the fluid-phase marker 70 kDa dextran. Furthermore, the uptake of HSA was significantly impaired in the presence of the selective macropinocytosis inhibitor EIPA.

4.2.5: Degradation kinetics and HSA disappearance in fixed BOECs

4.2.5.1: Degradation kinetics of endocytosed cargo in BOECs

The kinetics of HSA degradation in cultured BOECs was investigated to assess how long it takes for endocytosed cargo to reach lysosomal compartments. For these uptake experiments, the ovalbumin-derived conjugate DQ-OVA was used (Figure 4.16A). DQ-OVA is a fluorescent probe extensively labelled with BODIPY FL fluorophores, and which in its native state does not fluoresce due to self-quenching. However, upon proteolytic degradation of DQ-OVA, the

BODIPY FL fluorophores released from the DQ-OVA polypeptide exhibit bright fluorescence indicating lysosomal processing of the fluorescence probe.

BOECs were allowed to continuously take up DQ-OVA for 0, 20, 40 or 60 minutes and DQ-OVA fluorescence was quantified by flow cytometry (Figure 4.16B). Analysis of single live CD144$^+$ cells revealed a considerable right-shift of the histograms with increasing time of DQ-OVA uptake. After 40 minutes uptake, the histogram was clearly separated from the control corresponding to BOECs without DQ-OVA uptake.

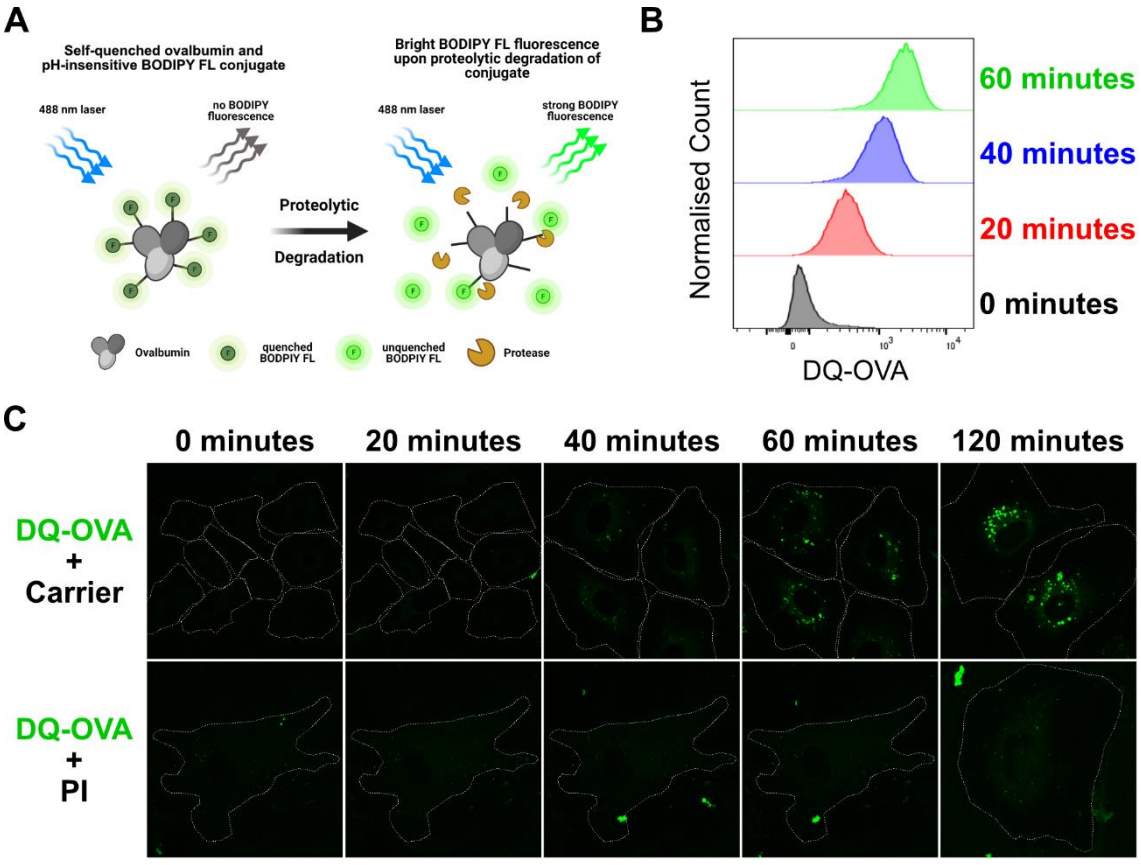

Figure 4.16: Continuous DQ-OVA uptake assay and degradation kinetics in live BOECs
(A) Schematic principle of DQ-OVA probe to assess proteolytic degradation in cultured cells. Bright DQ-OVA fluorescence is exhibited by probe upon proteolytic degradation in lysosomal compartments. **(B)** BOECs were allowed continuous uptake of DQ-OVA for 0 (grey), 20 (red), 40 (blue) or 60 (green) minutes at 37 °C. After the respective uptake time, cells were detached from the culture vessel, stained for CD144, and kept on ice until flow cytometric analysis of

DQ-OVA fluorescence was performed. Histograms are shown for single, live $CD144^+$ cells. **(C)** BOECs were pre-treated with DMSO carrier or protease inhibitor (PI) for 4 hours at 37 °C. Cells were pulsed with DQ-OVA probe in presence of DMSO carrier or PI and fluorescence directly followed at 37 °C and 5 % CO_2 using an Olympus FV3000 confocal fluorescence microscope. Cell boundaries are indicated by dotted lines.

To further characterise the degradation kinetics in live BOECs and evaluate the fluorescence levels of DQ-OVA by confocal microscopy, BOECs were cultured in DQ-OVA containing medium at 37 °C and 5 % CO_2 and the DQ-OVA fluorescent signal followed in single cells (Figure 4.16C). As expected, no DQ-OVA fluorescence was detected in cells immediately after the incubation with the fluorescent probe. After 40 minutes uptake of DQ-OVA, low levels of DQ-OVA fluorescence were detected in cultured BOECs. The signal of the fluorescent probe became considerably stronger after 60 minutes of continuous uptake and reached a peak after ~ 120 minutes. In the presence of protease inhibitor (PI), minimal fluorescence was detected during the time course confirming the requirement of proteolytic degradation for the exhibition of DQ-OVA fluorescence.

4.2.5.2: Disappearance of HSA-specific fluorescent signals in fixed BOECs

The fate of the endocytosed HSA was investigated in the BOECs. Initially, the disappearance of the HSA fluorescence signal during pulse-chase experiments was evaluated in fixed BOECs (Figure 4.17A). Cultured BOECs were pulsed for 30 minutes with HSA-AF488, excess fluorophore was washed away, and the internalised signal chased for 60 minutes. Cells were fixed at various time points and the HSA fluorescence was assessed by confocal microscopy (Figure 4.17A). After 30 minutes pulse, high levels of HSA fluorescence were detected in BOECs in the absence or presence of protease inhibitor (PI). The fluorescent signal then gradually decreased over 60 minutes chase period in the absence of PI, and only low levels of HSA fluorescence could be detected after 60 minutes chase. In contrast, BOECs treated with PI to block proteolytic degradation exhibited a

visible fluorescent signal after 60 minutes chase. However, the level of HSA-AF488 fluorescence appeared lower at the end of the chase in PI treated BOECs

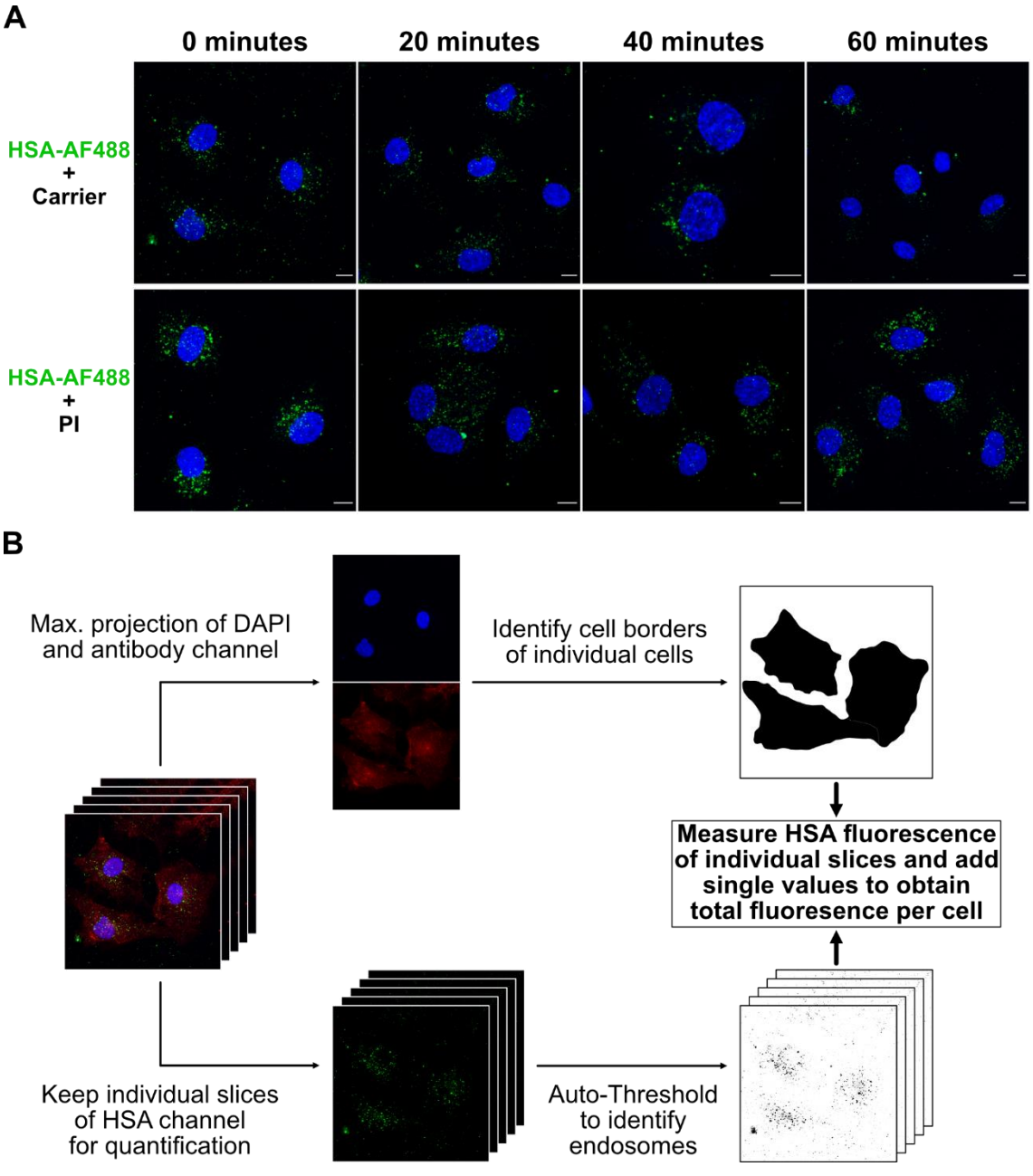

Figure 4.17: Disappearance of intracellular HSA fluorescence during pulse-chase experiments in fixed BOECs

(A) BOECs were pre-treated with DMSO or protease inhibitor (PI) for 4 hours at 37 °C. After pre-treatment, cells were pulsed with Alexa Fluor®-488-labelled HSA (HSA-AF488, green) for 30 minutes at 37 °C. Excess fluorophores were washed

away extensively and the fluorescent signal chased for 0, 20, 40 or 60 minutes at 37 °C. After the chase, cells were directly fixed with PFA or MeOH. For 0 minutes of chase, cells were directly fixed after ligand internalisation. DMSO or PI was present in the medium until cell fixation. Nuclei were visualised using DAPI (blue). Images represent maximum projections of whole cell z-stacks. Scale bars represent 10 µm. **(B)** Schematic overview of an ImageJ-based protocol for the quantification of intracellular HSA fluorescence in fixed BOECs. Maximum projections of acquired z-stacks were made for the DAPI and an unrelated antibody channel to create masks representing the outline of single cells. Using single slices of the HSA channel in combination with the defined cells masks, the total intracellular HSA fluorescence per cell was quantified in fixed BOECs.

To gain an unbiased assessment of intracellular HSA fluorescent levels of BOECs within a pulse-chase assay setup, an ImageJ-based quantification protocol was established to calculate the total HSA fluorescence per cell (Figure 4.17B). To this end, z-stacks of whole cells co-stained with DAPI and an unrelated antibody exhibiting background fluorescence were acquired and maximum projections created. Maximum projections of the DAPI and the antibody fluorescence were used to create cell masks representing the whole cytoplasm of single segregated cells. On the other hand, endosomal structures in single slices of the HSA fluorescence channel were identified using appropriate threshold algorithms. In combination with the defined cell masks, the total HSA fluorescence per cell present in thresholded endosomal structures of single slices was calculated.

The total HSA fluorescence per cell was normalised to the values for 0 minutes chase and data obtained from different pulse-chase experiment was pooled to evaluate the disappearance of endocytosed HSA in fixed BOECs (Figure 4.18). During the pulse-chase experiment, the total HSA fluorescence level per cell dropped gradually from 100 % at 0 minutes chase to around 45 % during the 60-minute chase period in presence of the DMSO carrier alone (Figure 4.18A). However, in presence of PI the detected fluorescence dropped to 55 % after 40 minutes chase and then remained relatively constant. After 60 minutes chase, 69 % of the HSA-AF488 fluorescence levels were detected in PI-treated cells (Figure 4.18A).

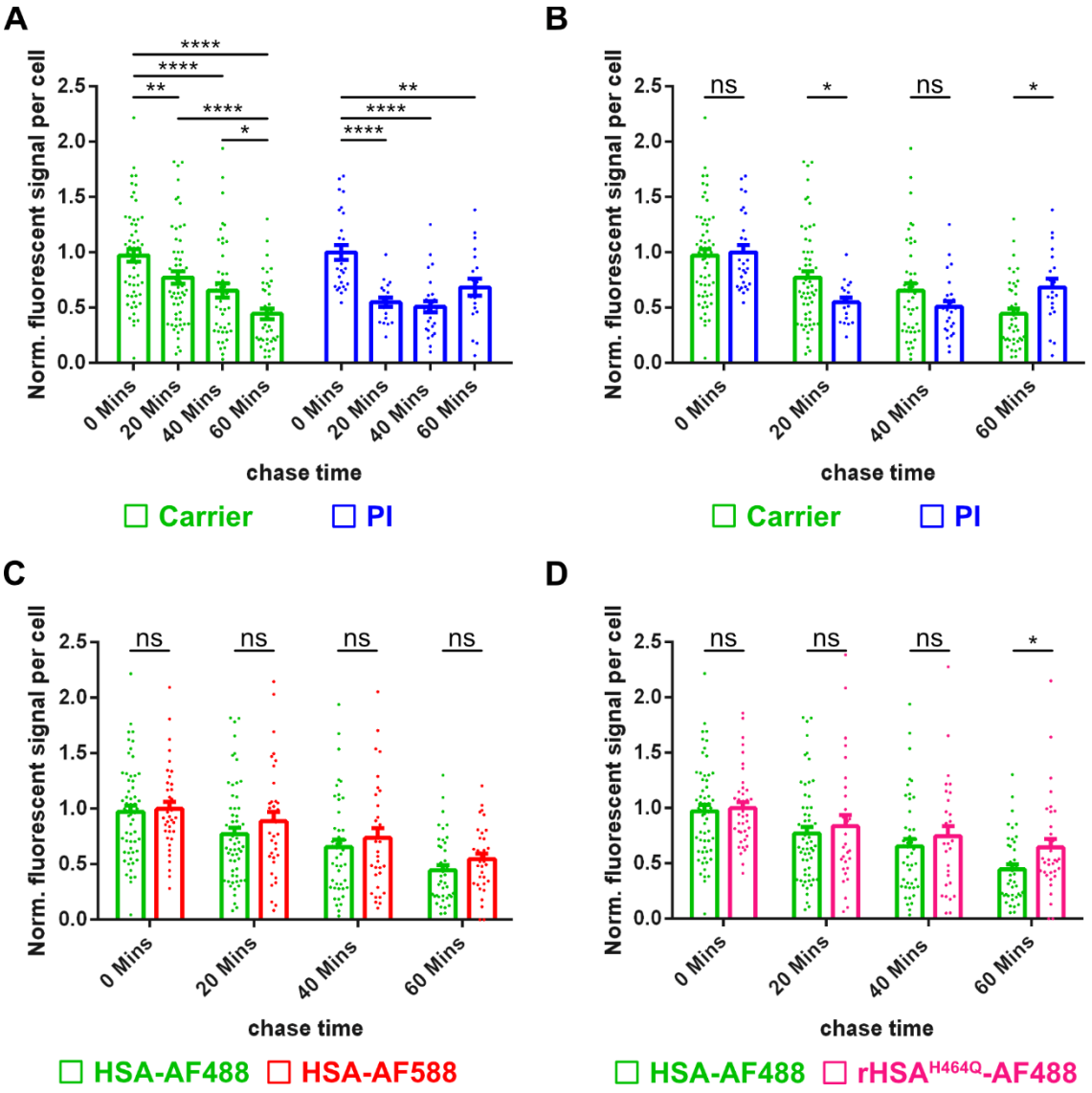

Figure 4.18: Quantification of intracellular HSA fluorescence in fixed BOECs during pulse-chase experiments

(A-D) BOECs were pre-treated with DMSO carrier (Carrier) or protease inhibitor (PI) for 4 hours at 37 °C. After pre-treatment, cells were allowed uptake of Alexa Fluor®-488-labelled HSA (HSA-AF488) for 30 minutes at 37 °C. Excess fluorophores were washed away extensively and the fluorescent signal chased for 0, 20, 40 or 60 minutes at 37 °C. After the chase, cells were directly fixed with PFA or MeOH. For 0 minutes of chase, cells were directly fixed after ligand internalisation. DMSO carrier or PI was present in the medium until cell fixation. Total intracellular HSA fluorescence per cell was quantified, as described in Figure 4.17 and the methods section. Values were normalised to the mean intracellular timepoint at 0 minutes of chase and results pooled from individual experiments. **(A-B)** The quantified intracellular fluorescence levels are shown for HSA-AF488 in presence of DMSO carrier (green) and PI (blue). **(C)** Comparison of intracellular fluorescent levels of HSA-AF488 (green) and HSA labelled with Alexa Fluor®-568 (HSA-AF568, red). **(D)** Quantification of total HSA fluorescence

for AF488-labelled wildtype HSA (HSA-AF488, green) and non-FcRn-binding rHSA^{H464Q} (rHSA^{H464Q}-AF488, pink). n ≥ 19 (number of cells) from 5 experiments. Errors are shown as SEM. p-values were calculated using Fisher's LSD test. * $p < 0.05$, ** $p < 0.01$, *** $p < 0.001$, **** $p < 0.0001$

To estimate the ratio of HSA fluorescence lost due to proteolytic degradation, the trend of the detected HSA fluorescence signal in absence or presence of PI was directly compared (Figure 4.18B). The level of normalised HSA fluorescence per cell was significantly higher in presence of PI after 60 minutes chase time (69 %) compared to the carrier control (45 %). The HSA fluorescence after 20 minutes was also significantly lower than for cells treated with DMSO carrier alone (55 % for PI, 77 % for DMSO carrier), whereas there was no difference in cells analysed after 0 or 40 minutes of chase (Figure 4.18B).

To evaluate if the observed reduction of HSA fluorescence in cultured BOECs is independent on the fluorescent-coupled HSA derivate, the fluorescent levels of two differently labelled HSA conjugates were quantified (Figure 4.18C). There was no difference in the disappearance of fluorescent signal per cell comparing HSA molecules labelled with Alexa Fluor®-488 (AF488) or Alexa Fluor®-568 (AF568) at any timepoint analysed during the pulse-chase experiment. Lastly, the disappearance of fluorescent signal corresponding to WT HSA and the non-FcRn-binding HSA variant rHSA^{H464Q} labelled with AF488 was compared. Within the first 40 minutes of chase, no difference between the fluorescent signal was observed. However, after 60 minutes chase the fluorescent signal for the non-FcRn-binding rHSA^{H464Q} variant (64 %) was significantly higher compared to the signal corresponding to intracellular WT HSA (45 %) (Figure 4.18D). The difference of fluorescent levels detected after 60 minutes of chase could be either due to recycling or more rapid degradation of intracellular WT HSA.

Collectively, DQ-OVA uptake experiments revealed that internalised cargo reached the degradative compartments of BOECs between 40 – 60 minutes. This time period is consistent with the findings on the disappearance of intracellular HSA fluorescence signals in fixed BOECs. The calculated HSA fluorescence

decreased by ~ 55 % following the 30 minutes pulse to the end of the 60 minutes chase. The use of protease inhibitor during the pulse-chase experiment dampened the HSA signal with a 31 % reduction after 60 minutes chase. A similar rate of disappearance of the fluorescent signal was observed for the non-FcRn-binding rHSA^{H464Q} variant in DMSO carrier-treated BOECs with a 36 % reduction after 60 minutes chase. These results indicate that there are likely to be two components associated with the disappearance of wildtype HSA fluorescence following uptake, namely (1) proteolytic degradation and (2) FcRn-dependent recycling of HSA.

4.2.6: Intracellular trafficking of HSA in fixed BOECs

4.2.6.1: HSA trafficking to early endosomes in fixed BOECs

After investigating the uptake of HSA and the time-dependent trafficking to degradative compartments, the intracellular itinerary of endocytosed HSA was next investigated in fixed BOECs by co-staining with endosomal markers. To assess whether endocytosed HSA is associated with early endosomal or macropinosomal compartments, cultured BOECs were pulsed with HSA-AF488 uptake (30 minutes), and the fluorescent signal was chased 60 minutes. After fixation at various time points, cells were stained with an EEA1-specific antibody to visualise early endosomes and macropinosomes (Figure 4.19A). Co-localisation of HSA-AF488 with EEA1-positive endosomal-like structures was observed in cells treated with DMSO carrier and PI. With increasing chase time, the HSA fluorescence signal decreased steadily from EEA1-positive endosomes and by 60 minutes chase no overlap was observed.

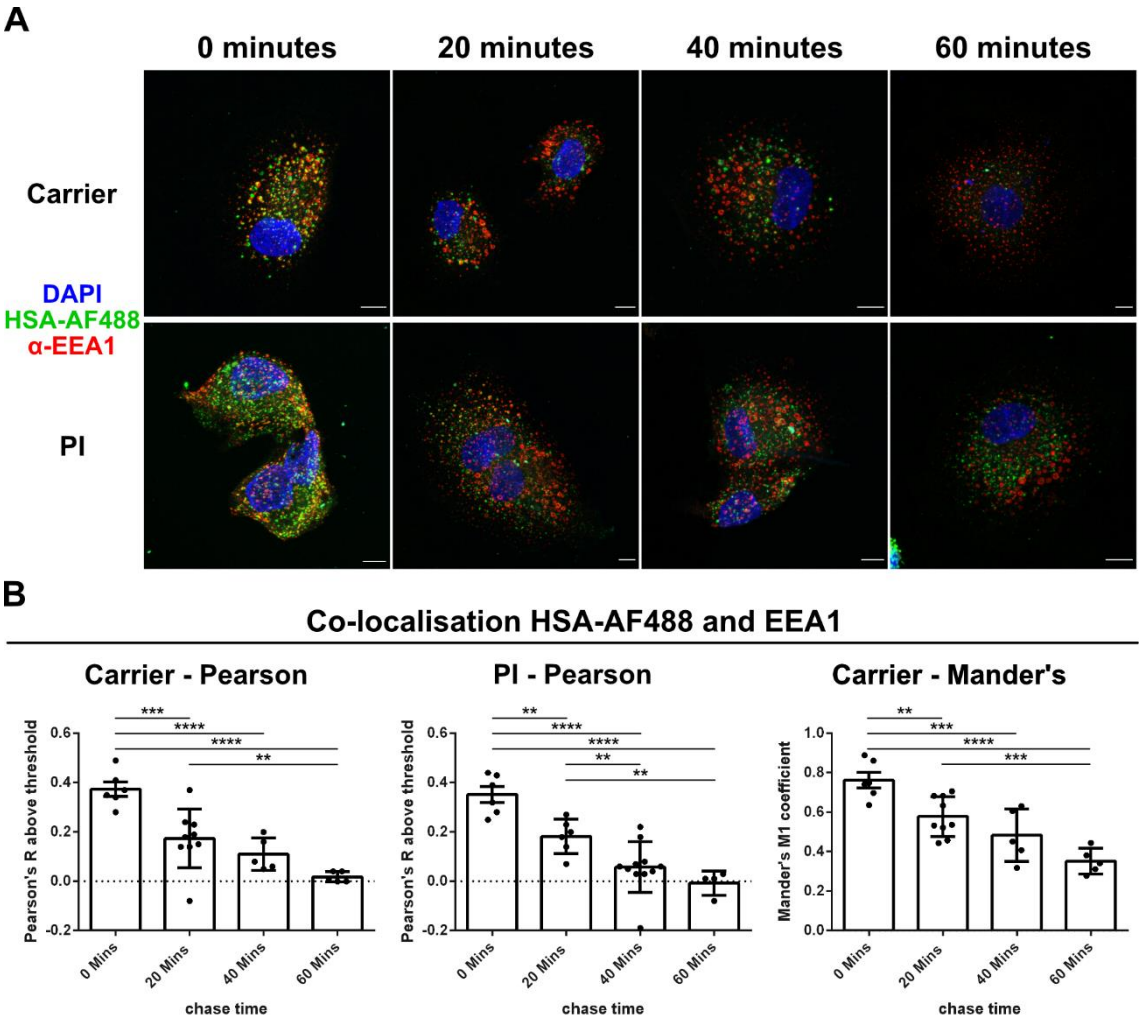

Figure 4.19: Co-localisation of internalised HSA and EEA1-positive endosomal structures in fixed BOECs

(A) BOECs were pre-treated with DMSO or protease inhibitor (PI) for 4 hours at 37 °C. After pre-treatment, cells were pulsed with Alexa Fluor®-488-labelled HSA (HSA-AF488, green) for 30 minutes at 37 °C. Excess fluorophores were washed away extensively and the fluorescent signal chased for 0, 20, 40 or 60 minutes at 37 °C. After the chase, cells were directly fixed with PFA and stained for EEA1 (red). For 0 minutes of chase, cells were directly fixed after ligand internalisation. DMSO carrier or PI was present in the medium until cell fixation. Nuclei were visualised using DAPI (blue). Images represent maximum projections of whole cell z-stacks. Scale bars represent 10 µm. **(B)** Representative quantification of co-localisation parameter, Pearson's and Mander's coefficient M1, in presence of DMSO carrier or PI. The parameters were calculated using the ImageJ plugin Coloc2 and values are shown for calculated parameters above threshold determined by the Costes' method. n ≥ 4 (number of cells). Errors are shown as SEM. p-values were calculated using Fisher's LSD test. ** $p < 0.01$, *** $p < 0.001$, **** $p < 0.0001$

To quantify the degree of overlap between HSA and EEA1-positive endosomal structures, co-localisation was calculated using the Coloc2 tool in ImageJ. For this analysis, region of interests resembling the outline of single cells were defined and co-localisation was quantified using acquired z-stacks (Figure 4.19B). The Pearson's coefficient declined from ~ 0.4 at 0 minutes steadily with increased chase time and reached 0 at 60 minutes. This reduction was observed for BOECs independently of the presence of PI. To estimate the percentage of HSA-positive pixels located to EEA1-positive structures, Mander's coefficient M1 was also calculated. With increasing chase time, M1 dropped from approximately 0.8 at 0 minutes to ~ 0.4 at 60 minutes chase. All three parameters indicated a considerable overlap of internalised HSA with EEA1-positive endosomal structures within the first 20 minutes after endocytosis. However, the co-localisation of HSA and EEA1-positive structures was reduced gradually over the subsequent chase period.

4.2.6.2: HSA trafficking to late endosomes and lysosomes in fixed BOECs

To further characterise the intracellular itinerary of endocytosed HSA in fixed BOECs, the overlap of HSA with the late endosomal and lysosomal markers, CD63 (Figure 4.20) and LAMP1 (Figure 4.21) was investigated. Again, BOECs were pulsed 30 minutes with HSA-AF488 and the fluorescent signal was chased for 60 minutes. After fixation at various time points, cells were stained either for CD63 or LAMP1 and co-localisation of endocytosed HSA and the late endosomal and lysosomal markers assessed. Due to the prominent perinuclear localisation of CD63- and LAMP1-positive endosomal structures in BOECs, it was not possible to calculate co-localisation coefficients in a reliable manner. Instead, line scans were performed to evaluate the overlap of the fluorescence profiles of HSA and CD63 or LAMP1, respectively. Additionally, the association of the non-FcRn-binding HSA variant HSA^{H464Q} with late endosomal and lysosomal structures was assessed to estimate the influence of FcRn interaction on the intracellular itinerary of HSA.

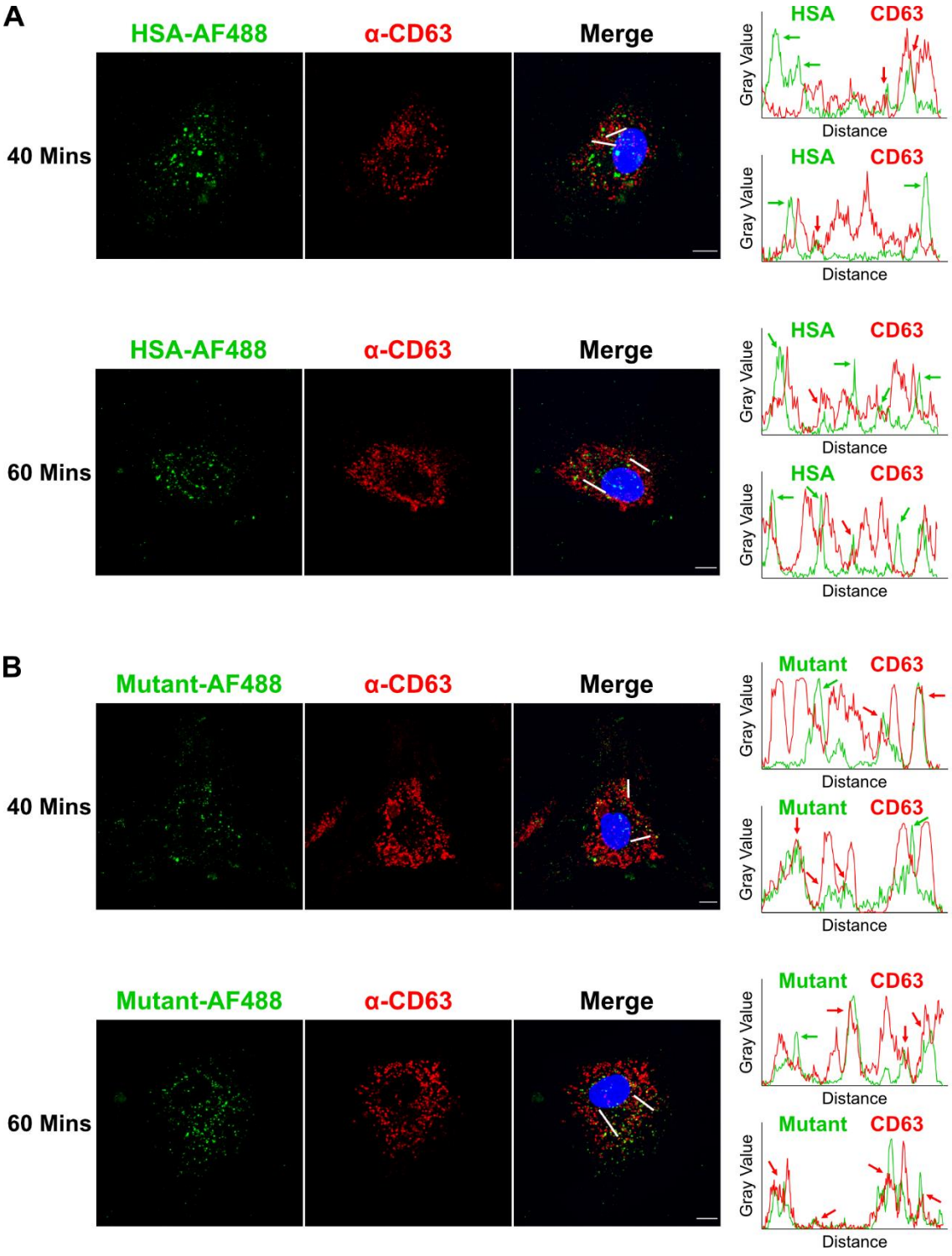

Figure 4.20: Co-localisation of internalised HSA and CD63-positive endosomal structures in fixed BOECs

BOECs were pulsed with Alexa Fluor®-488-labelled HSA (HSA-AF488, green) **(A)** or non-FcRn binding HSA^{H464Q} (Mutant-AF488, green) **(B)** for 30 minutes at 37 °C, as described in the methods section. Excess fluorophores were washed away extensively and the fluorescent signal chased for 40 or

60 minutes at 37 °C. After the chase, cells were directly fixed with PFA and stained for CD63 (red). Nuclei were visualised using DAPI (blue). The profiles of two line scans per image are shown for both fluorophores. The localisation of the respective line scans is indicated by white lines. Images represent maximum projections of whole cell z-stacks. Scale bars represent 10 µm.

After 40 and 60 minutes of chase, there was no co-localisation of HSA- and CD63-positive endosomal structures in fixed BOECs (Figure 4.20A). The line scans revealed that most fluorescent peaks of both molecules were not overlapping, rather, they were offset (indicated by green arrows). Only a minor fraction of HSA-AF488 and CD63 fluorescence peaks were overlapping (indicated by red arrows) indicating a small degree of co-localisation between HSA-AF488 and CD63.

For the non-FcRn-binding HSA variant rHSA^{H464Q} (mutant), more overlap of the mutant- and CD63-positive endosomal structures was observed (Figure 4.20B). In particular, after 60 minutes chase most of the fluorescence peaks for both molecules on the line scans were overlapping indicating the association of the non-FcRn-binding mutant with CD63-positive structures (indicated by red arrows). Only a small fraction of mutant-AF488 fluorescence peaks were not overlapping with CD63 signals (indicated by green arrows).

Similar trends were observed for the co-localisation of HSA with LAMP1-positive compartments (Figure 4.21). The fluorescence peaks of HSA resulting from the indicated line scans were not overlapping with the respective peaks of LAMP1 fluorescence (indicated by green arrows) after 40 or 60 minutes of chase (Figure 4.21A). However, a much higher degree of overlap was observed for the fluorescence peaks corresponding to the mutant and LAMP1 fluorescence (indicated by red arrows) in fixed BOECs after 40 and 60 minutes of chase (Figure 4.21B).

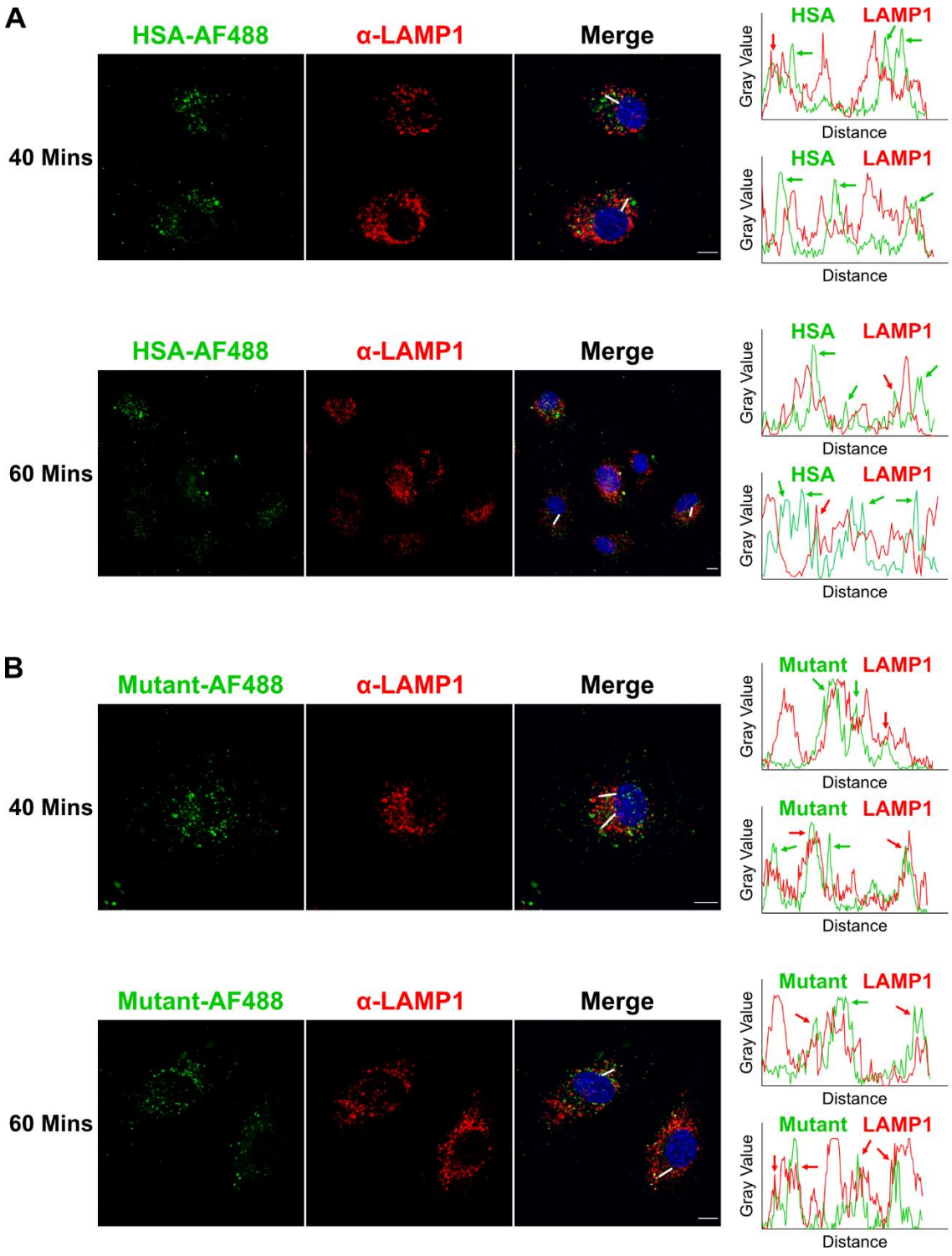

Figure 4.21: Co-localisation of internalised HSA and LAMP1-positive endosomal structures in fixed BOECs

BOECs were pulsed with Alexa Fluor®-488-labelled HSA (HSA-AF488, green) **(A)** or non-FcRn binding HSA^{H464Q} (Mutant-AF488, green) **(B)** for 30 minutes at 37 °C, as described in the methods section. Excess fluorophores were washed away extensively and the fluorescent signal chased for 40 or

60 minutes at 37 °C. After the chase, cells were directly fixed with PFA and stained for LAMP1 (red). Nuclei were visualised using DAPI (blue). The profiles of two line scans per image are shown for both fluorophores. The localisation of the respective line scans is indicated by white lines. Images represent maximum projections of whole cell z-stacks. Scale bars represent 10 µm.

Taken together, these data indicated that endocytosed HSA-AF488 is associated with enlarged EEA1-positive endosomal structures in BOECs, identified as macropinosomes by 70 kDa dextran uptake. With increasing chase time, the degree of co-localisation of HSA and EEA1 was reduced gradually. However, HSA fluorescence did not overlap with either CD63 or LAMP1 organelle markers indicating that HSA is, largely, excluded from late endosomal and lysosomal structures in fixed BOECs. In contrast, the non-FcRn-binding HSA variant HSA^{H464Q} showed more overlap with late endosomal and lysosomal markers suggesting a role for FcRn in regulating the sorting of HSA into the lysosomal pathway in BOECs.

4.2.7: Intracellular trafficking of HSA in live BOECs

4.2.7.1: HSA localisation to LysoTracker Red-positive compartments in live BOECs

The next step to decipher the intracellular itinerary of HSA in vascular endothelial cells, was to follow internalised HSA fluorescence in live BOECs by performing live cell experiments in a pulse-chase setup. Firstly, lysosomal compartments in live BOECs were visualised by LysoTracker Red staining, which accumulates in acidified endosomal structures (Figure 4.22A). LysoTracker Red localised to globular structures around the cell nucleus. The recording of time lapses of single cells revealed that LysoTracker Red-positive structures were immobile and no tubular carriers emerging from round endosomal structures were observed (Figure 4.22A).

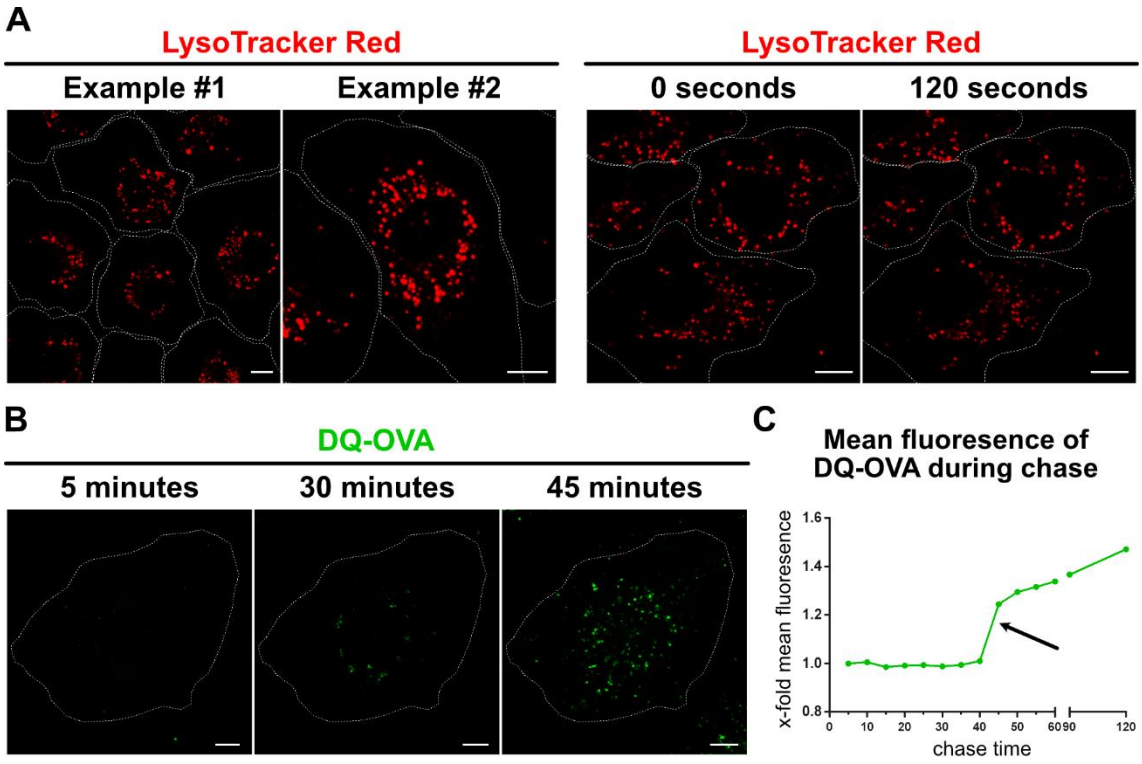

Figure 4.22: Lysosomal compartments in live BOECs and proteolytic DQ-OVA degradation in a pulse-chase setup
(A) Cultured BOECs were stained with LysoTracker™ Red DND-99 (red) for 60 minutes at 37 °C, as described in the methods section. **(B)** BOECs were pulsed with DQ-OVA (green) for 15 minutes at 37 °C, as described in the methods section, and the DQ-OVA fluorescence was chased in live cells. Images were recorded every 5 minutes. **(C)** The mean DQ-OVA fluorescence of confocal images of live BOECs during a pulse-chase assay was quantified over time using ImageJ. The mean fluorescence of cells at 0 minutes of chase (right after DQ-OVA uptake) was set to 1 and values expressed as x-fold. The black arrow indicates the appearance of bright DQ-OVA fluorescence after 45 minutes of chase. Live cells were imaged at 37 °C and 5 % CO_2 using an Olympus FV3000 confocal fluorescence microscope. Cell boundaries are indicated by dotted lines. Scale bars represent 10 µm.

To transfer the characterisation of degradation kinetics observed in continuous DQ-OVA uptake experiments to a pulse-chase setup using live cells, BOECs were pulsed with DQ-OVA for 15 minutes, excess fluorophores washed away and the DQ-OVA fluorescent signal indicating lysosomal degradation chased (Figure 4.22B-C). Bright DQ-OVA fluorescence was observed after 45 minutes of chase in live BOECs indicating proteolytic degradation of the endocytosed

ovalbumin conjugate (Figure 4.22B). Prior to 45 minutes chase, only background or low DQ-OVA-specific fluorescence was detected in BOECs. The quantification of mean DQ-OVA fluorescence showed a sharp increase of fluorescence after 45 minutes chase, indicating that endocytosed cargo reached degradative lysosomal compartments (Figure 4.22C). From 45 minutes onwards, the DQ-OVA fluorescence rose steadily as degradation of DQ-OVA conjugates proceeded.

Next, the co-localisation of endocytosed HSA-AF488 and LysoTracker Red was assessed in live BOECs during a pulse-chase assay (Figure 4.23A-B). Upon endocytosis, HSA-AF488 fluorescence was detected in punctuate structures in the cell periphery. These structures were negative for LysoTracker Red indicating a neutral luminal pH of HSA-positive endosomes (Figure 4.23A). After 20 minutes chase time, the majority of HSA-AF488 fluorescence overlapped with LysoTracker Red-positive compartments, indicating the acidification of HSA-positive endosomes allowing potential binding of endosomal HSA to FcRn (Figure 4.23A). Additionally, the emergence of tubular structures, albeit in a low frequency, emanating from globular endosomes could be observed initially after 20 minutes chase time.

With further increasing chase times, the co-localisation of HSA-AF488 and LysoTracker Red fluorescence increased and after 32 minutes of chase tubular carriers pinching off from globular endosomal structures were detected more frequently (Figure 4.23B). These tubular carriers were almost exclusively positive for HSA-AF488 (indicated by white arrows), but not LysoTracker Red, whereas globular endosomes remained mostly positive for both fluorescent markers (Figure 4.23B). HSA-AF488-positive tubular carriers continued to emerge from globular structures with increased chase time (up to 40 minutes) and were directed to the cell periphery. The absence of LysoTracker Red fluorescence within tubular carriers suggested that they have an intraluminal pH higher than the endosomal compartments. These results indicate that the endocytosed HSA-AF488 is exposed to an acidic pH compartment prior to the delivery to a degradative endosomal compartment.

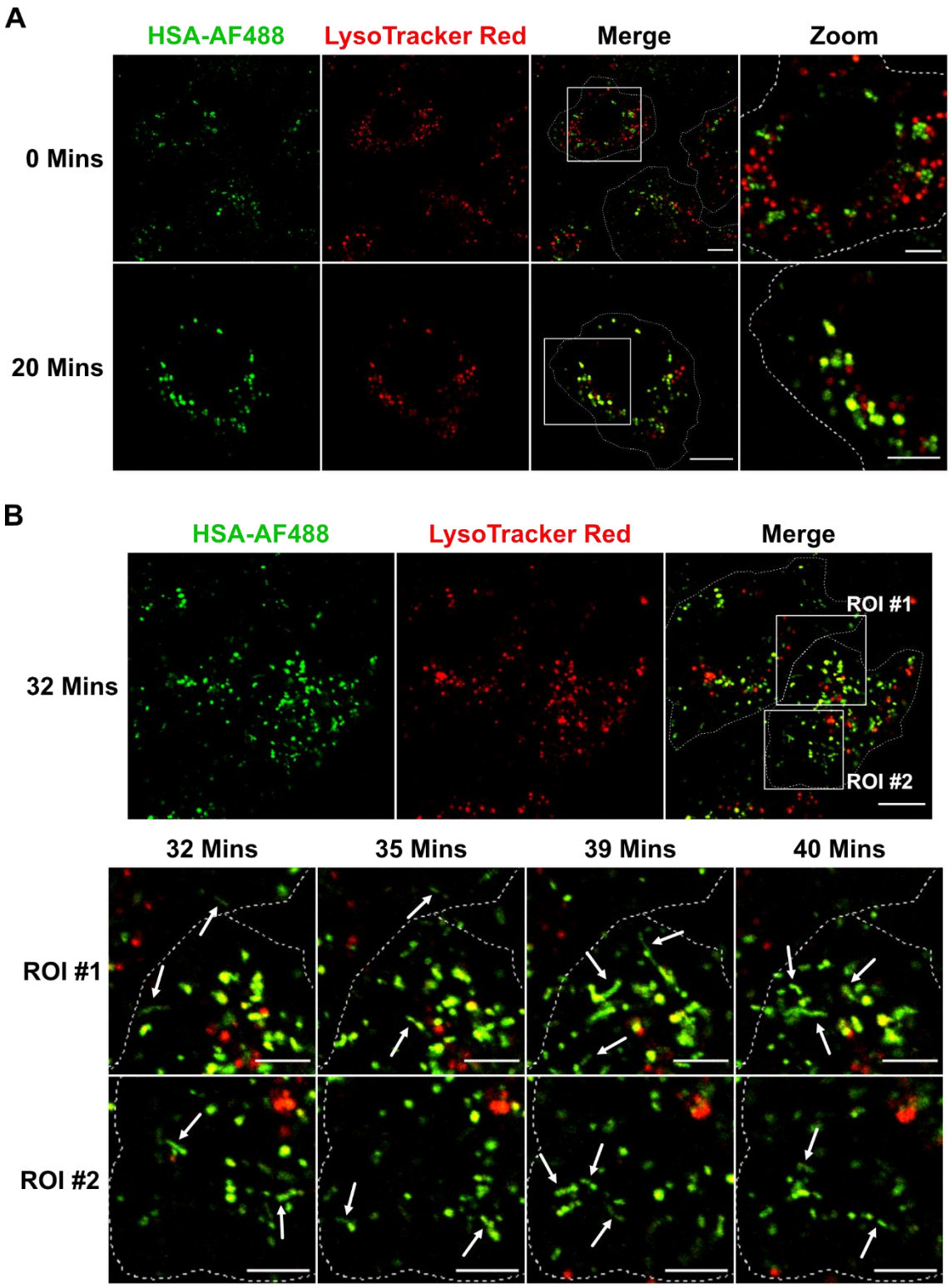

Figure 4.23: Localisation of endocytosed HSA-AF488 to LysoTracker Red-positive compartments in live BOECs

(A) Cultured BOECs were stained with LysoTracker™ Red DND-99 (red) for 60 minutes at 37 °C and subsequently pulsed with Alexa Fluor® 488-labelled HSA (HSA-AF488, green) for 15 minutes at 37 °C. Excess fluorophore was washed

away and the HSA-A488 fluorescence signal chased for 40 minutes in live cells by confocal microscopy. Example images are shown for 0 and 20 minutes chase. **(B)** Example image of a LysoTracker Red-stained BOEC pulsed with HSA-AF488 after 32 minutes chase. Two regions of interest (ROI) were defined to highlight the presence of HSA-AF488-positive tubular carriers (indicated by white arrows). Frames of the two ROIs are shown for 32, 35, 39 and 40 minutes chase. Live cells were imaged at 37 °C and 5 % CO_2 using an Olympus FV3000 confocal fluorescence microscope. Cell boundaries are indicated by dotted lines. Scale bars represent 5 µm (zoomed images) or 10 µm (Merge).

4.2.7.2: Intracellular trafficking of HSA-AF488 in FcRn-mCherry transduced live BOECs

To evaluate the co-localisation of HSA and FcRn in live cells, BOECs were transduced with FcRn-mCherry, pulsed with HSA-AF488 for 15 minutes at 37 °C and the signal chased up to 40 minutes. This chase time was chosen to exclude the influence of cargo being degraded in lysosomal compartments, which was shown to be observed after 45 minutes chase time in live BOECs, as described above (Figure 4.22). Within the first 5 minutes after internalisation, HSA-AF488 fluorescence was detected in globular punctate structures in the cell periphery, which were negative for FcRn-mCherry indicating that FcRn does not locate to newly formed macropinosomes in BOECs (Figure 4.24). From 10 minutes chase onwards, the overlap of HSA-A488- and FcRn-mCherry-specific fluorescent signals increased steadily indicating co-localisation of HSA and FcRn in globular endosomal structures (indicated by white arrows). The presence of these double-positive globular structures was also observed 20 minutes after the pulse (indicated by white arrows) and over the whole course of the pulse-chase experiment.

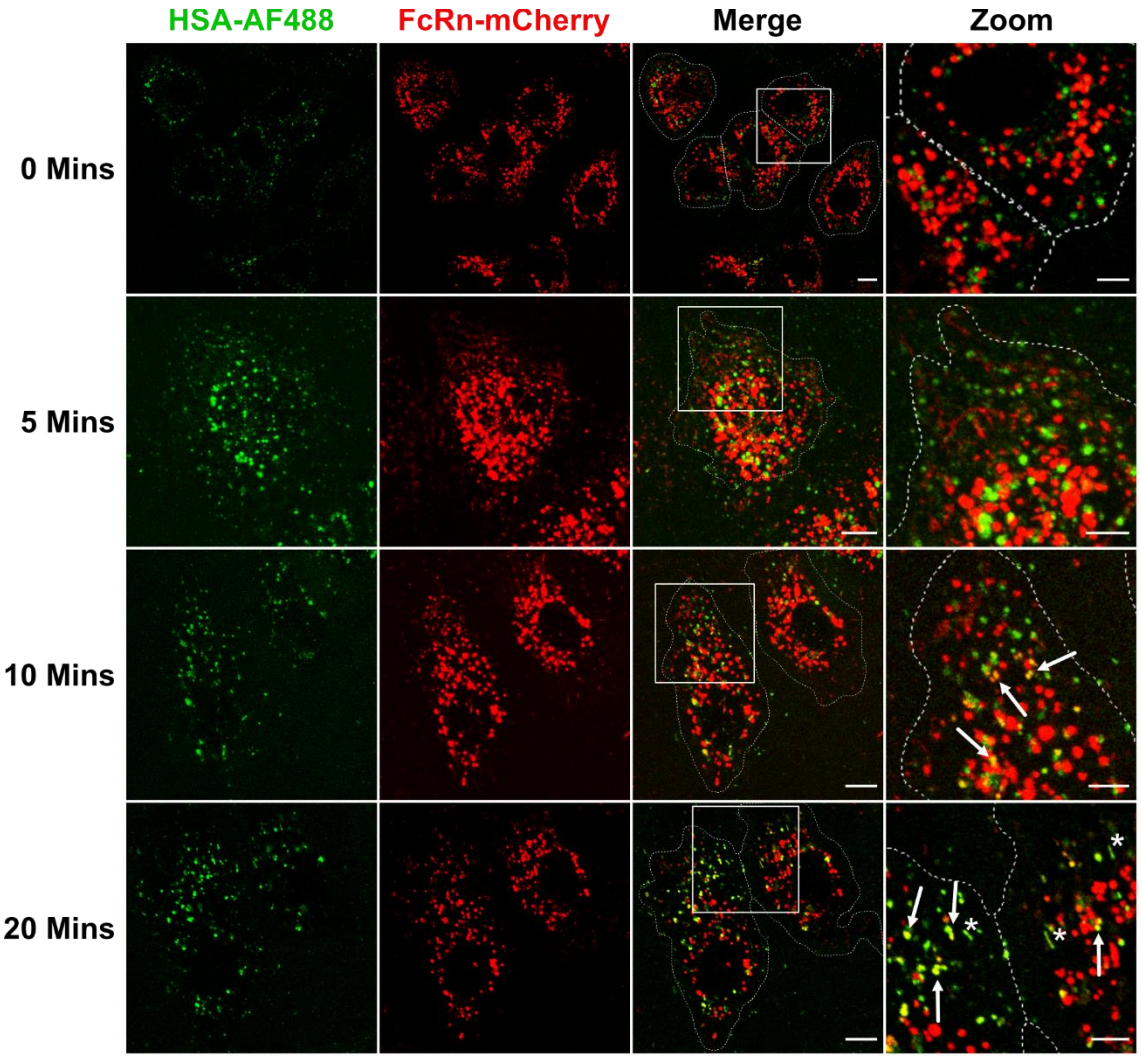

Figure 4.24: Intracellular HSA-AF488 trafficking in FcRn-mCherry transduced live BOECs
BOECs transduced with FcRn-mCherry (red) were pulsed with Alexa Fluor® 488-labelled HSA (HSA-AF488, green) for 15 minutes at 37 °C and the fluorescent signal chased for 40 minutes in live cells. Confocal microscopy images of live cells were taken right after the pulse as well as 5, 10 and 20 minutes chase. White arrows indicate HSA-AF488- and FcRn-mCherry-double-positive endosomal structures. White asterisks indicate HSA-AF488-positive tubular transport carriers. Cell boundaries are indicated by dotted lines. Scale bars represent 5 µm (Zoom) or 10 µm (Merge).

In addition to the globular structures, HSA-AF488 tubular carriers were detected after 20 minutes chase time (indicated by white asterisks) (Figure 4.24). Such tubular structures were detected usually after 20 – 30 minutes chase time across

several experiments. From the time lapse of the live cells, these tubular carriers were observed pinching off globular endosomal structures. Although predominantly positive for HSA-A488, FcRn-mCherry fluorescence was detected in some of these tubular structures suggesting the potential sorting of both HSA and FcRn into tubular carriers emerging from double-positive globular endosomes.

With ongoing chase time, tubular structures positive for HSA-A488 and FcRn-mCherry were observed more frequently (Figure 4.25 and Figure 4.26). To examine if tubular carriers are directed to the cell periphery, several frames of region of interests (ROIs) with 1-minute intervals were recorded between 25 to 28 minutes chase time (Figure 4.25).

The inspection of single frames revealed that HSA-AF488-positive tubular carriers, indicated by white arrows, directly emerged from HSA-AF488- and FcRn-mCherry-double-positive globular endosomal structures and, by assessing the replacement of tubular carriers between single frames, were directed to the cell surface rather than being trafficked to the perinuclear region of the cell (Figure 4.25). As described above, FcRn-mCherry fluorescence was detected in a fraction of tubular carriers, however they were predominantly positive for HSA-AF488.

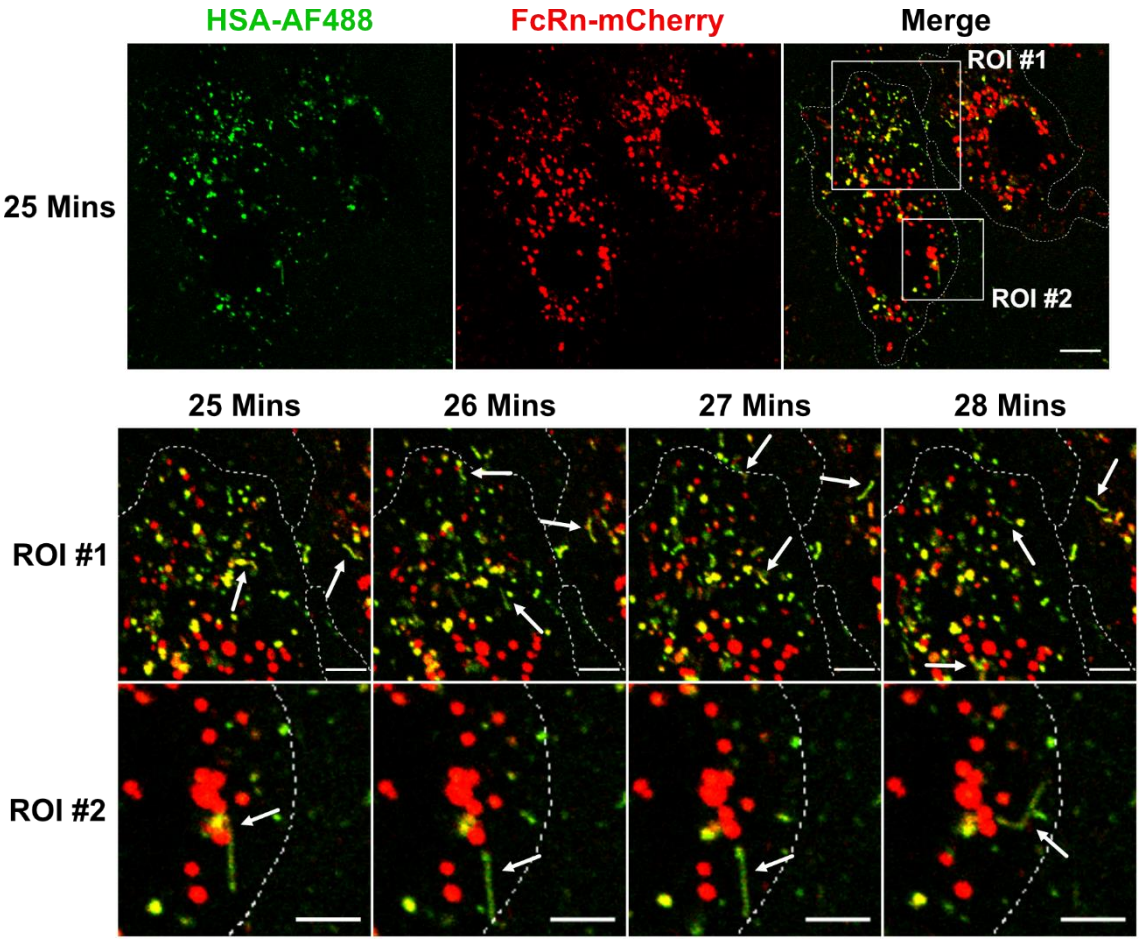

Figure 4.25: Emergence of HSA-AF488 tubular transport carriers in FcRn-mCherry transduced live BOECs
BOECs transduced with FcRn-mCherry (red) were pulsed with Alexa Fluor® 488-labelled HSA (HSA-AF488, green) for 15 minutes at 37 °C and the fluorescent signal chased for 40 minutes in live cells. Confocal microscopy images of live cells were taken after 25, 26, 27 and 28 minutes chase. Two regions of interest (ROIs) were defined to follow the itinerary of single tubular transport carriers. White arrows indicate HSA-AF488-positive tubular transport carriers. Cell boundaries are indicated by dotted lines. Scale bars represent 5 µm (ROI images) or 10 µm (Merge).

The emergence of HSA-A488- and partially FcRn-mCherry-positive tubular transport carriers, indicated by white arrows, was detected up to the end of the 40 minutes chase period (Figure 4.26A). Interestingly, after 40 minutes of chase tubular transport carriers exclusively positive for FcRn-mCherry, indicated by sky blue arrows, were detected for the first time over the course of the pulse-chase

experiment (Figure 4.26A). Similar to tubular carriers observed earlier, they emerged directly from globular endosomal structures.

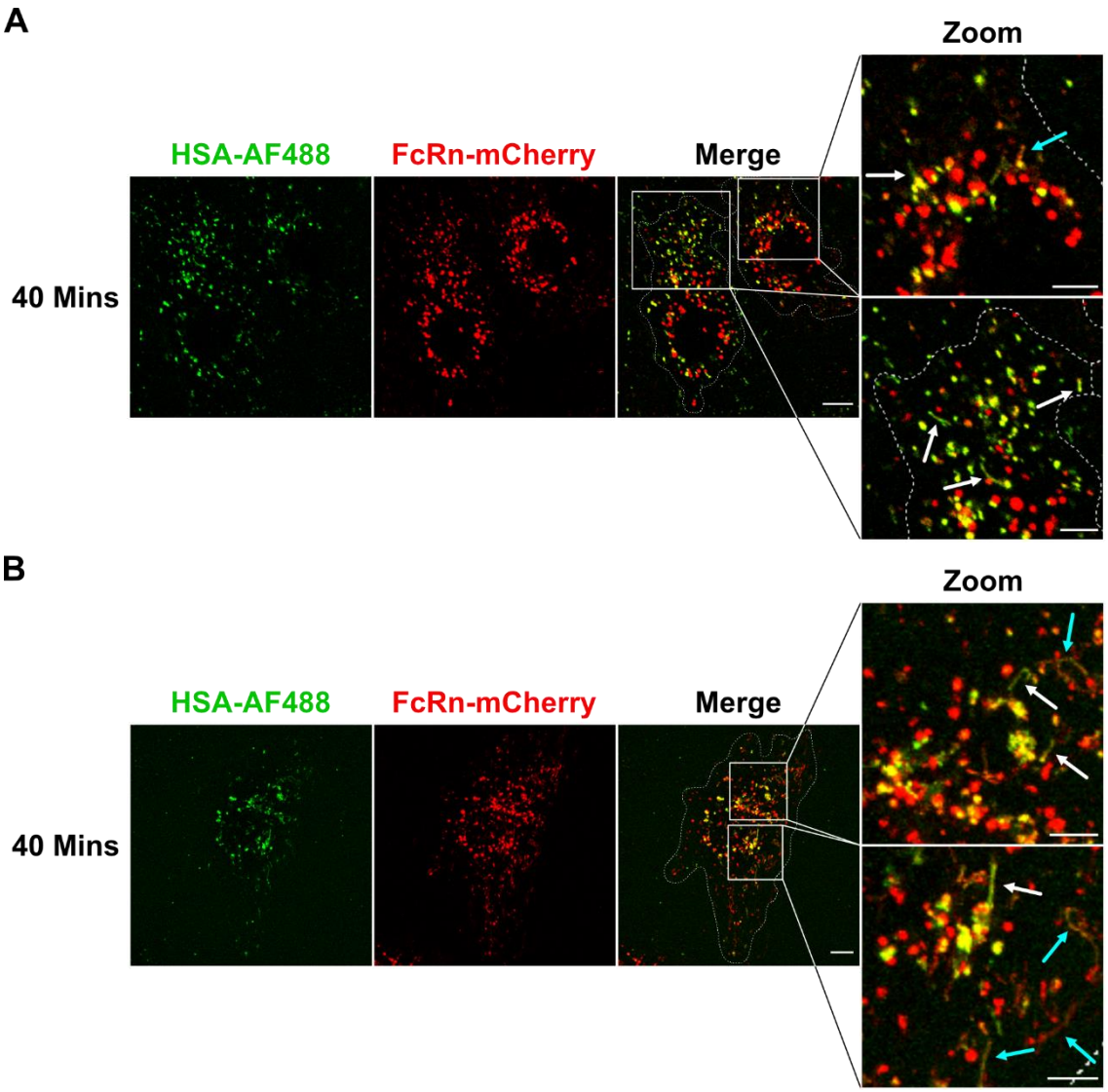

Figure 4.26: HSA-AF488- and FcRn-mCherry-double-positive tubular transport carriers in FcRn-mCherry transduced live BOECs
BOECs transduced with FcRn-mCherry (red) were pulsed with Alexa Fluor® 488-labelled HSA (HSA-AF488, green) for 15 minutes at 37 °C and the fluorescent signal chased for 40 minutes in live cells. Single planes **(A)** or z-stacks **(B)** of live BOECs were recorded after 40 minutes chase by confocal microscopy. For the z-stack, the maximum projection is shown. White arrows indicate HSA-AF488- and FcRn-mCherry-double-positive tubular transport carriers. Sky blue arrows indicate FcRn-mCherry-positive tubular transport cariers. Cell boundaries are indicated by dotted lines. Scale bars represent 5 µm (Zoom) or 10 µm (Merge).

To further assess the direction of detected tubular transport carriers and characterise their dimensions, z-stacks of whole live BOECs were recorded after 40 minutes of chase and displayed as maximum projections (Figure 4.26B). This allowed to better follow entire tubular transport carriers, usually emerging along the z axis, and leaving the focal plane of single observation planes, throughout the cell. Investigation of projected whole cell stacks revealed the existence of numerous tubular transport carriers positive for HSA-AF488 and FcRn-mCherry, indicated by white arrows. Additionally, FcRn-positive tubular carriers, indicated by sky blue arrows, were identified which were negative or only faintly positive for HSA-AF488 (Figure 4.26B). These tubular carriers were 0.5 – 0.6 µm thick and reached lengths up to 7 µm.

Collectively, these data revealed that immediately following endocytosis, AF488-labelled HSA was located to globular endosomal structures devoid of FcRn-mCherry. Subsequently, both HSA-AF488 and FcRn-mCherry were observed to co-localise after 10 minutes of chase and, with increasing chase time, HSA-AF488-positive transport carriers were observed to emerge from globular double-positive structures. After 40 minutes of chase, before endocytosed cargo starts to be degraded in the lysosomes of BOECs, tubular carriers continued to emerge from globular compartments; a subpopulation of tubules predominantly positive for FcRn-mCherry were observed indicating that the receptor is able to be sorted into tubular transport carriers independently from HSA.

4.2.7.3: Intracellular trafficking of rHSA^{H464Q}-AF488 in FcRn-mCherry transduced live BOECs

To evaluate if the sorting of endocytosed HSA molecules is dependent on the interaction with FcRn, pulse-chase experiments using the non-FcRn binding albumin variant rHSA^{H464Q}-AF488 were performed (Figure 4.27). Similar to HSA-AF488, rHSA^{H464Q}-AF488 was located to globular endosomal structures immediately following endocytoses and with increasing chase time co-localisation with FcRn-mCherry was observed in some compartments (Figure 4.27A). After

25 minutes chase time, tubular transport carriers positive for FcRn-mCherry, indicated by white arrows, were detected emerging from double-positive endosomal structures (Figure 4.27A). The inspection of multiple frames over a 5-minute time span (between 25 – 30 minutes chase) revealed that rHSA^{H464Q}-AF488 was excluded from FcRn-mCherry-positive tubules indicating an active sorting of FcRn-mCherry, but not of rHSA^{H464Q} molecules, into these tubular transport carriers.

With increasing chase time up to 40 minutes, co-localisation of rHSA^{H464Q}-AF488 and FcRn-mCherry persisted in globular endosomal structures (Figure 4.27B). In addition, FcRn-mCherry-positive tubular transport carriers (indicated by white arrows) continued to emerge from double-positive globular structures and rHSA^{H464Q}-AF488 remained excluded from tubular carriers emerging from endosomes (Figure 4.27B).

Together, these data suggested that FcRn-mCherry is actively partitioned into the tubular transport carriers originating from globular endosomal structures. In contrast, rHSA^{H464Q}-AF488, a non-FcRn binding albumin variant, is excluded from tubular carriers suggesting that binding to FcRn is a prerequisite for HSA molecules to be sorted, together with the receptor, into these tubular compartments.

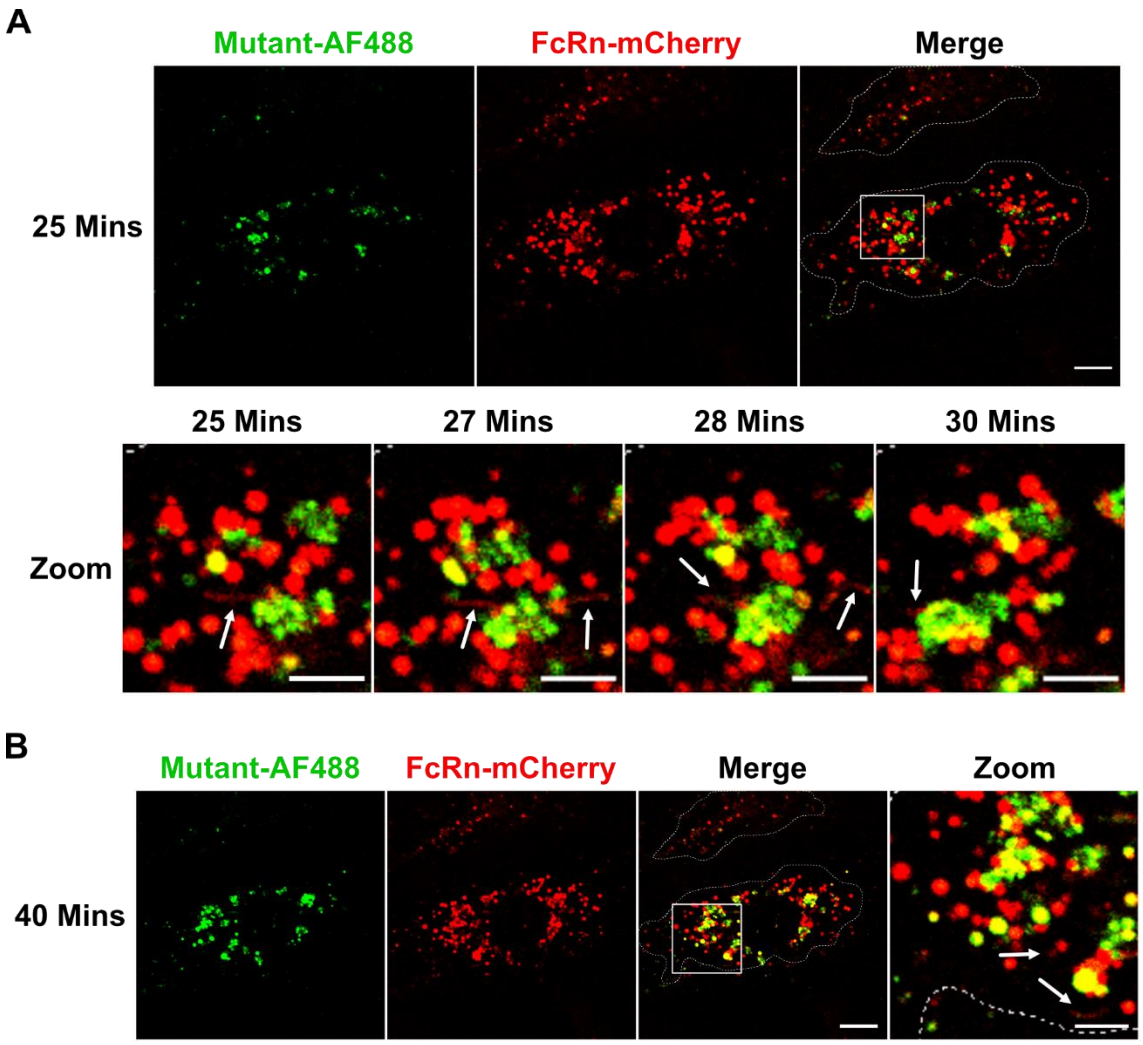

Figure 4.27: Trafficking of AF488-labelled rHSA^{H464Q} in FcRn-mCherry transduced live BOECs

BOECs transduced with FcRn-mCherry (red) were pulsed with Alexa Fluor® 488-labelled rHSA^{H464Q} (Mutant-AF488, green) for 15 minutes at 37 °C and the fluorescent signal chased for 40 minutes in live cells. Confocal microscopy images of live cells were taken after 25, 27, 28 and 30 minutes chase **(A)**.Additionally, images were taken after 40 minutes chase **(B)**. White arrows indicate FcRn-mCherry-positive tubular transport carriers. Cell boundaries are indicated by dotted lines. Scale bars represent 5 µm (Zoom) or 10 µm (Merge).

4.2.7.4: Co-uptake and intracellular trafficking of rHSA^{H464Q}-AF488 and HSA-AF568 in live BOECs

To assess the FcRn-dependent partitioning of HSA molecules into tubular transport carriers, a co-uptake experiment was performed using AF488-labelled rHSA^{H464Q} and AF568-labelled wildtype HSA and the fluorescence signal chased for up to 40 minutes (Figure 4.28). Both HSA variants co-localised to globular endosomal structures in the cell periphery following endocytosis for the first 25 minutes (data not shown). After 25 minutes, tubular transport carriers positive for HSA-AF568 (indicated by white arrows) were detected emerging from double-positive globular endosomes (Figure 4.28A). With increasing chase time, these structures were observed more frequently and rHSA^{H464Q}-AF488 remained excluded from these HSA-AF568-positive tubular transport carriers.

Closer inspection of regions of interest (ROIs) after 32 minutes chase time revealed that these tubular carriers indeed pinched off from the rHSA^{H464Q}- and HSA-double-positive globular structures, however fluorescence signals specific for HSA-A568 were exclusively detected in tubular transport carriers, whereas rHSA^{H464Q} was not partitioned into tubular structures (Figure 4.28B). Comparing single frames of the same ROIs at different chase times (32, 34, 38 and 40 minutes chase) suggested that the HSA-AF568-positive tubular transport carriers preferentially emerged in the cell periphery rather than in the perinuclear region of the cell and were directed to the edges of the cell.

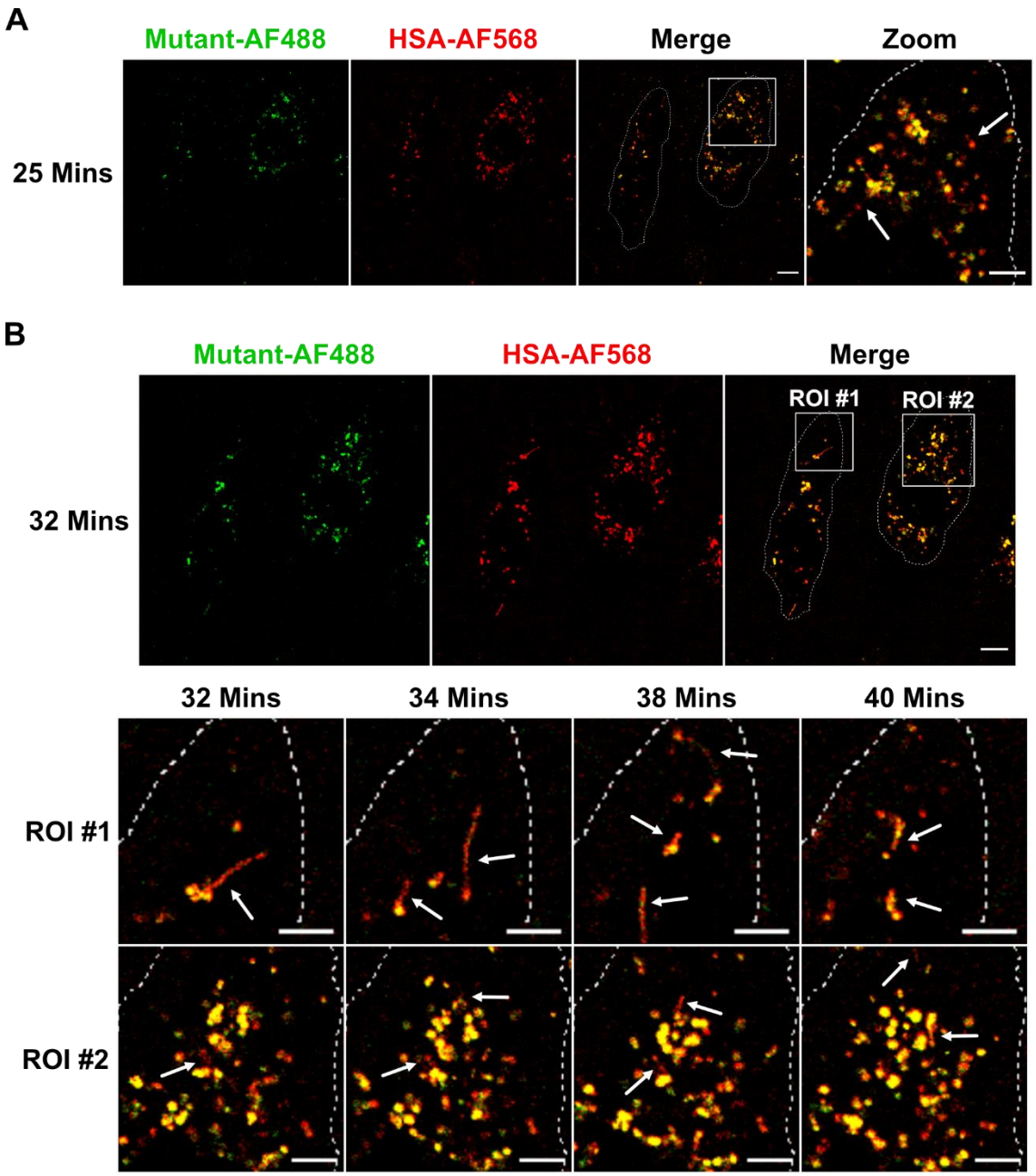

Figure 4.28: Trafficking of rHSA^{H464Q}-AF488 and HSA-AF568 in live BOECs BOECs were pulsed with Alexa Fluor® A488-labelled rHSA^{H464Q} (Mutant-AF488, green) and Alexa Fluor® 568-labelled HSA (HSA-AF568, red) for 15 minutes at 37 °C and the fluorescent signals chased for 40 minutes in live cells. Confocal microscopy images of live cells were taken after 25 minutes chase **(A)** or between 32 and 40 minutes chase **(B)**. Two regions of interest (ROIs) were defined to follow the itinerary of single tubular transport carriers. White arrows indicate HSA-AF568-positive tubular transport carriers. Cell boundaries are indicated by dotted lines. Scale bars represent 5 µm (zoomed images) or 10 µm (Merge).

In conclusion, these data revealed, based on qualitative assessment, that fluorescently wildtype HSA and non-FcRn binding rHSA^{H464Q} molecules are partitioned differentially within the endosomal network of live BOECs. AF568-HSA molecules were detected in tubular transport carriers emerging from globular endosomal structures, whereas non FcRn-binding rHSA^{H464Q}-AF488 was excluded from these tubular structures suggesting a FcRn-dependent sorting mechanism in endosomal structures mediating the partitioning of FcRn and its ligand into tubular carriers, which preferentially propagated towards the cell periphery and the surface of the cell.

4.3: Discussion

The vascular endothelium, comprised of a cellular monolayer lining the inner walls of blood vessels, is considered to be an important regulator of FcRn-mediated homeostasis *in vivo* (Pyzik *et al.*, 2019). Although albumin endocytosis and FcRn-mediated recycling of albumin has been described in immortalised endothelial cell lines, there is still a substantial gap of knowledge about FcRn-albumin cell biology in primary vascular endothelial cells due to the lack of a suitable primary cell models (Schmidt *et al.*, 2017; Grevys *et al.*, 2018). In this chapter, I have established vascular endothelial cell lines isolated from peripheral blood to study FcRn-albumin cell biology in primary human endothelial cells. I revealed that these blood outgrowth endothelial cells (BOECs) expressed FcRn located predominantly to EEA1-positive early endosomal structures, but not to late endosomes or lysosomes, and that BOECs are able to endocytose HSA efficiently via macropinocytosis. Endocytosed fluorescently labelled HSA was trafficked through early endosomes but did not co-localise within late endosomal compartments 60 minutes following endocytosis. Lentiviral transduction of FcRn-mCherry into BOECs revealed that the receptor was located within a highly dynamic tubulovesicular network and that endocytosed HSA molecules, able to bind FcRn, are sorted into FcRn-positive tubular carriers, whereas non-binding HSA variant rHSA^{H464Q} is excluded from tubular structures, indicating FcRn-

dependent rescue of endocytosed HSA in BOECs and recycling back to the plasma membrane.

Since the discovery of circulating endothelial progenitor cells in peripheral blood, many studies have focussed on exploiting the proliferative capacity of these progenitor cells to establish stable primary cell lines as an *in vitro* model for differentiated endothelial cells (Asahara *et al.*, 1997; Shi *et al.*, 1998). Although several BOEC generation and establishment protocols are available, most of them either require extensive passaging before obtaining stable cell lines and high cell numbers or large volumes of peripheral blood (Lin *et al.*, 2002; Martin-Ramirez *et al.*, 2012; Ormiston *et al.*, 2015). Here, I established a BOEC generation protocol, which only requires 30 ml of peripheral blood and allows the establishment of BOEC lines in T25 flasks after a single initial passaging step (Figure 4.1). BOEC lines established by this protocol maintained proliferative capacities and showed stable expression of the endothelial markers CD144 and vWF up to passage 14, exceeding the maximum passage number (6 – 8) described by other BOEC protocols (Lin *et al.*, 2000; Ecklu-Mensah *et al.*, 2018). However, recent studies highlight potential variability between single endothelial colony forming cell clones resulting in distinct cell morphologies and proliferative as well as functional differences (de Boer *et al.*, 2020). It would be instructive to compare the expression of genes regulating endothelial cell maintenance and function in BOEC clones by RNAseq to assess differences in transcriptomic profiles among single clones as well as transcriptomic stability of BOEC lines across several passages. This is particularly important since the data shown in this work was generated by using polyclonal BOEC lines derived from two individual donors, which might show variances in their genetic profile and their regulation of highly regulated networks such as endosomal trafficking, although no profound differences have been observed throughout this study.

Additionally, I evaluated whether primary BOEC lines are a suitable model for studying FcRn-albumin cell biology by investigating their expression of FcRn and endocytosis of fluorescently labelled HSA. BOECs expressed FcRn endogenously and the receptor was predominantly associated with enlarged

EEA1-positive endosomal structures, presumably early macropinosomes and early endosomes, whereas FcRn was excluded from late endosomes (Figure 4.7 and Figure 4.8). These findings are consistent with intracellular localisation of transgenic FcRn in BMDMs or immortalised cell lines (Ober *et al.*, 2004; Ward *et al.*, 2005; Mahmoud, 2015). In the latter, FcRn was additionally found to be associated with Rab11-positive recycling endosomes (Ward *et al.*, 2005). Unfortunately, the co-localisation of endogenous FcRn with Rab11-positive compartments could not be assessed because FcRn- and Rab11-specific antibodies were not compatible for obtaining consistent staining patterns using any of the fixation protocols. Transgenic FcRn-mCherry expressed by transduced BOECs was partially co-localised with fluorescently labelled transferrin shown to co-localise with transgenic Rab11-GFP-positive structures indicating potential association of FcRn with recycling endosomal compartments to some extent in BOECs (Figure 4.13). The introduction of Rab11-GFP via lentiviral transduction of BOECs could be a strategy to overcome this technical issue.

Cultured BOEC lines were capable of performing efficient albumin endocytosis via constitutive fluid phase endocytosis and high amounts of intracellular albumin fluorescent levels were detected after 15 – 30 minutes of uptake (Figure 4.14), whereas albumin internalisation by immortalised cell lines is mostly inefficient and high albumin levels are detected 1 – 4 hours of incubation, even under acidic conditions (Schmidt *et al.*, 2017; Grevys *et al.*, 2018; Nilsen *et al.*, 2020). Endocytosis of fluorescently labelled HSA by BOECs was sensitive to the macropinocytosis-selective inhibitor EIPA identifying macropinocytosis as major endocytic pathway for the uptake of extracellular albumin (Figure 4.15). In contrast, albumin internalisation in rat pulmonary microvascular endothelial cells is facilitated by surface-exposed glycoprotein 60 (gp60) binding and caveolin-dependent endocytosis highlighting potential differences in HSA uptake and trafficking across different donor species and endothelial cell origins (Vogel *et al.*, 2001; John *et al.*, 2003; Li *et al.*, 2013). Macropinocytosis has been identified as the major uptake albumin uptake pathway in cultured BMDMs and is also considered to be an important regulator of albumin homeostasis *in vivo* due to the abundancy of solute albumin in blood (Commisso, 2019; Toh *et al.*, 2020).

Hence, the ability to perform HSA fluid-phase endocytosis via macropinocytosis is a major advantage of using primary BOEC lines to investigate FcRn-albumin cell biology under physiologically relevant conditions compared to studies using immortalised cell lines, as the later required, firstly, the introduction of transgenic FcRn to facilitate efficient albumin endocytosis and, secondly, non-physiologically conditions for albumin uptake, namely acidic conditions to allow albumin to bind surface-exposed transgenic FcRn to initiate receptor-mediated endocytosis of the receptor-ligand complex (Schmidt *et al.*, 2017; Larsen *et al.*, 2018; Grevys *et al.*, 2018). Nonetheless, the contribution of other endocytic pathways in addition to macropinocytosis for HSA uptake by BOECs cannot be excluded from my study. In particular, the inhibition of macropinocytosis might lead to compensatory HSA endocytosis via other endocytic pathways explaining the intracellular albumin levels in EIPA-treated BOECs detected by flow cytometry compared to the control (Figure 4.15E-F). It would be instructive to perform HSA uptake experiments in the presence of inhibitors of other endocytic pathways, such as methyl-β-cyclodextrin which blocks caveolae-dependent endocytosis, to assess the contribution of alternative HSA uptake pathways by cultured BOECs.

Following endocytosis, HSA was located to enlarged EEA1-positive endosomal structures in fixed BOECs and subsequently transited EEA1-positive early endosomes with ongoing chase time (Figure 4.19). In contrast to the non-binding HSA mutant rHSA^{H464Q}, wildtype HSA was not associated with markers of the late endosomal/lysosomal structures over the chase time, indicating the avoidance of the degradative lysosomal pathway (Figure 4.20 and Figure 4.21). However, the analysis in my study was only assessed by line scans and not by calculation of co-localisation parameters, due to the predominant localisation of CD63- and LAMP1-positive endosomal structures to the perinuclear cloud of BOECs, a region highly dense in endosomal structures around the nucleus where relatively immobile endosomal populations, in particular endolysosomes, cluster together and might impact the quantification of co-localisation parameters (Jongsma *et al.*, 2016; Bonifacino and Neefjes, 2017).

To further investigate FcRn-dependent HSA trafficking within cultured BOECs, I used live cell imaging to assess whether there are distinct intracellular itineraries for wildtype HSA and the non-FcRn binding mutant rHSA^{H464Q}. To this end, transgenic FcRn-mCherry was introduced into cultured BOECs by lentiviral transduction (Figure 4.10). The introduction of transgenes into BOECs using lentiviral constructs had been described previously and the availability of these genetic tools make cultured BOECs an excellent cell model to investigate cell biological pathways in primary endothelial cells (Matsui *et al.*, 2007; Coppens *et al.*, 2013; Schillemans *et al.*, 2019). In particular, the ability of BOECs to maintain their phenotype and function across several passages enables the potential generation of knock-out BOEC lines or establish overexpression of particular genes in BOECs using CRISPR/Cas-engineering (Schillemans *et al.*, 2019). FcRn-KO or FcRn-overexpressing BOEC lines could be used to evaluate the importance of FcRn expression in regulating intracellular trafficking of endocytosed HSA molecules in primary endothelial cells.

In FcRn-mCherry transduced live BOECs, endocytosed HSA-AF488 was co-localised with FcRn-mCherry-positive endosomal structures 10 – 15 minutes after uptake (Figure 4.24) indicating distinct uptake pathways of the receptor and the soluble FcRn ligand from the cell surface. These findings are similar to observations made in primary macrophages (BMDMs), where FcRn uptake is presumably mediated by clathrin-mediated endocytosis whereas albumin is endocytosed via macropinocytosis (Figure 4.29) (Mahmoud, 2015). The emergence of HSA-AF488- and FcRn-mCherry-double-positive tubules was observed after 20 – 30 minutes uptake in live BOECs (Figure 4.29), whereas the non-FcRn binding rHSA^{H464Q}-AF488 was excluded from FcRn-mCherry-positive tubules emanating from globular endosomal structures (Figure 4.27) suggesting a FcRn-dependent sorting of the receptor-ligand complex from acidified endosomes into tubular transport carriers directed to the cell periphery (Figure 4.25). These results are in line with findings in BMDMs where wildtype HSA, but not rHSA^{H464Q}, is able to enter SNX5-positive tubules in a FcRn-mediated process for recycling of the ligand back to the plasma membrane (Toh *et al.*, 2020). Unfortunately, attempts to directly demonstrate FcRn-dependent

HSA recycling to the cell surface by BOEC were unsuccessful, by either Western Blot or ELISA of the spent medium, due to lack of sensitivity (data not shown). However, the velocities (~ 0.4 µm/s) (Figure 4.12) and morphology (0.5 – 0.6 µm diameter, 5 – 7 µm long) (Figure 4.11 and Figure 4.26) of FcRn-mCherry and HSA-AF488-positive tubular carriers observed resemble the phenotype of SNX5-positive tubular transport carriers mediating FcRn-dependent recycling of endocytosed HSA in primary BMDMs (Van Weering *et al.*, 2012; Allison *et al.*, 2013; Toh *et al.*, 2020), suggesting a similar function of the tubules observed in cultured BOECs. Additionally, co-uptake of fluorescently labelled wildtype HSA and non-FcRn binding rHSA^{H464Q} revealed that, although both ligands were co-localised in globular endosomal structures, only wildtype HSA was sorted into tubular transport carriers, a process presumably mediated by interaction with FcRn in live BOECs (Figure 4.28). The emergence of HSA-positive transport carriers emanating from globular structures was observed before internalised cargo is degraded in late endosomes and lysosomes of live BOECs which is estimated to occur 45 – 60 minutes after cargo uptake (Figure 4.29), as assessed by DQ-OVA uptake experiments (Figure 4.16 and Figure 4.22).

Together these data, albeit only qualitative, revealed distinct intracellular itineraries of wildtype HSA and non-FcRn binding rHSA^{H464Q} in live BOECs mediated by FcRn. The interaction of wildtype HSA with FcRn in early or maturing macropinosomal structures led to the sorting of the ligand-receptor complex into tubular transport carriers, whereas non-FcRn binding rHSA^{H464Q} was excluded from these tubules and eventually was trafficked to late endosomes and lysosomes where the internalised cargo is degraded (Figure 4.29). However, it remains unclear at which stage of macropinosome maturation HSA and FcRn interact and partitioning of the receptor-ligand complex is facilitated. Newly formed macropinosomes were found to be initially devoid of EEA1 and instead are enriched in phosphatidylinositol 3-phosphate (PtdIns(3)P) (Kerr *et al.*, 2006). During their maturation, macropinosomes acquire SNX5 and the early endosome markers EEA1 and Rab5 before eventually fusing with late endosomes and lysosomes (Lim *et al.*, 2008; Kerr and Teasdale, 2009). However, the exact

mechanism and regulation of macropinosome maturation in different cell types is poorly understood.

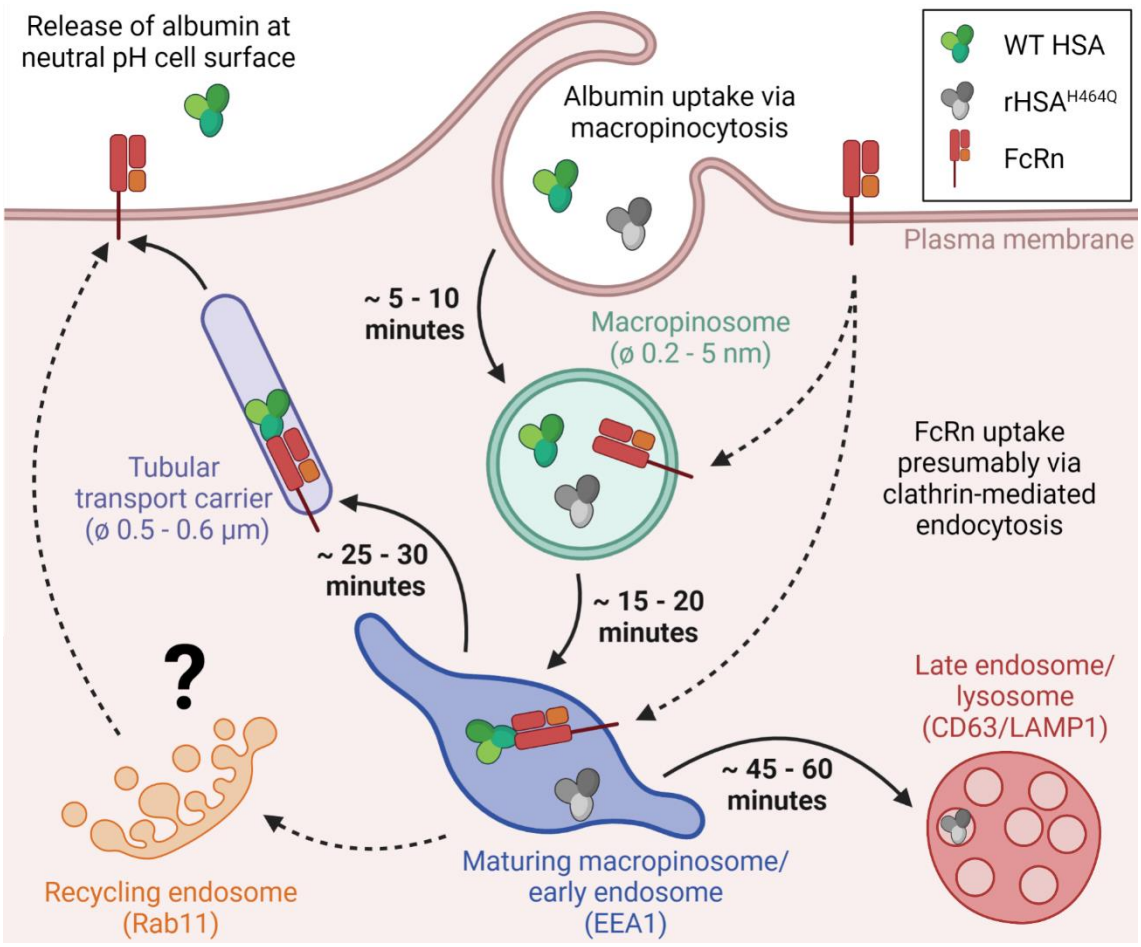

Figure 4.29: Intracellular albumin trafficking in cultured blood outgrowth endothelial cells
Cartoon showing the intracellular trafficking pathways of wildtype (WT) HSA (green) and the non-binding mutant rHSA^{H464Q} (grey) mediated by FcRn (red/orange). Albumin and rHSA^{H464Q} are endocytosed predominantly via macropinocytosis and co-localise with membrane bound FcRn in maturing macropinosomes and early endosomes (light green and blue) 15 – 20 minutes after uptake. Presumably, FcRn is internalised via clathrin-mediated endocytosis. rHSA^{H464Q} mutant reaches late endosomes and lysosomes (red) 45 – 60 minutes after uptake and is degraded, whereas WT HSA is sorted into tubular transport carriers (purple) emanating from globular endosomes in a FcRn-dependent manner 25 – 30 minutes after endocytosis. These tubular transport carriers presumably mediate FcRn-dependent albumin recycling back to the cell surface, either directly or via other compartments such as recycling endosomes (orange). The figure was created with BioRender.com.

In particular, it is uncertain how HSA-positive maturing macropinosomes acquire FcRn which was shown to be internalised by clathrin-mediated endocytosis and subsequently localises predominantly to EEA1-positive early endosomes in immortalised HeLa cells (Mahmoud, 2015). The localisation of FcRn to enlarged EEA1-positive endosomal structures in BOECs suggested that the receptor might be directly sorted to maturing macropinosomes after internalisation from the cell surface (Figure 4.6 and Figure 4.7). It would also be possible that maturing early macropinosomes undergo homotypic fusion or fusion events with classical EEA1-positive endosomes to acquire additional FcRn for facilitating recycling of HSA. Understanding the spatiotemporal dimensions of the HSA interaction with FcRn in BOECs would be particularly useful understanding the endocytic pathway of FcRn and reveal how FcRn is trafficked to maturing macropinosomes containing endocytosed HSA.

It remains unclear whether HSA and FcRn-mCherry-positive tubular transport carriers observed in BOECs facilitate direct FcRn-mediated HSA recycling from early or maturing macropinosomes to the cell surface, as described for BMDMs, or if other endosomal compartments such as Rab11-positive recycling endosomes, as described for immortalised cell lines, are involved in this process (Chia *et al.*, 2018; Toh *et al.*, 2020).

The quantification of HSA recycling in cultured BOECs remains a major challenge, in particular due to low FcRn expression levels compared to BMDMs isolated from hFcRn$^{Tg/Tg}$ (line 276) mice (Figure 4.6A-B). FcRn-dependent albumin recycling was found to be a saturable process and hFcRn $^{Tg/Tg}$ BMDMs were shown to recycle ~ 50 % of endocytosed HSA molecules back to the cell surface (Bern *et al.*, 2015; Toh *et al.*, 2020). FcRn expression in BOECs was 6- to 7-fold lower compared to hFcRn$^{Tg/Tg}$ BMDMs suggesting significantly lower HSA recycling capacities of cultured BOECs which bears technical difficulties for detecting low amounts of recycled albumin in cell supernatants (Figure 4.6A-B). In contrast, kinetics of cargo transport from early endosomes to late endosomes and lysosomes in endothelial cells (~ 45 – 60 minutes) were considerably slower compared to CSF-1 activated BMDMs (~ 15 – 20 minutes) (Toh *et al.*, 2020)

which would allow more time for FcRn to rescue endocytosed albumin molecules from lysosomal degradation and compensate for lower FcRn expression levels. Therefore, it would be instructive to quantify albumin recycling by BOECs over an extended time. However, measuring recycling, especially over long periods, is complicated by the potential reuptake of recycled albumin via fluid phase macropinocytosis and has to be considered in the experimental setup.

Another consideration of the differences between endothelial cells and macrophages is that macrophages are highly specialised cells performing bulk endocytosis of components in their extracellular environment *in vivo* (Lim *et al.*, 2012). As consequence, endocytosed membrane components of BMDMs, such as lipids or membrane receptors, need to be recycled back to the plasma membrane in an efficient and rapid manner (Cox *et al.*, 2000). In contrast, endothelial cells *in vivo* act as a selective permeability barrier regulating the influx and efflux of molecules from the bloodstream to the extravascular space (Mehta and Malik, 2006). Despite being the most abundant protein in blood, ~ 66 % of total albumin mass *in vivo* is located to the extravascular space suggesting an important role of the endothelium in maintaining albumin homeostasis by mediating transcytosis of albumin from the circulation into the extravascular space (Sleep *et al.*, 2013). Hence, it would be advisable to investigate if other cell biological processes such as transcytosis play a role in intracellular trafficking of albumin in BOECs by performing trans-well assay using polarised cells or using three-dimensional vascular models formed by BOECs embedded in Matrigel (Dauwe *et al.*, 2016).

FcRn-mediated albumin trafficking and potential recycling can be further investigated by exploiting available genetic tools such as CRISPR/Cas-engineering for establishing FcRn KO BOEC lines to assess the intracellular itinerary of albumin in absence of the receptor (Schillemans *et al.*, 2019). Although HSA- and FcRn-mCherry-positive tubules in BOECs resembled SNX5-positive tubular transport carriers in BMDMs, it remains unclear whether SNX5, has a function in macropinosome maturation and FcRn-dependent recycling by BOECs, as for BMDMs (Lim *et al.*, 2012; Lim *et al.*, 2015). Identification of

macropinocytic regulators and the machinery of FcRn-dependent albumin recycling in primary endothelial cells would further enhance the understanding of FcRn-albumin cell biology in a physiologically relevant primary cell and would shed more light on the exact contributions of different cell types to albumin homeostasis *in vivo*.

Chapter 5: Immune tolerance induction in hemophilia A

5.1: Introduction

There are two major limitations in treating hemophilia A (HemA) patients with standard FVIII replacement therapy. Firstly, a prophylactic treatment for preventing bleeding events in HemA patients requires frequent injections (2 – 3 injections per week) of FVIII due the short circulatory half-life of the recombinant protein of about 12 hours *in vivo* (Lillicrap, 2008). This treatment is very cost-intensive and burdensome, especially for young HemA patients (Saxena, 2013). Secondly, standard protein replacement therapy leads to the development of inhibitory anti-FVIII antibodies in about 30 % of patients suffering from severe HemA (Meeks and Batsuli, 2016). These anti-FVIII inhibitory antibodies, also referred to as inhibitors, block functional epitopes of recombinant FVIII (rFVIII) neutralising its function *in vivo* or form immune complexes after binding to FVIII increasing the catabolism of rFVIII and further reducing its circulatory half-life (Lacroix-Desmazes *et al.*, 1999; Ananyeva *et al.*, 2004; Saint-Remy *et al.*, 2004).

To circumvent these issues of protein replacement therapy, several strategies to induce immune tolerance towards FVIII in HemA patients have been investigated (Meeks and Batsuli, 2016; Georgescu *et al.*, 2016). Until today, HemA patients, who developed inhibitors during FVIII replacement therapy, most commonly undergo highly expensive and burdensome immune tolerance induction (ITI) protocols relying on repetitious injections of rFVIII protein up to two times daily (Schep *et al.*, 2018). To reduce costs and especially the burden for patients, a major focus of HemA research is the development of alternative strategies for inducing immune tolerance in HemA patients. In particular, the use of half-life extended FVIII-fusion proteins and the *in vivo* or *in vitro* induction of FVIII-specific regulatory T cells (Tregs) are promising approaches to prevent the formation of FVIII-neutralising antibodies or eliminate pre-existing FVIII inhibitors in HemA patients (Sleep *et al.*, 2013; Pearson *et al.*, 2017; Smith *et al.*, 2020; Pilati and Howard, 2020).

FVIII-Albumin fusion proteins can potentially exploit FcRn-depending recycling pathways upon endocytosis and due to its increased size show lower renal clearance rates leading to the extension of circulatory half-life *in vivo* (Kontermann, 2016). The prolonged presence of the therapeutic protein in the circulatory system could lead to the induction of high zone tolerance towards FVIII in HemA patients minimising the development of inhibitors as well as eradicating pre-existing inhibitors (Diener and Feldmann, 1972; Kontermann, 2016). Additionally, the fusion of FVIII to the self-antigen albumin can lead to altered immune responses due to the presentation of albumin-derived Treg epitopes (Tregitopes) on FVIII-specific B cells (Ing *et al.*, 2016; Faraji *et al.*, 2018). Previous studies in HemA mouse models by the Becker-Gotot laboratory have revealed that the treatment of hemophilic mice with FVIII-Albumin fusion protein leads to reduced numbers of FVIII-specific B cells and lower anti-FVIII IgG titers compared to mice treated with rFVIII products indicating an immune tolerant phenotype towards FVIII in HemA mice receiving FVIII-Albumin fusion proteins (unpublished data). However, it is not known if the coupling of albumin and FVIII by succinimidyl esters, which was used to generate the fusion protein, blocked important epitopes of FVIII leading to the failure of FVIII-specific B cells to recognise and internalise the FVIII-Albumin fusion protein *in vivo*. Furthermore, the underlying mechanisms of immune tolerance induction upon FVIII-Albumin treatment remain poorly understood.

Tregs play an important role in suppressing potentially harmful immune responses against auto- and allo-antigens by directly suppressing immune cells, such as B cells, in a contact-dependent manner initiating apoptosis in these cells (Sakaguchi *et al.*, 2009; Gotot *et al.*, 2018). In addition, Tregs can suppress immune responses indirectly by either secrete immunosuppressive cytokines or cytokine deprivation (Sakaguchi *et al.*, 2008). Studies in the Becker-Gotot laboratory comparing the immune responses against FVIII in HemA and wildtype mice have shown that Tregs are essential for mediating tolerance towards exogeneous FVIII, and preventing the formation of inhibitors, by inducing apoptosis in FVIII-specific B cells via PD-1/PD-L1 signalling (Meißner, 2020). Notably, the induction of FVIII-specific Tregs *in vivo* and *in vitro* followed by

adoptive cell transfer into HemA mice effectively induces tolerance against rFVIII (Smith *et al.*, 2020; Chen *et al.*, 2020). Although there has been progress in understanding the underlying mechanisms of Treg induction over the last decade, a major drawback of using *in vitro* induced Tregs (iTregs) is their poor phenotypic and functional stability as well as the lack of reliable large-scale expansion and induction protocols, in particular for antigen-specific iTregs (Kanamori *et al.*, 2016). In 2019, Akamatsu and colleagues established a protocol for the chemical conversion of naïve and antigen-specific $CD4^+$ T cells into Foxp3-expressing Tregs by inhibition of cyclin-dependent kinase 8 (CDK8) and CDK19 (Akamatsu *et al.*, 2019). The use of this Treg conversion protocol in combination with the *in vitro* expansion of FVIII-specific $CD4^+$ T cells might be a valuable tool for the generation of high numbers of FVIII-specific Tregs *in vitro*, which could be readily examined in adoptive cell transfer experiments to determine if immune tolerance towards FVIII was induced in HemA mice.

In this chapter, I investigated if murine FVIII-specific B cells are able to recognise and internalise FVIII-Albumin fusion protein *ex vivo* by establishing an antigen uptake assay using imaging flow cytometry. In addition, I established an *in vitro* generation protocol for FVIII-specific $CD4^+$ T cells and assessed the potential to convert these antigen-specific cells into immunosuppressive Foxp3-expressing Tregs by inhibition of CDK8/CDK19 signalling.

5.2: Results

5.2.1: Uptake of FVIII-Albumin fusion protein by FVIII-specific B cells

5.2.1.1: Establishment of an in vitro antigen uptake assay for primary B cells using imaging flow cytometry

As described above, the treatment of HemA mice with FVIII-Albumin fusion protein leads to reduced numbers of FVIII-specific B cells and lower anti-FVIII antibody titers compared to mice treated with FVIII protein alone. However, it is not clear whether this immune tolerant phenotype is directly induced by the

presence of FVIII-Albumin fusion protein or if the fusion of FVIII to albumin by succinimidyl ester coupling sterically blocks epitopes of FVIII recognised by FVIII-specific B cells and thereby preventing antigen recognition and subsequent internalisation *in vivo*. To test if FVIII-specific B cells isolated from mouse spleens are able to internalise FVIII-Albumin fusion proteins, I have established an antigen uptake assay using imaging flow cytometry (Figure 5.1A). To this, end freshly isolated splenic B cells were incubated with APC-conjugated FVIII or FVIII-Albumin fusion protein on ice to allow surface binding to occur. Subsequently, unbound antigens were washed away and B cells incubated for up to 60 minutes at 37 °C to allow the internalisation of surface bound FVIII conjugate. Cells were then kept on ice and surface marker staining performed to identify live $B220^+$ B cells. Stained cells were fixed and analysed by imaging flow cytometry using an Amnis® Imagestream® system (Figure 5.1A).

Antigen-specific $B220^+$ B cells were identified, according to their surface expression of B220 and their FVIII-APC- (Figure 5.1B) or FVIII-Albumin-APC-specific fluorescent signal (Figure 5.1C). To assess the intracellular localisation of APC-conjugated FVIII and FVIII-Albumin fusion protein internalisation coefficients were calculated by defining a mask representing the cytosolic volume of the respective cells. The internalisation coefficients reflect the ratio of the APC-specific signal located to the cytosol within the defined mask versus the cell surface (outside of the mask). The calculation of mean internalisation coefficients revealed a significant increase of FVIII internalisation from ~ 0.29 to ~ 0.40 in live FVIII-specific $B220^+$ B cells from 0 minutes to 60 minutes uptake at 37 °C (Figure 5.1D). Similar effects were observed for FVIII-Albumin uptake, where the mean internalisation coefficient gradually increased from ~ 0.33 (0 minutes uptake) to ~ 0.70 (60 minutes uptake) indicating uptake of both proteins by antigen-specific $B220^+$ B cells (Figure 5.1E).

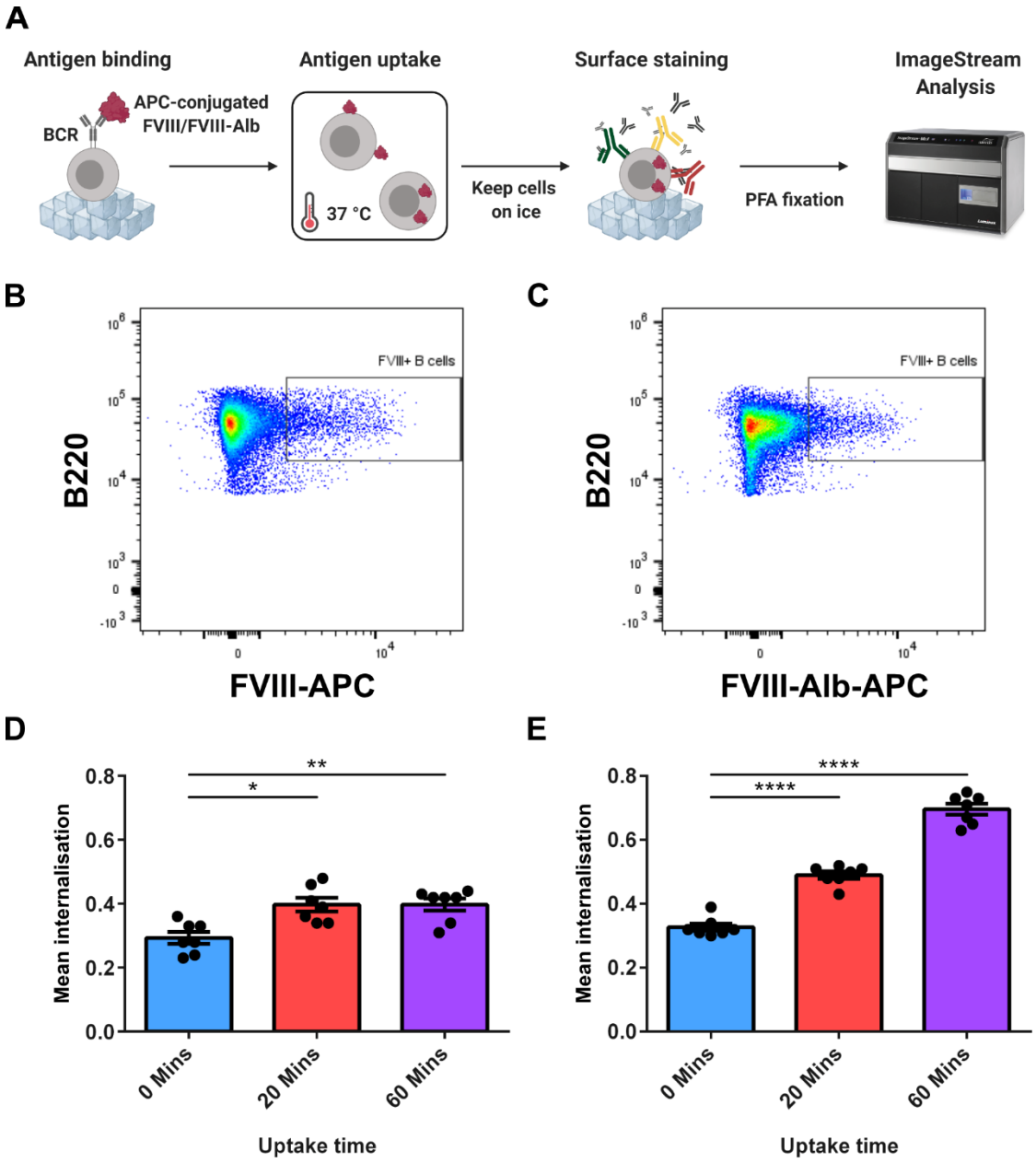

Figure 5.1: Internalisation of FVIII and FVIII-Albumin fusion protein by FVIII-specific B cells *in vitro*

(A) Antigen binding and internalisation assay using freshly isolated B220$^+$ B cells and APC-conjugated FVIII and FVIII-Albumin fusion protein. Antigens were bound on ice for 30 minutes and cells were subsequently incubated at 37 °C for up to 60 minutes to allow antigen internalisation. Afterwards, surface staining was performed on ice, cells were fixed and analysed by imaging flow cytometry using an Amnis® Imagestream® system. BCR, B Cell Receptor. **(B-C)** Representative dot plots for the gating of live FVIII-specific B220$^+$ B cells upon binding of APC-conjugated FVIII **(B)** or FVIII-Albumin fusion protein **(C)**. Samples shown were kept on ice after the antigen binding step (0 minutes uptake time). **(D-E)** Mean internalisation coefficients calculated for live FVIII-specific B220$^+$ B cells after the

uptake of APC-conjugated FVIII **(D)** or FVIII-Albumin fusion protein **(E)**. Cells were allowed antigen uptake for 0 (blue), 20 (red) or 60 minutes (purple), respectively. Internalisation was quantified on B cells isolated from individual mice (n = 7). Errors are shown as SEM. p-values were calculated using a paired one-way ANOVA in combination with Fisher's LSD test. * $p \leq 0.05$, ** $p \leq 0.01$, **** $p \leq 0.0001$

To validate the internalisation of the respective antigen by $B220^+$ B cells, microscopy images obtained by imaging flow cytometry were analysed and the localisation of APC-specific fluorescent signal was assessed in cells following either 0 minutes or 60 minutes uptake of FVIII (Figure 5.2) or FVIII-Albumin fusion protein (Figure 5.3), respectively.

At 0 minutes, both antigens, APC-conjugated FVIII (Figure 5.2) and FVIII-Albumin fusion protein (Figure 5.3), were located to the cell surface of $B220^+$ B cells in a ring-like structure surrounding the cytosolic area of the cells. In contrast, after 60 minutes uptake both antigens were located to intracellular punctate structures within the cytoplasm of the cell suggesting uptake of FVIII (Figure 5.2) and FVIII-Albumin fusion protein (Figure 5.3) by antigen-specific $B220^+$ B cells.

The increase of FVIII and FVIII-Albumin internalisation and the intracellular localisation of both antigens after 60 minutes incubation at 37 °C was observed across several experiments and independent of the genotype of isolated $B220^+$ B cells obtained from HemA or WT B6 mice.

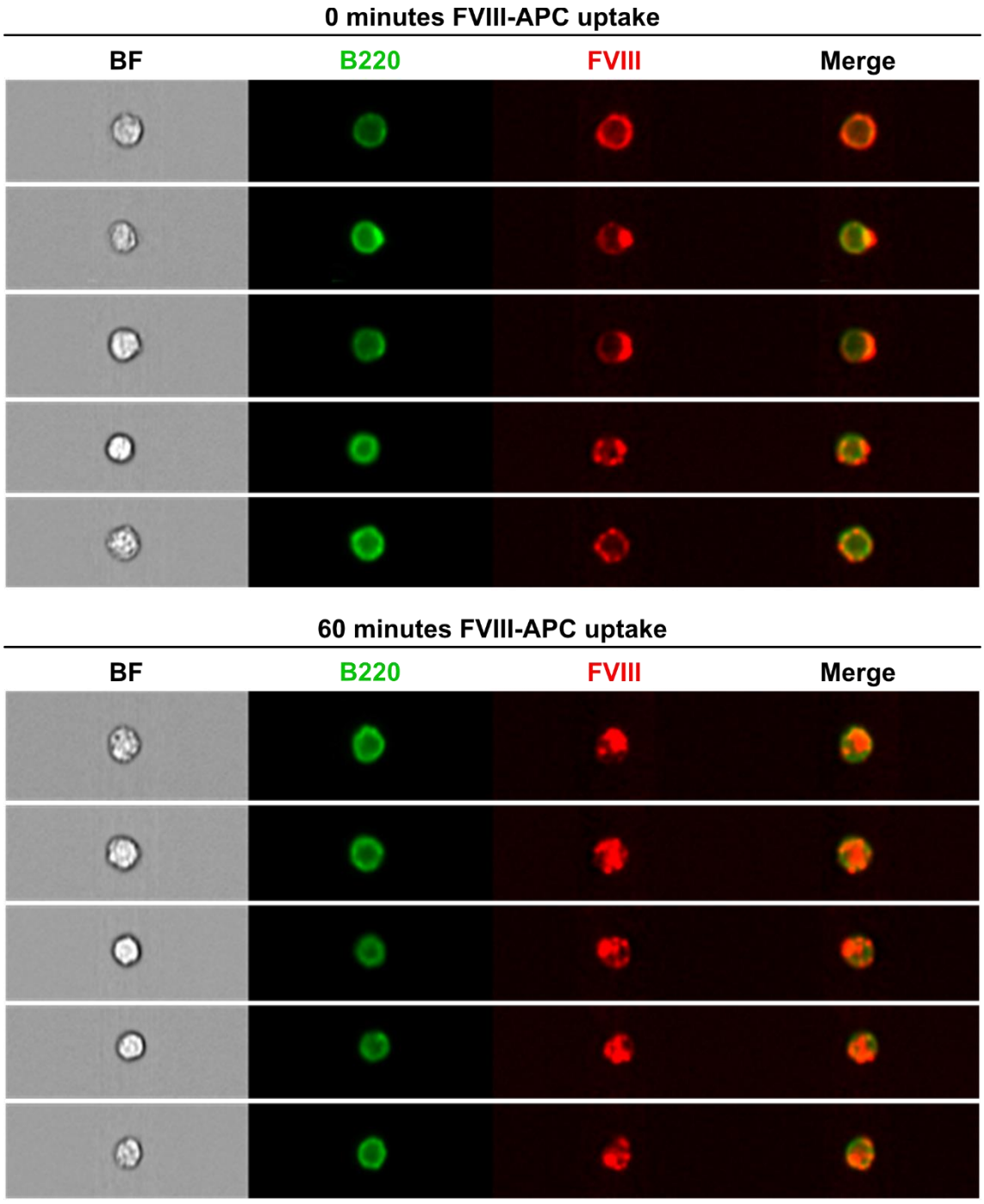

Figure 5.2: Microscopical analysis of recombinant FVIII internalisation by FVIII-specific B cells
Representative microscopy images obtained by imaging flow cytometry showing live B220$^+$ B cells positive for APC-conjugated FVIII following 0 minutes (upper images) or 60 minutes (lower images) antigen uptake. The image panels show signals resulting from the brightfield (BF), B220 (green) and the APC (FVIII, red) channel. Merge shows the overlap of the green and red channel.

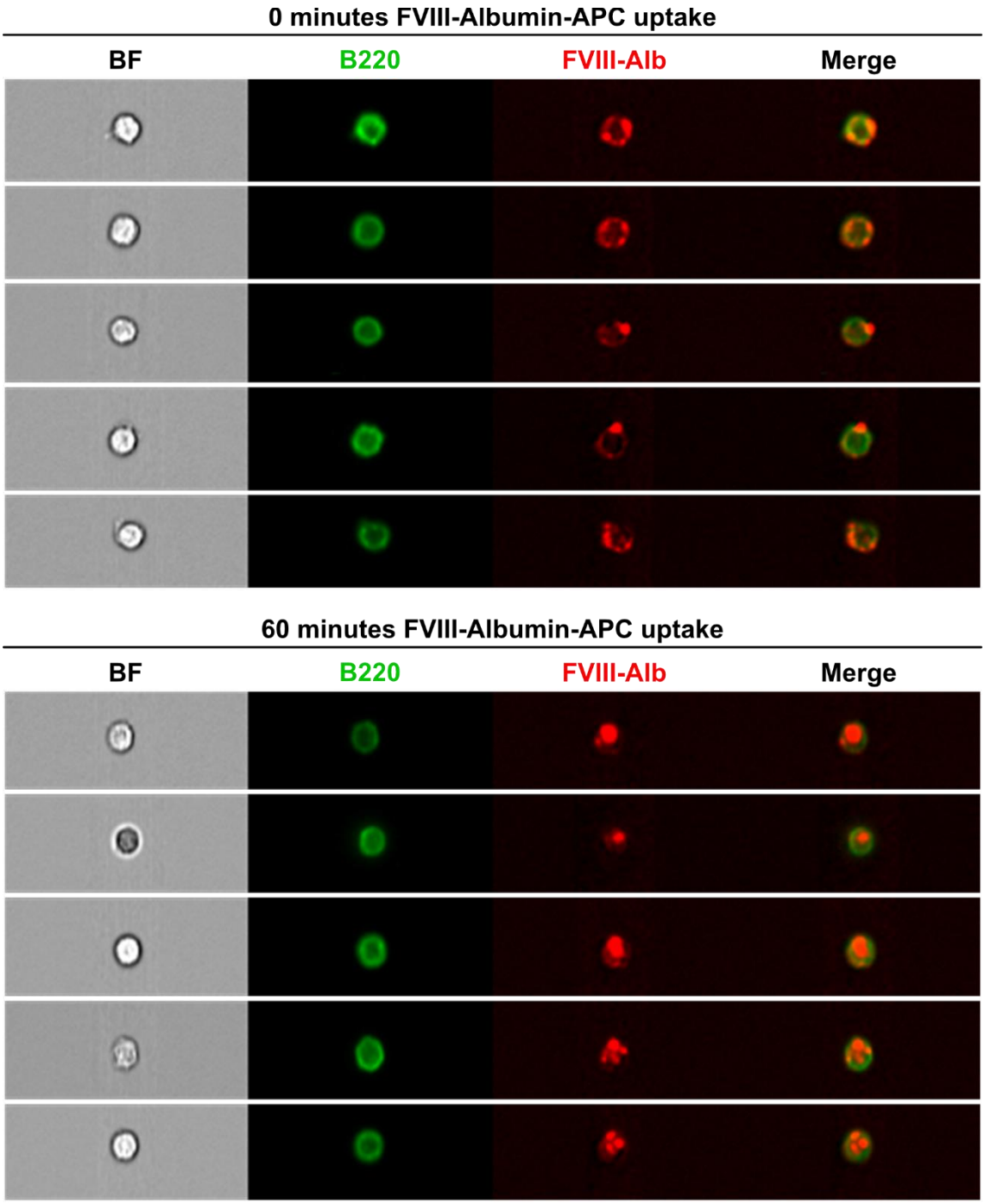

Figure 5.3: Microscopical analysis of FVIII-Albumin fusion protein internalisation by FVIII-specific B cells
Representative microscopy images obtained by imaging flow cytometry showing live B220^{+} B cells positive for APC-conjugated FVIII-Albumin fusion protein following 0 minutes (upper images) or 60 minutes (lower images) antigen uptake. The image panels show signals resulting from the brightfield (BF), B220 (green) and the APC (FVIII-Alb, red) channel. Merge shows the overlap of the green and red channel.

5.2.1.2: MSA blocking step to identify FVIII-Albumin fusion protein uptake by FVIII-specific B cells

Although these data indicated that both, APC-conjugated FVIII and FVIII-Albumin fusion protein, were endocytosed efficiently by B cells, it remained unclear what the influence of the albumin domain was on the internalisation of the fusion protein by B cells. The albumin domain of the fusion protein may mediate binding to surface receptors on B cells or potential recognition and internalisation by albumin-specific B cells rather than FVIII-specific cells. To evaluate if FVIII-Albumin fusion protein is recognised and internalised selectively by FVIII-specific B cells, a MSA blocking step prior to antigen binding was included in the antigen uptake assay using imaging flow cytometry and the effect of blocking on FVIII-Albumin internalisation was assessed (Figure 5.4 and Figure 5.5).

By comparing the dot plots of B cells following a 37 °C incubation for either 0 or 60 minutes with or without the MSA blocking step, it was found that the MSA blocking step did not influence the percentage of $FVIII^+$ $B220^+$ B cells detected (Figure 5.4). However, for FVIII-Albumin fusion protein (FVIII-Alb) a considerable effect of MSA blocking was observed (Figure 5.4). Without blocking, a substantially higher percentage of FVIII-Alb-positive $B220^+$ cells was observed (~ 59 %), compared with ~ 9 % following MSA blocking, indicating the contribution of not only the FVIII- but also the albumin-domain to the binding and internalisation of the fusion protein by B cells.

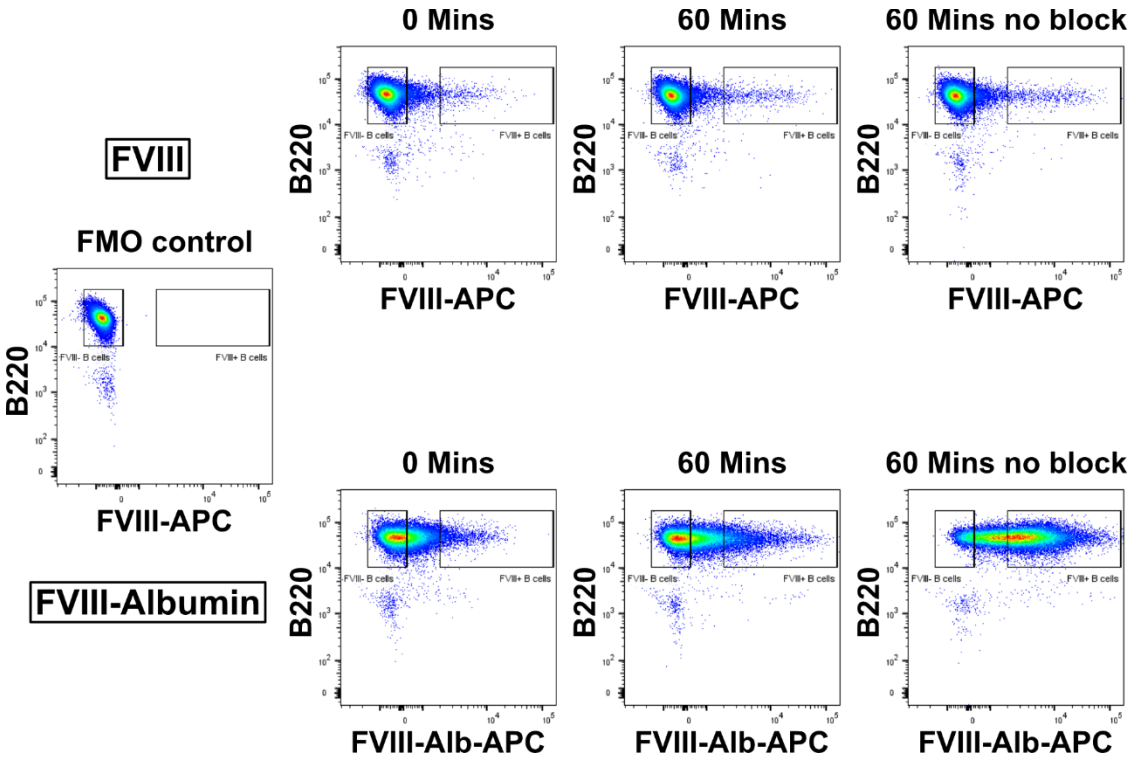

Figure 5.4: Effect of MSA blocking step on binding of FVIII-Albumin to the cell surface of B cells
Dot plots showing the gating of FVIII-APC- (upper row) or FVIII-Albumin-APC-specific (FVIII-Alb-APC, lower row) live B220$^+$ B cells following antigen uptake for 0 or 60 minutes. Prior to uptake, a MSA blocking step (incubation with 0.2 % w/v MSA in C-X-Vivo medium for 30 minutes on ice) was performed. Also shown is antigen uptake for 60 minutes without MSA blocking step. Fluorescence minus one (FMO) control for APC was included to confirm FVIII- and FVIII-Albumin-specific signals.

To assess whether the FVIII-Albumin fusion protein is internalised effectively by FVIII-specific B220$^+$ B cells, the mean internalisation coefficients were calculated after performing the antigen uptake assay in combination with the MSA blocking step (Figure 5.5).

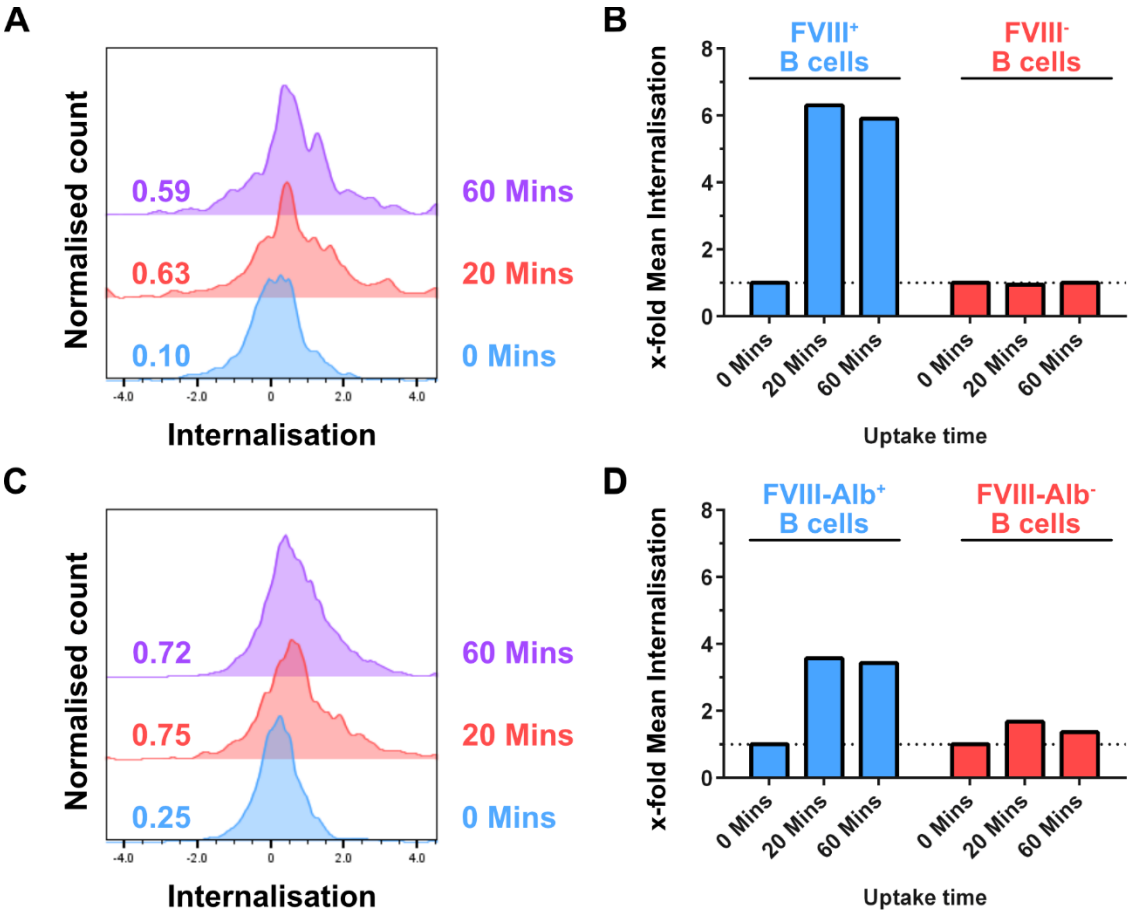

Figure 5.5: Internalisation of FVIII and FVIII-Albumin by FVIII-specific B cells upon MSA blocking
(A+C) Internalisation histograms of live B220$^+$ B cells positive for FVIII-APC **(A)** or FVIII-Albumin-APC (FVIII-Alb-APC) **(C)** following MSA blocking, as described in legend of Figure 5.4. The mean internalisation coefficients for FVIII-/FVIII-Alb-specific B cells after 0 minutes (blue), 20 minutes (red) or 60 minutes (purple) antigen uptake are indicated next to the respective histograms. **(B)** x-fold mean internalisation coefficients calculated for FVIII$^+$ (blue) and FVIII$^-$ (red) live B220$^+$ B cells after 0, 20 or 60 minutes uptake of FVIII-APC **(D)** x-fold mean internalisation coefficients calculated for FVIII-Alb$^+$ (blue) and FVIII-Alb$^-$ (red) live B220$^+$ B cells after 0, 20 or 60 minutes uptake. x-fold mean internalisation parameters were calculated by dividing the mean internalisation for a particular uptake time with the value obtained for cells after 0 minutes uptake.

Similar to above, the mean internalisation coefficient for FVIII-APC was considerably increased from ~ 0.10 at 0 minutes uptake to ~ 0.63 and ~ 0.59 after 20 minutes and 60 minutes uptake, respectively (Figure 5.5A). To test if the

increase of the FVIII internalisation coefficient is specific for FVIII$^+$ B cells, mean internalisation was additionally calculated for FVIII$^-$ B cells and the x-fold increase of internalisation coefficients compared to 0 minutes uptake was compared in FVIII$^+$ (blue) versus FVIII$^-$ (red) B cells (Figure 5.5B). The mean internalisation coefficient for FVIII$^+$ cells increased up to ~ 6-fold over the 60 minutes uptake period whereas the mean FVIII internalisation for FVIII$^-$ cells remained constant over the course of the antigen uptake period (Figure 5.5B). Analogous to FVIII, the mean internalisation coefficient for B cells incubated with FVIII-Albumin fusion proteins advanced from ~ 0.25 at 0 minutes uptake to ~ 0.75 and ~ 0.72 after 20 minutes and 60 minutes uptake, respectively (Figure 5.5C). Calculation of the x-fold increase in the mean internalisation coefficients revealed that FVIII-Albumin internalisation was increased up to ~ 4-fold in FVIII$^+$ B cells (blue) after 20 and 60 minutes uptake, whereas in FVIII-Albumin$^-$ B cells the coefficient remained relatively consistent not surpassing a ~ 1.7-fold increase of the FVIII-Albumin internalisation calculated for 0 minutes uptake (Figure 5.5D). Although, the x-fold increase of the mean internalisation coefficients of FVIII (~ 6-fold) and FVIII-Albumin (~ 4-fold) slightly varied, the difference between FVIII or FVIII-Albumin internalisation at 0 minutes versus 60 minutes uptake were similar (~ 0.50 versus ~ 0.47), indicating similar uptake kinetics and efficiencies of both FVIII derivates. Although blocking with MSA did not impair the internalisation of FVIII and FVIII-Albumin by B220$^+$ B cells, it is advisory to repeat the internalisation experiment after MSA blockade to obtain robust and quantitative data on the antigen internalisation.

Together, these data suggested the successful establishment of an imaging flow cytometry-based uptake assay to assess internalisation of fluorescently labelled antigens by B cells. The increase of FVIII- or FVIII-Albumin-specific internalisation parameters following antigen uptake indicated that both FVIII derivates are recognised and efficiently internalised by FVIII-specific B cells isolated from mouse spleens. The internalisation coefficients for FVIII$^-$ B cells remained consistent over the uptake period confirming that the increase of internalisation is a specific effect of FVIII or FVIII-Albumin fusion protein being internalised by antigen-specific B cells. In addition, antigen uptake could be assessed

qualitatively by microscopy images obtained from imaging flow cytometry. FVIII and FVIII-Albumin fluorescent signals were located to the cell surface of antigen-specific B cells at 0 minutes uptake, whereas both fluorescently labelled proteins were present within the cytosol after 60 minutes uptake confirming internalisation. However, it remains to be investigated to which extent the increase of FVIII and FVIII-Albumin internalisation by $B220^+$ cells can be interpreted in a qualitative way using this ImageStream® approach.

5.2.2: *In vitro* expansion of FVIII-specific $CD4^+$ T cells

5.2.2.1: Establishment of FVIII-specific $CD4^+$ T cell expansion in vitro

To establish an *in vitro* platform for the generation of FVIII-specific $CD4^+$ T cells, a two-step protocol was designed consisting of a 3-day FVIII-specific expansion step using irradiated antigen presenting cells (APCs) loaded with FVIII protein followed by non-specific expansion of $CD4^+$ T cells using T cell activator-Dynabeads (Figure 5.6A). To test different conditions for efficient expansion of FVIII-specific $CD4^+$ T cells, cells were either isolated from naïve or FVIII-immunised (2 IU FVIII i.v. on day -14 and day -7) HemA mice. For the FVIII-specific expansion step, 5×10^5 $CD4^+$ T cells were co-cultured with 5×10^5 irradiated $CD4^-$ splenocytes, as the source of antigen presenting cells, in presence of FVIII. In addition, the effect of IL-2 addition during the antigen-specific expansion step was evaluated. Cells were cultured in 48-well plates and medium topped up every two days (indicated in pink in Figure 5.6A) and 1×10^6 cells were collected every three days to assess the ratio of FVIII-specific T cells using the fluorescently labelled FVIII-specific MHC class II tetramer presenting TASSYFTNMFATWSPSKARL peptide (Figure 5.6A, indicated in brown). After 3 days of FVIII-specific expansion, $CD4^+$ T cells were passaged and subsequently stimulated in the presence of T cell activator-Dynabeads and IL-2 in an unspecific manner. Samples were taken every three days during passaging until day 12 of the experiment and the presence of FVIII-specific $CD4^+$ T cells assessed by flow cytometry (Figure 5.6A).

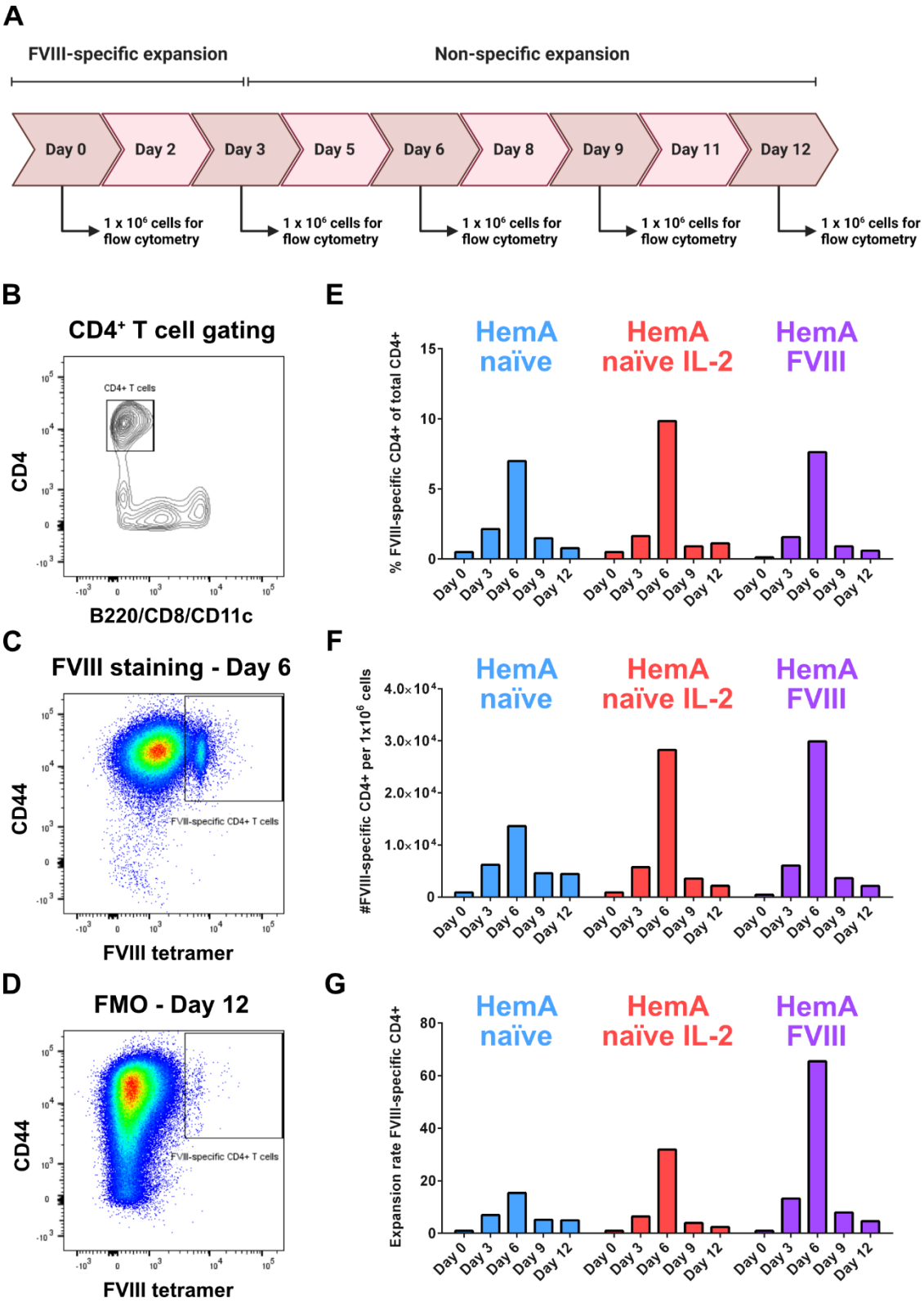

Figure 5.6: *In vitro* expansion of FVIII-specific CD4⁺ T cells
(A) Schematic overview of the *in vitro* expansion of FVIII-specific CD4⁺ T cells. Briefly, 5 x 10^5 CD4⁺ T cells isolated from murine spleens were co-cultured with 5 x 10^5 irradiated CD4⁻ murine splenocytes in presence of 10 IU/ml FVIII protein

and 50 U/ml interleukin-2 (IL-2) for 72 hours. Afterwards, $CD4^+$ T cells were expanded non-specifically in presence of 50 U/ml IL-2 using T cell activator-Dynabeads (1:1 ratio). Cell culture medium was topped up every 2 days (pink) and 1 x 10^6 cells were assessed for FVIII-specificity by flow cytometry every 3 days (brown). The expansion protocol was carried out for 12 days. **(B)** Representative contour blot (Day 6, HemA naïve) showing $CD4^+$ T cell gating, according to the surface expression of CD4 and lack of B220, CD8 and CD11c expression of single, live cells. **(C)** Representative dot blot (Day 6) showing the gating for FVIII-specific $CD4^+$ T cells out of single, live $CD4^+$ cells. FVIII-specific $CD4^+$ T cells were identified as $CD44^+$FVIII-tetramer$^+$ cells. **(D)** Fluorescence minus one (FMO) control at day 12 (HemA naïve IL-2) for FVIII tetramer staining of expanded single, live $CD4^+$ cells to identify FVIII-specific $CD4^+CD44^+$ T cells. **(E-G)** Statistical parameters of *in vitro* expansion protocols extracted from flow cytometry data. Representative data is shown for the FVIII-specific expansion of $CD4^+$ T cells isolated from naïve HemA mice without (blue) versus with (red) IL-2 stimulation during the FVIII-specific expansion and of $CD4^+$ T cells isolated from immunised HemA mice (2 IU FVIII i.v. at day -14 and day -7, purple). **(E)** Ratio of FVIII-specific $CD4^+CD44^+$ T cells among total $CD4^+$ T cells over the *in vitro* expansion period. **(F)** Number of FVIII-specific $CD4^+CD44^+$ T cells per 1 x 10^6 total cells. Absolute numbers were calculated using APC-conjugated counting beads. **(G)** Specific expansion rate of FVIII-specific $CD4^+CD44^+$ T cells in relation to absolute numbers of FVIII-specific cells at day 0.

Single, live cells were gated on $CD4^+$ T cells, according to their surface expression of $CD4^+$ and the lack of B220, CD8 and CD11c expression on their cell surface (Figure 5.6B). $CD4^+$ T cells were evaluated for their FVIII-specificity by their ability to bind fluorescently labelled FVIII tetramer and the expression of the activation marker CD44 (Figure 5.6C). The gate for FVIII-specific $CD4^+CD44^+$ T cells was defined using a fluorescence minus one (FMO) control, in which cells were stained with the particular antibody panel but the FVIII tetramer staining was left out (Figure 5.6D). The ratio of FVIII-specific $CD4^+$ T cells increased from initially 0.1 – 0.5 % at day 0 to ~ 1.5 – 2 % during the 3-day FVIII-specific expansion step in all three conditions (Figure 5.6E). After subsequent non-specific T cell stimulation using T cell activator-Dynabeads the ratio of FVIII-specific $CD4^+$ T cells among total T cells rose to ~ 7 – 10 % at day 6 before gradually decreasing back to initial levels (0.5 – 1 %) at day 12 (Figure 5.6E). The highest ratio (~ 10 % at day 6) of FVIII-specific $CD4^+$ T cells was obtained by adding IL-2 during the FVIII specific expansion step (red) compared to

$CD4^+$ T cells which were initially stimulated by FVIII-presenting cells in absence of IL-2 (blue and purple) (Figure 5.6E). Similar observations were made by investigating the total number of FVIII-specific $CD4^+$ T cells per 1 x 10^6 total cells (Figure 5.6F). Total numbers of antigen-specific $CD4^+$ T cells were calculated using APC-labelled counting beads. Numbers of FVIII-specific $CD4^+$ T cells increased from initially ~ 500 – 900 steadily to up to ~ 3 x 10^4 antigen-specific $CD4^+$T cells per 1 x 10^6 total cells before dropping to only ~ 2 – 4,5 x 10^3 FVIII-specific $CD4^+$ T cells per 1 x 10^6 cells at day 12 (Figure 5.6F). In particular, high total numbers for FVIII-specific $CD4^+$ T cells were ob for cells isolated from naïve HemA mice stimulated with IL-2 during FVIII-specific expansion (red) and cells isolated from immunised HemA mice (purple) reaching ~ 2.8 x 10^4 and ~ 2.9 x 10^4 FVIII-specific $CD4^+$ T cells per 1x10^6 total cells at day 6, respectively (Figure 5.6F). Using these cell counts, the specific expansion rates of FVIII-specific $CD4^+$T cells were calculated (Figure 5.6G). Again, evaluation of specific expansion rates suggested an efficient stimulation and proliferation of FVIII-specific $CD4^+$T cells isolated from FVIII-immunised HemA mice (purple) reaching a specific expansion rate of ~ 65 at day 6 (Figure 5.6G). Cells isolated from naïve mice which were stimulated in the absence (blue) or presence of IL-2 (red) during FVIII-specific expansion were expanded up to ~ 15-fold or ~ 30-fold, respectively (Figure 5.6G). The FVIII-specific $CD4^+$ T cells isolated from FVIII-immunised HemA mice were expanded only slightly more efficiently than cells isolated from naïve HemA mice. Overall, the stimulation of cells from naïve HemA mice with IL-2 during the FVIII-specific expansion step led to the highest ratio of antigen-specific $CD4^+$ T cells among total $CD4^+$ T cells. The effective expansion of FVIII-specific $CD4^+$ T cells after 6 days was observed across several repeats (n = 3). Thus, this expansion protocol was used for following experiments.

5.2.2.2: Extended FVIII-specific expansion of FVIII-specific $CD4^+$ T cells in vitro

In general, the expansion of $CD4^+$ T cells specifically binding to the FVIII tetramer was successful and purities of up to 10 % were obtained, however the percentage of FVIII-specific $CD4^+$ T cells decreased during non-specific cell stimulation using

T cell activator-Dynabeads. To improve the enrichment of antigen-specific $CD4^+$ T cells in culture and to increase their stability, the FVIII-specific expansion step was extended to 6 days by adding fresh irradicated $CD4^-$ splenocytes, as the source of antigen-presenting cells, on day 3 in the presence of FVIII protein and IL-2 (Figure 5.7A). After FVIII-specific expansion, cells were stimulated with T cell activator-Dynabeads in a non-specific manner. As described above, medium was topped up every two days and 1 x 10^6 cells were collected every three days to assess the ratio of FVIII-specific $CD4^+$ T cells in culture (Figure 5.7A).

Single, live cells were gated on $CD4^+$ T cells, according to their surface expression of $CD4^+$ and the lack of B220, CD8 and CD11c expression on their cell surface (Figure 5.7B). $CD4^+$ T cells were evaluated for their FVIII-specificity by their ability to bind fluorescently labelled FVIII tetramer and the expression of the activation marker CD44 (Figure 5.7C). The gate for FVIII-specific $CD4^+CD44^+$ T cells was defined using a fluorescence minus one (FMO) control missing the FVIII tetramer staining (Figure 5.7D).

The extended FVIII-specific expansion step led to the steady increase of FVIII-specific $CD4^+$ T cell ratio among $CD4^+$ T cells isolated from naïve HemA mice (red) from ~ 2 % at day 0 to ~ 9.3 % at day 9 (Figure 5.7E). During non-specific expansion using T cell activator-Dynabeads, the ratio of FVIII-specific $CD4^+$ T cells among total $CD4^+$ T cells dropped slightly to ~ 8.6 % at day 9 and eventually to ~ 6.8 % at day 12. The incubation of $CD4^+$ T cells from HemA mice with IL-2 in the absence of irradiated APCs (green) did not significantly increase the proportion of FVIII-specific $CD4^+$ T cell cells (~ 2 – 3 %) (Figure 5.7E). Furthermore, the extension of the FVIII-specific expansion step to 6 days led to the generation of ~ 3 x 10^4 per 1 x10^6 total cells and a specific expansion rate of ~ 50 at day 9 (not shown), similar to the maximum numbers obtained at day 6 using the initial protocol involving 3 days of antigen-specific expansion (Figure 5.7F). In contrast to the first protocol, the number and percentage of FVIII-specific $CD4^+$ T cells after 6 days of FVIII-specific expansion remained relatively constant during the non-specific expansion using T cell activator-Dynabeads

(Figure 5.7F). However, these data represent only preliminary results, and it is advisory to repeat the expansion experiments using an extended FVIII-specific expansion step to verify the increased stability of FVIII-specific CD4⁺ T cells.

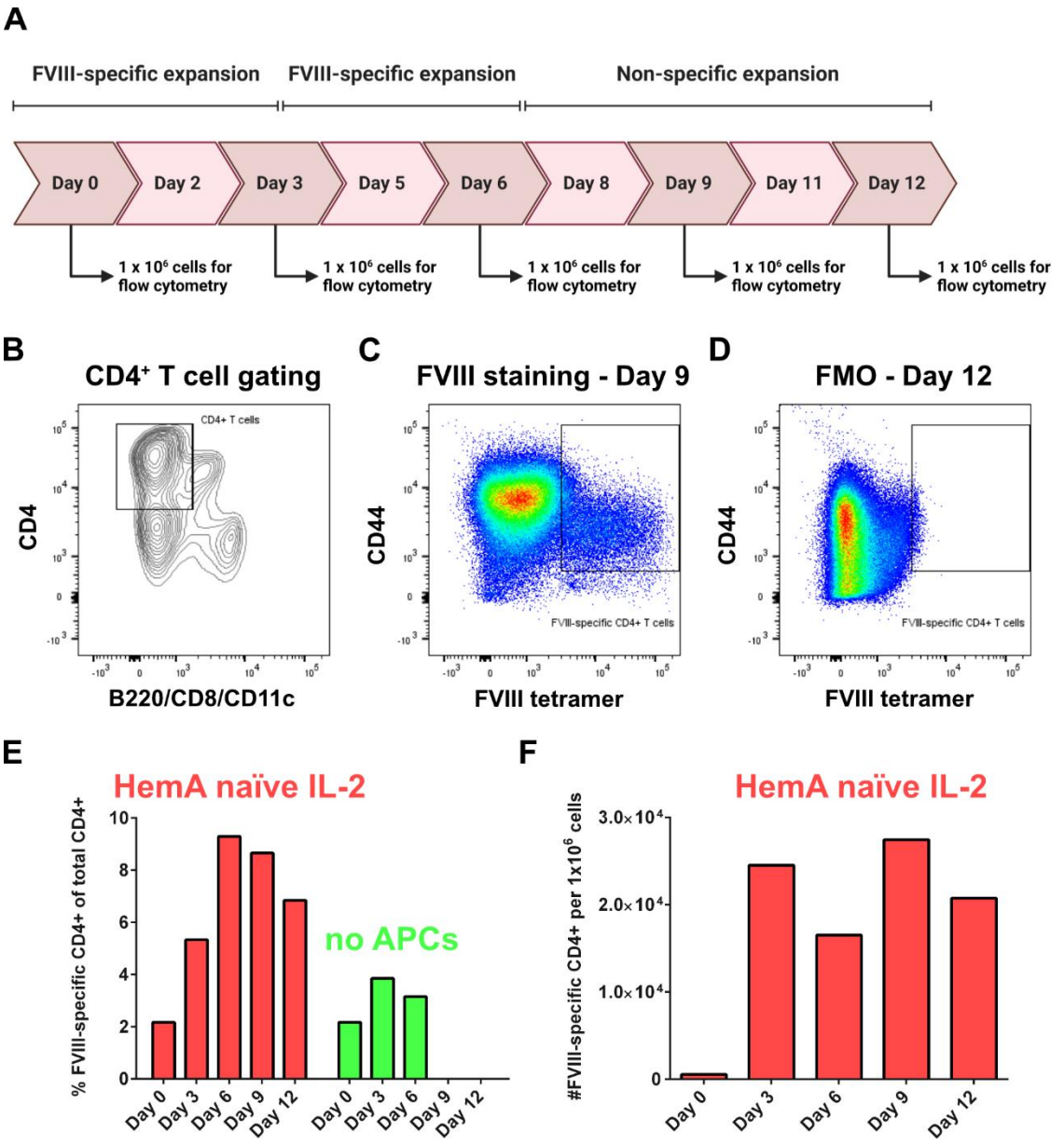

Figure 5.7: Optimised protocol for the *in vitro* expansion of FVIII-specific CD4⁺T cells

(A) Schematic overview of *in vitro* expansion of FVIII-specific CD4⁺ T cells. Briefly, 5 x 10^5 CD4⁺ T cells isolated from murine spleens were co-cultured twice with 5 x 10^5 irradiated CD4⁻ murine splenocytes in presence of 10 IU/ml FVIII protein and 50 U/ml interleukin-2 (IL-2) for 72 hours, respectively. Afterwards,

$CD4^+$ T cells were expanded in presence of 50 U/ml IL-2 using T cell activator-Dynabeads (1:1 ratio). Cell culture medium was topped up every 2 days (pink) and 1 x 10^6 cells were assessed for FVIII-specificity by flow cytometry every 3 days (brown). The expansion protocol was carried out for 12 days. **(B)** Representative contour blot (Day 9, HemA naïve IL-2) showing $CD4^+$ T cell gating, according to the surface expression of CD4 and lack of B220, CD8 and CD11c expression of single, live cells. **(C)** Representative dot blot (Day 9, HemA naïve IL-2) showing the gating for FVIII-specific $CD4^+$ T cells out of single, live $CD4^+$ cells. FVIII-specific $CD4^+$ T cells were identified as $CD44^+$FVIII-$tetramer^+$ cells. **(D)** Fluorescence minus one (FMO) control at day 12 (HemA naïve IL-2) for FVIII tetramer staining of expanded single, live $CD4^+$ cells. **(E-G)** Statistical parameters of *in vitro* expansion protocols extracted from flow cytometry data. Representative data is shown for the FVIII-specific expansion of $CD4^+$ T cells isolated from naïve HemA mice stimulated with 10 IU/ml FVIII protein and 50 U/ml IL-2 in presence (red) versus absence (green) of irradiated $CD4^-$ splenocytes (APCs) during two rounds of FVIII-specific expansion. **(E)** Ratio of FVIII-specific $CD4^+CD44^+$ T cells among total $CD4^+$ T cells over the *in vitro* expansion period. **(F)** Number of FVIII-specific $CD4^+CD44^+$ T cells per 1 x 10^6 total cells. Absolute numbers were calculated using APC-conjugated counting beads.

Taken together, I have established a viable protocol for the *in vitro* expansion of FVIII-specific $CD4^+$ T cells consisting of two rounds of APC-mediated, FVIII-specific T cell expansion followed by non-specific T cell stimulation using T cell activator-Dynabeads. The expansion protocol led to an increase in the percentage of FVIII-specific $CD4^+$ T cells in the total $CD4^+$ T cell population up to 10 % after 9 days of culture (specific expansion of ~ 50-fold), which were able to recognize the FVIII-derived MHC II tetramer (TASSYFTNMFATWSPSKARL) after up to 12 days of culture *in vitro*.

5.2.3: Chemical *in vitro* conversion of $CD4^+$ T cells into Foxp3-expressing regulatory T cells

5.2.3.1: Establishment of a chemical conversion protocol to induce $CD25^+Foxp3^+$ regulatory T cells in vitro

To establish a protocol for the efficient *in vitro* conversion of $CD4^+$ T cells into Foxp3-expressing regulatory T cells (Tregs), I adapted a chemical conversion

method of Akamatsu and colleagues (Akamatsu *et al.*, 2019) using the CDK8/CDK19 inhibitor, AS2863619 (AS). In particular, $CD4^+$ T cells were isolated from murine spleens and depleted of $CD25^+$ Tregs by MACS. Treg-depleted $CD4^+$ T cells were converted into $CD25^+Foxp3^+$ Tregs for 72 hours in presence of T cell activator-Dynabeads, TGF-β and AS at 37 °C and 5 % CO_2 and their phenotype then assessed by flow cytometry (Figure 5.8A).

Cells were gated on single, live cells and the Treg phenotype assessed by the expression of surface CD25 and intracellular Foxp3 (Figure 5.8B). Before chemical conversion, Treg-depleted $CD4^+$ cells did not express CD25 and Foxp3 confirming the successful depletion of Tregs (Figure 5.8B). The stimulation of $CD4^+$ T cells with T cell activator-Dynabeads led to the upregulation of CD25 expression indicating activation of cultured $CD4^+$ T cells, whereas no induction of Foxp3 expression was observed (Figure 5.8B). In contrast, the stimulation of Treg-depleted $CD4^+$ T cells with T cell activator-Dynabeads in presence of TGF-β only or TGF-β together with the CDK8/19 inhibitor, AS, drastically increased the expression of both, CD25 and Foxp3, in cultured cells indicating the induction of Tregs under these culture conditions (Figure 5.8B). While after the stimulation in presence of TGF-β and DMSO carrier ~ 52 % of $CD4^+$ cells exhibited a Treg phenotype ($CD25^+Foxp3^+$), the proportion of $CD25^+Foxp3^+$ Tregs among $CD4^+$ T cells was significantly increased upon stimulation in presence of TGF-β and AS to ~ 92 % (Figure 5.8C). The ratio of Tregs upon T cell activator-Dynabeads stimulation in absence of TGF-β and AS remained unchanged (~ 1.5 %) compared with the untreated Treg-depleted $CD4^+$ cell population (Figure 5.7C). The successful conversion of ~ 80 – 90 % of $CD4^+$ T cells into $CD25^+Foxp3^+$ Tregs after 72 hours of culture in presence of TGF-β and AS was observed across several experiments (n = 3)

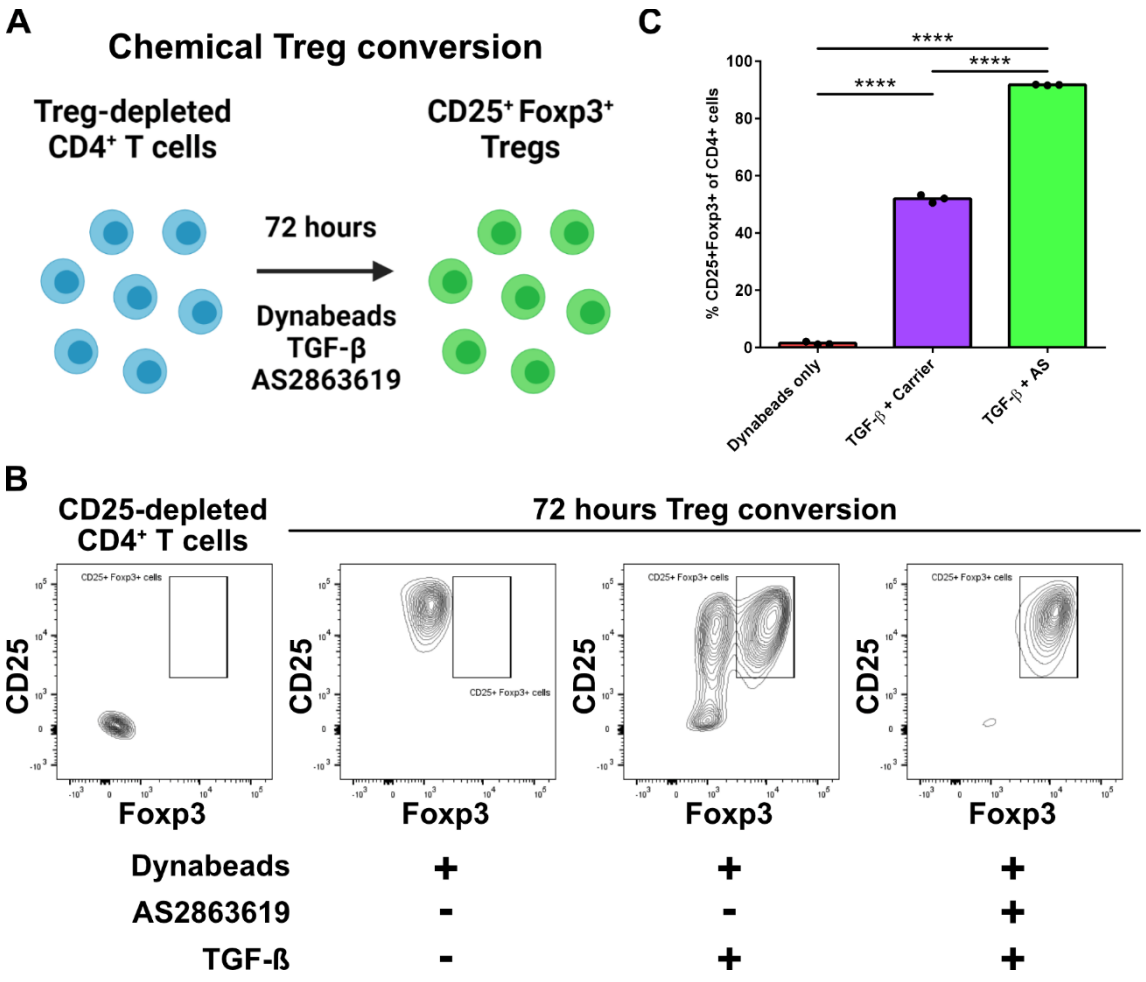

Figure 5.8: *In vitro* conversion of CD4⁺ T cells into CD25⁺Foxp3⁺ regulatory T cells by chemical inhibition of CDK8/19

(A) Schematic overview of the *in vitro* conversion of Treg-depleted CD4⁺ T cells to CD25⁺Foxp3⁺ regulatory T cells (Tregs). Briefly, Treg-depleted CD4⁺ T cells were stimulated with T cell activator-Dynabeads (Dynabeads, 1:1 ratio) and 50 U/ml interleukin-2 (IL-2) for 72 hours in presence of 2.5 µg/ml TGF-β and 1 mM of the CDK8/19 inhibitor, AS2863619 (AS). **(B)** Representative contour plots of CD25⁺-depleted CD4⁺ T cells before conversion (left) and after 72 hours Treg conversion under different conditions. Cells were pre-gated on single-live CD4⁺ T cells and Tregs identified, according to their expression of surface CD25 and intracellular Foxp3 (CD25⁺Foxp3⁺). **(C)** Ratio of CD25⁺Foxp3⁺ Tregs among total CD4⁺ T cells after performing Treg conversion in presence of T cell activator-Dynabeads only (red), TGF-β only (TGF-β + Carrier, purple) or TGF-β and AS (green). A representative Treg conversion experiment is shown. p-values were calculated using Fisher's LSD test. **** $p < 0.0001$

5.2.3.2: Phenotype stability of in vitro induced CD25⁺Foxp3⁺ regulatory T cells

A major downfall of *in vitro* induced Tregs has been their poor stability in culture.

To evaluate the stability of induced Tregs by this chemical conversion method,

cells were rested for up to 72 hours in T cell medium in either the absence or the presence of the conversion reagents, TGF-β and AS, following their chemical conversion and their Treg phenotype assessed by flow cytometry daily (Figure 5.9A).

Again, the conversion of Treg-depleted $CD4^+$ T cells in presence of TGF-β led to a significantly increased induction of Treg phenotype (~ 75 – 80 %) compared to the other two culture conditions (Figure 5.9B). However, after 24 hours of resting, in the absence of the conversion reagents, the ratio of Tregs among total $CD4^+$ T cells declined dramatically to ~ 26 % before dropping to under 2 % after 48 and 72 hours resting suggesting the rapid loss of the acquired Treg phenotype under resting conditions (Figure 5.8B). The presence of the conversion reagents, TGF-β and AS, had no significant effect on the Treg phenotype stability (Figure 5.9B). A similar effect was observed for Tregs induced by TGF-β only where the ratio of $CD4^+$ T cells exhibiting a $CD25^+Foxp3^+$ Treg phenotype dropped rapidly from ~ 22 % to under 1 % within 48 hours of resting (Figure 5.9B). The ratio of $CD4^+$ cells exhibiting a Treg phenotype in the carrier only control remained low (~ 0.5 %) except for peaking at ~ 4.5 % after 24 hours resting (Figure 5.9B).

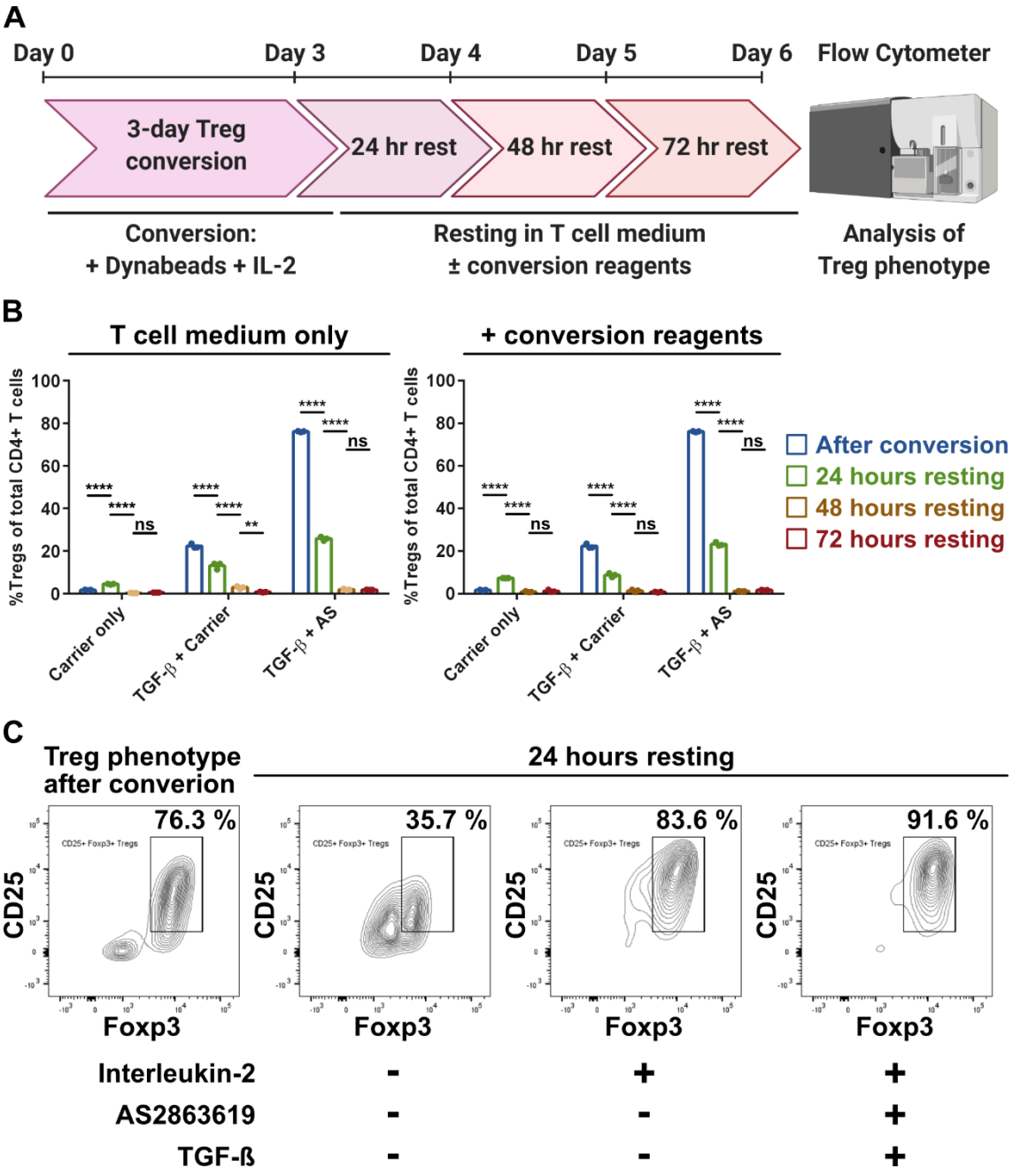

Figure 5.9: Phenotypic stability of *in vitro* induced CD25⁺Foxp3⁺ regulatory T cells

(A) Schematic overview of the *in vitro* conversion of Treg-depleted CD4⁺ T cells to CD25⁺Foxp3⁺ regulatory T cells (Tregs) followed by 72 hours resting. Briefly, Treg-depleted CD4⁺ T cells were stimulated with T cell activator-Dynabeads (Dynabeads, 1:1 ratio) and 50 U/ml interleukin-2 (IL-2) for 72 hours in presence of 2.5 µg/ml TGF-β and 1 mM of the CDK8/19 inhibitor, AS2863619 (AS). Subsequently, induced Tregs were rested in T cell medium in either the absence or the presence of conversion reagents for 72 hours. The Treg phenotype was assessed daily by flow cytometry **(B)** Ratio of CD25⁺Foxp3⁺ Tregs among total CD4⁺ cells directly after the conversion (blue) and after 24 hours (green),

48 hours (orange) or 72 hours (red) resting in T cell medium in absence (left) versus presence (right) of conversion reagents. Treg phenotype was either induced by T cell activator-Dynabeads only (Carrier only), TGF-β only (TGF-β + Carrier) or TGF-β and AS. **(C)** Contour plots of $CD4^+$ T cells converted to Tregs with TGF-β and AS immediately after conversion (left) or after 24 hours in T cell medium only or in T cell medium supplemented with 50 U/ml IL-2 in either the absence or the presence of conversion reagents (TGF-β and AS2863619). Bold numbers indicate the ratio of $CD25^+Foxp3^+$ Tregs among total $CD4^+$ T cells identified in the respective contour plot. Errors are shown as SEM. p-values were calculated using Fisher's LSD test. ** $p < 0.01$, **** $p < 0.0001$

To assess the influence of IL-2 on the stability of chemically converted Treg cells *in vitro*, Treg-depleted $CD4^+$ T cells were stimulated with T cell activator-Dynabeads for 72 hours in presence of TGF-β and AS and subsequently rested for 24 hours in either standard T cell medium or T cell medium supplemented with IL-2 only or IL-2 as well as TGF-β and AS (Figure 5.9C). While the ratio of $CD25^+Foxp3^+$ Tregs dropped dramatically from ~ 76 % to ~ 36 % after 24 hours resting in absence of IL-2, the Treg phenotype was preserved in $CD4^+$ T cells incubated for 24 hours in presence of IL-2 only (~ 84 %) or in presence of IL-2 in combination with TGF-β and AS (~ 92 %), suggesting an important function of IL-2 in the survival and maintenance of chemically converted Tregs *in vitro* (Figure 5.9C). The effect of IL-2 on the stability of induced $CD25^+Foxp3^+$ Tregs *in vitro* and the loss of the acquired Treg phenotype after 24 hours of culture was observed across several experiments (n = 2).

5.2.4: Suppressive capacity of *in vitro* induced $CD25^+Foxp3^+$ regulatory T cells

5.2.4.1: In vitro suppression of $CD8^+$ T cells by freshly converted $CD25^+Foxp3^+$ regulatory T cells

To test the suppressive capacity of chemically converted $CD25^+Foxp3^+$ Tregs, an *in vitro* suppression assay was performed. To this end, $CD11c^+$ dendritic cells (DCs) were loaded with SIINFEKL peptide and CFSE-labelled $CD8^+$ cells isolated

from OT-1 mice were co-cultured with *in vitro* converted Tregs (Figure 5.10A). The proliferation of $CD8^+$ responder T cells in presence of Tregs induced under different conditions was assessed by flow cytometry, according to their CFSE fluorescence (Figure 5.10A).

Cells were gated on single, live $CD8^+$ T cells and proliferation models were calculated to fit the corresponding CFSE histograms obtained from the different co-culture conditions (Figure 5.10B). In the absence of any $CD4^+$ T cells (blue) OT-1 $CD8^+$ T cells proliferated extensively, while their proliferation was drastically suppressed in co-culture settings using $CD4^+$ T cells stimulated in the presence of T cell activator Dynabeads and IL-2 (Dynabeads only, red), a non-Treg control, or Tregs induced by either T cell activator Dynabeads, IL-2 and TGF-β (TGF-β + Carrier, purple) or T cell activator Dynabeads, IL-2, TGF-β and AS (TGF-β + AS, green) (Figure 5.10B). The calculation of the division index, estimating how many divisions CFSE-labelled cells underwent on average, revealed that while $CD8^+$ T cells underwent ~ 0.31 divisions on average in presence of $CD4^+$ T cells stimulated with T cell activator-Dynabeads only (red), the average number of $CD8^+$ T cell divisions was significantly reduced to ~ 0.18 in the presence of Tregs induced by TGF-β and AS (green). The division index of $CD8^+$ T cells in the presence of TGF-β-induced Tregs (purple) was similar to the division index observed for TGF-β- and AS-induced Tregs (~ 0.2 versus ~ 0.18) (Figure 5.10C). In comparison to the absence of $CD4^+$ T cells during the suppression assay (blue) resulting in a division index of ~ 2.75, the absolute division indices were significantly lower in the co-culture settings with differently stimulated $CD4^+$ T cells. This indicated that $CD8^+$ T cell division was suppressed via a non-Treg specific suppression mechanism mediated by $CD4^+$ T cells after extensive stimulation with T cell activator-Dynabeads.

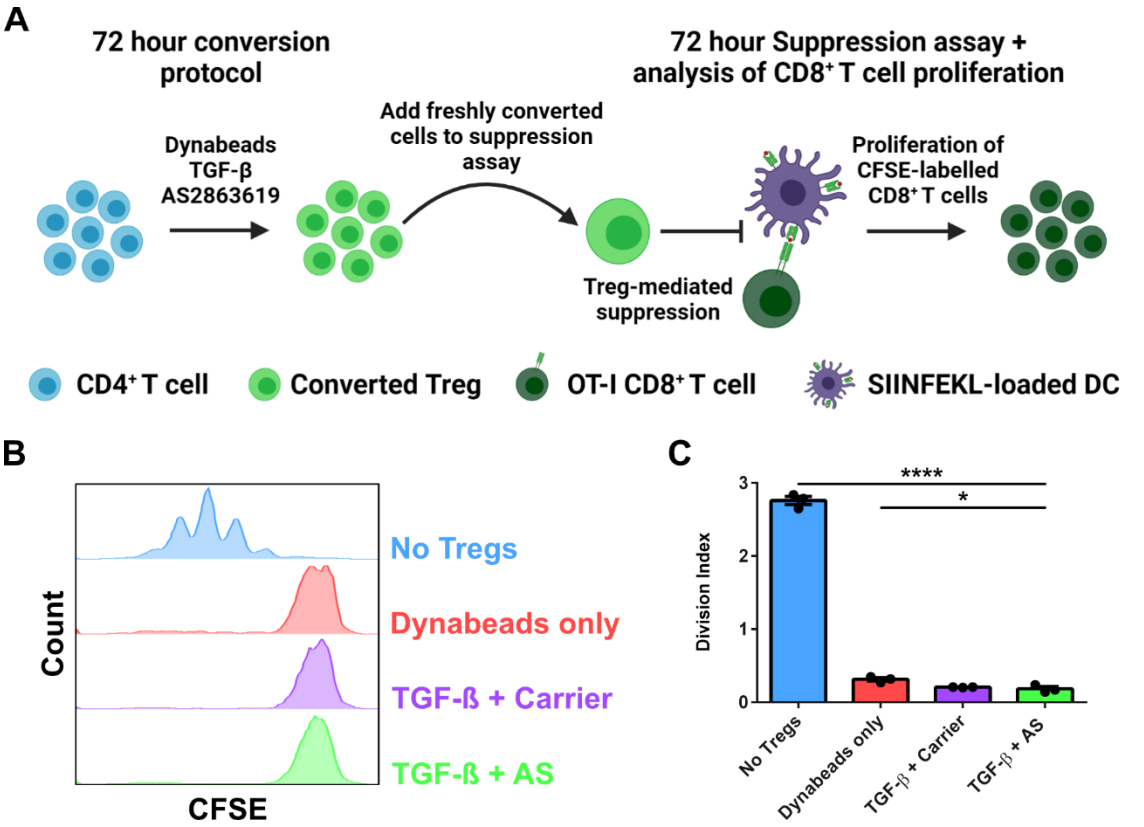

Figure 5.10: Suppressive capacity of freshly induced CD25⁺Foxp3⁺ regulatory T cells *in vitro*

(A) Schematic overview of chemical Treg conversion followed by an *in vitro* suppression assay. Briefly, Treg-depleted $CD4^+$ T cells were converted into Tregs for 72 hours in presence of T cell activator-Dynabeads (Dynabeads, 1:1 ratio), 50 U/ml interleukin-2 (IL-2), 2.5 µg/ ml TGF-β and 1 mM AS2863619 (AS). As controls, Tregs were induced in the presence of T cell activator beads and IL-2 (red) or in the presence of T cell activator beads, IL-2 and TGF-β (purple). 1 x 10^5 freshly converted Tregs were co-cultured with 1 x 10^4 SIINFEKL-loaded $CD11c^+$ dendritic cells (DC) and 1 x 10^5 CFSE-labelled OT-1 $CD8^+$ T cells for 72 hours. The proliferation of $CD8^+$ T cells in absence versus presence of differentially induced Tregs was assessed by flow cytometry. **(B)** Representative CFSE-histograms of single live $CD8^+$ T cells in absence (blue) versus presence of Tregs induced by T cell activator-Dynabeads only (red), TGF-β (TGF-β + Carrier, purple) or TGF-β and AS (green). **(C)** Division indices were calculated by fitting a proliferation model to CFSE-histograms of single, live $CD8^+$ T cells. The division indices are shown for co-culture conditions using Tregs induced by T cell activator-Dynabeads only (red), TGF-β only (TGF-β + Carrier, purple) or TGF-β in combination with AS (green). Errors are shown as SEM. p-values were calculated using Fisher's LSD test. * $p < 0.05$, **** $p < 0.0001$

5.2.4.2: Suppressive capacity of induced CD25$^+$Foxp3$^+$ regulatory T cells after resting in presence of interleukin-2

To reduce the influence of non-Treg mediated suppression mechanisms, such as by nutrient and cytokine deprivation by the activated CD4$^+$ T cells, induced Tregs were rested for 24 hours in the presence or absence of IL-2 prior to performing *in vitro* suppression assays (Figure 5.11A). The presence of IL-2 in the resting medium was to conserve the Treg phenotype of induced cells during the resting period (Figure 5.9C). In addition, freshly isolated and Treg-depleted CD4$^+$ T cells (naïve CD4$^+$ T cells from spleens) were co-cultured with SIINFEKL-loaded CD11c$^+$ DCs and CFSE-labelled OT-1 CD8$^+$ T cells as a control containing equal cell numbers as in Treg co-cultures (Figure 5.11A).

Cells were gated on single, live CD8$^+$ T cells and proliferation models were calculated to fit the corresponding CFSE histograms obtained from the different co-culture conditions (Figure 5.11B+D). The proliferation of CFSE-labelled CD8$^+$ T cells in the presence of Tregs induced by T cell activator-Dynabeads only (red), and 24 hours resting in the absence of IL-2, was similar to the proliferation in the presence of freshly isolated CD4$^+$ T cells (blue) (Figure 5.11B). Stronger inhibition of CD8$^+$ T cell proliferation was observed in the co-culture conditions with Tregs that were induced using TGF-β (purple) or TGF-β and AS (green) and rested for 24 hours in absence of IL-2 (Figure 5.11B). Quantification of division indices revealed that while CD8$^+$ T cells underwent on average ~ 0.40 and ~ 0.34 cell divisions in presence of naïve CD4$^+$ T cells (blue) or CD4$^+$ T cells stimulated with T cell activator-Dynabeads only, respectively, the CD8$^+$ T cell-specific division index was significantly reduced to ~ 0.30 and ~ 0.25, respectively, in presence of rested Tregs induced by TGF-β only (purple) or TGF-β in combination with AS (green) (Figure 5.11C).

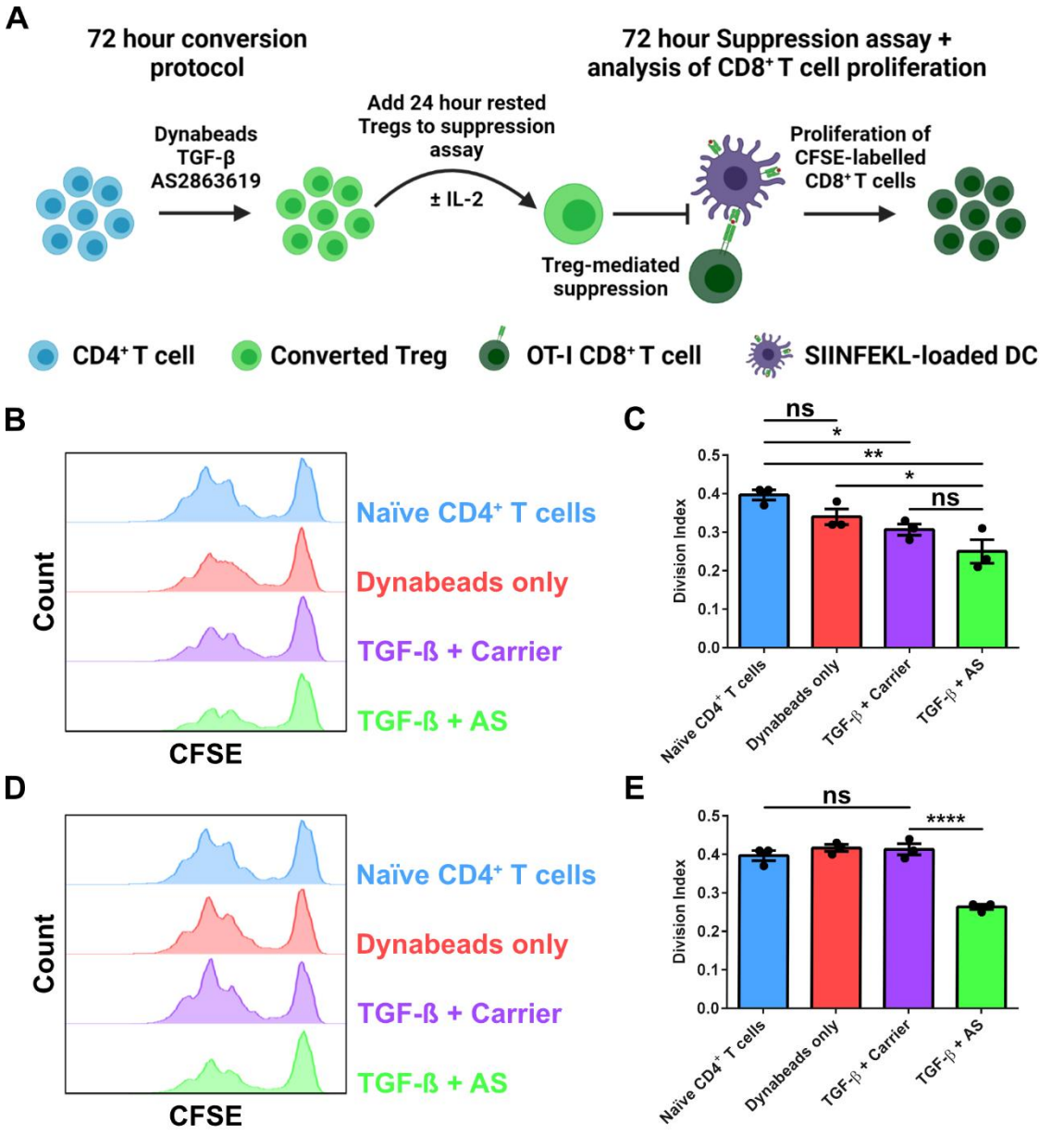

Figure 5.11: Suppressive capacity of *in vitro* induced CD25$^+$Foxp3$^+$ regulatory T cells in absence and presence of IL-2

(A) Schematic overview of chemical Treg conversion followed by resting and an *in vitro* suppression assay. Briefly, Treg-depleted CD4$^+$ T cells were converted into Tregs for 72 hours in presence of T cell activator-Dynabeads (Dynabeads, 1:1 ratio), 50 U/ml interleukin-2 (IL-2), 2.5 µg/ml TGF-β and 1 mM AS2863619 (AS), and subsequently rested for 24 hours in T cell medium in absence versus presence of IL-2 (50 U/ml). As controls, Tregs were induced in the presence of T cell activator beads and IL-2 (red) or in the presence of T cell activator beads, IL-2 and TGF-β (purple). 1 x 10^5 rested Tregs were co-cultured with 1 x 10^4 SIINFEKL-loaded CD11c$^+$ dendritic cells (DC) and 1 x 10^5 CFSE-labelled OT-1 CD8$^+$ T cells for 72 hours. The proliferation of CD8$^+$ T cells in presence of freshly isolated CD4$^+$ T cells versus differentially induced Tregs was assessed by

flow cytometry. **(B+D)** Representative CFSE-histograms of single live $CD8^+$ T cells in absence (blue) versus presence of Tregs induced by T cell activator-Dynabeads only (red), TGF-β only (TGF-β + Carrier, purple) or TGF-β and AS (green) after 24 hours resting in T cell medium in absence **(B)** or presence **(D)** of IL-2 (50 U/ml). **(C+E)** Division indices were calculated by fitting a proliferation model to CFSE-histograms of single, live $CD8^+$ T cells. The division indices are shown for co-culture conditions using freshly isolated $CD4^+$ T cells (naïve $CD4^+$ T cells, blue) and Tregs induced by T cell activator-Dynabeads only (red), TGF-β only (TGF-β + Carrier, purple) or TGF-β in combination with AS (green) after resting 24 hours in T cell medium in absence **(C)** versus presence **(E)** of IL-2 (50 U/ml). Errors are shown as SEM. p-values were calculated using Fisher's LSD test. * $p < 0.05$, ** $p < 0.01$, **** $p < 0.0001$

Interestingly, Tregs induced with T cell activator-Dynabeads only (red) or in combination with TGF-β (purple) and then rested in the presence of IL-2 did not show any additional suppressive capacity compared to the naïve $CD4^+$ control (blue) (Figure 5.11D). Tregs induced by TGF-β and AS (green), however, maintained their suppressive capacity after 24 hours resting in presence of IL-2 (Figure 5.11D). This effect was confirmed by the quantification of the respective division indices (Figure 5.11E). While the co-culturing of CFSE-labelled $CD8^+$ T cells with naïve $CD4^+$ T cells (blue), T cell activator-Dynabeads stimulated $CD4^+$ T cells (red) or TGF-β induced Tregs (purple) resulted in division indices of ~ 0.4, the $CD8^+$ T cell-specific division index was significantly reduced to ~ 0.26 in presence of Tregs induced by TGF-β and AS (green) (Figure 5.11E). These data indicated that Tregs induced by the combination of TGF-β and AS exhibited suppressive capacities even in the presence of the T cell proliferation-promoting cytokine IL-2. In contrast, although suppressing $CD8^+$ T cell proliferation in the absence of IL-2, TGF-β induced Tregs failed to maintain suppressive functions when passaged with IL-2.

In summary, a reliable *in vitro* protocol for the chemical conversion of $CD4^+$ T cells into $CD25^+Foxp3^+$ Tregs using TGF-β and the CDK8/19 inhibitor, AS, was established resulting in highly effective (up to ~ 90 %) induction of Treg phenotype *in vitro*. Although induced Tregs showed poor phenotype stability in absence of IL-2, a high purity of Tregs (~ 80 – 90 %) was maintained after 24 hours resting

in presence of IL-2 and, in addition, the suppressive capacity of TGF-β and AS induced Tregs was conserved in presence of the proinflammatory cytokine IL-2. However, the data on the suppressive capacity of induced Tregs represent preliminary observations and it is advisory to repeat these experiments to confirm the suppressive capacity of converted $CD25^{+}Foxp3^{+}$ Tregs *in vitro*, especially in regard to the presence of IL-2.

5.3: Discussion

Up to now, immune tolerance induction (ITI) protocols involving repetitious injections of high doses of recombinant FVIII (rFVIII) are the most effective way to eliminate pre-existing inhibitory antibodies (inhibitors) against FVIII in HemA patients and restore sufficient blood coagulation capacities (Brackmann *et al.*, 2018). These protocols are very burdensome and expensive, and hence the development of more patient friendly and cost-effective ITI strategies is essential for establishing tolerance towards FVIII in HemA patients effectively.

One promising approach involves the use of half-life extended FVIII-Albumin fusion protein, which, in previous studies by the Becker-Gotot laboratory, was found to induce an immune tolerant phenotype upon intravenous administration to HemA mice (unpublished data). The molecular mechanisms of immune tolerance induction by FVIII-Albumin fusion proteins and potential differences in cell biological processes of uptake and internalisation of rFVIII and albumin fusion proteins are poorly understood.

In this chapter, I have established an imaging flow cytometry-based antigen uptake assay to assess the ability of FVIII-specific B cells to recognise and internalise succinimidyl ester-conjugated FVIII-Albumin fusion protein *in vitro* (Figure 5.1A). To my knowledge, the use of imaging flow cytometry combining the strengths of flow cytometry, to investigate isolated cell populations in a high throughput manner, and fluorescence microscopy, to visualise the localisation of the fluorescent signal, is a novel approach in investigating protein internalisation by primary antigen-specific B cells. Other studies using imaging flow cytometry

mainly focussed on phagocytosis of pathogens by immune cells, such as neutrophils and macrophages, or the internalisation of antibodies by carcinoma cell lines to assess the potential of mediating antibody-dependent cellular toxicity (ADCC) (Havixbeck *et al.*, 2015; Hazin *et al.*, 2015; Haridas *et al.*, 2017; Smirnov *et al.*, 2017).

Imaging flow cytometry and the calculation of internalisation parameters revealed that FVIII-Albumin fusion protein was internalised by FVIII-specific B cells in similar fashion to recombinant FVIII (Kogenate® FS) which has been approved for standard protein replacement therapy in human HemA patients (Figure 5.1). Internalisation of both proteins could also be proven, albeit qualitatively, by confocal imaging of B cells recorded during imaging flow cytometry. FVIII and FVIII-Albumin were located to the cell surface of FVIII-specific B cells immediately after antigen binding, whereas FVIII- and FVIII-Albumin-specific signals were detected intracellularly after 60 minutes uptake (Figure 5.2 and Figure 5.3). The uptake also occurred after MSA blocking of B cells to inhibit the interaction of albumin epitopes of the FVIII-Albumin fusion protein (Figure 5.4 and Figure 5.5). These findings indicate that FVIII-Albumin fusion protein can be recognised and internalised by FVIII-specific B cells in a similar fashion to FVIII and suggest that the fusion of FVIII and albumin by succinimidyl ester coupling neither blocks FVIII epitopes important for antigen recognition nor affects internalisation of the large fusion protein by B cells.

Although internalisation coefficients of FVIII and FVIII-Albumin fusion protein by FVIII-specific B cells indicated similar internalisation of both proteins, one caveat to the quantification is the low frequency of FVIII-specific B cells in the total pool of B cells isolated from HemA mice resulting in the analysis of internalisation in a minor proportion of total B cells. One strategy to improve the analyses of internalisation coefficients could be the use of B cell-restricted mouse models, such as NOD.IgHEL mice in which all B lymphocytes express Ig molecules specific for hen egg lysozyme (HEL) (Silveira *et al.*, 2002). Performing the imaging flow cytometry-based antigen uptake assay with B cells isolated from NOD.IgHEL mice using fluorescently labelled HEL, and FVIII as a control antigen,

may provide useful insights into the sensitivity and scalability of internalisation coefficients obtained by these experiments.

Additionally, imaging flow cytometry is a useful tool to investigate alternative intracellular trafficking pathways and peptide presentation of FVIII fusion proteins upon internalisation by antigen-specific B cells. Endosomal tracers, such as LysoTracker Red or DQ-OVA, can be included to analyse co-localisation with internalised antigens and compare intracellular trafficking of FVIII and FVIII fusion proteins in a spatiotemporal manner.

This internalisation coefficient analysis protocol is widely applicable to other fluorescently labelled antigens and could be used for the identification of epitopes recognised by specific B cells. Blocking or mutagenesis approaches could help to identify particular epitopes or amino acid sequences important for the efficient recognition and subsequent internalisation by B cells. Furthermore, the imaging flow cytometry-based approach can be used to screen fusion protein libraries to identify specific conjugates with altered internalisation efficiencies within an antigen-specific B cell population.

Another approach to induce immune tolerance induction and diminish inhibitor titers in HemA patients is the adoptive transfer of *in vitro* expanded FVIII-specific regulatory T cells (Tregs) to directly suppress rFVIII-induced immune reactions and potentially induce apoptosis of FVIII-specific B cells, in a similar to *in vivo* induced peripheral Tregs (Miao, 2010; Gotot *et al.*, 2018; Smith *et al.*, 2020). However, the generation of high numbers of antigen-specific Tregs is still inefficient and expensive and, in particular, *in vitro* induced Tregs exhibit poor functional stability after cell transfer (Kanamori *et al.*, 2016). For example, in graft versus host disease (GVHD) models, *in vitro* induced Treg failed to protect mice from lethal GVHD and, moreover, after losing Foxp3 expression, reverted irreversibly into a proinflammatory IFNγ-secreting phenotype (Beres *et al.*, 2011).

Here, I have established two complementary *in vitro* protocols for the generation of FVIII-specific Tregs; firstly, the expansion of FVIII-specific $CD4^+$ cells from primary splenic $CD4^+$ T cells (Figure 5.6 and Figure 5.7) and, secondly, the

chemical conversion of naïve conventional $CD4^+$ cells into $CD25^+Foxp3^+$ Tregs exhibiting immunosuppressive properties on cytotoxic $CD8^+$ T cells (Figure 5.8). Combining these protocols potentially leads to the efficient induction of high numbers of FVIII-specific Tregs mediating immune tolerance induction *in vivo* upon adoptive cell transfer.

The *in vitro* expansion protocol consisting of two rounds of antigen-specific stimulation using irradiated APCs increased the ratio of FVIII-specific $CD4^+$ T cells from 1 – 2 % up to 10 % after 9 days of culture (Figure 5.7E). The extension of the FVIII-specific expansion step to 6 days led to the persistence of FVIII-specific $CD4^+$ T cell during the subsequent non-specific expansion using T cell activator-Dynabeads (Figure 5.7). In contrast, the percentage of FVIII-specific $CD4^+$ T cells after 3 days of APC stimulation rapidly decreased during the non-specific expansion step (Figure 5.6). Presumably, the extended FVIII-specific expansion step guaranteed that, prior to extensive stimulation with T cell activator-Dynabeads, FVIII-unspecific $CD4^+$ T cells died due to the lack of stimulation and survival cues, whereas after only 3 days of FVIII-specific stimulation FVIII-unspecific $CD4^+$ T cells survived and eventually overgrew FVIII-specific $CD4^+$ T cells during T cell activator-Dynabeads stimulation.

One strength of this approach, in particular in comparison to the work of Smith and colleagues (Smith *et al.*, 2020), is the use of a fluorescently labelled MHC II tetramer presenting FVIII-derived TASSYFTNMFATWSPSKARL peptide to $CD4^+$ T cells allowing the direct identification of expanded $CD4^+$ T cells capable of recognising this particular FVIII epitope. In contrast, the antigen-specificity of expanded $CD4^+$ T cells in most other studies was only examined by surface marker expression or functional assays due to limited availability of peptide-loaded MHC II tetramer to directly prove antigen-derived peptide recognition by expanded $CD4^+$ T cells (Yamazaki *et al.*, 2003; Cohen *et al.*, 2005; Smith *et al.*, 2020). Here, I assessed the FVIII-specificity of expanded $CD4^+$ T cells using a single FVIII tetramer, which might underestimate the actual ratio of expanded FVIII-specific $CD4^+$ T cells recognising distinct FVIII epitopes. The use of additional FVIII-derived tetramers could help to identify the total pool of polyclonal

FVIII-specific $CD4^+$ T cells after *in vitro* expansion. Functional assays, such as measuring cytokine production or cytotoxicity assay, might also help to estimate the percentage of *in vitro* expanded $CD4^+$ T cells responding to FVIII stimulation. However, the TASSYFTNMFATWSPSKARL peptide, representing amino acids 2010 – 2019 located in the A3 domain of human FVIII, was shown to be recognised by inhibitors across various patients and is therefore a good hallmark to assess FVIII-specificity of $CD4^+$ T cells and efficiency of antigen-specific expansion *in vitro* (Kopecky *et al.*, 2006; UniProt Consortium, 2021). Furthermore, the FVIII tetramer can be used to sort for FVIII-specific $CD4^+$ T cell by flow cytometry prior to or after *in vitro* expansion to obtain higher ratios of FVIII-recognising $CD4^+$ T cells among the total $CD4^+$ T cell pool. Unfortunately, attempts to sort FVIII-specific $CD4^+$ T cells prior to expansion failed due to low numbers of tetramer-positive $CD4^+$ T cells after isolation and low survival of sorted cells during *in vitro* culture. It remains to be investigated if culture conditions for the *in vitro* expansion of FVIII-specific $CD4^+$ T cells can further be improved by using isolated populations of antigen presenting cells such as small peritoneal macrophages, which were shown to efficiently contribute to co-stimulation of naïve $CD4^+$ T cells, and alternative protein loading protocols (Takenaka *et al.*, 2018). In addition, sorting experiments have to be repeated to assess the efficiency of the *in vitro* expansion of freshly isolated FVIII tetramer-specific $CD4^+$ T cells.

One major advantage of the *in vitro* expansion of FVIII-specific $CD4^+$ T cells, compared to direct induction of antigen-specific $CD25^+Foxp3^+$ Tregs, is the poor phenotypic stability of *in vitro* cultured Tregs, which are described to lose $Foxp3^+$ expression upon extensive stimulation and to lose suppressive capacities in the presence of T-helper polarising cytokines such as IL-4 and IL-6 (Hoffmann *et al.*, 2009; Sawant and Vignali, 2014). Additionally, the total $CD4^+$ T cell pool comprises only 5 – 10 % Tregs in mice and only 1 – 2 % in humans, therefore, the direct expansion of rare antigen-specific Tregs, such as FVIII-specific Tregs, within the small polyclonal population of Tregs is particular challenging (Masteller *et al.*, 2006). Instead, expansion of more frequent FVIII-specific $CD4^+$ T cells and their subsequent conversion to a Foxp3-expressing phenotype is a more

promising approach to generate high numbers of antigen-specific Tregs suitable for adoptive cell transfers to induce immune tolerance towards FVIII.

Indeed, the chemical conversion of conventional $CD4^+$ T cells using the CDK8/19 inhibitor, AS2863619, efficiently induced a $CD25^+Foxp3^+$ phenotype in ~ 80 – 90 % of the cells after 72 hours of culture (Figure 5.8B-C), findings consistent with that described by Akamatsu and colleagues (Akamatsu *et al.*, 2019). However, AS-converted Tregs exhibited poor phenotype stability *in vitro* and significantly decreased Foxp3-expression after 24 hours in absence of IL-2 (Figure 5.9B). These findings are similar to that reported for other *in vitro* induced Tregs and some natural occurring Tregs *in vivo* (Chen *et al.*, 2011; Ye *et al.*, 2018). This behaviour may be due to the lack of demethylation at the Helios and Foxp3 gene loci in *in vitro* AS-induced Tregs (Akamatsu *et al.*, 2019). Demethylation at these gene loci is essential for maintaining long-term Treg stability *in vitro* and *in vivo*, especially in presence of proinflammatory cytokines, such as IL-1, IL-6 and IL-23 (Sawant and Vignali, 2014).

Some studies suggest that *in vitro* induced Tregs maintain their Treg phenotype in the appropriate microenvironment after adoptive cell transfer *in vivo* due to the constant supply of IL-2 and other Treg survival cues (Chen *et al.*, 2011). Furthermore, demethylation at Helios and Foxp3 gene loci can be induced *in vivo* by antigen stimulation in presence of IL-2 (Chen *et al.*, 2011). In regard to the environment of the HemA context, where transferred FVIII-specific Tregs might be stimulated constantly by the presence of injected FVIII and provided Treg survival cues such as IL-2, *in vitro* generated Tregs might be capable of maintaining their phenotype and immunosuppressive functions for extended time periods. If this was the case, then *in vitro* generated Tregs may provide long-term immune tolerance towards recombinant FVIII *in vivo* and suppress or prevent inhibitor formation. This proposal is supported by the improved stability of Treg phenotype of AS-induced Tregs in culture medium supplemented with IL-2 (Figure 5.9C). However, it remains unclear whether other cytokines released during anti-FVIII immune responses might abrogate AS-induced Treg phenotype as reported in the GVHD models (Beres *et al.*, 2011). It is instructive to examine

the phenotypic and functional stability of AS-induced Tregs in the presence of different proinflammatory and T helper cell-inducing cytokines and assess whether long-term stability and survival of AS-induced Tregs is maintained by the induction of Foxp3- and Helios-demethylation after cell transfer *in vivo*. Alternatively, demethylation of Helios and Foxp3 gene loci in *in vitro* AS-induced Tregs could be enhanced by addition of TET-inducing agents including vitamin C or hydrogen sulfide (Kanamori *et al.*, 2016).

Despite their poor phenotypic stability, *in vitro* induced Tregs exhibit similar immunosuppressive capacities compared to isolated natural occurring Tregs, presumably because of the pre-activation *in vitro* (Benson *et al.*, 2007; Dons *et al.*, 2012). Interestingly, while similar immuno-suppressive activities were observed for freshly isolated Tregs and TGF-β- or AS-induced Tregs after resting in the absence of IL-2, only AS-induced Tregs maintained their immunosuppressive functions after resting in the presence of IL-2 (Figure 5.11B-E). This might be due to the heterogeneity of TGF-β-induced T cells with a large percentage of non-Tregs after conversion (Figure 5.8B-C). However, it should be noted that the suppressive activity of AS-induced Tregs was demonstrated for $CD8^+$ T cells and it remains to be investigated if these Tregs are capable of suppressing antigen-specific B cells and inducing apoptosis, which would prevent the formation of anti-FVIII antibodies. For this to take place, it is essential that immunosuppressive capacities of AS-induced Tregs are maintained, particularly in potentially pro-inflammatory or T helper cell inducing microenvironments.

Although the adoptive transfer of polyclonal *in vitro* induced Tregs leads to reduced anti-FVIII immune responses in HemA mice by processes such as infectious tolerance, it is believed that the transfer of FVIII-specific Tregs is significantly more effective and does not require such high cell numbers as transferring polyclonal Treg populations (Masteller *et al.*, 2006; Sarkar *et al.*, 2014; Smith *et al.*, 2020). Antigen-specific Tregs can directly and indirectly suppress target immune cells by cell contact- and cytokine-dependent pathways, respectively, whereas polyclonal Tregs are only capable of mediating indirect

suppression (Schmidt *et al.*, 2012; Weingartner and Golding, 2017). Hence, it is beneficial to provide an *in vitro* protocol for the generation of FVIII-specific Tregs to efficiently induce immune tolerance towards FVIII in the context of HemA without the requirement to adoptively transfer a high number of cells into the patient. The combination of the two established protocols, namely expansion of antigen-specific $CD4^+$ T cells and efficient conversion of conventional $CD4^+$ T cells into immunosuppressive $CD25^+Foxp3^+$ Tregs, reflects such an approach and has many advantages compared with most established *in vitro* Treg generation protocols (Yamazaki *et al.*, 2003; Sarkar *et al.*, 2014; Smith *et al.*, 2020). In particular, it provides a fast and cost-effective platform for the large-scale generation of highly enriched FVIII-specific Tregs, which maintain their phenotype and immunosuppressive functions even without TCR stimulation but in presence of IL-2. However, it remains to be investigated how both protocols can be combined to guarantee the effective expansion of $CD4^+$ T cells recognising immunogenic FVIII epitopes while maintaining the $CD25^+Foxp3^+$ Treg phenotype and immunosuppressive function. Further experiments are required to examine FVIII-specific $CD4^+$ T cells can be converted into $CD25^+Foxp3^+$ Tregs after extensive *in vitro* expansion or if the AS-induction of the Treg phenotype has to be conducted simultaneously to $CD4^+$ T cell expansion in order to reach sufficient conversion rates.

One concern about combining FVIII-specific $CD4^+$ T cell expansion and the chemical conversion of expanded cells into $CD25^+Foxp3^+$ Tregs is the identification of their antigen-specificity by using FVIII tetramer. The transcription factor Foxp3 is located to the nucleoplasm and Foxp3 staining requires fixation and permeabilisation of the cells, whereas FVIII tetramer staining is not compatible with cell fixation and permeabilisation protocols (The Human Protein Atlas, 2021c). Instead, Tregs could be identified by a $CD25^+CD127^{low/-}$ phenotype, as proposed by Yu and colleagues, while simultaneously examining FVIII-specificity using FVIII tetramer (Yu *et al.*, 2012). However, this phenotype is predominantly described for naturally occurring Tregs in human peripheral blood and it remains to be investigated if *in vitro* induced murine $CD25^+Foxp3^+$ Tregs can be identified by the same biomarkers. Alternatively, Foxp3 reporter

mice, such as Foxp3^{DTR} knock-in mice expressing enhanced GFP from the Foxp3 locus, can help to directly visualise induction of Foxp3 expression in converted Tregs and allow for simultaneous FVIII tetramer staining without requiring cell fixation and permeabilisation (Kim *et al.*, 2007).

In conclusion, adoptive cell transfer of *in vitro* expanded and induced FVIII-specific Tregs alongside with protein replacement therapy using half-life extended FVIII-Albumin fusion proteins has the potential to effectively prevent FVIII inhibitor formation and induce long-term immune tolerance in HemA patients without the need of undergoing currently established burdensome ITI protocols or highly expensive gene therapy approaches.

Chapter 6: General discussion

Human serum albumin is the most abundant protein in blood serum, accounting for over 50 % of the total serum protein fraction, and functions as a transport shuttle for various metabolites and molecules while also regulating the colloid oncotic osmotic pressure (Quinlan *et al.*, 2005). Albumin, as well as IgG molecules, exhibit prolonged circulatory half-lives of around 3 weeks in humans substantially exceeding half-life properties of other serum proteins which usually are cleared from the circulation within hours or days (Waldmann *et al.*, 1971; Quinlan *et al.*, 2005; Takata *et al.*, 2011). The extended half-life of albumin is considered to be largely mediated by the pH-dependent interaction with the intracellular neonatal Fc receptor (FcRn) within acidified endosomal structures protecting endocytosed ligand from lysosomal degradation and facilitating recycling back to the plasma membrane (Chaudhury *et al.*, 2003). Although FcRn-dependent albumin recycling has been intensively studied in FcRn-transfected immortalised cell lines, there is a substantial gap of knowledge about FcRn-albumin cell biology in primary cells (Mahmoud, 2015; Schmidt *et al.*, 2017; Chia *et al.*, 2018; Grevys *et al.*, 2018). Understanding FcRn-mediated albumin trafficking and recycling in physiologically relevant primary cells is particularly important as several reports suggest major differences in albumin endocytosis and intracellular FcRn localisation between primary cells and immortalised cell lines, which raises questions regarding the intracellular itineraries of the ligand and the receptor in primary cells (Gan *et al.*, 2009; Anderson, 2014; Mahmoud, 2015; Chia *et al.*, 2018; Toh *et al.*, 2020).

Recently, FcRn-dependent albumin recycling mediated by tubular carriers have been described in primary macrophages (Toh *et al.*, 2020). To gain more insights into how FcRn-bound albumin is partitioned into tubules in primary macrophages, I established a multiplexed approach using two independent biophysical methods, namely FLIM-FRET and RICS, to characterise the intracellular receptor ligand interaction within endosomal structures in a spatiotemporal manner. The FLIM data demonstrated that fluorescently labelled albumin and FcRn interact in endosomal structures as well as in tubules emanating from globular endosomes.

RICS analyses identified a higher fraction of wildtype HSA to be less mobile within endosomal structures in the presence of FcRn compared with the non-binding mutant of HSA, rHSA^{H464Q}.

To study FcRn-cell biology in primary endothelial cells, I established blood outgrowth endothelial cells (BOECs) isolated from peripheral blood of healthy human donors. My findings revealed that BOECs were capable of performing effective fluid phase endocytosis of albumin via macropinocytosis and upon internalisation, HSA co-localised with FcRn in early macropinosome structures. Wildtype HSA was sorted into FcRn-positive tubular structures emerging from the body of macropinosomes, whereas the non-FcRn binding rHSA^{H464Q} was excluded from these tubules. These data indicate similarities in FcRn-albumin cell biology between BMDMs and cultured BOECs highlighting the potential role of macrophages and the vascular endothelium in regulating albumin homeostasis *in vivo* (Toh *et al.*, 2020).

In Chapter 5, I explored the potential of albumin fusion proteins to induce immune tolerance which would be an additional benefit of the lifetime extension of therapeutics in the clinic. In particular, I investigated how fluorescently labelled FVIII-Albumin fusion protein is internalised by FVIII-specific B cells and assessed the potential to induce immune tolerance against recombinant FVIII using *in vitro* generated FVIII-specific regulatory T cells in the context of hemophilia A. My findings suggest that FVIII and FVIII-Albumin fusion proteins are recognised and subsequently internalised by FVIII-specific B cells in a similar fashion. Together with studies by the Becker-Gotot group showing that administration of FVIII-Albumin induces an immunotolerant phenotype in HemA mice (unpublished data), these findings indicate a direct contribution of FVIII-Albumin to immune tolerance towards FVIII.

Furthermore, I established *in vitro* protocols to, on the one hand, specifically expand FVIII-specific CD4$^+$ T cells and, on the other hand, efficiently convert conventional CD4$^+$ T cells into immunosuppressive CD25$^+$Foxp3$^+$ Tregs. The combination of both protocols potentially enables the *in vitro* generation of high numbers of FVIII-specific CD25$^+$Foxp3$^+$ Tregs which, upon adoptive cell transfer,

have the potential to induce immune tolerance towards recombinant FVIII and prevent the formation of inhibitory anti-FVIII antibodies or, alternatively, facilitate the elimination of pre-existing inhibitors in HemA patients.

6.1: Unveiling intracellular receptor-ligand interaction by multiplexed biophysical approaches

The application of biophysical methods to cell biology has become increasingly popular over the last decade and led to better understanding of various processes including biological phase separation, DNA repair, wound healing, membrane organisation, and cytoskeleton interactions (Lommerse *et al.*, 2004; Kapus and Janmey, 2013; Hinde *et al.*, 2014; Khan and Arany, 2015; Lou *et al.*, 2019; Yoshizawa *et al.*, 2020). In particular, fluorescence lifetime imaging microscopy (FLIM) in combination with Förster resonance energy transfer (FRET) and fluorescence spectroscopy (FFS) have been used intensively to unveil and map intracellular interactions between macromolecules and the mobility of intracellular molecules within a defined region of interest (ROI), respectively (Hink, 2014; Lou *et al.*, 2019; Priest *et al.*, 2019; Manko *et al.*, 2020).

The application of FLIM-FRET and FFS-derived raster image correlation spectroscopy (RICS) to unveil intracellular interaction of endocytosed albumin with its receptor, FcRn, in primary macrophages led to the identification of spatiotemporal resolution of receptor-ligand interactions in endosomal structures and the quantification of endocytosed albumin molecules which interact with FcRn within the lumen of endosomes in primary macrophages. This multiplexed approach, which was established in this study, could now be used to also investigate FcRn-albumin interactions in other physiologically relevant cell types, such as blood outgrowth endothelial cells (BOECs), to identify potential cell type-specific differences. Furthermore, other intracellular receptor interactions with their particular ligands within endosomal structures, such as G-coupled protein receptors, toll-like receptors and cargo-selective receptors such as vacuolar protein sorting-associated (Vps) proteins involved in sorting nexin-mediated

protein trafficking, could be characterised in a spatiotemporal manner by these biophysical approaches (Cullen, 2008; Gangloff, 2012; Hanyaloglu, 2018; Retamal *et al.*, 2019).

A strength of this current study was the inclusion of C-terminal and N-terminal labelled FcRn-mCherry constructs, which revealed the efficiency of detected FRET transfer to be sensitive to the exact localisation of the acceptor fluorophore, and the use of the non-FcRn binding rHSA^{H464Q} mutant, which confirmed the specificity of the molecular interactions detected by the biophysical approaches. The use of appropriate controls, such as non-, low- or high-binding ligand variants or low- and high-affinity receptors, would also be important applying these techniques to other receptor-ligand systems to exclude the influence of artefacts.

Another strength of the current study is the use of two independent biophysical techniques, FLIM-FRET and RICS. The use of these two techniques allows the characterisation of interaction of fluorescently labelled ligand with either fluorescently labelled or endogenous receptor molecules. The analysis of ligand binding to endogenous receptors by RICS provides a technique to analyse the properties of non-transfected primary cells isolated from transgenic mouse lines.

The combination of FLIM-FRET and RICS could also be used for screening studies to identify low-affinity or high-affinity binding mutants of ligands or the optimisation of recombinant fusion proteins for therapeutic applications, and to characterise and quantify receptor-ligand interactions within endosomal structures of cells, which represent a physiological environment where many interactions occur.

6.2: Primary blood outgrowth endothelial cells as a primary cell model for studying cell biological processes

Most cell biological pathways and processes have been extensively studied using immortalised cell lines due to their ready availability, easy handling, and rapid proliferation. However, several reports raise concerns about using immortalised

cell lines to study cell type-specific functions, such as endocytosis or intracellular cargo trafficking, because comparative analyses have revealed significant differences in the proteomes and transcriptomes of immortalised cell lines compared to the corresponding primary cells resulting in altered functional properties (Horvath *et al.*, 2008; Pan *et al.*, 2009; Anderson, 2014; Das *et al.*, 2016). For endothelial cells, fundamental differences have been identified in the gene expression profiles of immortalised cell lines compared with primary cells, and the later have been shown to closely resemble gene expression profiles of uncultured *ex vivo* endothelium (Unger *et al.*, 2002; Boerma *et al.*, 2006; Frausto and Aldave, 2014). Although these findings highlight the importance for establishing primary endothelial cell models to investigate endothelial-specific cell biology *in vitro*, primary endothelial cells used previously have often exhibited poor phenotypic stability, proliferative properties, and lifespan *in vitro* as well as batch- or donor-specific differences upon isolation (Bouïs *et al.*, 2001). Additionally, the heterogeneity of endothelial cells regarding their function and origin has to be taken into account to choose suitable primary cells for studying particular biological processes (Bachetti and Morbidelli, 2000).

The establishment of differentiated endothelial cells derived from circulating endothelial cell progenitors present in human peripheral blood, known as blood outgrowth endothelial cells (BOECs), may overcome the issues arising from previous primary endothelial cell models. BOEC lines can be established from small volumes (≥ 2 ml) of human peripheral blood from healthy donors making them readily available and easy to isolate (Ecklu-Mensah *et al.*, 2018). In contrast to many other primary endothelial cells derived from specialised vessels or tissues, BOECs, due to their occurrence in peripheral blood, presumably reflect an endothelial cell population contributing to the formation of the cellular monolayer lining the inner wall of blood vessels throughout the body (Lin *et al.*, 2000; Bachetti and Morbidelli, 2000). Indeed, BOECs were shown to express classic endothelial markers including CD144 (VE-Cadherin), CD31 (PECAM-1) and von Willebrand factor (vWF) resembling a microvasculature signature and, compared to widely used HUVEC cells, express high amounts of angiogenetic

factors suggesting the potential of BOECs to drive *de novo* formation of blood vessels (Lin *et al.*, 2002; Coppens *et al.*, 2013).

My findings supported the hypothesis that cultured BOECs reflect a suitable primary cell model for investigating endothelium-specific cell biological processes. BOEC lines exhibited stable endothelial cell marker expression and high proliferative properties up to passage 14 and the ability to successfully cryopreserve these primary cells supported the long-term culture of single BOEC clones. The longevity of BOECs, and availability of genetic tools suitable for BOECs, allows the generation of stable BOEC lines harbouring knock-ins or -outs of various target genes (Lin *et al.*, 2002; Matsui *et al.*, 2007; Schillemans *et al.*, 2019). Furthermore, I have shown that cultured BOECs are capable of performing effective fluid phase uptake via macropinocytosis, an important endocytic pathway for the regulation of various endothelial functions such as nutrient uptake, receptor signalling and angiogenesis (Basagiannis *et al.*, 2016; Kim *et al.*, 2017).

Although the stable expression of endothelial-specific markers is widely accepted, the transcriptomic signature of cultured BOECs, and to which extent this signature resembles the expression profile of *ex vivo* endothelium, remains unknown. A recent study by Boer *et al*. highlighted donor- and clone-specific differences in the morphology, genetic profile and proliferative capacities of BOECs (de Boer *et al.*, 2020). Hence, it would be very instructive to further characterise the genetic signature of cultured BOECs by bioinformatical-based methods such as RNAseq to assess variations in gene expression between individual BOEC clones derived from different donors, and from different passages of a single BOEC line, and to compare BOEC-derived expression profiles with *ex vivo* endothelium. Such studies will also help to identify potential cell heterogeneity within BOEC lines and evaluate how closely they resemble the endothelium *in vivo.* Expression profiles will also identify the activation state of BOEC monolayers maintained under continuous culture in the presence of endothelial-specific growth factors.

The use of cultured BOEC monolayers provides valuable insights understanding endothelial-specific cell biological pathways. For future studies, it would be informative to conduct experiments using BOECs under physiologically relevant culture conditions. *In vivo*, endothelial cells are polarised and regulate the exchange of molecules between the circulation and the extravascular space while being exposed to a constant flow generated by the blood stream. It would be beneficial to study cell biological processes such as endocytosis and protein trafficking mediated by BOECs within advanced culture setups such as flow chambers or three-dimensional angiogenesis models using Matrigel. In addition to cell biological studies, BOECs could also be used to characterise endothelium-mediated immune regulation in co-culture assays and their potential angiogenetic capacities make them an attractive tool for investigating gene therapeutical approaches for the treatment of vasculature- and blood-related diseases such as von Willebrand disease and hemophilia A.

6.3: Intracellular trafficking of HSA in primary blood outgrowth endothelial cells

In addition to innate immune cells, the vascular endothelium has been identified as an important regulator of albumin homeostasis *in vivo* (Pyzik *et al.*, 2019). I established BOECs as a suitable primary endothelial cell model to study FcRn-dependent albumin cell biology and demonstrated that, albumin was efficiently endocytosed by BOECs via macropinocytosis.

After internalisation, albumin was located to enlarged, EEA1-positive endosomal structures, presumably early macropinosomes, and was excluded from late endosomes and lysosomes indicating that internalised albumin is protected from degradation. In contrast, non-FcRn binding rHSA^{H464Q} mutant showed higher overlap with late endosomal and lysosomal markers suggesting that WT albumin is rescued from degradation in a FcRn-dependent manner. In live BOECs, albumin, but not rHSA^{H464Q}, was sorted into tubular transport carriers emanating from globular endosomes after 20 – 30 minutes uptake, well before cargo was

shown to reach degradative compartments in BOECs (~ 45 – 60 minutes). The morphology and progression of the tubules, that were observed to emerge from large globular endosomes, resemble SNX5-positive tubular transport carriers which have been shown to mediate recycling in primary macrophages, suggesting an albumin recycling pathway, similar to macrophages, also exists in primary endothelial cells (Van Weering *et al.*, 2012; Allison *et al.*, 2013; Toh *et al.*, 2020).

However, albumin recycling in primary macrophages was shown to be significantly more rapid and efficient (Toh *et al.*, 2020) compared to cultured BOEC monolayers. Presumably, this is due to the increased endocytic capacity of macrophages, representing highly specialised antigen presenting cells, whereas endothelial cells are considered to exhibit only low levels of constitutive macropinocytic activity (Lin *et al.*, 2020). My findings revealed that primary macrophages isolated from hFcRn$^{Tg/Tg}$ line 276 mice, which were used for the characterisation of FcRn-mediated albumin recycling (Toh *et al.*, 2020), expressed 6 – 7-fold higher amounts of FcRn compared to BOECs indicating that the higher FcRn expression levels in the transgenic macrophages possibly contribute to increased recycling efficiencies. A lower efficiency of FcRn-dependent recycling efficiency might explain the difficulty in the detection of recycled albumin in BOEC supernatants by ELISA and Western Blot. The use of transgenic overexpression of FcRn in BOECs might help to further investigate FcRn-albumin cell biology and to assess recycling efficiencies in these primary endothelial cells. Alternatively, stable FcRn knock-out BOEC lines could be generated by CRISPR/Cas9-engineering to evaluate the intracellular itinerary of albumin in the absence of the receptor.

The high number of endothelial cells (~ 6 x 10^{13}) *in vivo* and large endothelial surface area (4000 – 7000 m^2) strongly suggest an important role of the endothelium in maintaining high albumin serum concentrations and extending its circulatory half-life (Aird, 2005). Further insights into determining the amount of endocytosed albumin which is recycled to the circulation by endothelial cells will help to evaluate their overall contribution to albumin homeostasis *in vivo*.

Although, the occurrence of tubular transport carriers emanating from globular structures suggests direct recycling of albumin back to the plasma membrane by BOECs, as observed for primary macrophages (Toh *et al.*, 2020), the involvement of Rab11-positive recycling endosomes cannot be excluded and needs to be further investigated.

As endothelial cells fulfill important functions in regulating the exchange of compounds between the blood circulation and the extravascular space *in vivo* by mediating transcytosis of molecules including albumin, the transcytosis process might also contribute to FcRn-albumin cell biology in cultured BOECs (Mehta and Malik, 2006). It would be instructive to investigate how FcRn-dependent albumin trafficking is regulated in polarised BOECs using trans-well assays or three-dimensional angiogenesis models to better mimic the state of endothelial cells *in vivo*.

In general, *in vitro* cell models reflect an isolated cell population cultured under optimal growth conditions in presence of growth factors and other stimuli. Although primary cells are a good approximation to reflect physiologically relevant conditions, a concern of using endothelial cell models might be the homogeneity of cultured cells, whereas the endothelium *in vivo* is highly heterogenous and is composed of various endothelial cell types fulfilling specialised functions (Potente and Mäkinen, 2017). Additionally, batch- or clone-dependent differences of BOEC lines need to be addressed by omics approaches such as RNAseq.

In conclusion, my findings highlight the strengths of BOECs as a model for primary endothelial cells, and strongly suggest that endothelial cells contribute to albumin homeostasis *in vivo* by mediating the FcRn-dependent recycling of endocytosed albumin via tubular transport carriers. The exact mechanism, and the transport machinery involved, remains to be addressed in future studies. Furthermore, BOECs have considerable potential to be exploited for a variety of functional properties of endothelium *in vivo*, such as polarisation and angiogenesis.

6.4: Potential use of half-life extended albumin fusion proteins for the treatment of hemophilia A

The long circulatory half-life mediated by FcRn-dependent recycling makes albumin an attractive candidate to design therapeutic fusion proteins exhibiting enhanced pharmacological properties (Sleep *et al.*, 2013). Nowadays, recombinant albumin is produced on an industrial scale and has been shown to be stable and immunologically inert in *in vivo* models (Sleep, 2015; Pilati and Howard, 2020). In particular, the generation of albumin fusion proteins for the treatment of blood-related diseases such as hemophilia A and B would improve treatment options reducing the number of intravenous injections of recombinant coagulation factor VIII and IX, respectively, during protein replacement therapy. Indeed, Idelvion®, an albumin fusion with FIX approved for the treatment of hemophilia B patients, exhibits enhanced half-life properties *in vivo*, and, furthermore, *in vitro* studies have revealed that Idelvion® is recycled by immortalised cell lines in a FcRn-dependent manner similar to albumin alone (Choy, 2016; Chia *et al.*, 2018).

The development of albumin fusion proteins, similar to Idelvion®, for the treatment of hemophilia A (HemA) is complicated by the frequent occurrence of inhibitory antibodies against recombinant FVIII, which diminishes the therapeutic function of recombinant FVIII during protein replacement therapy (Gouw *et al.*, 2013; Meeks and Batsuli, 2016). Hence, it is important to consider potential immune responses against recombinant therapeutics administered to HemA patients. Studies by the Becker-Gotot laboratory suggest that the administration of FVIII-Albumin fusion protein into HemA mice leads to an immune tolerant phenotype, characterised by decreased numbers of FVIII-specific B cells and lower FVIII inhibitor titers compared to HemA mice treated with recombinant FVIII (unpublished data). Hence, the fusion of FVIII to the self-protein, albumin, may enhance tolerance induction to FVIII epitopes. In this work, I identified a similar uptake efficiency for fluorescently labelled FVIII and FVIII-Albumin fusion protein by FVIII-specific B cells, using imaging flow cytometry. This result indicates that despite the fusion to albumin, FVIII-Albumin is recognised by FVIII-specific cells

and may have the potential to induce immune tolerance in an active manner. Induced tolerance could potentially be mediated by two processes: Firstly, FVIII-Albumin might undergo FcRn-dependent recycling *in vivo* resulting in increased serum concentration and prolonged circulatory half-life which leads to the induction of high-zone tolerance in HemA mice (Figure 6.1) (Diener and Feldmann, 1972). Secondly, FVIII-Albumin-recognising B cells might present not only FVIII- but also albumin-derived peptides upon internalisation of the fusion protein. This could lead to the recognition of albumin peptides presented on B cells by albumin-specific Tregs, which in turn could initiate B cell apoptosis via the PD-1/PD-L1 axis and thereby preventing the formation of inhibitors (Figure 6.1). At present, it remains unclear, to what extent either of these proposed mechanisms contribute to the immune tolerance induction observed in HemA mice receiving FVIII-Albumin treatment. To resolve this question, it will be important to investigate any differences in intracellular trafficking pathways of FVIII and the fusion protein, and also to identify the peptides presented by FVIII-specific B cells derived from FVIII-albumin internalisation and processing.

Of note is that B cells express only low levels of FcRn, hence, it is unlikely that internalised FVIII-Albumin is protected from lysosomal degradation (The Human Protein Atlas, 2021a). This issue could be investigated by quantification of the co-localisation of FVIII and FVIII-Albumin with LysoTracker, using the antigen uptake assay and imaging flow cytometry analysis I established.

Another interesting strategy to explore would be the combination of FVIII-Albumin treatment together with the transfer of FVIII-specific Tregs, to induce immune tolerance *in vivo*. The two *in vitro* protocols I have established would allow the generation of high numbers of FVIII-specific Tregs with the capacity to suppress unwanted immune responses against recombinant FVIII or FVIII-Albumin. The pharmacological properties of the extended half-life of FVIII-Albumin might also be able to enhance the stimulation of the adoptively transferred FVIII-specific Tregs *in* vivo, and extend their survival, to result in long-term immune tolerance induction in HemA patients.

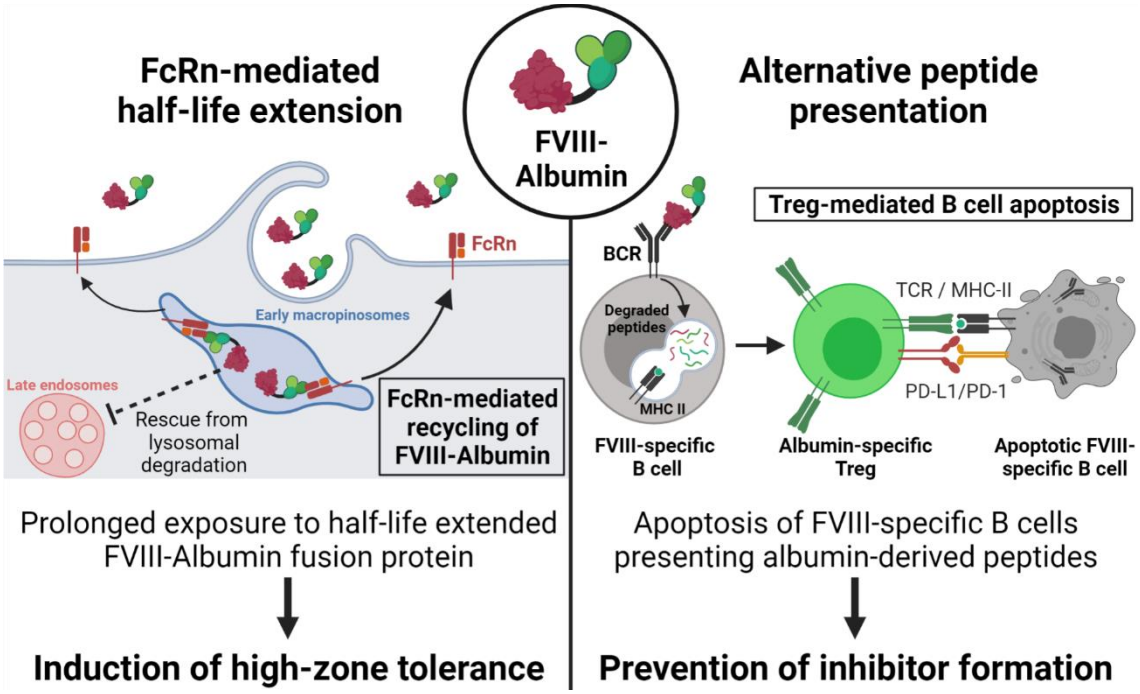

Figure 6.1: Graphical summary of proposed mechanisms for FVIII-Albumin-mediated immune tolerance induction

The cartoon summarises the two potential advantages of using FVIII-Albumin fusion proteins for the treatment of Hemophilia A, namely the induction of high-zone tolerance due to an increased half-life and the prevention of inhibitor formation. Firstly, FVIII-Albumin is internalised via macropinocytosis by antigen-presenting cells expressing FcRn. After endocytosis, FVIII-Albumin can interact with FcRn within acidified early macropinosomes via the albumin domain of the fusion protein. The receptor-ligand complex is partitioned into tubular transport carriers mediating FcRn-dependent recycling. The ability to interact with FcRn rescues FVIII-Albumin from lysosomal degradation and, together with the recycling pathway, results in extended half-life of the fusion protein eventually inducing high-zone tolerance. Secondly, FVIII-Albumin is recognised and internalised by FVIII-specific B cells. The fusion protein is degraded into peptides which are loaded onto MHC II molecules for the presentation of FVIII-Albumin-derived peptides to $CD4^+$ T cells. FVIII-specific B cells presenting peptides derived from the albumin domain of the fusion protein are recognised by naturally occurring albumin-specific Tregs. This interaction leads to the induction of apoptosis in FVIII-specific B cells mediated by Tregs via the PD-1/PD-L1 axis and prevents the formation of inhibitory FVIII antibodies by FVIII-specific plasma cells. The figure was created with BioRender.com.

6.5 Conclusion and future directions

In conclusion, this work provides a deeper understanding of the intracellular interaction of FcRn and albumin in primary macrophages and also the FcRn-albumin biology in primary endothelial cells. Furthermore, I have investigated the internalisation of albumin fusion protein by B cells which potentially modifies immune responses to induce tolerance to the fusion protein. The characterisation of both the cell biological and immunological aspects of albumin fusion proteins is essential to assess the potential of half-life extended therapeutics for effective clinical application in diseases such as hemophilia A.

In particular, the developed biophysical techniques to characterise intracellular receptor ligand interactions within endosomes have a wide applicability and can be expanded to study the interaction of potential albumin fusion protein therapeutics with FcRn. Furthermore, the established FLIM-FRET and FFS-based RICS approach paves the way to study and compare the FcRn albumin recycling system in different cell types such as macrophages and primary endothelial cells using BOEC lines. BOECs represent a viable platform to study cell biological processes such as endocytosis and intracellular trafficking of albumin and albumin fusion proteins in primary endothelial cells to pinpoint their potential role in albumin homeostasis *in vivo*. It remains to be investigated to which extent these processes differ in polyclonal BOEC lines or BOEC lines isolated from different donors. It is advisory to characterise the genetic profile of distinct BOEC lines and compare their cell biological properties. A more comprehensive understanding of albumin cell biology in primary endothelial cells would elucidate how endocytosed albumin is processed by endothelial cells *in vivo* and reveal the potential to target endothelial cell specifically using albumin fusion proteins for extended half-life or targeted delivery of various compounds such as anti-cancer drugs (Sleep, 2015).

The established protocols for the expansion of FVIII-specific $CD4^+$ T helper cells and the *in vitro* induction of $Foxp3^+$ Tregs allow for the potential generation of high numbers of FVIII-specific Tregs with immunosuppressive potential.

However, it has yet to be identified how long phenotype and function of expanded FVIII-specific $CD4^+$ T helper cells and induced $Foxp3^+$ Tregs can be maintained, especially in *in vivo* settings. In future, the combination and optimisation of both protocols would lead to phenotypic and functional stability of induced, antigen-specific Tregs, and reduce the risk of unwanted immune reactions *in vivo*.

Eventually, the use of efficient FVIII-Albumin fusion proteins in combination with the adoptive transfer of FVIII-specific $Foxp3^+$ Tregs would present a potential therapy approach for Hemophilia A patients, which could resolve the two major downfalls of current therapies, namely the short half-life of recombinant FVIII and the development of inhibitory antibodies due to adverse immune reactions against the therapeutic protein.

References

Aird WC. Phenotypic Heterogeneity of the Endothelium. Circ. Res. 2007; 100: 158–173

Aird WC. Spatial and temporal dynamics of the endothelium. J. Thromb. Haemost. 2005; 3: 1392–1406

Akamatsu M, Mikami N, Ohkura N, Kawakami R, Kitagawa Y, Sugimoto A, Hirota K, Nakamura N, Ujihara S, Kurosaki T, Hamaguchi H, Harada H, Xia G, Morita Y, Aramori I, Narumiya S and Sakaguchi S. Conversion of antigen-specific effector/memory T cells into Foxp3-expressing Treg cells by inhibition of CDK8/19. Sci. Immunol. 2019; 4: eaaw2707

Akilesh S, Christianson GJ, Roopenian DC and Shaw AS. Neonatal FcR Expression in Bone Marrow-Derived Cells Functions to Protect Serum IgG from Catabolism. J. Immunol. 2007; 179: 4580–4588

Aledort L, Mannucci PM, Schramm W and Tarantino M. Factor VIII replacement is still the standard of care in haemophilia A. Blood Transfus. 2019; 17: 479–486

Allen JA, Halverson-Tamboli RA and Rasenick MM. Lipid raft microdomains and neurotransmitter signalling. Nat. Rev. Neurosci. 2007 82 2006; 8: 128–140

Allison R, Lumb JH, Fassier C, Connell JW, Ten Martin D, Seaman MNJ, Hazan J, Reid E, Martin D Ten, Seaman MNJ, Hazan J and Reid E. An ESCRT–spastin interaction promotes fission of recycling tubules from the endosome. J. Cell Biol. 2013; 202: 527–543

American Type Culture Collection, 2022NCTC clone 929 [L cell, L-929, derivative of Strain L] | ATCC. https://www.atcc.org/products/ccl-1#detailed-product-information (access date: 14.03.2022)

Amsellem S, Gburek J, Hamard G, Nielsen R, Willnow TE, Devuyst O, Nexo E, Verroust PJ, Christensen EI and Kozyraki R. Cubilin Is Essential for Albumin Reabsorption in the Renal Proximal Tubule. J. Am. Soc. Nephrol. 2010; 21: 1859–1867

Ananyeva NM, Lacroix-Desmazes S, Hauser CA, Shima M, Ovanesov M V, Khrenov A V and Saenko EL. Inhibitors in hemophilia A: mechanisms of inhibition, management and perspectives. Blood Coagul. Fribrinolysis 2004; 15: 109–124

Andersen JT, Daba MB, Berntzen G, Michaelsen TE and Sandlie I. Cross-species Binding Analyses of Mouse and Human Neonantal Fc Receptor Show Dramatic Differences in Immunoglobulin G and Albumin Binding. 2010; 285: 4826–4836

Andersen JT, Dalhus B, Cameron J, Daba MB, Plumridge A, Evans L, Brennan SO, Gunnarsen KS, Bjørås M, Sleep D and Sandlie I. Structure-based mutagenesis reveals the albumin-binding site of the neonatal Fc receptor. Nat. Commun. 2012; 3: 610

Andersen JT, Dalhus B, Viuff D, Ravn BT, Gunnarsen KS, Plumridge A, Bunting K, Antunes F, Williamson R, Athwal S, Allan E, Evans L, Bjørås M, Kjærulff S, Sleep D, Sandlie I and Cameron J. Extending serum half-life of albumin by engineering neonatal Fc receptor (FcRn) binding. J. Biol. Chem. 2014; 289: 13492–13502

Andersen JT, Pehrson R, Tolmachev V, Daba MB, Abrahmsén L and Ekblad C. Extending Half-life by Indirect Targeting of the Neonatal Fc Receptor (FcRn) Using a Minimal Albumin Binding Domain. J. Biol. Chem. 2011; 286: 5234–5241

Anderson CL. There's been a Flaw in Our Thinking. Front. Immunol. 2014; 5: 540

André S, Meslier Y, Dimitrov JD, Repessé Y, Kaveri S V, Lacroix-Desmazes S and Dasgupta S. A Cellular Viewpoint of Anti-FVIII Immune Response in Hemophilia A. Clin. Rev Allerg Immunol 2009; 37: 105–113

Antohe F, Rădulescu L, Gafencu A, Ghe V, Simionescu M, Rădulescu L, Gafencu A, Gheţie V and Simionescu M. Expression of functionally active FcRn and the differentiated bidirectional transport of IgG in human placental endothelial cells. Hum. Immunol. 2001; 62: 93–105

Antonescu CN, McGraw TE and Klip A. Reciprocal Regulation of Endocytosis and Metabolism. Cold Spring Harb. Perspect. Biol. 2014; 6: a016964

Appelqvist H, Wäster P, Kågedal K and Öllinger K. The lysosome: from waste bag to potential therapeutic target. J. Mol. Cell Biol. 2013; 5: 214–226

Araki N, Hamasaki M, Egami Y and Hatae T. Effect of 3-methyladenine on the fusion process of macropinosomes in EGF-stimulated A431 cells. Cell Struct. Funct. 2006; 31: 145–157

Arques S. Human serum albumin in cardiovascular diseases. Eur. J. Intern. Med. 2018; 52: 8–12

Arques S and Ambrosi P. Human Serum Albumin in the Clinical Syndrome of Heart Failure. J. Card. Fail. 2011; 17: 451–458

Asahara T, Murohara T, Sullivan A, Silver M, Van Der Zee R, Li T, Witzenbichler B, Schatteman G and Isner JM. Isolation of Putative Progenitor Endothelial Cells for Angiogenesis. Science 1997; 275: 964–967

Ashbrook JD, Spector AA, Santos EC and Fletcher JE. Long Chain Fatty Acid Binding to Human Plasma Albumin. J. Biol. Chem. 1975; 250: 2333–2338

Attia FM, Maaty A and Kalil FA. Circulating endothelial cells as a marker of vascular dysfunction in patients with systemic lupus erythematosus by real-time polymerase chain reaction. Arch. Pathol. Lab. Med. 2011; 135: 1482–1485

Autin L, Miteva MA, Lee WH, Mertens K, Radtke K-P and Villoutreix BO. Molecular models of the procoagulant Factor VIIIa–Factor IXa complex. J. Thromb. Haemost. 2005; 3: 2044–2056

Avery LB, Wang M, Kavosi MS, Joyce A, Kurz JC, Fan YY, Dowty ME, Zhang M, Zhang Y, Cheng A, Hua F, Jones HM, Neubert H, Polzer RJ and O'Hara DM. Utility of a human FcRn transgenic mouse model in drug discovery for early assessment and prediction of human pharmacokinetics of monoclonal antibodies. MAbs 2016; 8: 1064–1078

Azevedo C, Nilsen J, Grevys A, Nunes R, Andersen JT and Sarmento B. Engineered albumin-functionalized nanoparticles for improved FcRn binding enhance oral delivery of insulin. J. Control. Release 2020; 327: 161–173

Babst M, Katzmann DJ, Snyder WB, Wendland B and Emr SD. Endosome-associated complex, ESCRT-II, recruits transport machinery for protein sorting at the multivesicular body. Dev. Cell 2002; 3: 283–289

Bache KG, Brech A, Mehlum A and Stenmark H. Hrs regulates multivesicular body formation via ESCRT recruitment to endosomes. J. Cell Biol. 2003; 162: 435–442

Bachetti T and Morbidelli L. Endothelial Cells in Culture: A Model for Studying Vascular Functions. Pharmacol. Res. 2000; 42: 9–19

Baetz NW and Goldenring JR. Distinct patterns of phosphatidylserine localization within the Rab11a-containing recycling system. Cell. Logist. 2014; 4: e28680

Baetz NW and Goldenring JR. Rab11-family interacting proteins define spatially and temporally distinct regions within the dynamic Rab11a-dependent recycling system. Mol. Biol. Cell 2013; 24: 643–658

Bal W, Sokołowska M, Kurowska E and Faller P. Binding of transition metal ions to albumin: Sites, affinities and rates. Biochim. Biophys. Acta - Gen. Subj. 2013; 1830: 5444–5455

Basagiannis D, Zografou S, Murphy C, Fotsis T, Morbidelli L, Ziche M, Bleck C, Mercer J and Christoforidis S. VEGF induces signalling and angiogenesis by directing VEGFR2 internalisation via macropinocytosis. J. Cell Sci. 2016; 129: 4091–4104

Benson MJ, Pino-Lagos K, Rosemblatt M and Noelle RJ. All-trans retinoic acid mediates enhanced T reg cell growth, differentiation, and gut homing in the face of high levels of co-stimulation. J. Exp. Med. 2007; 204: 1765–1774

Beres A, Komorowski R, Mihara M and Drobyski WR. Instability of Foxp3 Expression Limits the Ability of Induced Regulatory T Cells to Mitigate Graft versus Host Disease. Clin. Cancer Res. 2011; 17: 3969–3983

Bern M, Knudsen M, Nilsen J, Sandlie I, Andersen JT, Sand KMK, Nilsen J, Sandlie I and Andersen JT. The role of albumin receptors in regulation of albumin homeostasis: Implications for drug delivery. J. Control. Release 2015; 211: 144–162

Berntorp E, Fischer K, Hart DP, Mancuso ME, Stephensen D, Shapiro AD and Blanchette V. Haemophilia. Nat. Rev. Dis. Prim. 2021 71 2021; 7: 45

Bhopale GM and Nanda RK. Blood coagulation factor VIII: An overview. J. Biosci. 2003; 28: 783–789

Bi L, Lawler AM, Antonarakis SE, High KA, Gearhart JD and Kazazian HHJ. Targeted disruption of the mouse factor VIII gene produces a model of haemophilia A. Nat. Genet. 1995; 10: 119–121

Bissig C and Gruenberg J. Lipid Sorting and Multivesicular Endosome Biogenesis. Cold Spring Harb. Perspect. Biol. 2013; 5: a016816

Black BL, Croom J, Eisen EJ, Petro AE, Edwards CL and Surwit RS. Differential effects of fat and sucrose on body composition in A/J and C57BL/6 mice. Metabolism. 1998; 47: 1354–1359

Blanchette VS, Key NS, Ljung LR, Manco-Johnson MJ, van den Berg HM and Srivastava A. Definitions in hemophilia: communication from the SSC of the ISTH. J. Thromb. Haemost. 2014; 12: 1935–1939

Blander JM. The comings and goings of MHC class I molecules herald a new dawn in cross-presentation. Immunol. Rev. 2016; 272: 65–79

Blasius AL and Beutler B. Intracellular Toll-like Receptors. Immunity 2010; 32: 305–315

Bodega F, Zocchi L and Agostoni E. Albumin transcytosis in mesothelium. Am. J. Physiol. - Lung Cell. Mol. Physiol. 2002; 282: L3–L11

de Boer S, Bowman M, Notley C, Mo A, Lima P, de Jong A, Dirven R, Weijers E, Lillicrap D, James P, Eikenboom J, de Boer S, Bowman M, Notley C, Mo A, Lima P, de Jong A, Dirven R, Weijers E, Lillicrap D, James P and Eikenboom J. Endothelial characteristics in healthy endothelial colony forming cells; generating a robust and valid ex vivo model for vascular disease. J. Thromb. Haemost. 2020; 18: 2721–2731

Boerma M, Burton GR, Wang J, Fink LM, McGehee RE and Hauer-Jensen M. Comparative expression profiling in primary and immortalized endothelial cells: Changes in gene expression in response to hydroxy methylglutaryl-coenzyme A reductase inhibition. Blood Coagul. Fibrinolysis 2006; 17: 173–180

Bolli A, Marino M, Rimbach G, Fanali G, Fasano M and Ascenzi P. Flavonoid binding to human serum albumin. Biochem. Biophys. Res. Commun. 2010; 398: 444–449

Bonifacino JS and Neefjes J. Moving and positioning the endolysosomal system. Curr. Opin. Cell Biol. 2017; 47: 1–8

Bonifacino JS and Traub LM. Signals for Sorting of Transmembrane Proteins to Endosomes and Lysosomes. Annu. Rev. Biochem. 2003; 72: 395–447

Borvak J, Richardson J, Medesan C, Antohe F, Radu C, Simionescu M, Ghetie V and Ward ES. Functional expression of the MHC class I-related receptor, FcRn, in endothelial cells of mice. Int. Immunol. 1998; 10: 1289–1298

Bouïs D, Hospers GAP, Meijer C, Molema G and Mulder NH. Endothelium in vitro: A review of human vascular endothelial cell lines for blood vessel-related research. Angiogenes. 2001 42 2001; 4: 91–102

Brackmann HH, Eickhoff HJ, Oldenburg J and Hammerstein U. Long-term therapy and on-demand treatment of children and adolescents with severe haemophilia A: 12 years of experience. Haemostasis 1992; 22: 251–258

Brackmann HH and Gormsen J. Massive factor-VIII infusion in haemophiliac with factor-VIII inhibitor, high responder. Lancet 1977; 310: 933

Brackmann HH, Oldenburg J and Schwaab R. Immune Tolerance for the Treatment of Factor VIII Inhibitors - Twenty Years' 'Bonn Protocol'. Vox Sang. 1996; 70: 30–35

Brackmann HH, White GC, Berntorp E, Andersen T and Escuriola-Ettingshausen C. Immune tolerance induction: What have we learned over time? Haemophilia 2018; 24: 3–14

Brambell FWR, Hemmings WA and Morris IG. A Theoretical Model of γ-Globulin Catabolism. Nat. 1964 2034952 1964; 203: 1352–1355

Braulke T and Bonifacino JS. Sorting of lysosomal proteins. Biochim. Biophys. Acta - Mol. Cell Res. 2009; 1793: 605–614

Bright NA, Davis LJ and Luzio JP. Endolysosomes Are the Principal Intracellular Sites of Acid Hydrolase Activity. Curr. Biol. 2016; 26: 2233–2245

Bryant P, Boukouvala A, McDaniel J and Nance D. Hemophilia A in Females: Considerations for Clinical Management. Acta Haematol. 2020; 143: 289–294

Bryniarski MA, Yee BM, Chaves LD, Stahura CM, Yacoub R and Morris ME. Megalin-mediated albumin endocytosis in cultured murine mesangial cells. Biochem. Biophys. Res. Commun. 2020; 529: 740–746

Buccione R, Orth JD and McNiven MA. Foot and mouth: podosomes, invadopodia and circular dorsal ruffles. Nat. Rev. Mol. Cell Biol. 2004; 5: 647–657

Buckley CM and King JS. Drinking problems: mechanisms of macropinosome formation and maturation. FEBS J. 2017; 284: 3778–3790

Bujny M V, Popoff V, Johannes L and Cullen PJ. The retromer component sorting nexin-1 is required for efficient retrograde transport of Shiga toxin from early endosome to the trans Golgi network. J. Cell Sci. 2007; 120: 2010–2021

Burmeister WP, Gastinel LN, Simister NE, Blum ML and Bjorkman PJ. Crystal structure at 2.2 Å resolution of the MHC-related neonatal Fc receptor. Nature 1994; 372: 336–343

Byams VR, Kouides PA, Kulkarni R, Baker JR, Brown DL, Gill JC, Grant AM, James AH, Konkle BA, Maahs J, Dumas MM, McAlister S, Nance D, Nugent D, Philipp CS, Soucie JM, Stang E and HTCN Investigators. Surveillance of female patients with inherited bleeding disorders in United States Haemophilia Treatment Centres. Haemophilia 2011; 17: 6–13

Cadena Castaneda D, Brachet G, Goupille C, Ouldamer L and Gouilleux-Gruart V. The neonatal Fc receptor in cancer FcRn in cancer. Cancer Med. 2020; 9: 4736–4742

Carter DC, He XM, Munson SH, Twigg PD, Gernert KM, Broom MB and Miller TY. Three-dimensional structure of human serum albumin. Science 1989; 244: 1195–1198

Challa DK, Wang X, Montoyo HP, Velmurugan R, Ober RJ and Ward ES. Neonatal Fc receptor expression in macrophages is indispensable for IgG homeostasis. MAbs 2019; 11: 848–860

Chaudhary N, Gomez GA, Howes MT, Lo HP, McMahon K-A, Rae JA, Schieber NL, Hill MM, Gaus K, Yap AS and Parton RG. Endocytic Crosstalk: Cavins, Caveolins, and Caveolae Regulate Clathrin-Independent Endocytosis. PLOS Biol. 2014; 12: e1001832

Chaudhury C, Brooks CL, Carter DC, Robinson JM and Anderson CL. Albumin Binding to FcRn: Distinct from the FcRn−IgG Interaction. Biochemistry 2006; 45: 4983–4990

Chaudhury C, Mehnaz S, Robinson JM, Hayton WL, Pearl DK, Roopenian DC and Anderson CL. The major histocompatibility complex-related Fc receptor for IgG (FcRn) binds albumin and prolongs its lifespan. J. Exp. Med. 2003; 197: 315–22

Chen AC, Cai X, Li C, Khoryati L, Gavin MA and Miao CH. A Treg-Selective IL-2 Mutein Prevents the Formation of Factor VIII Inhibitors in Hemophilia Mice Treated With Factor VIII Gene Therapy. Front. Immunol. 2020; 11: 638

Chen Q, Kim YC, Laurence A, Punkosdy GA and Shevach EM. IL-2 Controls the Stability of Foxp3 Expression in TGF-β–Induced Foxp3 + T Cells In Vivo. J. Immunol. 2011; 186: 6329–6337

Chen T-C, Cobbold SP, Fairchild PJ and Waldmann H. Generation of anergic and regulatory T cells following prolonged exposure to a harmless antigen. J. Immunol. 2004; 172: 5900–5907

Cheng Y, Boll W, Kirchhausen T, Harrison SC and Walz T. Cryo-electron tomography of clathrin coated vesicles – structural implications for coat assembly. J. Mol. Biol. 2007; 365: 892–899

Chia J, Louber J, Glauser I, Taylor S, Bass GT, Dower SK, Gleeson PA and Verhagen AM. Half-life-extended recombinant coagulation factor IX-albumin fusion protein is recycled via the FcRn-mediated pathway. J. Biol. Chem. 2018; 293: 6363–6373

Chia J, Pestel S, Glauser I, Emmrich K, Hardy MP, Mischnik M, Raquet E, Tomasetig V, Claar P, Zalewski A, Bass GT, Turnbull V, Chen C-G, Wilson MJ, Panousis C, Weimer T, Andrews A, Verhagen AM and Dower SK. Increased potency of recombinant VWF D′D3 albumin fusion proteins engineered for enhanced affinity for coagulation factor VIII. J. Thromb. Haemost. 2021; 00: 1–16

Cho JY, Guo C, Torello M, Lunstrum GP, Iwata T, Deng C and Horton WA. Defective lysosomal targeting of activated fibroblast growth factor receptor 3 in achondroplasia. 2004; 101: 609–614

Choi K, Kennedy M, Kazarov A, Papadimitriou JC and Keller G. A common precursor for hematopoietic and endothelial cells. Development 1998; 125: 725–732

Choy M. Pharmaceutical Approval Update. Pharm. Ther. 2016; 41: 288

Christianson GJ, Brooks W, Vekasi S, Manolfi EA, Niles J, Roopenian SL, Roths JB, Rothlein R and Roopenian DC. Beta 2-microglobulin-deficient mice are protected from hypergammaglobulinemia and have defective antibody responses because of increased IgG catabolism. J. Immunol. 1997; 159: 4781–4792

Chvatchko Y, Hoogewerf AJ, Meyer A, Alouani S, Juillard P, Buser R, Conquet F, Proudfoot AE, Wells TN and Power CA. A key role for CC chemokine receptor 4 in lipopolysaccharide-induced endotoxic shock. J. Exp. Med. 2000; 191: 1755–1763

Cohen GB, Kaur A and Johnson RP. Isolation of viable antigen-specific CD4 T cells by CD40L surface trapping. J. Immunol. Methods 2005; 302: 103–115

Commisso C. The pervasiveness of macropinocytosis in oncological malignancies. Philos. Trans. R. Soc. B 2019; 374: 20180153

Cooper PR, Kliwinski CM, Perkinson RA, Ragwan E, Mabus JR, Powers GD, Dorai H, Giles-Komar J and Hornby PJ. The contribution of cell surface FcRn in monoclonal antibody serum uptake from the intestine in suckling rat pups. Front. Pharmacol. 2014; 5: 225

Coppens V, Heremans Y, Leuckx G, Suenens K, Jacobs-Tulleneers-Thevissen D, Verdonck K, Lahoutte T, Luttun A, Heimberg H and De Leu N. Human blood outgrowth endothelial cells improve islet survival and function when co-transplanted in a mouse model of diabetes. Diabetologia 2013; 56: 382–390

Cormier M, Batty P, Tarrant J and Lillicrap D. Advances in knowledge of inhibitor formation in severe haemophilia A. Br. J. Haematol. 2020; 189: 39–53

Costes S V., Daelemans D, Cho EH, Dobbin Z, Pavlakis G and Lockett S. Automatic and Quantitative Measurement of Protein-Protein Colocalization in Live Cells. Biophys. J. 2004; 86: 3993–4003

Cox D, Lee DJ, Dale BM, Calafat J and Greenberg S. A Rab11-containing rapidly recycling compartment in macrophages that promotes phagocytosis. Proc. Natl. Acad. Sci. 2000; 97: 680–685

Coyle TE, Reding MT, Lin JC, Michaels LA, Shah A and Powell J. Phase I study of BAY 94-9027, a PEGylated B-domain-deleted recombinant factor VIII with an extended half-life, in subjects with hemophilia A. J. Thromb. Haemost. 2014; 12: 488–496

Cullen PJ. Endosomal sorting and signalling: an emerging role for sorting nexins. Nat. Rev. Mol. Cell Biol. 2008; 9: 574–582

Cullen PJ and Korswagen HC. Sorting nexins provide diversity for retromer-dependent trafficking events. Nat. Cell Biol. 2012; 14: 29–37

Cullen PJ and Steinberg F. To degrade or not to degrade: mechanisms and significance of endocytic recycling. Nat. Rev. Mol. Cell Biol. 2018; 19: 679–696

D'Amico G and Bazzi C. Pathophysiology of proteinuria. Kidney Int. 2003; 63: 809–825

D'hooghe L, Chalmers AD, Heywood S and Whitley P. Cell surface dynamics and cellular distribution of endogenous FcRn. PLoS One 2017; 12: e0182695

Dai J, Li J, Bos E, Porcionatto M, Premont RT, Bourgoin S, Peters PJ and Hsu VW. ACAP1 Promotes Endocytic Recycling by Recognizing Recycling Sorting Signals. Dev. Cell 2004; 7: 771–776

Daro E, Sluijs P van der, Galli T and Mellman I. Rab4 and cellubrevin define different early endosome populations on the pathway of transferrin receptor recycling. Proc. Natl. Acad. Sci. 1996; 93: 9559–9564

Das A, Kim SH, Arifuzzaman S, Yoon T, Chai JC, Lee YS, Park KS, Jung KH and Chai YG. Transcriptome sequencing reveals that LPS-triggered transcriptional responses in established microglia BV2 cell lines are poorly representative of primary microglia. J. Neuroinflammation 2016 131 2016; 13: 182

Dasgupta S, Navarrete A-M, Bayry J, Delignat S, Wootla B, André S, Christophe O, Nascimbeni M, Jacquemin M, Martinez-Pomares L, Geijtenbeek TBH, Moris A, Saint-Remy J-M, Kazatchkine MD, Kaveri S V. and Lacroix-Desmazes S. A role for exposed mannosylations in presentation of human therapeutic self-proteins to CD4+ T lymphocytes. Proc. Natl. Acad. Sci. 2007; 104: 8965–8970

Dauwe D, Pelacho B, Wibowo A, Walravens A, Verdonck K, Gillijns H, Caluwe E, Pokreisz P, van Gastel N, Carmeliet G, Depypere M, Maes F, Driessche N Vanden, Droogne W, van Cleemput J, Vanhaecke J, Prosper F, Verfaillie C, Luttun A and Janssens S. Neovascularization Potential of Blood Outgrowth Endothelial Cells From Patients With Stable Ischemic Heart Failure Is Preserved. J. Am. Heart Assoc. 2016; 5: e002288

Delevoye C, Miserey-Lenkei S, Montagnac G, Gilles-Marsens F, Paul-Gilloteaux P, Giordano F, Waharte F, Marks MS, Goud B and Raposo G. Recycling Endosome Tubule Morphogenesis from Sorting Endosomes Requires the Kinesin Motor KIF13A. Cell Rep. 2014; 6: 445–454

Van Deurs B, Holm P, Kayser L, Sandvig K and Hansen S. Multivesicular bodies in HEp-2 cells are maturing endosomes. Eur. J. Cell Biol. 1993; 61: 208–224

Diener E and Feldmann M. Mechanisms at the cellular level during induction of high zone tolerance in vitro. Cell. Immunol. 1972; 5: 130–136

Digman MA, Brown CM, Sengupta P, Wiseman PW, Horwitz AR and Gratton E. Measuring Fast Dynamics in Solutions and Cells with a Laser Scanning Microscope. Biophys. J. 2005; 89: 1317–1327

Digman MA, Caiolfa VR, Zamai M and Gratton E. The Phasor Approach to Fluorescence Lifetime Imaging Analysis. Biophys. J. 2008; 94: L14–L16

Digman MA and Gratton E. Analysis of diffusion and binding in cells using the RICS approach. Microsc. Res. Tech. 2009; 72: 323–332

Doherty GJ and McMahon HT. Mechanisms of Endocytosis. Annu. Rev. Biochem. 2009; 78: 857–902

Donaldson JG and Williams DB. Intracellular Assembly and Trafficking of MHC Class I Molecules. Traffic 2009; 10: 1745–1752

Dons EM, Raimondi G, Cooper DKC and Thomson AW. Induced regulatory T cells: mechanisms of conversion and suppressive potential. Hum. Immunol. 2012; 73: 328–334

Donsante A, Miller DG, Li Y, Vogler C, Brunt EM, Russell DW and Sands MS. AAV vector integration sites in mouse hepatocellular carcinoma. Science 2007; 317: 477

Doodnauth SA, Grinstein S and Maxson ME. Constitutive and stimulated macropinocytosis in macrophages: roles in immunity and in the pathogenesis of atherosclerosis. Philos. Trans. R. Soc. B Biol. Sci. 2019; 374: 20180147

Dumont JA, Liu T, Low SC, Zhang X, Kamphaus G, Sakorafas P, Fraley C, Drager D, Reidy T, McCue J, Franck HWG, Merricks EP, Nichols TC, Bitonti AJ, Pierce GF and Jiang H. Prolonged activity of a recombinant factor VIII-Fc fusion protein in hemophilia A mice and dogs. Blood 2012; 119: 3024–3030

Dunn KW and Maxfield FR. Delivery of ligands from sorting endosomes to late endosomes occurs by maturation of sorting endosomes. J. Cell Biol. 1992; 117: 301–310

Ecklu-Mensah G, Olsen RW, Bengtsson A, Ofori Id MF, Hviidid L, Jensen ATR and Adamsid Y. Blood outgrowth endothelial cells (BOECs) as a novel tool for studying adhesion of Plasmodium falciparum-infected erythrocytes. PLoS One 2018; 13: e0204177

Elkin SR, Lakoduk AM and Schmid SL. Endocytic pathways and endosomal trafficking: a primer. Wien. Med. Wochenschr. 2016; 166: 196–204

Englen MD, Valdez YE, Lehnert NM and Lehnert BE. Granulocyte/macrophage colony-stimulating factor is expressed and secreted in cultures of murine L929 cells. J. Immunol. Methods 1995; 2: 281–283

Faraji F, Karjoo Z, Moghaddam MV, Heidari S, Emameh RZ and Falak R. Challenges related to the immunogenicity of parenteral recombinant proteins: Underlying mechanisms and new approaches to overcome it. Int. Rev. Immunol. 2018; 37: 301–315

Ferguson SM and Camilli P De. Dynamin, a membrane-remodelling GTPase. Nat. Rev. Mol. Cell Biol. 2012; 13: 75–88

Finco DR. Kidney Function. Clin. Biochem. Domest. Anim. 1997; 5: 441–484

Franchini M. The modern treatment of haemophilia: a narrative review. Blood Transfus. 2013; 11: 178–182

Franchini M and Mannucci PM. Past, present and future of hemophilia: a narrative review. Orphanet J. Rare Dis. 2012; 7: 24

Frausto RF and Aldave AJ. Comparing the Transcriptome of Ex Vivo Endothelium with Culutred Human Corneal Endothelial cells with Cultured Human Corneal Endothelial Cells. ARVO Annu. Meet. Abstr. 2014; 55: 3585

Fu RY, Chen AC, Lyle MJ, Chen C-Y, Lien Liu C and Miao CH. CD4+ T Cells Engineered with FVIII-CAR and Murine Foxp3 Suppress Anti-Factor VIII Immune Responses in Hemophilia A Mice. Cell. Immunol. 2020; 358: 104216

Fukuda M. Lysosomal membrane glycoproteins. Structure, biosynthesis, and intracellular trafficking. J. Biol. Chem. 1991; 266: 21327–21330

Furuta K, Walseng E and Roche PA. Internalizing MHC class II–peptide complexes are ubiquitinated in early endosomes and targeted for lysosomal degradation. Proc. Natl. Acad. Sci. 2013; 110: 20188–20193

Gallon M and Cullen PJ. Retromer and sorting nexins in endosomal sorting. Biochem. Soc. Trans. 2015; 43: 33–47

Gan Z, Ram S, Ober RJ and Ward ES. Using multifocal plane microscopy to reveal novel trafficking processes in the recycling pathway. J. Cell Sci. 2013; 126: 1176–1188

Gan Z, Ram S, Vaccaro C, Ober RJ, Sally Ward E, Ward SE and Ward ES. Analyses of the Recycling Receptor, FcRn, in Live Cells Reveal Novel Pathways for Lysosomal Delivery. Traffic 2009; 10: 600–614

Gangloff M. Different dimerisation mode for TLR4 upon endosomal acidification? Trends Biochem. Sci. 2012; 37: 92–98

Gao Z, Bai G, Chen J, Zhang Q, Pan P, Bai F and Geng P. Development, characterization, and evaluation of a fusion protein of a novel glucagon-like peptide-1 (GLP-1) analog and human serum albumin in Pichia pastoris. Biosci. Biotechnol. Biochem. 2009; 73: 688–694

Garagiola I, Palla R and Peyvandi F. Risk factors for inhibitor development in severe hemophilia A. Thromb. Res. 2018; 168: 20–27

Georgescu MT, Lai JD, Hough C and Lillicrap D. War and peace: Factor VIII and the adaptive immune response. Cell. Immunol. 2016; 301: 2–7

Ghetie V, Hubbard JG, Kim J-K, Tsen M-F, Lee Y and Ward ES. Abnormally short serum half-lives of IgG in β2-microglobulin-deficient mice. Eur. J. Immunol. 1996; 26: 690–696

Gillooly DJ, Raiborg C and Stenmark H. Phosphatidylinositol 3-phosphate is found in microdomains of early endosomes. Histochem Cell Biol 2003; 120: 445–453

Gireud-Goss M, Reyes S, Wilson M, Farley M, Memarzadeh K, Srinivasan S, Sirisaengtaksin N, Yamashita S, Tsunoda S, Lang FF, Waxham MN and Bean AJ. Distinct mechanisms enable inward or outward budding from late endosomes/multivesicular bodies. Exp. Cell Res. 2018; 372: 1–15

Goldenring JR. Recycling endosomes. Curr. Opin. Cell Biol. 2015; 35: 117–22

Gotot J, Dhana E, Yagita H, Kaiser R, Ludwig-Portugall I and Kurts C. Antigen-specific Helios − , Neuropilin-1 − Tregs induce apoptosis of autoreactive B cells via PD-L1. Immunol. Cell Biol. 2018; 96: 852–862

Gotot J, Gottschalk C, Leopold S, Knolle PA, Yagita H, Kurts C and Ludwig-Portugall I. Regulatory T cells use programmed death 1 ligands to directly suppress autoreactive B cells in vivo. Proc. Natl. Acad. Sci. U. S. A. 2012; 109: 10468–10473

Gouw SC, van der Bom JG, Ljung R, Escuriola C, Cid AR, Claeyssens-Donadel S, van Geet C, Kenet G, Mäkipernaa A, Molinari AC, Muntean W, Kobelt R, Rivard G, Santagostino E, Thomas A and van den Berg HM. Factor VIII Products and Inhibitor Development in Severe Hemophilia A. N. Engl. J. Med. 2013; 368: 231–239

Grevys A, Nilsen J, Sand KMK, Daba MB, Øynebråten I, Bern M, McAdam MB, Foss S, Schlothauer T, Michaelsen TE, Christianson GJ, Roopenian DC, Blumberg RS, Sandlie I and Andersen JT. A human endothelial cell-based recycling assay for screening of FcRn targeted molecules. Nat. Commun. 2018; 9: 621

Griffiths G, Back R and Marsh M. A quantitative analysis of the endocytic pathway in baby hamster kidney cells. J. Cell Biol. 1989; 109: 2703–2720

Griffiths G, Hoflack B, Simons K, Mellman I and Kornfeld S. The mannose 6-phosphate receptor and the biogenesis of lysosomes. Cell 1988; 52: 329–341

Gruenberg J. The endocytic pathway: A mosaic of domains. Nat. Rev. Mol. Cell Biol. 2001; 2: 721–730

Gruenberg J, Griffiths G and Howell KE. Characterization of the early endosome and putative endocytic carrier vesicles in vivo and with an assay of vesicle fusion in vitro. J. Cell Biol. 1989; 108: 1301–1316

Haigler HT, McKanna JA and Cohen S. Rapid stimulation of pinocytosis in human carcinoma cells A-431 by epidermal growth factor. J. Cell Biol. 1979; 83: 82–90

Hamasaki M, Araki N and Hatae T. Association of early endosomal autoantigen 1 with macropinocytosis in EGF-stimulated a431 cells. Anat. Rec. 2004; 277A: 298–306

Hanyaloglu AC. Advances in Membrane Trafficking and Endosomal Signaling of G Protein-Coupled Receptors. Int. Rev. Cell Mol. Biol. 2018; 339: 93–131

van Haren SD, Herczenik E, ten Brinke A, Mertens K, Voorberg J and Meijer AB. HLA-DR-presented Peptide Repertoires Derived From Human Monocyte-derived Dendritic Cells Pulsed With Blood Coagulation Factor VIII. Mol. Cell. Proteomics 2011; 10: M110.002246

Haridas V, Ranjbar S, Vorobjev IA, Goldfeld AE and Barteneva NS. Imaging flow cytometry analysis of intracellular pathogens. Methods 2017; 112: 91–104

Harris ES and Nelson WJ. VE-Cadherin: At the Front, Center, and Sides of Endothelial Cell Organization and Function. Curr. Opin. Cell Biol. 2010; 22: 651–658

Hart DP. FVIII Immunogenicity - Bioinformatic Approaches to Evaluate Inhibitor Risk in Non-severe Hemophilia A. Front. Immunol. 2020; 11: 1498

Hartenbach S and Fussenegger M. Autoregulated, bidirectional and multicistronic gas-inducible mammalian as well as lentiviral expression vectors. J. Biotechnol. 2005; 120: 83–98

Hausl C, Ahmad RU, Sasgary M, Doering CB, Lollar P, Richter G, Schwarz HP, Turecek PL and Reipert BM. High-dose factor VIII inhibits factor VIII–specific memory B cells in hemophilia A with factor VIII inhibitors. Blood 2005; 106: 3415–3422

Havixbeck JJ, Wong ME, More Bayona JA and Barreda DR. Multi-parametric analysis of phagocyte antimicrobial responses using imaging flow cytometry. J. Immunol. Methods 2015; 423: 85–92

Hazin J, Moldenhauer G, Altevogt P and Brady NR. A novel method for measuring cellular antibody uptake using imaging flow cytometry reveals distinct uptake rates for two different monoclonal antibodies targeting L1. J. Immunol. Methods 2015; 423: 70–77

Heap RE, Luis Marín-Rubio J, Peltier J, Heunis T, Dannoura A, Moore A and Trost M. Proteomics characterisation of the L929 cell supernatant and its role in BMDM differentiation. Life Sci. Alliance 2021; 4: e202000957

Van Helden PMW, Van Haren SD, Fijnvandraat K, Van den Berg HM and Voorberg J. Factor VIII-specific B cell responses in haemophilia A patients with inhibitors. Haemophilia 2010; 16: 35–43

Henley JR, Krueger EWA, Oswald BJ and McNiven MA. Dynamin-mediated Internalization of Caveolae. J. Cell Biol. 1998; 141: 85–99

Hinde E, Digman MA, Welch C, Hahn KM and Gratton E. Biosensor FRET detection by the phasor approach to fluorescence lifetime imaging microscopy (FLIM). Microsc. Res. Tech. 2012; 75: 271

Hinde E, Kong X, Yokomori K and Gratton E. Chromatin Dynamics during DNA Repair Revealed by Pair Correlation Analysis of Molecular Flow in the Nucleus. Biophys. J. 2014; 107: 55–65

Hink MA. Quantifying intracellular dynamics using fluorescence fluctuation spectroscopy. Protoplasma 2014; 251: 307–316

Hirschi KK, Ingram DA and Yoder MC. Assessing identity, phenotype, and fate of endothelial progenitor cells. Arterioscler. Thromb. Vasc. Biol. 2008; 28: 1584–1595

Hoffmann P, Boeld TJ, Eder R, Huehn J, Floess S, Wieczorek G, Olek S, Dietmaier W, Andreesen R and Edinger M. Loss of FOXP3 expression in natural human CD4+CD25+ regulatory T cells upon repetitive in vitro stimulation. Eur. J. Immunol. 2009; 39: 1088–1097

Hogquist KA, Jameson SC, Heath WR, Howard JL, Bevan MJ and Carbone FR. T cell receptor antagonist peptides induce positive selection. Cell 1994; 76: 17–27

Hoon J-LJ-L, Wong W-KW-K and Koh C-GC-G. Functions and Regulation of Circular Dorsal Ruffles. Mol. Cell. Biol. 2012; 32: 4246–4257

Hopkins CR and Trowbridge IS. Internalization and processing of transferrin and the transferrin receptor in human carcinoma A431 cells. J. Cell Biol. 1983; 97: 508–521

Horvath RJ, Nutile-McMenemy N, Alkaitis MS and DeLeo JA. Differential migration, LPS-induced cytokine, chemokine, and NO expression in immortalized BV-2 and HAPI cell lines and primary microglial cultures. J. Neurochem. 2008; 107: 557–569

Hsing LC and Rudensky AY. The lysosomal cysteine proteases in MHC class II antigen presentation. Immunol. Rev. 2005; 207: 229–241

Hu Q, Zhang A, Liu A-G, Wang S-M, Wang Y-Q and Zhang L-Q. A Retrospective Analysis of Intracranial Hemorrhage in Children with Hemophilia A. Curr. Med. Sci. 2018; 38: 875–879

Huotari J and Helenius A. Endosome maturation. EMBO J. 2011; 30: 3481–3500

Hurley JH and Emr SD. The ESCRT Complexes: Structure and Mechanism of a Membrane-Trafficking Network. Annu. Rev. Biophys. Biomol. Struct. 2006; 35: 277–298

Ing M, Gupta N, Teyssandier M, Maillère B, Pallardy M, Delignat S and Lacroix-Desmazes S. Immunogenicity of long-lasting recombinant factor VIII products. Cell. Immunol. 2016; 301: 40–48

Ingram DA, Mead LE, Tanaka H, Meade V, Fenoglio A, Mortell K, Pollok K, Ferkowicz MJ, Gilley D and Yoder MC. Identification of a novel hierarchy of endothelial progenitor cells using human peripheral and umbilical cord blood. Blood 2004; 104: 2752–2760

Iorio A, Stonebraker JS, Chambost H, Makris M, Coffin D, Herr C, Germini F, Stonebraker JS, Iorio A, Byams V, El-Ekiaby M, Makris M, O'Hara J, Chambost H, Pierce GF and Weill A. Establishing the prevalence and prevalence at birth of hemophilia in males a meta-analytic approach using national registries. Ann. Intern. Med. 2019; 171: 542–546

Israel EJ, Taylor S, Wu Z, Mizoguchi E, Blumberg RS, Bhan A and Simister NE. Expression of the neonatal Fc receptor, FcRn, on human intestinal epithelial cells. Immunology 1997; 92: 69–74

Israel EJ, Wilsker DF, Hayes KC, Schoenfeld D and Simister NE. Increased clearance of IgG in mice that lack β2-microglobulin: possible protective role of FcRn. Immunology 1996; 89: 573–578

Ivens IA, Baumann A, McDonald TA, Humphries TJ, Michaels LA and Mathew P. PEGylated therapeutic proteins for haemophilia treatment: a review for haemophilia caregivers. Haemophilia 2013; 19: 11–20

Jameson DM, Ross JA and Albanesi JP. Fluorescence fluctuation spectroscopy: ushering in a new age of enlightment for cellular dynamics. Biophys. Rev. 2009; 1: 105–118

John TA, Vogel SM, Tiruppathi C, Malik AB and Minshall RD. Quantitative analysis of albumin uptake and transport in the rat microvessel endothelial monolayer. Am. J. Physiol. - Lung Cell. Mol. Physiol. 2003; 284: L187–L196

Johnson AO, Subtil A, Petrush R, Kobylarz K, Keller SR and McGraw TE. Identification of an Insulin-responsive, Slow Endocytic Recycling Mechanism in Chinese Hamster Ovary Cells. J. Biol. Chem. 1998; 273: 17968–17977

Jongsma MLM, Berlin I, Wijdeven RHM, Janssen L, Janssen GMC, Garstka MA, Janssen H, Mensink M, van Veelen PA, Spaapen RM and Neefjes J. An ER-Associated Pathway Defines Endosomal Architecture for Controlled Cargo Transport. Cell 2016; 166: 152–166

Jovčevska I and Muyldermans S. The Therapeutic Potential of Nanobodies. BioDrugs 2019 341 2019; 34: 11–26

Jovic M, Sharma M, Rahajeng J and Caplan S. The early endosome: a busy sorting station for proteins at the crossroads. Histol Histopathol. 2010; 25: 99–112

Jung N and Haucke V. Clathrin-Mediated Endocytosis at Synapses. Traffic 2007; 8: 1129–1136

Kanamori M, Nakatsukasa H, Okada M, Lu Q and Yoshimura A. Induced Regulatory T Cells: Their Development, Stability, and Applications. Trends Immunol. 2016; 37: 803–811

Kapus A and Janmey P. Plasma Membrane-Cortical Cytoskeleton Interactions: A Cell Biology Approach with Biophysical Considerations. Compr Physiol 2013; 3: 1231–1281

Kerr MC, Lindsay MR, Luetterforst R, Hamilton N, Simpson F, Parton RG, Gleeson PA and Teasdale RD. Visualisation of macropinosome maturation by the recruitment of sorting nexins. J. Cell Sci. 2006; 119: 3967–3980

Kerr MC and Teasdale RD. Defining Macropinocytosis. Traffic 2009; 10: 364–371

Khaddaj Mallat R, Mathew John C, Kendrick DJ and Braun AP. The vascular endothelium: A regulator of arterial tone and interface for the immune system. Crit. Rev. Clin. Lab. Sci. 2017; 54: 458–470

Khan I and Arany P. Biophysical Approaches for Oral Wound Healing: Emphasis on Photobiomodulation. Adv. Wound Care 2015; 4: 724–737

Kim B, Li J, Jang C and Arany Z. Glutamine fuels proliferation but not migration of endothelial cells. EMBO J. 2017; 36: 2321–2333

Kim J, Bronson CL, Hayton WL, Radmacher MD, Roopenian DC, Robinson JM, Anderson CL, J K, CL B, WL H, MD R, DC R, JM R and CL A. Albumin turnover: FcRn-mediated recycling saves as much albumin from degradation as the liver produces. Am. J. Physiol. Gastrointest. Liver Physiol. 2006; 290: G352–G360

Kim JM, Rasmussen JP and Rudensky AY. Regulatory T cells prevent catastrophic autoimmunity throughout the lifespan of mice. Nat. Immunol. 2007; 8: 191–197

Kirchhausen T and Harrison SC. Protein organization in clathrin trimers. Cell 1981; 23: 755–761

Kitazawa T, Igawa T, Sampei Z, Muto A, Kojima T, Soeda T, Yoshihashi K, Okuyama-Nishida Y, Saito H, Tsunoda H, Suzuki T, Adachi H, Miyazaki T, Ishii S, Kamata-Sakurai M, Iida T, Harada A, Esaki K, Funaki M, Moriyama C, Tanaka E, Kikuchi Y, Wakabayashi T, Wada M, Goto M, Toyoda T, Ueyama A, Suzuki S, Haraya K, Tachibana T, Kawabe Y, Shima M, Yoshioka A and Hattori K. A bispecific antibody to factors IXa and X restores factor VIII hemostatic activity in a hemophilia A model. Nat. Med. 2012; 18: 1570–1574

Kleijmeer MJ, Morkowski S, Griffith JM, Rudensky AY and Geuze HJ. Major histocompatibility complex class II compartments in human and mouse B lymphoblasts represent conventional endocytic compartments. J. Cell Biol. 1997; 139: 639–649

Knobe K and Berntorp E. Haemophilia and Joint Disease: Pathophysiology, Evaluation, and Management: J. Comorbidity 2011; 1: 51–59

Kobayashi H and Fukuda M. Arf6, Rab11 and transferrin receptor define distinct populations of recycling endosomes. Commun. Integr. Biol. 2013; 6: e25036

Koivusalo M, Welch C, Hayashi H, Scott CC, Kim M, Alexander T, Touret N, Hahn KM and Grinstein S. Amiloride inhibits macropinocytosis by lowering submembranous pH and preventing Rac1 and Cdc42 signaling. J. Cell Biol. 2010; 188: 547–563

Kolin DL and Wiseman PW. Advances in image correlation spectroscopy: Measuring number densities, aggregation states, and dynamics of fluorescently labeled macromolecules in cells. Cell Biochem. Biophys. 2007; 49: 141–164

Kolter T and Sandhoff K. Principles of Lysosomal Membrane Digestion: Stimulation of Sphingolipid Degradation by Sphingo-lipid Activator Proteins and Anionic Lysosomal Lipids. Annu. Rev. Cell Dev. Biol. 2005; 21: 81–103

Kontermann RE. Expert Opinion on Biological Therapy Half-life extended biotherapeutics Half-life extended biotherapeutics. Expert Opin. Biol. Ther. 2016; 16: 903–915

Kopecky EM, Greinstetter S, Pabinger I, Buchacher A, Römisch J and Jungbauer A. Mapping of FVIII inhibitor epitopes using cellulose-bound synthetic peptide arrays. J. Immunol. Methods 2006; 308: 90–100

Kuhlmann M, Hamming JBR, Voldum A, Tsakiridou G, Larsen MT, Schmøkel JS, Sohn E, Bienk K, Schaffert D, Sørensen ES, Wengel J, Dupont DM and Howard KA. An Albumin-Oligonucleotide Assembly for Potential Combinatorial Drug Delivery and Half-Life Extension Applications. Mol. Ther. Nucleic Acids 2017; 9: 284–293

Lacroix-Desmazes S, Moreau A, Sooryanarayana, Bonnemain C, Stieltjes N, Pashov A, Sultan Y, Hoebeke J, Kazatchkine MD and Kaveri S V. Catalytic activity of antibodies against factor VIII in patients with hemophilia A. Nat. Med. 1999; 5: 1044–1047

Lacroix-Desmazes S, Navarrete A-M, André S, Bayry J, Kaveri S V. and Dasgupta S. Dynamics of factor VIII interactions determine its immunologic fate in hemophilia A. Blood 2008; 112: 240–249

Lambot N, Lybaert P, Boom A, Delogne-Desnoeck J, Vanbellinghen AM, Graff G, Lebrun P and Meuris S. Evidence for a clathrin-mediated recycling of albumin in human term placenta. Biol. Reprod. 2006; 75: 90–97

Larsen MT, Kuhlmann M, Hvam ML and Howard KA. Albumin-based drug delivery: harnessing nature to cure disease. Mol. Cell. Ther. 2016; 4: 3

Larsen MT, Rawsthorne H, Schelde KK, Dagnaes-Hansen F, Cameron J and Howard KA. Cellular recycling-driven in vivo half-life extension using recombinant albumin fusions tuned for neonatal Fc receptor (FcRn) engagement. J. Control. Release 2018; 287: 132–141

Latvala S, Jacobsen B, Otteneder MB, Herrmann A and Kronenberg S. Distribution of FcRn Across Species and Tissues. J. Histochem. Cytochem. 2017; 65: 321–333

Lawe DC, Chawla A, Merithew E, Dumas J, Carrington W, Fogarty K, Lifshitz L, Tuft R, Lambright D and Corvera S. Sequential Roles for Phosphatidylinositol 3-Phosphate and Rab5 in Tethering and Fusion of Early Endosomes via Their Interaction with EEA1. J. Biol. Chem. 2001; 277: 8611–8617

Lawrence SA, Blankenship R, Brown R, Estwick S, Ellis B, Thangaraju A and Datta-Mannan A. Influence of FcRn binding properties on the gastrointestinal absorption and exposure profile of Fc molecules. Bioorg. Med. Chem. 2021; 32: 115942

Le TP and Chung S. Regulation of apical constriction via microtubule- and Rab11-dependent apical transport during tissue invagination. Mol. Biol. Cell 2021; 32: 1033–1047

Lenting PJ, Denis C V. and Christophe OD. Emicizumab, a bispecific antibody recognizing coagulation factors IX and X: How does it actually compare to factor VIII? Blood 2017; 130: 2463–2468

Lenting PJ, Muczynski V, Aymé G, Denis C V. and Christophe OD. Von Willebrand Factor Interaction with FVIII: Development of Long Acting FVIII Therapies. Blood 2016; 128: SCI-8

Lewis WH. Pinocytosis. Bull. Johns Hopkins Hosp. 1931; 49: 17–27

Li H, Li J, Wasserloos KJ, Wallace C, Sullivan MG, Bauer PM, Donna B, Lee JS, Watkins SC, Croix CMS, Pitt BR and Zhang L. Caveolae-Dependent and -Independent Uptake of Albumin in Cultured Rodent Pulmonary Endothelial Cells. PLoS One 2013; 8: e81903

Li L, Wan T, Wan M, Liu B, Cheng R and Zhang R. The effect of the size of fluorescent dextran on its endocytic pathway. Cell Biol. Int. 2015; 39: 531–539

Li R, Yang H, Jia D, Nie Q, Cai H, Fan Q, Wan L, Li L and Lu X. Fusion to an albumin-binding domain with a high affinity for albumin extends the circulatory half-life and enhances the in vivo antitumor effects of human TRAIL. J. Control. Release 2016; 228: 96–106

Li T, Balthasar JP, Li T and Balthasar JP. FcRn Expression in Wildtype Mice, Transgenic Mice, and in Human Tissues. 2018; 8: 0115

Lieu ZZ and Gleeson PA. Identification of different itineraries and retromer components for endosome-to-Golgi transport of TGN38 and Shiga toxin. Eur. J. Cell Biol. 2010; 89: 379–393

Lillicrap D. Extending half-life in coagulation factors: where do we stand? Thromb. Res. 2008; 122: S2–S8

Lim JP and Gleeson PA. Macropinocytosis : an endocytic pathway for internalising large gulps. Immunol. Cell Biol. 2011; 89: 836–843

Lim JP, Gosavi P, Mintern JD, Ross EM and Gleeson PA. Sorting nexin 5 selectively regulates dorsal-ruffle-mediated macropinocytosis in primary macrophages. J. Cell Sci. 2015; 128: 4407–4419

Lim JP, Teasdale RD and Gleeson PA. SNX5 is essential for efficient macropinocytosis and antigen processing in primary macrophages. Biol. Open 2012; 1: 904–914

Lim JP, Wang JTH, Kerr MC, Teasdale RD and Gleeson PA. A role for SNX5 in the regulation of macropinocytosis. BMC Cell Biol. 2008; 9: 58

Lin XP, Mintern JD and Gleeson PA. Macropinocytosis in Different Cell Types: Similarities and Differences. Membranes 2020; 10: 177

Lin Y, Chang L, Solovey A, Healey JF, Lollar P and Hebbel RP. Use of blood outgrowth endothelial cells for gene therapy for hemophilia A. Blood 2002; 99: 457–62

Lin Y, Weisdorf DJ, Solovey A and Hebbel RP. Origins of circulating endothelial cells and endothelial outgrowth from blood. J. Clin. Invest. 2000; 105: 71–77

Liu C-L, Ye P, Yen BC and Miao CH. In Vivo Expansion of Regulatory T cells With IL-2/IL-2 mAb Complexes Prevents Anti-factor VIII Immune Responses in Hemophilia A Mice Treated With Factor VIII Plasmid-mediated Gene Therapy. Mol. Ther. 2011; 19: 1511–1520

Liu H, Sun M, Liu Z, Kong C, Kong W, Ye J, Gong J, Huang DCS and Qian F. KRAS-enhanced macropinocytosis and reduced FcRn-mediated recycling sensitize pancreatic cancer to albumin-conjugated drugs. J. Control. Release 2019; 296: 40–53

Lois C, Hong EJ, Pease S, Brown EJ and Baltimore D. Germline transmission and tissue-specific expression of transgenes delivered by lentiviral vectors. Science 2002; 295: 868–872

Lommerse PHM, Spaink HP and Schmidt T. In vivo plasma membrane organization: results of biophysical approaches. Biochim. Biophys. Acta 2004; 1664: 119–131

Lotvall J and Valadi H. Cell to Cell Signalling via Exosomes Through esRNA. Cell Adh. Migr. 2007; 1: 156–158

Lou J, Scipioni L, Wright BK, Bartolec TK, Zhang J, Masamsetti VP, Gaus K, Gratton E, Cesare AJ and Hinde E. Phasor histone FLIM-FRET microscopy quantifies spatiotemporal rearrangement of chromatin architecture during the DNA damage response. Proc. Natl. Acad. Sci. 2019; 116: 7323–7332

Lu L and Hong W. From endosomes to the trans-Golgi network. Semin. Cell Dev. Biol. 2014; 31: 30–39

Luzio JP, Pryor PR and Bright NA. Lysosomes: fusion and function. Nat. Rev. Mol. Cell Biol. 2007; 8: 622–632

Lyseng-Williamson KA. Coagulation Factor IX (Recombinant), Albumin Fusion Protein (Albutrepenonacog Alfa; Idelvion®): A Review of Its Use in Haemophilia B. Drugs 2017; 77: 97–106

Mahmoud IS. Endosomal Recycling of Membrane Cargo and Rab-Mediated Golgi Trafficking (PhD Thesis). Melbourne: The University of Melbourne, 2015

Mahmoud IS, Louber J, Dower SK, Verhagen AM and Gleeson PA. Signal dependent transport of a membrane cargo from early endosomes to recycling endosomes. Eur. J. Cell Biol. 2017; 96: 418–431

Mancuso ME, Mahlangu JN and Pipe SW. The changing treatment landscape in haemophilia: from standard half-life clotting factor concentrates to gene editing. Lancet 2021; 397: 630–640

Manders EM, Stap J, Brakenhoff GJ, van Driel R and Aten JA. Dynamics of three-dimensional replication patterns during the S-phase, analysed by double labelling of DNA and confocal microscopy. J. Cell Sci. 1992; 103: 857–862

Manko H, Normant V, Perraud Q, Steffan T, Gasser V, Boutant E, Réal É, Schalk IJ, Mély Y and Godet J. Flim-fret measurements of protein-protein interactions in live bacteria. J. Vis. Exp. 2020; 162: e61602

Mannucci PM. Hemophilia: Treatment options in the twenty-first century. J. Thromb. Haemost. 2003; 1: 1349–1355

Mannucci PM. Hemophilia therapy: the future has begun. Haematologica 2020; 105: 545–553

Mannucci PM and Tuddenham EGD. The Hemophilias - From royal genes to gene therapy. N Engl J Med 2001; 344: 1773–1779

Marsh EW, Leopold PL, Jones NL and Maxfield FR. Oligomerized transferrin receptors are selectively retained by a lumenal sorting signal in a long-lived endocytic recycling compartment. J. Cell Biol. 1995; 129: 1509–22

Martin-Ramirez J, Hofman M, Biggelaar M Van Den, Hebbel RP and Voorberg J. Establishment of outgrowth endothelial cells from peripheral blood. Nat. Protoc. 2012; 7: 1709–1715

Masteller EL, Tang Q and Bluestone JA. Antigen-specific regulatory T cells - Ex vivo expansion and therapeutic potential. Semin. Immunol. 2006; 18: 103–110

Masters JR. HeLa cells 50 years on: the good, the bad and the ugly. Nat. Rev. Cancer 2002; 2: 315–319

Matsui H, Shibata M, Brown B, Labelle A, Hegadorn C, Andrews C, Hebbel RP, Galipeau J, Hough C and Lillicrap D. Ex Vivo Gene Therapy for Hemophilia A That Enhances Safe Delivery and Sustained In Vivo Factor VIII Expression from Lentivirally Engineered Endothelial Progenitors. Stem Cells 2007; 25: 2660–2669

Mattie S, McNally EK, Karim MA, Vali H and Brett CL. How and why intralumenal membrane fragments form during vacuolar lysosome fusion. Mol. Biol. Cell 2017; 28: 309–321

Maxfield FR and McGraw TE. Endocytic recycling. Nat. Rev. Mol. Cell Biol. 2004; 5: 121–132

Mayor S and Pagano RE. Pathways of clathrin-independent endocytosis. Nat. Rev. Mol. Cell Biol. 2007; 8: 603–612

Mayor S, Presley JF and Maxfield FR. Sorting of Membrane Components from Endosomes and Subsequent Recycling to the Cell Surface Occurs by a Bulk Flow Process. J. Cell Biol. 1993; 121: 1257–1269

Mayor S, Sabharanjak S and Maxfield FR. Cholesterol-dependent retention of GPI-anchored proteins in endosomes. EMBO J. 1998; 17: 4626–4638

McGough IJ and Cullen PJ. Recent Advances in Retromer Biology. Traffic 2011; 12: 963–971

McMahon HT and Boucrot E. Molecular mechanism and physiological functions of clathrin-mediated endocytosis. Nat. Rev. Mol. Cell Biol. 2011; 12: 517–533

Medina RJ, O'neill CL, Sweeney M, Guduric-Fuchs J, Gardiner TA, Simpson DA and Stitt AW. Molecular analysis of endothelial progenitor cell (EPC) subtypes reveals two distinct cell populations with different identities. BMC Med. Genomics 2010; 3: 18

Meeks SL and Batsuli G. Hemophilia and inhibitors: current treatment options and potential new therapeutic approaches. Hematol. Am. Soc. Hematol. Educ. Progr. 2016; 2016: 657–662

Meeks SL and Lacroix-Desmazes S. Emerging benefits of Fc fusion technology in the context of recombinant factor VIII replacement therapy. Haemophilia 2020; 26: 958–965

Mehta D and Malik AB. Signaling Mechanisms Regulating Endothelial Permeability. Physiol. Rev. 2006; 86: 279–367

Meißner M. Cellular and Molecular Mechanisms of Immune Tolerance Induction in Hemophilia A (PhD Thesis). Bonn: Rheinische Friedrich-Wilhelms-Universität, 2020

Mellman I. Endocytosis and Molecular Sorting. Annu. Rev. Cell Dev. Biol 1996; 12: 575–625

Merino-Trigo A, Kerr MC, Houghton F, Lindberg A, Mitchell C, Teasdale RD and Gleeson PA. Sorting nexin 5 is localized to a subdomain of the early endosomes and is recruited to the plasma membrane following EGF stimulation. J. Cell Sci. 2004; 117: 6413–6424

Mester S, Evers M, Meyer S, Nilsen J, Greiff V, Sandlie I, Leusen J and Andersen JT. Extended plasma half-life of albumin-binding domain fused human IgA upon pH-dependent albumin engagement of human FcRn in vitro and in vivo. MAbs 2021; 13: e1893888

De Meyer SF, Vanhoorelbeke K, Chuah MK, Pareyn I, Gillijns V, Hebbel RP, siré Collen D, Deckmyn H and VandenDriessche T. Phenotypic correction of von Willebrand disease type 3 blood-derived endothelial cells with lentiviral vectors expressing von Willebrand factor. Blood 2006; 107: 4728–4736

Miao CH. Immunomodulation for inhibitors in hemophilia A: the important role of Treg cells. Expert Rev. Hematol. 2010; 3: 469–483

Miesbach W, O'Mahony B, Key NS and Makris M. How to discuss gene therapy for haemophilia? A patient and physician perspective. Haemophilia 2019; 25: 545–557

Minshall RD, Tiruppathi C, Vogel SM, Niles WD, Gilchrist A, Hamm HE and Malik AB. Endothelial cell-surface gp60 activates vesicle formation and trafficking via G(i)-coupled Src kinase signaling pathway. J. Cell Biol. 2000; 150: 1057–70

Mitta B, Weber CC, Rimann M and Fussenegger M. Design and in vivo characterization of self-inactivating human and non-human lentiviral expression vectors engineered for streptogramin-adjustable transgene expression. Nucleic Acids Res. 2004; 32: e106

Mohrmann K, Gerez L, Oorschot V, Klumperman J and Sluijs P van der. Rab4 Function in Membrane Recycling from Early Endosomes Depends on a Membrane to Cytoplasm Cycle. J. Biol. Chem. 2002; 277: 32029–32035

Montoyo HP, Vaccaro C, Hafner M, Ober RJ, Mueller W and Ward ES. Conditional deletion of the MHC class I-related receptor FcRn reveals the sites of IgG homeostasis in mice. Proc. Natl. Acad. Sci. U. S. A. 2009; 106: 2788–2793

Mony VK, Benjamin S and O'Rourke EJ. A lysosome-centered view of nutrient homeostasis. Autophagy 2016; 12: 619–631

Morosky S, Wells AI, Lemon K, Evans AS, Schamus S, Bakkenist CJ and Coyne CB. The neonatal Fc receptor is a pan-echovirus receptor. Proc. Natl. Acad. Sci. 2019; 116: 3758–3763

van Mourik JA, de Wit TR and Voorberg J. Biogenesis and exocytosis of Weibel-Palade bodies. Histochem. Cell Biol. 2002; 117: 113–122

Mousavi SA, Malerød L, Berg T and Kjeken R. Clathrin-dependent endocytosis. Biochem. J. 2004; 377: 1–16

Nabi IR and Le PU. Caveolae/raft-dependent endocytosis. J. Cell Biol. 2003; 161: 673–677

Nature Publishing Group, 2020: Henrietta Lacks: science must right a historical wrong. https://www.nature.com/articles/d41586-020-02494-z (access date: 23.02.2022)

Nault J-C, Datta S, Imbeaud S, Franconi A, Mallet M, Couchy G, Letouzé E, Pilati C, Verret B, Blanc J-F, Balabaud C, Calderaro J, Laurent A, Letexier M, Bioulac-Sage P, Calvo F and Zucman-Rossi J. Recurrent AAV2-related insertional mutagenesis in human hepatocellular carcinomas. Nat. Genet. 2015; 47: 1187–1193

Navaroli DM, Bellvé KD, Standley C, Lifshitz LM, Cardia J, Lambright D, Leonard D, Fogarty KE and Corvera S. Rabenosyn-5 defines the fate of the transferrin receptor following clathrin-mediated endocytosis. Proc. Natl. Acad. Sci. 2012; 109: E471–E480

Navarrete A, Dasgupta S, Delignat S, Caligiuri G, Christophe OD, Bayry J, Nicoletti A, Kaveri S V. and Lacroix-Desmazes S. Splenic marginal zone antigen-presenting cells are critical for the primary allo-immune response to therapeutic factor VIII in hemophilia A. J. Thromb. Haemost. 2009; 7: 1816–1823

Newton EE, Wu Z and Simister NE. Characterization of basolateral-targeting signals in the neonatal Fc receptor. J. Cell Sci. 2005; 118: 2461–2469

Nielsen E, Severin F, Backer JM, Hyman AA and Zerial M. Rab5 regulates motility of early endosomes on microtubules. Nat. Cell Biol. 1999; 1: 376–382

Nightingale TD, McCormack JJ, Grimes W, Robinson C, Lopes da Silva M, White IJ, Vaughan A, Cramer LP and Cutler DF. Tuning the endothelial response: differential release of exocytic cargos from Weibel-Palade bodies. J. Thromb. Haemost. 2018; 16: 1873–1886

Nilsen J, Bern M, Sand KMK, Grevys A, Dalhus B, Sandlie I and Andersen JT. Human and mouse albumin bind their respective neonatal Fc receptors differently. Sci. Rep. 2018; 8: 14648

Nilsen J, Trabjerg E, Grevys A, Azevedo C, Brennan SO, Stensland M, Wilson J, Sand KMK, Bern M, Dalhus B, Roopenian DC, Sandlie I, Rand KD and Andersen JT. An intact C-terminal end of albumin is required for its long half-life in humans. Commun. Biol. 2020; 3: 181

Nilsson IM, Berntorp E, Loefqvist T and Pettersson H. Twenty-five years' experience of prophylactic treatment in severe haemophilia A and B. J. Intern. Med. 1992; 232: 25–32

Nolan B, Mahlangu J, Perry D, Young G, Liesner R, Konkle B, Rangarajan S, Brown S, Hanabusa H, Pasi KJ, Pabinger I, Jackson S, Cristiano LM, Li X, Pierce GF and Allen G. Long-term safety and efficacy of recombinant factor VIII Fc fusion protein (rFVIIIFc) in subjects with haemophilia A. Haemophilia 2016; 22: 72–80

Norris A and Grant BD. Endosomal microdomains: Formation and function. Curr. Opin. Cell Biol. 2020; 65: 86–95

Nowrouzi A, Penaud-Budloo M, Kaeppel C, Appelt U, Le Guiner C, Moullier P, Kalle C Von, Snyder RO and Schmidt M. Integration Frequency and Intermolecular Recombination of rAAV Vectors in Non-human Primate Skeletal Muscle and Liver. Mol. Ther. 2012; 20: 1177–1186

Nyfeler B, Reiterer V, Wendeler MW, Stefan E, Zhang B, Michnick SW and Hauri HP. Identification of ERGIC-53 as an intracellular transport receptor of α1-antitrypsin. J. Cell Biol. 2008; 180: 705–712

Ober RJ, Martinez C, Lai X, Zhou J and Ward ES. Exocytosis of IgG as mediated by the receptor, FcRn: An analysis at the single-molecule level. Proc. Natl. Acad. Sci. U. S. A. 2014; 101: 11076–11081

Ober RJ, Martinez C, Vaccaro C, Zhou J and Ward ES. Visualizing the site and dynamics of IgG salvage by the MHC class I-related receptor, FcRn. J. Immunol. 2004; 172: 2021–2029

Oganesyan V, Damschroder MM, Cook KE, Li Q, Gao C, Wu H and Dall'Acqua WF. Structural Insights into Neonatal Fc Receptor-based Recycling Mechanisms. J. Biol. Chem. 2014; 289: 7812–7824

Oldenburg J, Austin SK and Kessler CM. ITI choice for the optimal management of inhibitor patients – from a clinical and pharmacoeconomic perspective. Haemophilia 2014; 20: 17–26

Oldenburg J, Mahlangu JN, Kim B, Schmitt C, Callaghan MU, Young G, Santagostino E, Kruse-Jarres R, Negrier C, Kessler C, Valente N, Asikanius E, Levy GG, Windyga J and Shima M. Emicizumab Prophylaxis in Hemophilia A with Inhibitors. N. Engl. J. Med. 2017; 377: 809–818

Ormiston ML, Toshner MR, Kiskin FN, Huang CJZ, Groves E, Morrell NW and Rana AA. Generation and Culture of Blood Outgrowth Endothelial Cells from Human Peripheral Blood. J. Vis. Exp. 2015; 106: e53384

Pálfy M, Reményi A and Korcsmáros T. Endosomal crosstalk: meeting points for signaling pathways. Trends Cell Biol. 2012; 22: 447–456

Palm W. Metabolic functions of macropinocytosis. Philos. Trans. R. Soc. Lond. B. Biol. Sci. 2019; 374: 20180285

Pan C, Kumar C, Bohl S, Klingmueller U and Mann M. Comparative Proteomic Phenotyping of Cell Lines and Primary Cells to Assess Preservation of Cell Type-specific Functions. Mol. Cell. Proteomics 2009; 8: 443–450

Paraan M, Mendez J, Sharum S, Kurtin D, He H and Stagg SM. The structures of natively assembled clathrin-coated vesicles. Sci. Adv. 2020; 6: eaba8397

Park C-Y, Lee DR, Sung JJ and Kim D-W. Genome-editing technologies for gene correction of hemophilia. Hum. Genet. 2016; 135: 977–981

Parton RG and Howes MT. Revisiting caveolin trafficking: the end of the caveosome. J. Cell Biol. 2010; 191: 439–441

Parton RG and Simons K. The multiple faces of caveolae. Nat. Rev. Mol. Cell Biol. 2007 83 2007; 8: 185–194

Patel HH, Murray F and Insel PA. Caveolae as organizers of pharmacologically relevant signal transduction molecules. Annu. Rev. Pharmacol. Toxicol. 2008; 48: 359–391

Pavelka M, Ellinger A, Debbage P, Loewe C, Vetterlein M and Roth J. Endocytic routes to the Golgi apparatus. Histochem. Cell Biol. 1998; 109: 555–570

Pearson RM, Casey LM, Hughes KR, Miller SD and Shea LD. In vivo reprogramming of immune cells: Technologies for induction of antigen-specific tolerance. Adv. Drug Deliv. Rev. 2017; 114: 240–255

Pelkmans L, Bürli T, Zerial M and Helenius A. Caveolin-Stabilized Membrane Domains as Multifunctional Transport and Sorting Devices in Endocytic Membrane Traffic. Cell 2004; 118: 767–780

Pelkmans L and Helenius A. Endocytosis Via Caveolae. Traffic 2002; 3: 311–320

Pelkmans L and Zerial M. Kinase-regulated quantal assemblies and kiss-and-run recycling of caveolae. Nature 2005; 436: 128–133

Peters T. All about albumin : biochemistry, genetics, and medical applications. Clin. Chem. 1997; 43: 2014a – 2015

Petkova SB, Akilesh S, Sproule TJ, Christianson GJ, Al Khabbaz H, Brown AC, Presta LG, Meng YG and Roopenian DC. Enhanced half-life of genetically engineered human IgG1 antibodies in a humanized FcRn mouse model: Potential application in humorally mediated autoimmune disease. Int. Immunol. 2006; 18: 1759–1769

Pfistershammer K, Stöckl J, Siekmann J, Turecek PL, Schwarz HP and Reipert BM. Recombinant factor VII and factor VIII-von Willebrand factor complex do not present danger signals for human dendritic cells. Thromb. Haemost. 2006; 96: 309–316

Pilati D and Howard KA. Albumin-based drug designs for pharmacokinetic modulation. 2020; 16: 783–795

Piper RC and Katzmann DJ. Biogenesis and Function of Multivesicular Bodies. Annu. Rev. Cell Dev. Biol. 2007; 23: 519–547

Piper RC and Luzio JP. Late Endosomes: Sorting and Partitioning in Multivesicular Bodies. Traffic 2001; 2: 612–621

Pitas RE, Boyles J, Mahley RW and Bissell DM. Uptake of chemically modified low density lipoproteins in vivo is mediated by specific endothelial cells. J. Cell Biol. 1985; 100: 103–117

Pols MS and Klumperman J. Trafficking and function of the tetraspanin CD63. Exp. Cell Res. 2009; 315: 1584–1592

Pool JG, Hershgold EJ and Pappenhagen AR. High-potency Antihæmophilic Factor Concentrate prepared from Cryoglobulin Precipitate. Nature 1964; 203: 312

Popova N V, Deyev IE and Petrenko AG. Clathrin-mediated endocytosis and adaptor proteins. Acta Naturae 2013; 5: 62–73

Potente M and Mäkinen T. Vascular heterogeneity and specialization in development and disease. Nat. Rev. Mol. Cell Biol. 2017; 18: 477–494

Prekeris R. Rabs, Rips, FIPs, and Endocytic Membrane Traffic. Sci. World J. 2003; 3: 870–880

Price LKH, Choi HU, Rosenberg L and Stanley ER. The predominant form of secreted colony stimulating factor-1 is a proteoglycan. J. Biol. Chem. 1992; 267: 2190–2199

Priest DG, Solano A, Lou J and Hinde E. Fluorescence fluctuation spectroscopy: an invaluable microscopy tool for uncovering the biophysical rules for navigating the nuclear landscape. Biochem. Soc. Trans. 2019; 47: 1117–1129

Pulix M, Lukashchuk V, Smith DC and Dickson AJ. Molecular characterization of HEK293 cells as emerging versatile cell factories. Curr. Opin. Biotechnol. 2021; 71: 18–24

Pyzik M, Rath T, Kuo TT, Win S, Baker K, Hubbard JJ, Grenha R, Gandhi A, Krämer TD, Mezo AR, Taylor ZS, McDonnell K, Nienaber V, Andersen JT, Mizoguchi A, Blumberg L, Purohit S, Jones SD, Christianson G, Lencer WI, Sandlie I, Kaplowitz N, Roopenian DC and Blumberg RS. Hepatic FcRn regulates albumin homeostasis and susceptibility to liver injury. Proc. Natl. Acad. Sci. 2017; 114: E2862–E2871

Pyzik M, Sand KMK, Hubbard JJ, Andersen JT, Sandlie I and Blumberg RS. The Neonatal Fc Receptor (FcRn): A Misnomer? Front. Immunol. 2019; 10: 1540

Qiao SW, Kobayashi K, Johansen F, Sollid L, Andersen JT, Milford E, Roopenian DC, Lencer W and Blumberg. Dependence of antibody-mediated presentation of antigen on FcRn. Proc. Natl. Acad. Sci. U. S. A. 2008; 105: 9337–9342

Qin JY, Zhang L, Clift KL, Hulur I, Xiang AP, Ren BZ and Lahn BT. Systematic comparison of constitutive promoters and the doxycycline-inducible promoter. PLoS One 2010; 5: e10611

Quinlan GJ, Martin GS and Evans TW. Albumin: Biochemical properties and therapeutic potential. Hepatology 2005; 41: 1211–1219

Racoosin EL and Swanson JA. Macrophage Colony-Stimulating Factor (rM-CSF) Stimulates Pinocytosis In Bone Marrow-Derived Macrophages. J. Exp. Med. 1989; 170: 1635–1648

Racoosin EL and Swanson JA. Macropinosome Maturation and Fusion with Tubular Lysosomes in Macrophages. J. Cell Biol. 1993; 121: 1011–1020

Raheel H, Ghaffari S, Khosraviani N, Mintsopoulos V, Auyeung D, Wang C, Hye Kim Y, Mullen B, Sung H-K, Ho M, Fairn G, Neculai D, Febbraio M, Heit B and Warren Lee XL. CD36 mediates albumin transcytosis by dermal but not lung microvascular endothelial cells: role in fatty acid delivery. Am J Physiol Lung Cell Mol Physiol 2019; 316: 740–750

Rahman A and Swärd K. The role of caveolin-1 in cardiovascular regulation. Acta Physiol. (Oxf). 2009; 195: 231–245

Raiborg C, Bache KG, Gillooly DJ, Madshus IH, Stang E and Stenmark H. Hrs sorts ubiquitinated proteins into clathrin-coated microdomains of early endosomes. Nat. Cell Biol. 2002; 4: 394–398

Rajavel K, Ayash-Rashkovsky M, Tang Y, Gangadharan B, de la Rosa M and Ewenstein B. Co-Prevalence of Pre-Existing Immunity to Different Serotypes of Adeno-Associated Virus (AAV) in Adults with Hemophilia. Blood 2019; 134: 3349

Rangarajan S, Walsh L, Lester W, Perry D, Madan B, Laffan M, Yu H, Vettermann C, Pierce GF, Wong WY and Pasi KJ. AAV5-Factor VIII Gene Transfer in Severe Hemophilia A. N. Engl. J. Med. 2017; 377: 2519–2530

Rath T, Baker K, Dumont JA, Peters RT, Jiang H, Qiao S-W, Lencer WI, Pierce GF and Blumberg RS. Fc-fusion proteins and FcRn: structural insights for longer-lasting and more effective therapeutics. Crit. Rev. Biotechnol. 2013; 35: 235–254

Ravichandran Y, Goud B and Manneville JB. The Golgi apparatus and cell polarity: Roles of the cytoskeleton, the Golgi matrix, and Golgi membranes. Curr. Opin. Cell Biol. 2020; 62: 104–113

Reinisch A, Hofmann N a, Obenauf AC, Kashofer K, Rohde E, Schallmoser K, Flicker K, Lanzer G, Linkesch W, Speicher MR and Strunk D. Humanized large-scale expanded endothelial colony – forming cells function in vitro and in vivo. Blood 2009; 113: 6716–6725

Reipert BM, van den Helden PMW, Schawarz H-P and Hausl C. Mechanisms of action of immune tolerance induction against factor VIII in patients with congenital haemophilia A and factor VIII inhibitors. Br. J. Haematol. 2007; 136: 12–25

Reiss UM, Zhang L and Ohmori T. Hemophilia gene therapy—New country initiatives. Haemophilia 2021; 27: 132–141

Ren M, Xu G, Zeng J, De Lemos-Chiarandini C, Adesnik M and Sabatini DD. Hydrolysis of GTP on rab11 is required for the direct delivery of transferrin from the pericentriolar recycling compartment to the cell surface but not from sorting endosomes. Cell Biol. 1998; 95: 6187–6192

Repessé Y, Dasgupta S, Navarrete A-M, Delignat S, Kaveri S V. and Lacroix-Desmazes S. Mannose-sensitive receptors mediate the uptake of factor VIII therapeutics by human dendritic cells. J. Allergy Clin. Immunol. 2012; 129: 1172–1173

Retamal JS, Ramírez-García PD, Shenoy PA, Poole DP and Veldhuis NA. Internalized GPCRs as Potential Therapeutic Targets for the Management of Pain. Front. Mol. Neurosci. 2019; 12: 273

Ribeiro AG, Alves JEF, Soares JCS, dos Santos KL, Jacob ÍTT, da Silva Ferreira CJ, dos Santos JC, de Azevedo RDS, de Almeida SMV and de Lima M do CA. Albumin roles in developing anticancer compounds. Med. Chem. Res. 2021; 30: 1469–1495

Richter WF, Christianson GJ, Frances N, Grimm HP, Proetzel G and Roopenian DC. Hematopoietic cells as site of first-pass catabolism after subcutaneous dosing and contributors to systemic clearance of a monoclonal antibody in mice. MAbs 2018; 10: 803–813

Rink J, Ghigo E, Kalaidzidis Y and Zerial M. Rab Conversion as a Mechanism of Progression from Early to Late Endosomes. Cell 2005; 122: 735–749

Rocha N and Neefjes J. MHC class II molecules on the move for successful antigen presentation. EMBO J. 2008; 27: 1–5

Rodal SK, Skretting G, Garred Ø, Vilhardt F, Deurs B van and Sandvig K. Extraction of Cholesterol with Methyl-β-Cyclodextrin Perturbs Formation of Clathrin-coated Endocytic Vesicles. Mol. Biol. Cell 1999; 10: 961–974

Rogers B, Dong D, Li Zhijun and Li Zhiyu. Recombinant human serum albumin fusion proteins and novel applications in drug delivery and therapy. Curr. Pharm. Des. 2015; 21: 1899–1907

Roopenian DC and Akilesh S. FcRn: The neonatal Fc receptor comes of age. Nat. Rev. Immunol. 2007; 7: 715–725

Roopenian DC, Christianson GJ, Proetzel G and Sproule TJ. Human FcRn Transgenic Mice for Pharmacokinetic Evaluation of Therapeutic Antibodies Proetzel, G. and Wiles, M. V (eds.). Methods Mol. Biol. 2010; 602: 93–104

Roopenian DC, Christianson GJ, Sproule TJ, Brown AC, Akilesh S, Jung N, Petkova S, Avanessian L, Choi EY, Shaffer DJ, Eden PA and Anderson CL. The MHC Class I-Like IgG Receptor Controls Perinatal IgG Transport, IgG Homeostasis, and Fate of IgG-Fc-Coupled Drugs. J. Immunol. 2003; 170: 3528–3533

Roopenian DC, Low BE, Christianson GJ, Proetzel G, Sproule TJ and Wiles M V. Albumin-deficient mouse models for studying metabolism of human albumin and pharmacokinetics of albumin-based drugs. MAbs 2015; 7: 344–351

Rossow MJ, Sasaki JM, Digman MA and Gratton E. Raster image correlation spectroscopy in live cells. Nat. Protoc. 2010; 5: 1761–1774

Van Roy M, Ververken C, Beirnaert E, Hoefman S, Kolkman J, Vierboom M, Breedveld E, 't Hart B, Poelmans S, Bontinck L, Hemeryck A, Jacobs S, Baumeister J and Ulrichts H. The preclinical pharmacology of the high affinity anti-IL-6R Nanobody® ALX-0061 supports its clinical development in rheumatoid arthritis. Arthritis Res. Ther. 2015; 17: 135

Russo LM, Sandoval RM, McKee M, Osicka TM, Collins AB, Brown D, Molitoris BA and Comper WD. The normal kidney filters nephrotic levels of albumin retrieved by proximal tubule cells: Retrieval is disrupted in nephrotic states. Kidney Int. 2007; 71: 504–513

Sachse M, Ramm G, Strous G and Klumperman J. Endosomes: multipurpose designs for integrating housekeeping and specialized tasks. Histochem. Cell Biol. 2002; 117: 91–104

Sadler JE. Biochemistry and Genetics of von Willebrand factor. Annu. Rev. Biochem. 1998; 67: 395–424

Safinia N, Sagoo P, Lechler R and Lombardi G. Adoptive regulatory T cell therapy: Challenges in clinical transplantation. Curr. Opin. Organ Transplant. 2010; 15: 427–434

Saint-Remy J-MR, Lacroix-Desmazes S and Oldenburg J. Inhibitors in haemophilia: pathophysiology. Haemophilia 2004; 10: 146–151

Sakagami M, Omidi Y, Campbell L, Kandalaft LE, Morris CJ, Barar J and Gumbleton M. Expression and transport functionality of FcRn within rat alveolar epithelium: a study in primary cell culture and in the isolated perfused lung. Pharm. Res. 2006; 23: 270–279

Sakaguchi S, Wing K and Yamaguchi T. Dynamics of peripheral tolerance and immune regulation mediated by Treg. Eur. J. Immunol. 2009; 39: 2331–2336

Sakaguchi S, Yamaguchi T, Nomura T and Ono M. Regulatory T Cells and Immune Tolerance. Cell 2008; 133: 775–787

Sallusto F, Cella M, Danieli C and Lanzavecchia A. Dendritic cells use macropinocytosis and the mannose receptor to concentrate macromolecules in the major histocompatibility complex class II compartment: downregulation by cytokines and bacterial products. J. Exp. Med. 1995; 182: 389–400

Samelson-Jones BJ and Arruda VR. Translational Potential of Immune Tolerance Induction by AAV Liver-Directed Factor VIII Gene Therapy for Hemophilia A. Front. Immunol. 2020; 11: 618

Sánchez LM, Penny DM and Bjorkman PJ. Stoichiometry of the Interaction between the Major Histocompatibility Complex-Related Fc Receptor and Its Fc Ligand. Biochemistry 1999; 38: 9471–9476

Sand KMK, Bern M, Nilsen J, Noordzij HT, Sandlie I, Andersen JT, Knudsen Sand KM, Bern M, Nilsen J, Noordzij HT, Sandlie I and Andersen JT. Unraveling the interaction between FcRn and albumin: Opportunities for design of albumin-based therapeutics. Front. Immunol. 2015; 6: 682

Sand KMK, Dalhus B, Christianson GJ, Bern M, Foss S, Cameron J, Sleep D, Bjørås M, Roopenian DC, Sandlie I and Andersen JT. Dissection of the neonatal Fc receptor (FcRn)-albumin interface using mutagenesis and anti-FcRn albumin-blocking antibodies. J. Biol. Chem. 2014; 289: 17228–17239

Sandvig K, Torgersen ML, Raa HA and Van Deurs B. Clathrin-independent endocytosis: From nonexisting to an extreme degree of complexity. Histochem. Cell Biol. 2008; 129: 267–276

Sankar AD, Weyand AC and Pipe SW. The evolution of recombinant factor replacement for hemophilia. Transfus. Apher. Sci. 2019; 58: 596–600

Sarav M, Wang Y, Hack BK, Chang A, Jensen M, Bao L and Quigg RJ. Renal FcRn Reclaims Albumin but Facilitates Elimination of IgG. J. Am. Soc. Nephrol. 2009; 20: 1941–1952

Sarkar D, Biswas M, Liao G, Seay HR, Perrin GQ, Markusic DM, Hoffman BE, Brusko TM, Terhorst C and Herzog RW. Ex vivo expanded autologous polyclonal regulatory T cells suppress inhibitor formation in hemophilia. Mol. Ther. - Methods Clin. Dev. 2014; 1: 14030

Sawant D V. and Vignali DAA. Once a Treg, always a Treg? Immunol. Rev. 2014; 259: 173–191

Saxena K. Barriers and perceived limitations to early treatment of hemophilia. J. Blood Med. 2013; 4: 49–56

Schenone M, Furie BC and Furie B. The blood coagulation cascade. Curr. Opin. Hematol. 2004; 11: 272–277

Schep SJ, Schutgens REG, Fischer K and Boes ML. Review of immune tolerance induction in hemophilia A. Blood Rev. 2018; 32: 326–338

Schillemans M, Kat M, Westeneng J, Gangaev A, Hofman M, Nota B, van Alphen FPJ, de Boer M, van den Biggelaar M, Margadant C, Voorberg J and Bierings R. Alternative trafficking of Weibel-Palade body proteins in CRISPR/Cas9-engineered von Willebrand factor-deficient blood outgrowth endothelial cells. Res. Pract. Thromb. Haemost. 2019; 3: 718–732

Schmid SL, Fuchs R, Male P and Mellman I. Two distinct subpopulations of endosomes involved in membrane recycling and transport to lysosomes. Cell 1988; 52: 73–83

Schmidt A, Oberle N and Krammer PH. Molecular Mechanisms of Treg-Mediated T Cell Suppression. Front. Immunol. 2012; 3: 51

Schmidt EGW, Hvam ML, Antunes F, Cameron J, Viuff D, Andersen B, Kristensen NN and Howard KA. Direct demonstration of a neonatal Fc receptor (FcRn)-driven endosomal sorting pathway for cellular recycling of albumin. J. Biol. Chem. 2017; 292: 13312–13322

Schmidt MM, Townson SA, Andreucci AJ, King BM, Schirmer EB, Murillo AJ, Dombrowski C, Tisdale AW, Lowden PA, Masci AL, Kovalchin JT, Erbe D V., Wittrup KD, Furfine ES and Barnes TM. Crystal Structure of an HSA/FcRn Complex Reveals Recycling by Competitive Mimicry of HSA Ligands at a pH-Dependent Hydrophobic Interface. Structure 2013; 21: 1966–1978

Schröder BA, Wrocklage C, Hasilik A and Saftig P. The proteome of lysosomes. Proteomics 2010; 10: 4053–4076

Schulte S. Innovative coagulation factors: albumin fusion technology and recombinant single-chain factor VIII. Thromb. Res. 2013; 131: S2–S6

Scott DW. Genetic Engineering of T Cells for Immune Tolerance. Mol. Ther. - Methods Clin. Dev. 2020; 16: 103–107

Seaman MNJ. Identification of a novel conserved sorting motif required for retromer-mediated endosome-to-TGN retrieval. J. Cell Sci. 2007; 120: 2378–2389

Shahane G, Ding W, Palaiokostas M and Orsi M. Physical properties of model biological lipid bilayers: insights from all-atom molecular dynamics simulations. J. Mol. Model. 2019; 25: 76

Shi Q, Rafii S, Wu Hong-De M, Wijelath ES, Yu C, Ishida A, Fujita Y, Kothari S, Mohle R, Sauvage LR, Moore MAS, Storb RF and Hammond WP. Evidence for Circulating Bone Marrow-Derived Endothelial Cells. Blood 1998; 92: 362–367

Shih S, Katzmann D, Schnell J, Sutano M, Emr S and Hicke L. Epsins and Vps27p/Hrs contain ubiquitin-binding domains that function in receptor endocytosis. Nat. Cell Biol. 2002; 4: 389–393

Shima M, Hanabusa H, Taki M, Matsushita T, Sato T, Fukutake K, Fukazawa N, Yoneyama K, Yoshida H and Nogami K. Factor VIII-Mimetic Function of Humanized Bispecific Antibody in Hemophilia A. N. Engl. J. Med. 2016; 374: 2044–2053

Sicard A, Boardman DA and Levings MK. Taking regulatory T-cell therapy one step further. Curr. Opin. Organ Transplant. 2018; 23: 509–515

Silveira PA, Johnson E, Chapman HD, Bui T, Tisch RM and Serreze D V. The preferential ability of B lymphocytes to act as diabetogenic APC in NOD mice depends on expression of self-antigen-specific immunoglobulin receptors. Eur. J. Immunol. 2002; 32: 3657–3666

Simister NE and Ahouse JC. The structure and evolution of FcRn. Res. Immunol. 1996; 147: 333–337

Simister NE and Mostov KE. An Fc receptor structurally related to MHC class I antigens. Nature 1989; 337: 184–187

Sitar ME and Cakatay U. Human Serum Albumin and Its Relation with Oxidative Stress. Clin. Lab. 2013; 59: 945–952

Sleep D. Albumin and its application in drug delivery. Expert Opin. Drug Deliv. 2015; 12: 793–812

Sleep D, Cameron J and Evans LR. Albumin as a versatile platform for drug half-life extension. Biochim. Biophys. Acta - Gen. Subj. 2013; 1830: 5526–5534

van der Sluijs P, Hull M, Webster P, Mâle P, Goud B and Mellman I. The small GTP-binding protein rab4 controls an early sorting event on the endocytic pathway. Cell 1992; 70: 729–740

Smedsrød B, Pertoft H, Eriksson S, Fraser JR and Laurent TC. Studies in vitro on the uptake and degradation of sodium hyaluronate in rat liver endothelial cells. Biochem. J. 1984; 223: 617–626

Smirnov A, Solga MD, Lannigan J and Criss AK. High-Throughput Particle Uptake Analysis by Imaging Flow Cytometry. Curr. Protoc. Cytom. 2017; 80: 11.22.1-11.22.17

Smith BM, Lyle MJ, Chen AC, Miao CH and Al SET. Antigen - specific in vitro expansion of factor VIII - specific regulatory T cells induces tolerance in hemophilia A mice. J. Thromb. Haemost. 2020; 18: 328–340

Soran H and Younis N. Insulin detemir: a new basal insulin analogue. Diabetes, Obes. Metab. 2006; 8: 26–30

Soucie JM, Evatt B and Jackson D. Occurrence of hemophilia in the United States. Am. J. Hematol. 1998; 59: 288–294

Sowa G. Caveolae, caveolins, cavins, and endothelial cell function: New insights. Front. Physiol. 2012; 2: 120

Sposini S and Hanyaloglu AC. Spatial encryption of G protein-coupled receptor signaling in endosomes; Mechanisms and applications. Biochem. Pharmacol. 2017; 143: 76

Stanford S, Pink R, Creagh D, Clark A, Lowe G, Curry N, Pasi J, Perry D, Fong S, Hayes G, Chandrakumaran K and Rangarajan S. Adenovirus-associated antibodies in UK cohort of hemophilia patients: A seroprevalence study of the presence of adenovirus-associated virus vector–serotypes AAV5 and AAV8 neutralizing activity and antibodies in patients with hemophilia A. Res. Pract. Thromb. Haemost. 2019; 3: 261–267

Steinman L, Ho PP, Robinson WH, Utz PJ and Villoslada P. Antigen-specific tolerance to self-antigens in protein replacement therapy, gene therapy and autoimmunity. Curr. Opin. Immunol. 2019; 61: 46–53

Stewart SA, Dykxhoorn DM, Palliser D, Mizuno H, Yu EY, An DS, Sabatini DM, Chen IS, Hahn WC, Sharp PA, Weinberg RA and Novina CD. Lentivirus-delivered stable gene silencing by RNAi in primary cells. RNA 2003; 9: 493–501

Story CM, Mikulska JE and Simister NE. A major histocompatibility complex class I-like Fc receptor cloned from human placenta: possible role in transfer of immunoglobulin G from mother to fetus. J. Exp. Med. 1994; 180: 2377–2381

Subramanian GM, Fiscella M, Lamousé-Smith A, Zeuzem S and McHutchison JG. Albinterferon α-2b: A genetic fusion protein for the treatment of chronic hepatitis C. Nat. Biotechnol. 2007; 25: 1411–1419

Sudlow G, Birkett DJ and Wade DN. The Characterization of Two Specific Drug Binding Sites on Human Serum Albumin. Mol. Pharmacol. 1975; 11: 824–832

Suetsugu S, Yamazaki D, Kurisu S and Takenawa T. Differential Roles of WAVE1 and WAVE2 in Dorsal and Peripheral Ruffle Formation for Fibroblast Cell Migration. Dev. Cell 2003; 5: 595–609

Swanson JA. Phorbol esters stimulate macropinocytosis and solute flow through macrophages. J. Cell Sci. 1989; 94: 135–142

Swanson JA. Shaping cups into phagosomes and macropinosomes. Nat. Rev. Mol. Cell Biol. 2008 98 2008; 9: 639–649

Swanson JA and Watts C. Macropinocytosis. Trends Cell Biol. 1995; 5: 424–428

Takata S, Wada H, Tamura M, Koide T, Higaki M, Mikura S, Yasutake T, Hirao S, Nakamura M, Honda K, Nagatomo T, Tanaka Y, Sohara E, Watanabe M, Yokoyama T, Saraya T, Kurai D, Ishii H and Goto H. Kinetics of c-reactive protein (CRP) and serum amyloid A protein (SAA) in patients with community-acquired pneumonia (CAP), as presented with biologic half-life times. Biomarkers 2011; 16: 530–535

Takenaka E, Van Vo A, Yamashita-Kanemaru Y, Shibuya A and Shibuya K. Selective DNAM-1 expression on small peritoneal macrophages contributes to CD4+ T cell costimulation. Sci. Rep. 2018; 8: 15180

Tenten V, Menzel S, Kunter U, Sicking E-M, van Roeyen CRC, Uhlig S, LAnzmich R, Willemsen B, Dijkman H, Grepl M, Wild K, Kriz W, Smeets B, Fliege J and Moeller MJ. Albumin is recycled from the primary urine by tubular transcytosis. J. Am. Soc. Nephrol. 2013; 24: 1966–1980

Tesar DB and Björkman PJ. An intracellular traffic jam: Fc receptor-mediated transport of immunoglobulin G. Curr. Opin. Struct. Biol. 2010; 20: 226–233

The Human Protein Atlas, 2021a: FCGRT blood. https://www.proteinatlas.org/ENSG00000104870-FCGRT/blood (access date: 23.09.2021)

The Human Protein Atlas, 2021b: FCRGT cell type. https://www.proteinatlas.org/ENSG00000104870-FCGRT/celltype (access date: 23.09.2021)

The Human Protein Atlas, 2021c: FOXP3 cell. https://www.proteinatlas.org/ENSG00000049768-FOXP3/cell (access date: 23.09.2021)

Tiruppathi C, Finnegan A and Malik AB. Isolation and characterization of a cell surface albumin-binding protein from vascular endothelial cells. Proc. Natl. Acad. Sci. U. S. A. 1996; 93: 250–4

Tiruppathi C, Song W, Bergenfeldt M, Sass P and Malik AB. Gp60 activation mediates albumin transcytosis in endothelial cells by tyrosine kinase-dependent pathway. J. Biol. Chem. 1997; 272: 25968–25975

Toh WH, Louber J, Mahmoud IS, Chia J, Bass GT, Dower SK, Verhagen AM, Gleeson PA and Gleeson PA. FcRn mediates fast recycling of endocytosed albumin and IgG from early macropinosomes in primary macrophages. J. Cell Sci. 2020; 133: jcs235416

Tooze J and Hollinshead M. Tubular early endosomal networks in AtT20 and other cells. J. Cell Biol. 1991; 115: 635–653

Tran THT, Zeng Q and Hong W. VAMP4 cycles from the cell surface to the trans-Golgi network via sorting and recycling endosomes. J. Cell Sci. 2007; 120: 1028–1041

Traub LM and Bonifacino JS. Cargo Recognition in Clathrin-Mediated Endocytosis. Cold Spring Harb. Perspect. Biol. 2013; 5: a016790

Turk B and Turk V. Lysosomes as ‘Suicide Bags’ in Cell Death: Myth or Reality? J. Biol. Chem. 2009; 284: 21783–21787

Ullrich O, Reinsch S, Urbé S, Zerial M and Parton RG. Rab11 Regulates Recycling through the Pericentriolar Recycling Endosome. J. Cell Biol. 1996; 135: 913–924

Unger RE, Krump-Konvalinkova V, Peters K and James Kirkpatrick C. In Vitro Expression of the Endothelial Phenotype: Comparative Study of Primary Isolated Cells and Cell Lines, Including the Novel Cell Line HPMEC-ST1.6R. Microvasc. Res. 2002; 64: 384–397

Ungewickell E. Clathrin: A good view of a shapely leg. Curr. Biol. 1999; 9: R32–R35

UniProt Consortium, 2021: UniProtKB - P00451 (FA8_HUMAN). https://www.uniprot.org/uniprot/P00451 (access date: 23.09.2021)

Urbé S, Huber LA, Zerial M, Tooze SA and Parton RG. Rab11, a small GTPase associated with both constitutive and regulated secretory pathways in PC12 cells. FEBS Lett. 1993; 334: 175–182

Valentino LA, Kempton CL, Kruse-Jarres R, Mathew P, Meeks SL and Reiss UM. US Guidelines for immune tolerance induction in patients with haemophilia a and inhibitors. Haemophilia 2015; 21: 559–567

Vargas J, Gusella GL, Najfeld V, Klotman ME and Cara A. Novel integrase-defective lentiviral episomal vectors for gene transfer. Hum. Gene Ther. 2004; 15: 361–372

Vaughn DE, Milburn CM, Penny DM, Martin WL, Johnson JL and Bjorkman PJ. Identification of critical IgG binding epitopes on the neonatal Fc receptor. J. Mol. Biol. 1997; 274: 597–607

Villaseñor R, Kalaidzidis Y and Zerial M. Signal processing by the endosomal system. Curr. Opin. Cell Biol. 2016; 39: 53–60

Vischer U and Wagner D. CD63 is a component of Weibel-Palade bodies of human endothelial cells. Blood 1993; 82: 1184–1191

Van Vliet C, Thomas EC, Merino-Trigo A, Teasdale RD and Gleeson PA. Intracellular sorting and transport of proteins. Prog. Biophys. Mol. Biol. 2003; 83: 1–45

Vogel SM, Minshall RD, Pilipović M, Tiruppathi C and Malik AB. Albumin uptake and transcytosis in endothelial cells in vivo induced by albumin-binding protein. Am. J. Physiol. - Lung Cell. Mol. Physiol. 2001; 281: L1512–L1522

Waldmann TA, Strober W and Blaese RM. Metabolism of Immunoglobulins. Prog. Immunol. 1971891–903

Walsh CE, Jiménez-Yuste V, Auerswald G and Granchar S. The burden of inhibitors in haemophilia patients. Thromb. Haemost. 2016; 116 Suppl: S10–S17

Wang JTH, Teasdale RD and Liebl D. Macropinosome quantitation assay. MethodsX 2014; 1: 36–41

Ward ES, Martinez C, Vaccaro C, Zhou J, Tang Q and Ober RJ. From Sorting Endosomes to Exocytosis: Association of Rab4 and Rab11 GTPases with the Fc Receptor, FcRn, during Recycling. Mol. Biol. Cell 2005; 16: 2028–2038

Ward ES and Ober RJ. Chapter 4 Multitasking by Exploitation of Intracellular Transport Functions: The Many Faces of FcRn. Adv. Immunol. 2009; 103: 77–115

Ward ES, Zhou J, Ghetie V and Ober RJ. Evidence to support the cellular mechanism involved in serum IgG homeostasis in humans. Int. Immunol. 2003; 15: 187–195

Watt SM, Gschmeissner SE and Bates PA. PECAM-1: Its expression and function as a cell adhesion molecule on hemopoietic and endothelial cells. Leuk. Lymphoma 1995; 17: 229–244

Van Weering JRT, Sessions RB, Traer CJ, Kloer DP, Bhatia VK, Stamou D, Carlsson SR, Hurley JH and Cullen PJ. Molecular basis for SNX-BAR-mediated assembly of distinct endosomal sorting tubules. EMBO J. 2012; 31: 4466–4480

Weflen A, Baier N, Tang Q, Van den Hof M, Blumberg RS, Lencer WI and Massol R. Multivalent immune complexes divert FcRn to lysosomes by exclusion from recycling sorting tubules. Mol. Biol. Cell 2013; 24: 2398–2405

Weingartner E and Golding A. Direct control of B cells by Tregs: An opportunity for long-term modulation of the humoral response. Cell. Immunol. 2017; 318: 8–16

Welz T, Wellbourne-Wood J and Kerkhoff E. Orchestration of cell surface proteins by Rab11. Trends Cell Biol. 2014; 24: 407–415

Wernick NLB, Haucke V and Simister NE. Recognition of the Tryptophan-based Endocytosis Signal in the Neonatal Fc Receptor by the μ Subunit of Adaptor Protein-2. J. Biol. Chem. 2005; 280: 7309–7316

West AP and Bjorkman PJ. Crystal Structure and Immunoglobulin G Binding Properties of the Human Major Histocompatibility Complex-Related Fc Receptor. Biochemistry 2000; 39: 9698–9708

West AP, Herr AB and Bjorkman PJ. The Chicken Yolk Sac IgY Receptor, a Functional Equivalent of the Mammalian MHC-Related Fc Receptor, Is a Phospholipase A2 Receptor Homolog. Immunity 2004; 20: 601–610

White GC 2nd, Rosendaal F, Aledort LM, Lusher JM, Rothschild C and Ingerslev J. Definitions in hemophilia. Recommendation of the scientific subcommittee on factor VIII and factor IX of the scientific and standardization committee of the International Society on Thrombosis and Haemostasis. Thromb. Haemost. 2001; 85: 560

Wight J, Paisley S and Knight C. Immune tolerance induction in patients with haemophilia A with inhibitors: a systematic review. Haemophilia 2003; 9: 436–463

Wilson NS and Villadangos JA. Regulation of Antigen Presentation and Cross-Presentation in the Dendritic Cell Network: Facts, Hypothesis, and Immunological Implications. Adv. Immunol. 2005; 86: 241–305

De Wit H, Lichtenstein Y, Geuze HJ, Kelly RB, Van Der Sluijs P and Klumperman J. Synaptic Vesicles Form by Budding from Tubular Extensions of Sorting Endosomes in PC12 Cells. Mol. Biol. Cell 1999; 10: 4163–4176

Wroblewska A, Reipert BM, Pratt KP and Voorberg J. Dangerous liaisons: how the immune system deals with factor VIII. J. Thromb. Haemost. 2013; 11: 47–55

Wu Z and Simister NE. Tryptophan- and Dileucine-based Endocytosis Signals in the Neonatal Fc receptor. J. Biol. Chem. 2001; 276: 5240–5247

Yamasaki K, Chuang VTG, Maruyama T and Otagiri M. Albumin–drug interaction and its clinical implication. Biochim. Biophys. Acta - Gen. Subj. 2013; 1830: 5435–5443

Yamazaki S, Iyoda T, Tarbell K, Olson K, Velinzon K, Inaba K and Steinman RM. Direct Expansion of Functional CD25+ CD4+ Regulatory T Cells by Antigen-processing Dendritic Cells. J. Exp. Med. 2003; 198: 235–247

Ye C, Brand D and Zheng SG. Targeting IL-2: an unexpected effect in treating immunological diseases. Signal Transduct. Target. Ther. 2018; 3: 2

Yoshizawa T, Nozawa R-S, Jia TZ, Saio T and Mori E. Biological phase separation: cell biology meets biophysics. Biophys. Rev. 2020; 12: 519–539

Yu N, Li Xiaomei, Song W, Li D, Yu D, Zeng X, Li M, Leng X and Li Xiangpei. CD4+CD25+CD127low/− T Cells: A More Specific Treg Population in Human Peripheral Blood. Inflammation 2012; 35: 1773–1780

Yuan J, Xu WW, Jiang S, Yu H and Poon HF. The Scattered Twelve Tribes of HEK293. Biomed. Pharmacol. J. 2018; 11: 621–623

Yumoto R, Suzuka S, Oda K, Nagai J and Takano M. Endocytic Uptake of FITC-Albumin by Human Alveolar Epithelial Cell Line A549. Drug Metab. Pharmacokinet. 2012; 27: 336–343

Zaman R, Islam RA, Ibnat N, Othman I, Zaini A, Lee CY and Chowdhury EH. Current strategies in extending half-lives of therapeutic proteins. J. Control. Release 2019; 301: 176–189

Zhang J, Vernes JM, Wen X, Oh E, Scales SJ and Meng YG. Reproducible quantification of IgG uptake at endogenous and overexpressed FcRn levels at pH 7.4: Comparison of a wild type IgG and a stronger FcRn binding variant. J. Immunol. Methods 2020; 480: 112767

Zhao X, Zhang G, Liu S, Xie Z, Wei W, Gao Correspondence GF and Et Al Z. Human Neonatal Fc Receptor Is the Cellular Uncoating Receptor for Enterovirus B. Cell 2019; 177: 1553–1565

Zhou K, Wang Y, Huang X, Luby-Phelps K, Sumer BD and Gao J. Tunable, Ultrasensitive pH-Responsive Nanoparticles Targeting Specific Endocytic Organelles in Living Cells. Angew. Chemie Int. Ed. 2011; 50: 6109–6114

Zhu X, Meng G, Dickinsion BL, Li X, Mizoguchi E, Miao L, Wang Y, Rober C, Wu B, Smith PD, Lencer WI and Blumberg RS. MHC Class I-Related Neonatal Fc Receptor for IgG Is Functionally Expressed in Monocytes, Intestinal Macrophages and Dendritic Cells. J Immunol 2001; 166: 3266–3276